Project No. 15-7983

Steady-State Thermal-Hydraulic Analysis and Bowing Reactivity Evaluation Methods Based on Neutron and Gamma Transport Calculations

Reactor Concepts Research Development and Demonstration (RCRD&D)

Janelle Wharry
Purdue University

Collaborators
University of Michigan

Thomas Sowinski, Federal POC
Matthew Denman, Technical POC

NEUP Nuclear Energy University Programs
U.S. Department of Energy

UM/NRDSL-18/09

Steady-State Thermal-Hydraulic Analysis and Bowing Reactivity Evaluation Methods Based on Neutron and Gamma Transport Calculations

W. S. Yang, P. Deng, G. Yang, and B. K. Jeon
Department of Nuclear Engineering and Radiological Sciences
University of Michigan

J. Wharry and T. Jing
School of Nuclear Engineering
Purdue University

T. K. Kim
Nuclear Engineering Division
Argonne National Laboratory

December 29, 2018

Executive Summary

With the advancement of computer technology, the variational nodal transport code VARIANT is now routinely used for sodium-cooled fast reactor (SFR) design analysis. In particular, VARIANT transport calculations are usually performed for whole core neutronics analyses and for fuel cycle analyses with REBUS-3. However, the steady-state thermal-hydraulics analysis with the SE2-ANL coed and the assembly bowing reactivity calculation with the structural analysis with the NUBOW-3D code are still performed with the DIF3D finite difference diffusion theory code. Furthermore, the DIF3D diffusion calculation for these applications is performed with only six triangular meshes per hexagonal assembly, and the SE2-ANL code determines the pin power distributions approximately by assuming that the power distribution within an assembly is separable in the radial and axial directions.

In order to overcome the limitations and to improve the accuracy of the existing methods, it was proposed to develop the relevant computational methods based on the transport calculations with the VARIANT and PROTEUS-SN codes. The objectives of this study are to develop a new heating calculation method based on the coupled neutron and gamma transport calculations with VARIANT, to implement the new heating calculation method into the SE2-ANL steady-state thermal-hydraulics analysis code with improved numerical algorithms and additional capabilities for automatic flow allocation calculations, and to develop a method to calculate bowing reactivity coefficients based on the VARIANT core solutions and the PROTEUS-SN assembly solutions, which can be used in NUBOW-3D calculations.

A new, coupled neutron and gamma heating calculation procedure has been developed based on VARIANT transport calculations. In the new heating calculation procedure, the neutron flux distribution is first determined by solving an eigenvalue transport problem using the VARIANT transport code. Using the calculated neutron flux, the intra-nodal gamma source distributions are calculated to be consistent with the neutron flux distribution with the GAMSOR code. For this, the GAMSOR code has been updated to generate the intra-nodal gamma source distributions in the form of the VARSRC dataset of VARIANT. With this gamma source distribution, the gamma flux distribution is determined by solving a fixed-source gamma transport problem using VARIANT again. With the neutron and gamma flux distributions, the heat generation rates are evaluated at individual fuel pins and assembly duct walls, without assuming separable axial and radial profiles for the intra-assembly power distribution.

For pin and duct wall power evaluation, a method has been developed to reconstruct higher-order intra-assembly neutron and gamma flux distributions from the VARIANT solutions. The intra-nodal neutron and gamma fluxes are constructed for each node using the corresponding flux moment solutions and the three-dimensional basis functions of VARIANT. The continuous flux distribution is then evaluated along each pin and the duct mid-wall for subsequent power density calculations. The heat generation rates in fuel pins and duct walls are calculated using the evaluated neutron and gamma fluxes and the corresponding KERMA (Kinetic Energy Release in MAterials) factors. To reduce the computational time and memory requirements, a user option is available to approximate the axial power distribution in each pin or duct wall segment within a VARIANT node by a quadratic polynomial. The polynomial is determined to preserve the power densities at the top and bottom of the pin or duct segment as

well as the segment-averaged value. The developed power evaluation scheme has been implemented in a computer code called CURVE (Computational Utility to Reconstruct VARIANT solution for power Evaluation). The basic functionalities of CURVE have been verified using an analytic benchmark problem and a simple three-dimensional core problem. Additional tests have been performed by calculating pin powers for the ABR-1000 metal core design and comparing the results with the values obtained with the RCT code. The resulting segment-averaged pin power densities of CURVE agreed well with the RCT results within 2% difference. The discrepancy is mainly due to the multi-step interpolation scheme of RCT to determine the planar flux distribution using the DIF3D-Nodal solution based on the transverse integration method.

Verification tests of the new heating calculation method have been performed by comparing the assembly and pin power distributions with the reference Monte Carlo solution for the ABTR benchmark problem. Coupled neutron and gamma heating calculations were performed with VARIANT P_5 transport and P_1 diffusion calculations. VARIANT diffusion calculations were performed to quantify the transport effects on the pin power evaluations. Comparison of assembly power distributions showed that for most of the fuel assemblies, the assembly powers obtained from VARIANT calculations agreed very well with the reference MCNP6 solution within 1% and the transport solution yielded more accurate results than the diffusion solution. For fuel assemblies, the RMS error of the transport solution was 0.36% while the RMS error of the diffusion solution was 0.80%. For non-fueled assemblies, the RMS error of the transport solution was 2.1% and the diffusion solution showed an RMS error of 3.7%. The intra-nodal pin power distributions were compared for an inner core fuel assembly IC33, a fuel test assembly MC41, and an outer core fuel assembly OC52, which showed significant intra-assembly flux variations. In general, the pin segment powers determined from VARIANT transport calculations agreed well with the reference MCNP6 results with a maximum deviation of 4.15% in assembly OC52 and a RMS deviation of 1.13% in all tested assemblies. The P_1 diffusion calculations with the same pin power reconstruction scheme increased the maximum and RMS deviations to 5.19% and 1.80%, respectively. The performance of the new heating calculation scheme has also been compared with the existing heating calculation scheme for the ABTR benchmark. The pin segment powers were calculated using both schemes for the fuel assemblies IC33 and OC52 and compared to the reference MCNP6 results. The existing pin power reconstruction scheme of SE2-ANL based on the DIF3D finite difference diffusion calculations increased the maximum and RMS deviations to 6.45% and 1.96%, respectively.

Additional verification tests on the new heating calculation method were performed using the EBR-II Run 138B benchmark problem. The assembly power distribution in the core was calculated and compared to the reference MCNP6 results. The assembly powers in the core obtained from VARIANT diffusion calculations showed a maximum error of -2.86% for fuel assemblies and 11.70% for structural assemblies and a RMS error of 1.36% for fuel assemblies and 10.33% for structure assemblies. Because of the significant transport effect in the small EBR-II core, the maximum and RMS errors in assembly powers were significantly reduced with the VARIANT transport calculations. The maximum error was reduced to 0.68% for fuel assemblies and to 4.05% for structure assemblies and the RMS error was reduced to 0.34% for fuel assemblies and 3.37% for structure assemblies. In addition, the pin power calculation scheme was tested by comparing the pin segment powers in a driver fuel assembly and a blanket assembly with the corresponding MCNP6 reference results. For the driver fuel

assembly, the VARIANT/CURVE results showed a maximum pin power error of -4.36% at the top of active core. For the blanket assembly, which showed an assembly power error of 5.88%, the CURVE computed pin segment powers based on the VARIANT transport solutions showed a maximum error of 11.38%.

The new, coupled neutron and gamma heating calculation scheme has been incorporated in the SE2-ANL code. Several improvements have also been made on the computational methods and models. First, the Cheng-Todreas correlations have been implemented for better prediction of the mixing parameters. The limit on the axial mesh size due to the numerical instability problem of the current explicit difference scheme for axial discretization has also been eliminated by replacing the explicit difference scheme with the θ-method. This allows the use of the inter-assembly gap flow model with much smaller number of axial meshes. Furthermore, an automated flow allocation scheme has been implemented to determine assembly flow rates such that the peak cladding mid-wall temperatures of individual orifice zones are equalized over the burn cycle. To incorporate these improvements, the SE-ANL code has been restructured and a large fraction of it has been completely rewritten, resulting in a new version named SE2-UM.

To verify the SE2-UM code, full-core subchannel analyses were performed for the 1000-MWt Advanced Burner Reactor (ABR-1000) metal core design using both the SE2-UM and the existing SE2-ANL codes. Orifice zones and the corresponding assembly flow rates were determined with the SE2-ANL code. The same orifice zones and flow rates were used for the temperature calculations with the SE2-UM code. SE2-ANL was interfaced with the existing heating calculation scheme based on DIF3D finite difference diffusion solutions while SE2-UM was interfaced with the new heating calculation scheme based on VARIANT transport solutions. Non-negligible deviations in the mixed mean outlet temperatures were observed in the control and reflector assemblies. The maximum difference in the mixed mean outlet temperature was 14.3 °C, which occurred in a reflector assembly. The major differences between the two subchannel analyses included the differences in the heat source distributions and in the inter-assembly heat transfer models. In order to eliminate the impact of the difference in the heat source distributions, the same pin power distribution from the existing heating calculation scheme was used in both the SE2-ANL and the SE2-UM calculations. To eliminate the impact of the difference in the inter-assembly heat transfer models, two SE2-ANL subchannel analyses were performed with both the inter-assembly conduction model and inter-assembly gap flow model. With the same heat source distribution but different inter-assembly heat transfer models, the maximum differences in mixed mean outlet temperatures among fuel, control, and reflector assemblies were 0.3°C, 2.1°C, and 2.7°C, respectively. When the inter-assembly gap flow model was used both in SE2-UM and SE2-ANL, the differences in the coolant outlet temperatures were further reduced. The maximum temperature differences among the fuel, reflector assemblies were 0.2°C and 1.8 °C, respectively. However, there were relatively large differences between SE2-UM and SE2-ANL results in two control assemblies, i.e., the central assembly and the tenth assembly of the seventh ring. These differences were due to the influence of inconsistent boundary conditions in two models. From the above comparisons, it was concluded that the observed differences in mixed mean outlet temperature were mainly due to the different heat source distributions obtained with the DIF3D diffusion calculations for SE2-ANL and with the VARIANT transport calculations for SE2-UM.

To examine the calculation accuracy of SE2-UM further, the coolant outlet temperatures of the EBR-II reactor were calculated for three cycles of Run 163A, Run 164A, and Run 165A and compared with the measured values. The results showed that the coolant outlet temperatures calculated with SE2-UM and SE2-ANL agreed well. The maximum difference between these two calculation results were -11.0 °C, 10.0 °C and -5.1 °C in Run 163A, 164A, and 165A, respectively. Except for four assemblies 2B1, 7A3, 7D4, and 16E9, whose thermocouple readings appear to be biased, the root mean square deviations of the 18 calculated temperatures with SE2-UM from the measured values were all 7.0 °C for Run 163A, 164A, and 165A. Except for these four assemblies, the maximum differences between the calculated temperatures with SE2-UM and the measured values were 12.1 °C, 12.7 °C and 11.2 °C in Run 163A, 164A, and 165A, respectively.

The fully automatic orifice zoning and flow allocation capability of SE2-UM was tested using the ABR-1000 metal core design. In the ABR-1000 problem, all the assemblies were grouped into fourteen orifice zones. The first six orifice zones were fueled orifice zones, the seventh orifice zone was for the control assemblies, and the other orifices zone were for the reflector and shield assemblies. The flow rates of fueled orifice zones were iteratively determined to equalize the peak 2σ cladding middle wall temperatures. After three iterations, the maximum difference of peak 2σ cladding middle wall temperatures among fueled orifice zones was reduced to 0.3 °C. The maximum of peak 2σ cladding inner wall temperatures at BOEC and EOEC were 638.8 °C and 636.4 °C, respectively. These peak 2σ cladding inner wall temperatures at BOEC and EOEC satisfy the design limit based on the fuel-cladding eutectic temperature of 650 °C with a sufficient margin.

A perturbation theory method for accurate evaluation of the reactivity worth of the assembly displacement has been developed based on the global VARIANT solutions with homogenized assembly models and the local PROTEUS-SN solutions with heterogeneous single assembly models. A new numerical scheme of perturbation calculation was developed. In the proposed numerical scheme, the perturbation calculation is performed by following the material movement, which is analogous to the Lagrangian frame of reference in a fluid field. This scheme provides a unique convenience for modeling heterogeneous assembly displacements by eliminating the need to consider complex intersections of finite element meshes of PROTEUS-SN and shifted assemblies. Discretized formulation was derived based on the finite element method and the spherical harmonics method.

A computer code RAINBOW was developed to calculate the reactivity changes due to assembly bowing in sodium cooled fast rectors. Assembly bowing is modeled by shifting axially discretized assembly segments, and heterogeneous assembly configurations are represented by unstructured finite element meshes. A perturbation theory calculation capability has been implemented in RAINBOW to calculate the reactivity changes for the displacements of axial assembly segments in each of six directions normal to the duct wall surfaces. Numerical tests of the displacement worth calculation capability were performed using 2D mini-core model, 3D mini-core model, and AFR-100 model. Reference solutions were obtained from MCNP6 Monte Carlo simulations by the difference in eigenvalue between the perturbed and unperturbed cases.

Three 2D mini-core models were derived from the ABTR core design. The test results showed that the assembly displacement worths obtained from RAINBOW perturbation calculations agreed very well with the MCNP6 results. Statistical analysis showed that the

RAINBOW results were statistically consistent with the MCNP6 results. Three 3D mini-core models were derived by extruding the 2D models in axial direction with 100 cm in height. Each assembly was divided into 10 equal axial segments, and the perturbation calculations were performed for the displacements of the upper five axial segments because of axial symmetry. The results of single assembly segment displacement showed limited agreement with MCNP6 reference results mainly due to the MCNP6 statistical uncertainties since the displacement of single axial segment results in a tiny change in eigenvalue.

In order to introduce a large perturbation relative to the standard deviation of MCNP6 results, the six assemblies in the third ring were simultaneously shifted outward from the core center from their original positions. For 13 out of 15 perturbed cases considered, the RAINBOW results agreed with the reference MCNP6 results within two standard deviation of the MCNP6 results. However, the displacements of segments 3 and 4 in the mini-core model B with control assemblies out showed exceptionally large differences. By recalculating the reference solutions by the statistical average of five independent MCNP6 simulations with different random seed numbers, it was found that the observed deviations are due to the underestimated standard deviations in single MCNP6 simulations. When the statistically estimated MCNP6 reference solutions were used, the RAINBOW perturbation theory calculation results agreed well with the reference solutions within one standard deviation for 14 cases out of 15 and within two standard deviations for all 15 cases.

The reactivity change due to displacements of individual assembly segments were calculated for the AFR-100 core using RAINBOW. In the RAINBOW calculations, the reactivity worth of each segment due to directional displacement were computed by shifting each segment by 1.5 mm in six planar directions. The RAINBOW calculation results were spot-checked by comparing the reactivity change due to outward shifting of six fuel assembly in the outer core. Partially heterogeneous assembly model of AFR-100 was built with the MCNP6, in which the assembly duct and inter-assembly gap were explicitly modeled while all the pins and sodium coolant within duct were homogenized. By comparing two MCNP6 simulation results separately obtained with unperturbed and shifted assemblies, the total reactivity change due to the 2 mm displacements in 36 segments of six fuel assemblies was -7.69 $\pm$ 1.36 pcm. Comparatively, the directional perturbation calculation with RAINBOW resulted in -6.14 pcm reactivity change, which was within 2σ uncertainty of the reference result. Considering that the MCNP6 uncertainty was underestimated because of the dependence of fission source distributions in successive cycles, the RAINBOW code agreed with the MCNP6 reference calculation statistically.

Table of Contents

List of Figures

List of Tables

1. Introduction

To support the national missions on the sodium-cooled fast reactor (SFR) development, a wide range of modeling and simulation tools were developed as schematically shown in Fig. 1.1 for major components. Most of these codes were initiated more than twenty years ago and designed to accommodate the computing resources, tools and methods that were available at that time. For example, the neutronics analysis code DIF3D [1] was based on the broad-group diffusion theory approximation. Since then, considerable advances in methods and codes have been made along with the advancement of computer technology. Now the VARIANT transport code [2] is routinely used for whole core neutronics analyses based on homogenized assembly models and for fuel cycle analyses with the REBUS-3 code [3]. Significant improvements have also been made in the area of nuclear data and multi-group cross section generation, resulting in the state-of-the-art code MC^2-3 [4].

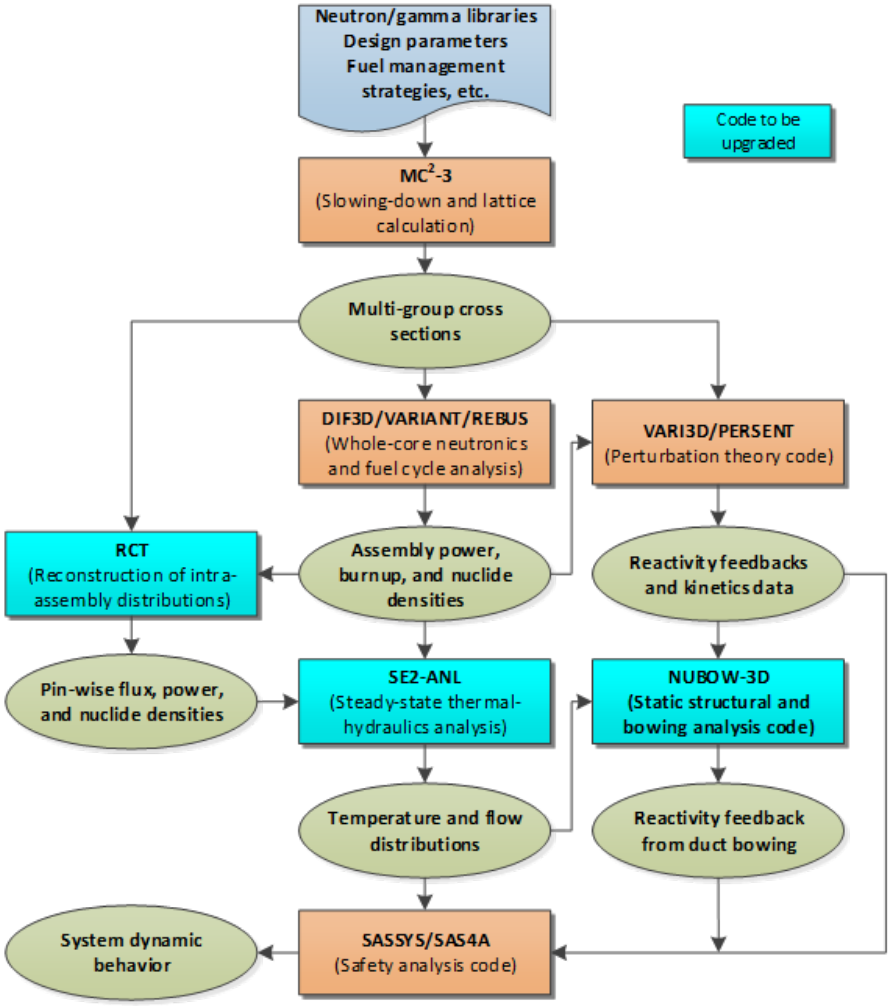

Fig. 1.1 Suite of U.S. Fast Reactor Analysis Codes

For reactivity and sensitivity coefficient calculations, the generalized perturbation theory code VARI3D based on the diffusion theory code has been extended to the PERSENT [5] code

based on the transport theory. In addition, as part of the Nuclear Energy Advanced Modeling and Simulation (NEAMS) program of the Department of Energy, Office of Nuclear Energy (DOE-NE), the Simulation-based High-efficiency Advanced Reactor Prototyping (SHARP) suite of codes is being developed for advanced reactor core simulation, including the neutron transport code PROTEUS [6], the computational fluid dynamics code Nek5000 [7], and the structural mechanics code Diablo [8]. The set of SHARP simulation tools will provide a highly detailed description of the reactor core and the nuclear plant behavior by exploiting the power of near peta-scale computers.

However, several codes based on the broad-group diffusion approximation are still utilized in the fast reactor design and analysis. In particular, the SE2-ANL [9] code for steady-state thermal-hydraulics analysis and the NUBOW-3D [10] code to estimate the reactivity feedback due to assembly bowing still use the neutron flux, gamma flux, and/or adjoint neutron flux from diffusion calculations. Once the high-fidelity SHARP codes are fully developed, they could be used for whole-core thermal-hydraulic analysis and assembly bowing reactivity evaluation. However, it would take significant time and efforts to complete the development. In addition, these high-fidelity tools are being developed aiming at high-performance computing platforms, which would not be available to most designers in near future.

As a near-term alternative to the high-fidelity SHARP codes, we proposed to develop practical tools for the DOE-NE's Advanced Reactor Technology (ART) campaign. In order to overcome the limitations and to improve the accuracy of the existing methods based on the diffusion theory, it was proposed to develop the relevant computational methods based on the transport calculations with the VARIANT and PROTEUS-SN [11] codes. The variational nodal transport code VARIANT solves the steady-state neutron transport equation for Cartesian and hexagonal core geometries with homogenized assemblies using the complete spherical harmonics expansion for angular treatment. The PROTEUS-SN code is a discrete ordinate transport code based on the unstructured finite element mesh, and thus it allows the explicit representation of detailed geometry for reactor simulations.

The objectives of this study were to develop a new heating calculation method based on the coupled neutron and gamma transport calculations with VARIANT, to implement the new heating calculation method into the SE2-ANL steady-state thermal-hydraulics analysis code with improved numerical algorithms and additional capabilities for automatic flow allocation calculations, and to develop a method to calculate bowing reactivity coefficients based on the VARIANT core solutions and the PROTEUS-SN assembly solutions, which can be used in NUBOW-3D calculations. The enhanced computational capabilities and improved prediction accuracies for the steady-state temperature distributions and the reactivity feedback due to assembly bowing would allow to explore a broader range of design space, incorporate innovative design features, and contribute to reducing the economic penalties due to the conservative design margins to accommodate the prediction uncertainties.

In this study, a new, coupled neutron and gamma heating calculation scheme has been developed to determine the pin power distributions more accurately by eliminating the limitations of the current procedure based on the DIF3D finite difference diffusion theory calculations [12,13]. For this, the GAMSOR code [14,15] has been extended to generate the intra-nodal gamma source distribution to be consistent with the trial functions of VARIANT. In the new heating calculation procedure, the neutron flux distribution is determined first by

solving an eigenvalue transport problem using VARIANT. The obtained neutron flux is then used in GAMSOR to calculate the gamma source distribution. Using this gamma source distribution, the gamma flux distribution is determined by solving a fixed-source transport problem using VARIANT again. Using the computed neutron and gamma flux distributions, the power distribution in each fuel pin and duct wall is determined using a new utility code CURVE (Computational Utility to Reconstruct VARIANT solution for power Evaluation), which has been developed to evaluate the VARIANT flux solution at each fuel pin position and along the duct mid-wall. For each pin segment contained in a VARIANT node, the axial power shape is represented as a quadratic profile.

The SE2-ANL code has been modified to interface with the new, coupled neutron and gamma heating calculation scheme. In addition, several improvements have been made on the computational methods and models of SE2-ANL [16,17]. The Cheng-Todreas correlations [18] have been implemented for better prediction of the mixing parameters. The limit on the axial mesh size due to the numerical instability problem of the current explicit difference scheme for axial discretization has also been eliminated by replacing the explicit difference scheme with the θ-method of the SLTHEN code [19]. This allows the use of the inter-assembly gap flow model with much smaller number of axial meshes. Furthermore, an automated flow allocation scheme has been implemented to determine assembly flow rates such that the peak cladding mid-wall temperatures of individual orifice zones are equalized over the burn cycle. To incorporate these improvements, the SE-ANL code has been restructured and a large fraction of it has completely be rewritten, resulting in a new version named SE2-UM [17].

A perturbation theory method has been developed for efficient evaluation of the assembly bowing reactivity coefficients in sodium cooled fast reactors [20,21]. Assembly bowing is modeled by shifting axially discretized assembly segments, and heterogeneous assembly configurations are represented by unstructured finite element meshes. Perturbation theory calculations are performed by following material movements, which provides unique convenience for modeling heterogeneous assembly displacements by eliminating the need to consider complex intersections of geometrical meshes and shifted assemblies. Forward and adjoint flux distributions in heterogeneous assemblies are reconstructed using the VARIANT transport solutions for homogenized-assembly core models and the PROTEUS-SN transport solutions for heterogeneous single-assembly models. This perturbation theory method has been implemented into a computer code RAINBOW (ReActivity INduced by assembly BOWing) [22].

This report is organized as follows. The overall computational procedures for the steady-state thermal-hydraulics analysis with SE2-UM and the assembly bowing reactivity estimation with NUBOW-3D are discussed in Section 2, followed by three parallel sections for newly developed coupled neutron and gamma heating, stead-state thermal-hydraulics, and assembly bowing reactivity coefficient calculations. Sections 3 presents the new, coupled neutron and gamma heating calculation method based on VARIANT transport solutions. Section 4 discusses the steady-state thermal-hydraulic analysis methods of the SE2-UM code. Section 5 describes the perturbation theory method for bowing reactivity coefficient calculation implemented in the RAINBOW code. At last, Section 6 provides the concluding remarks.

2. Overview of Overall Computational Procedures

The overall computational procedures for steady-state thermal-hydraulic and assembly bowing reactivity calculations with newly developed codes SE2-UM and RAINBOW are illustrated in Fig. 2.1. The overall procedure for the assembly bowing reactivity calculation with NUBOW-3D consists of two major branches. One is the whole-core subchannel analysis using SE2-UM to determine proper flow allocations to individual assemblies and the resulting temperature distributions in fuel pins and assembly ducts. This steady-state thermal-hydraulics analysis is interfaced with the coupled neutron and gamma heating calculation based on the VARIANT nodal transport solutions. The other is the calculation of the assembly bowing reactivity coefficients with RAINBOW using the VARIANT transport solutions for homogenized-assembly core models and the PROTEUS-SN transport solutions for heterogeneous single-assembly models.

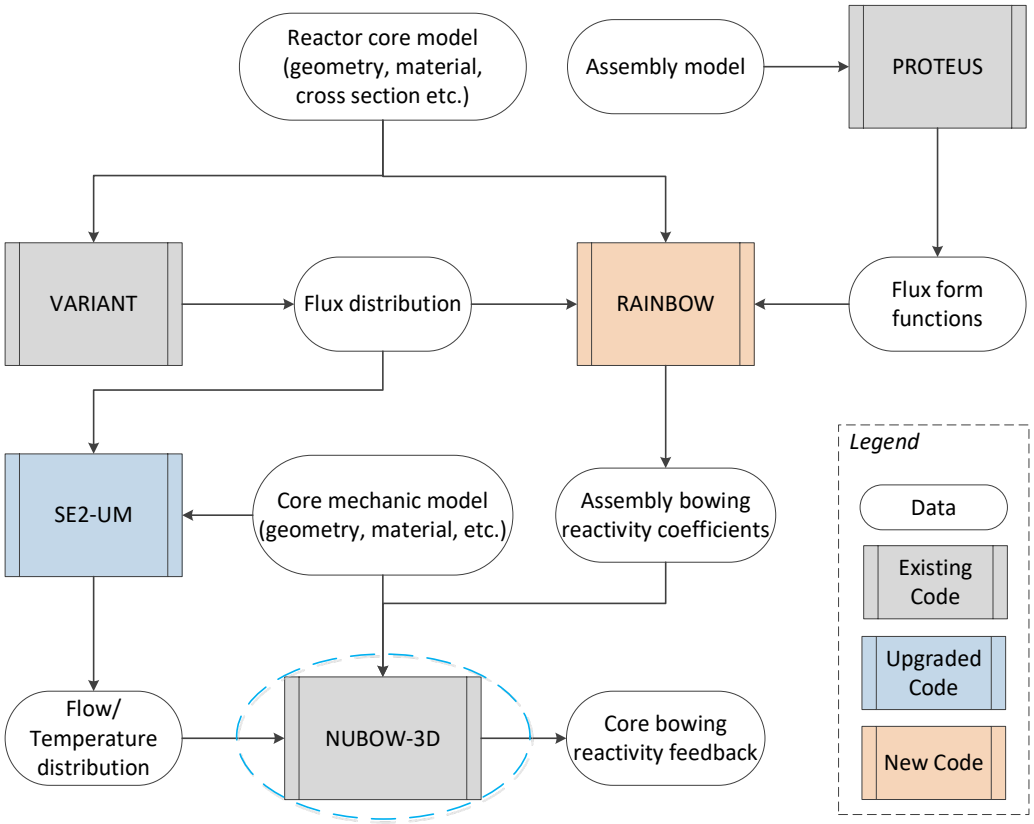

Fig. 2.1 Steady-State Thermal-Hydraulic Analysis and Bowing Reactivity Evaluation

In the SE2-UM thermal-hydraulic analysis, orifice zoning of assemblies and flow allocation to the assemblies in each orifice zone are iteratively determined with the overall goal of equalizing fuel pin damage accrual and thus pin reliability. Specifically, the assembly flow rates are determined such that the peak cladding mid-wall temperatures of individual fuel assemblies are equalized over a fuel cycle. This goal is approximately achieved by determining orifice zoning and assembly flow rates such that the peak temperature at the beginning of cycle (BOC) and that at the end of cycle (EOC) are equalized. As schematically shown in Fig. 2.2,

the calculation of in-core temperature distributions starts with the REBUS-3 fuel cycle analysis to determine the fuel compositions at BOC and EOC. Using the obtained region dependent nuclide densities at BOC and EOC, composition dependent multigroup neutron and gamma cross sections are generated using the MC^2-3 code for the subsequent heating calculations. The atom densities in each composition used in cross section generation are determined by averaging the atom densities at the BOC and EOC. If necessary, such as with a large variation in fuel composition through the fuel cycle, the cross sections can be generated using the specific fuel compositions at BOC and EOC.

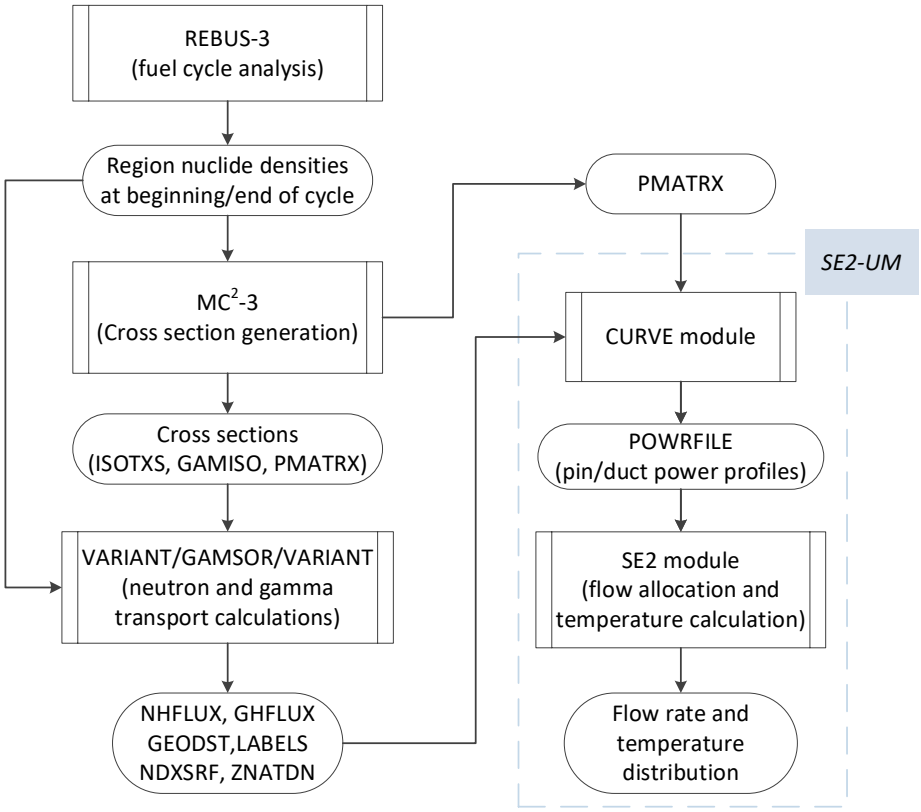

Fig. 2.2 Overall Computational Procedure to Determine In-core Temperature Distribution

The coupled neutron and gamma heating calculations are performed in the VARIANT/GAMSOR/VARIANT procedure. In the new heating calculation scheme, the neutron flux distribution is determined first by solving an eigenvalue transport problem using VARIANT. The obtained neutron flux is then used in GAMSOR to calculate the gamma source distribution. Using this gamma source distribution, the gamma flux distribution is determined by solving a fixed-source transport problem using VARIANT again. The detailed pin power distribution is then calculated in the CURVE module of SE2-UM by post-processing the VARIANT flux solutions stored in the interface files NHFLUX and GHFLUX. The heating cross sections are provided through the PMATRX dataset. Details of the new heating calculation scheme and interface files are provided in Section 3. The resulting heat source distributions are written in the dataset POWRFILE and transferred to the SE2 module of SE2-UM. The assembly flow rates and corresponding temperature distributions are iteratively determined in SE2 calculations to meet the equalized peak fuel cladding temperature condition

mentioned above. The detailed physics models and numerical methods of SE2-UM are discussed in Section 4.

The calculated assembly duct-wall temperatures with SE2-UM are passed to the structural analysis code NUBOW-3D to determine the deformed assembly configurations, which is out of the scope of this report. To evaluate the assembly boing reactivity, a deformed assembly is modeled by dividing an assembly into multiple axial segments and allowing different amount of displacement for individual segments. Assuming that the reactivity changes linearly with small assembly displacements, the reactivity change due to assembly bowing is calculated by combining a set of pre-calculated reactivity worth coefficients of each assembly segment per unit displacement in each of six directions normal to the assembly duct walls, which are obtained from a RAINBOW calculation, and the actual displacements of individual segments determined from a NUBOW-3D calculation. Fig. 2.3 shows the computational procedure to calculate the bowing reactivity coefficients using the RAINBOW code.

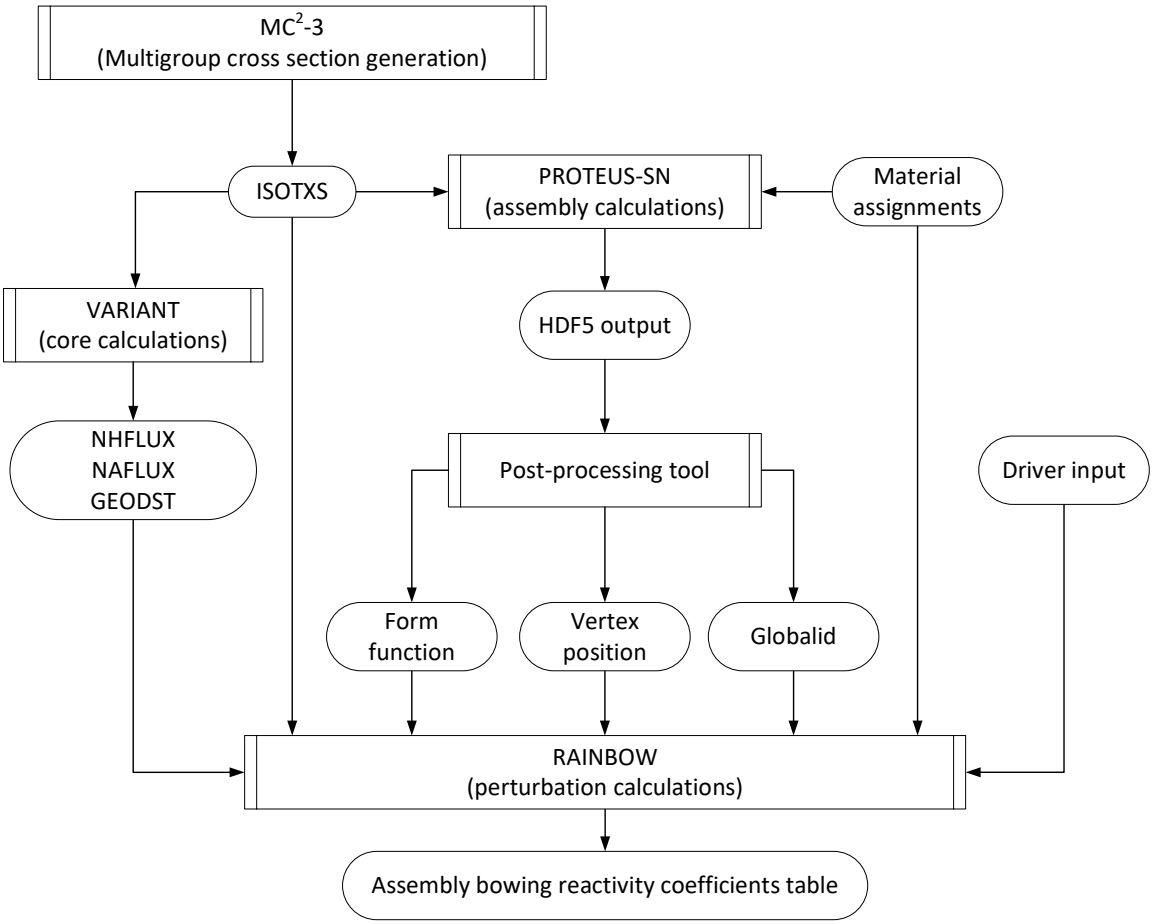

Fig. 2.3 Overall Solution Procedure for Calculating Bowing Reactivity Coefficients

Starting with the multigroup cross section generation using MC^2-3, this procedure involves a sequence of neutronics calculations along with the RAIBOW perturbation calculation. With the multigroup cross sections written in the ISOTXS format, two types of neutron transport calculation are performed. One is the full core VARIANT calculations with homogenized

assembly models, with which the global distributions of forward and adjoint angular fluxes are calculated and stored in the datasets NHFLUX and NAFLUX, respectively. The other is the PROTEUS-SN calculations for single heterogeneous assembly models, which provide the forward and adjoint angular flux distributions in each assembly type, from which the flux form functions are derived. The HDF5 [23] format output of PROTEUS-SN is processed by a utility program to obtain the finite-element mesh grid representing the heterogeneous assembly configuration. Since the material displacements in deformed assemblies are relatively small, in the RAINBOW perturbation calculation, the flux distribution in a heterogeneous assembly in the core is approximately retrieved by superimposing the local flux form function derived from the heterogeneous assembly solution of PROTEUS-SN on the global flux distribution of the VARIANT transport solution. The reconstructed flux distributions were verified to be sufficiently close to the reference flux distributions obtained from the full core PROTEUS-SN calculation with heterogeneous assembly models. Details of the developed perturbation theory method and the implementation in the RAINBOW code are presented in Section 5.

3. Coupled Neutron and Gamma Heating Calculation

The current coupled neutron and gamma heating calculation methodology for the steady-state thermal-hydraulics analyses with SE2-ANL was developed in late 1980s at Argonne National Laboratory (ANL) [14,15]. The cross sections were generated using the MC^2-2 code [24], and the neutron and gamma flux distributions were calculated with the triangular-z, finite-difference diffusion theory option of the DIF3D code [1] with only six triangular meshes per hexagonal assembly. The neutron flux distribution is determined first by solving an eigenvalue problem using DIF3D. The obtained neutron flux is then used in GAMSOR to calculate the gamma source distribution in the triangular-z mesh. Using this gamma source distribution, the gamma flux distribution is determined by solving a fixed-source problem using DIF3D again. For the subchannel analysis with SE2-ANL, the intra-assembly power distribution is reconstructed from the DIF3D diffusion flux solution by assuming the separability of the axial and planar flux distributions within an assembly [9]. This separability assumption could introduce significant errors in the pin power distribution near an inserted control-rod assembly or a reflector assembly, where the separability approximation becomes invalid. To overcome the limitations in the existing heating calculation scheme, a new, coupled neutron and gamma heating calculation scheme based on the MC^2-3 cross section generation and VARIANT nodal transport calculation has been developed. Fig. 3.1 shows the overall calculation procedure for the new heating calculation scheme.

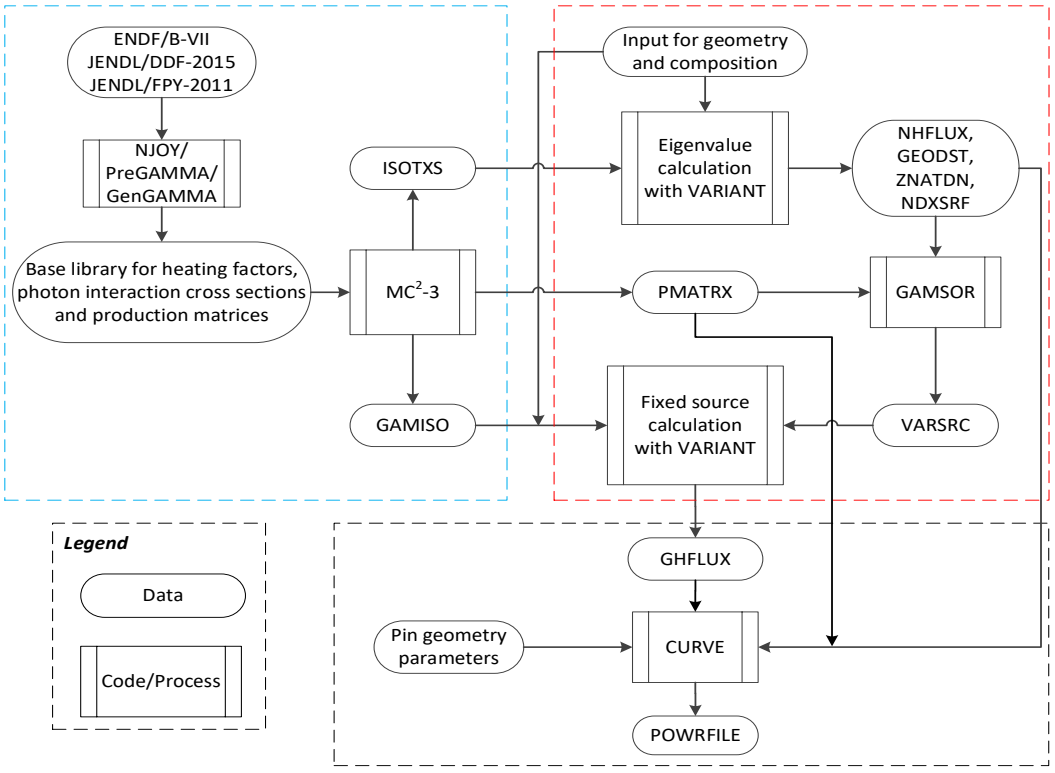

Fig. 3.1 Overall Computational Procedure for Coupled Neutron and Gamma Heating Calculation Based on VARIANT Nodal Transport Solutions

As shown in Fig. 3.1, the new heating calculation scheme consists of three major computational blocks. In the first block enclosed by dashed blue lines, three cross section datasets are generated using the MC^2-3 code: the neutron interaction cross section file ISOTXS, the gamma interaction cross section file GAMISO, and the PMATRX file containing the gamma production matrices and isotopic neutron and gamma heating or KERMA (Kinetic Energy Release in Materials) factors [25]. The second block enclosed by dashed red lines is the coupled neutron and gamma transport calculations using the VARIANT and GAMSOR codes. The neutron flux distribution is determined first by solving an eigenvalue transport problem using VARIANT. The obtained neutron flux solution is written into the dataset NHFLUX which is used in GAMSOR to calculate the gamma source distribution. With this gamma source distribution, the gamma flux distribution is determined by solving a fixed-source gamma transport problem using VARIANT again. The resulting gamma flux solution is written in the dataset GHFLUX, which has the same format as NHFLUX. In the third block enclosed by dashed black lines, the heat generation rates in individual fuel pins and duct walls are evaluated using the newly developed CURVE code. The evaluated power distributions are written into the code-dependent dataset POWRFILE.

In the following subsections, these three computation blocks are described in detail along with the verification test results of the new heating calculation scheme.

3.1. Multigroup Cross Section Generation

The MC^2-3 code was initially developed to generate multigroup neutron cross sections for fast reactor applications [26]. Later, it was extended to generate gamma production cross sections, photo-atomic (i.e., gamma) interaction cross sections, and neutron and gamma heating cross sections [27]. The NJOY code [25] was used to prepare the base gamma libraries of MC^2-3, including isotopic heating or KERMA factors, photon-atomic interaction cross sections, and photon production matrices. These cross sections were generated in 2,082 neutron and 21 gamma group structures. However, the delayed gamma production was not included and the resonance self-shielding was not accounted for neutron heating cross sections. The composition-dependent photon spectrum was not considered either. By eliminating these limitations of the existing libraries, new base gamma libraries of MC^2-3 have been generated based on the ENDF/B-VII data in a 94 gamma-group structure, and gamma spectrum calculation capabilities have been added to MC^2-3 [28].

3.1.1. Updated Gamma Libraries of MC^2-3

The code system and data sets used in generating the new gamma libraries of MC^2-3 are illustrated in Fig. 3.2. The NJOY code is used to generate the prompt gamma production matrices and the photo-atomic interaction cross sections as well as the isotopic neutron and gamma KERMA factors at the infinite dilute condition. At this stage, the 1/E weighting spectrum is used for group condensation. The NJOY input files are prepared by a newly developed utility code PreGAMMA, which was referred to as PMCS in Ref. 27. The PreGAMMA code also prepares the input files for the post-processing code GenGAMMA that converts the NJOY output in the GENDF format [25] into the gamma libraries of MC^2-3, i.e.,

the prompt photon production matrices, photo-atomic interaction cross sections, and neutron and gamma heating and damage factors. In order to include the delayed gamma and delayed beta contributions in the heating calculation, which were lacking in the existing MC^2-3 gamma libraries, the PreGAMMA code retrieves the delayed gamma and beta production data directly from the ENDF and JENDL libraries.

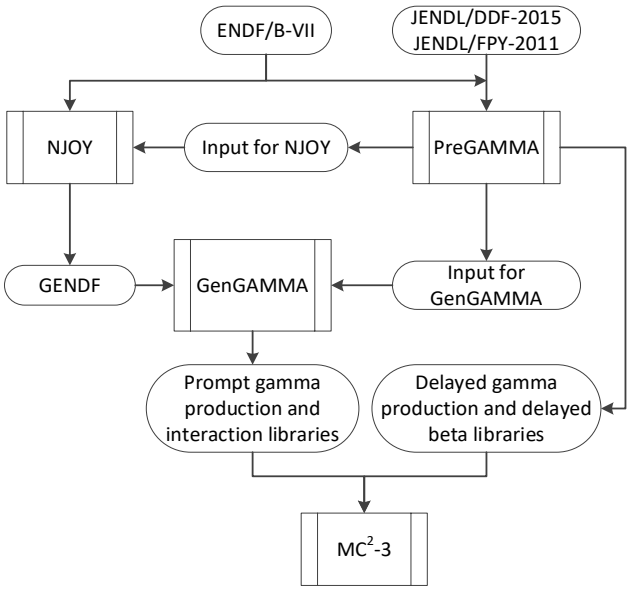

Fig. 3.2 Computational Procedure Used to Generate Gamma Libraries of MC^2-3 [28]

The new prompt and delayed gamma libraries have been generated in 2,082 neutron and 94 gamma group structures. These group structures are consistent with the existing MC^2-3 ultrafine neutron group structure and the 94 gamma group structure of the Cross Section Evaluation Working Group (CSEWG) [29]. The CSEWG 94-group structure is normally used in NJOY and is considered sufficiently fine since gamma cross sections do not have resonance structures in most energy range important for gamma heating calculation [28].

For most reactions, the ENDF gamma production data is given by the gamma yield (or multiplicities) per neutron interaction. In NJOY, the gamma yield factor ($Y^i_{x,n\to g}$), which is the number of gamma rays produced in gamma group *g* by a type x reaction of isotope *i* in neutron group n, is combined with the neutron interaction cross section (σ^i_{xn}) at the infinite dilute condition to form the gamma production matrix ($\gamma^i_{x,n\to g}$):

$$\gamma^i_{x,n\to g} = \sigma^i_{xn} Y^i_{x,n\to g} \tag{3.1}$$

In order to account for the resonance self-shielding of neutron interaction cross sections in the broad-group gamma production cross sections, for capture and fission reactions, the NJOY processed production matrix is converted into a yield matrix by diving the production matrix by the infinite dilute cross section and the resulting yield matrix is stored in the gamma production library. On the other hand, the gamma production matrix for inelastic scattering is

not converted into a yield matrix because the gamma production cross section is the preferred representation of gamma production data for inelastic scattering in the ENDF library [29]. Conversion of the gamma production matrix of inelastic scattering into yield matrix may introduce a larger error than the neglect of self-shielding effect since discrete and continuous inelastic scattering reactions produce different gamma energy distribution while inelastic scattering cross sections are usually smooth when represented in the ultrafine group structure of MC^2-3. Furthermore, only a small portion of gamma rays are produced by inelastic scattering reactions in the reactor core, reflector, and shield [15], and thus the neglect of self-shielding of inelastic scattering cross sections would not introduce a significant error in the gamma heating calculation.

Similarly, the NJOY processed KERMA factor $\kappa_{xg}^{i,X}$ for the type x reaction of isotope i with particle X (i.e., neutron or gamma) in group g is the product of the reaction cross section ($\sigma_{xg}^{i,X}$) and the average energy release per reaction ($h_{xg}^{i,X}$):

$$\kappa_{xg}^{i,X} = \sigma_{xg}^{i,X} h_{xg}^{i,X} \tag{3.2}$$

where the cross section is generated at the infinite dilute condition by NJOY. To account for the resonance self-shielding of neutron interaction cross sections in the broad-group neutron KERMA factors, PreGAMMA retrieves the partial kinetic energy release factors ($h_{xg}^{i,X}$) from the NJOY output by dividing the KERMA factor by the infinite dilute cross section and stores them in the gamma yield library. Later, the KERMA factors for given compositions are calculated by multiplying these energy release factors with self-shielded neutron cross sections generated by MC^2-3. On the other hand, the gamma KERMA factors obtained by NJOY are directly stored in the base library since gamma cross sections have no resonance.

For the delayed beta and gamma heating, which are not included in the prompt gamma libraries, PreGAMMA reads the kinetic energies of delayed betas and gammas from the ENDF/B File 1. Under the assumption that beta particles deposit their kinetic energies locally at the site of fission event, the heating contribution of delayed betas is added to the neutron heating factor of fission reaction. On the other hand, the delayed gamma heating contribution is taken into account by adding the delayed gamma production data to the prompt gamma production data. For this purpose, PreGAMMA constructs the decay chains of fission products by reading the fission yield and radioactive decay data from the JENDL fission yield (JENDL/FPY-2011) and decay (JENDL/DDF-2015) sub-libraries [30,31]. The delayed gamma yield matrices are then constructed by aggregating all the decay gamma spectra.

Although the ENDF/B VII.1 sub-libraries provide the decay data for all fission products, the accuracy of decay data is not guaranteed due to the incompleteness of experimental data for short-lived nuclides and complex decay scheme. In order to overcome these inaccuracies in the decay heat analysis, the JENDL decay data was compiled in 2011 with the fission-product decay data file. To match the average beta and gamma decay energies with their spectral data, the JENDL decay data uses the theoretically calculated spectra and the total absorption gamma-ray spectroscopy (TAGS) data for the nuclides with incomplete decay

scheme [30,31]. It is noted that the delayed gamma energies estimated with JENDL libraries showed better accuracies than those values derived from the fission yield and decay data of the ENDF/B-VII.1 library [28].

3.1.2. Broad-Group Cross Section Generation with MC²-3

The generation of multigroup cross sections requires neutron and gamma spectrum calculations for a specified configuration. The whole-core neutron slowing-down calculation in MC²-3 is usually performed in two-dimensional (2D) R-Z models by invoking the TWODANT S_N transport code [32]. The composition dependent gamma spectrum is determined by solving the multigroup (94 groups) fixed-source gamma transport equation:

$$\Omega \cdot \nabla \phi_g^\gamma + \Sigma_{tg}^\gamma \phi_g^\gamma = \sum_{g'} \Sigma_{s,g' \to g}^\gamma \phi_{g'}^\gamma + \sum_n \Gamma_{n \to g} \phi_n^n \tag{3.3}$$

where the superscripts n and γ denote the neutron and gamma quantities, respectively, and

$$\begin{aligned} \phi_g^\gamma &= \text{group } g \text{ gamma flux} \\ \phi_n^n &= \text{group } n \text{ neutron flux} \\ \Sigma_{tg}^\gamma &= \text{total gamma cross section for group } g \\ \Sigma_{s,g' \to g}^\gamma &= \text{group } g' \text{ to } g \text{ scattering cross section} \\ \Gamma_{n \to g} &= \text{gamma production cross section for neutrons} \\ &\quad \text{in group } n \text{ to produce photons in group } g. \end{aligned} \tag{3.4}$$

The gamma production cross section is constructed with gamma yield, microscopic neutron cross sections for all reaction types, and nuclide densities (N^i) in each composition as:

$$\Gamma_{n \to g} = \sum_{i,x} N^i \gamma_{x,n \to g}^i = \sum_i N^i \sum_x \sigma_{xn}^i Y_{x,n \to g}^i \tag{3.5}$$

The neutron flux in Eq. (3.3) is pre-determined from the neutron slowing-down calculation. The gamma transport calculation can now be performed for a homogeneous medium, a one-dimensional (1D) slab, or a cylindrical unit cell model in MC²-3. The gamma source intensity within the core is significantly higher than that in the reflector and shield. To reflect the gamma spectrum transition from one spatial region to another, and to account for the photon transport from fuel to non-fueled regions, the whole-core TWODANT gamma transport calculation can also be performed with a modified version of MC²-3.

The obtained neutron and gamma spectra are then used to condense the 2,082-group neutron and 94-group gamma cross sections of the base libraries. The broad-group interaction cross sections, gamma production cross sections, and KERMA factors of isotope i are determined as:

$$\sigma_{xG}^i = \frac{\sum_{g \in G} \sigma_{xg}^i \phi_g^X}{\sum_{g \in G} \phi_g^X}, \quad \sigma_{x,G' \to G}^i = \frac{\sum_{g \in G} \sum_{g' \in G'} \sigma_{x,g' \to g}^i \phi_{g'}^X}{\sum_{g' \in G'} \phi_{g'}^X} \tag{3.6}$$

$$\gamma^{i}_{x,G'\to G} = \frac{\sum_{g\in G}\sum_{g'\in G'}\sigma^{i}_{xg'}Y^{i}_{x,g'\to g}\phi^{n}_{g'}}{\sum_{g'\in G'}\phi^{n}_{g'}} \tag{3.7}$$

$$\kappa^{i,X}_{xG} = \frac{\sum_{g\in G}\kappa^{i,X}_{xg}\phi^{X}_{g}}{\sum_{g\in G}\phi^{X}_{g}} \tag{3.8}$$

where σ, γ, and κ represent the interaction cross section, gamma production cross section, and KERMA factor, respectively. The subscript x denotes the reaction type, g denotes the fine group index, and G denotes the broad group index. The superscript X denotes the affiliated particle, i.e., n for neutron and γ for gamma.

The above procedure for generating broad-group gamma production cross sections and KERMA factors is summarized in Fig. 3.3. The data marked with green color are obtained from the updated gamma library of MC^2-3. It should be noted that the 2082×94 gamma yield matrices include the contribution of delayed gamma production and the 2082-group neutron heating factors contains the energy portion of delayed betas, assuming delayed betas deposit their kinetic energies locally. The output data marked with orange color are stored in the code-dependent dataset PMATRX. The gamma production matrices and the neutron and gamma KERMA factors are combined with the self-shielded neutron cross sections and summed over all reaction types.

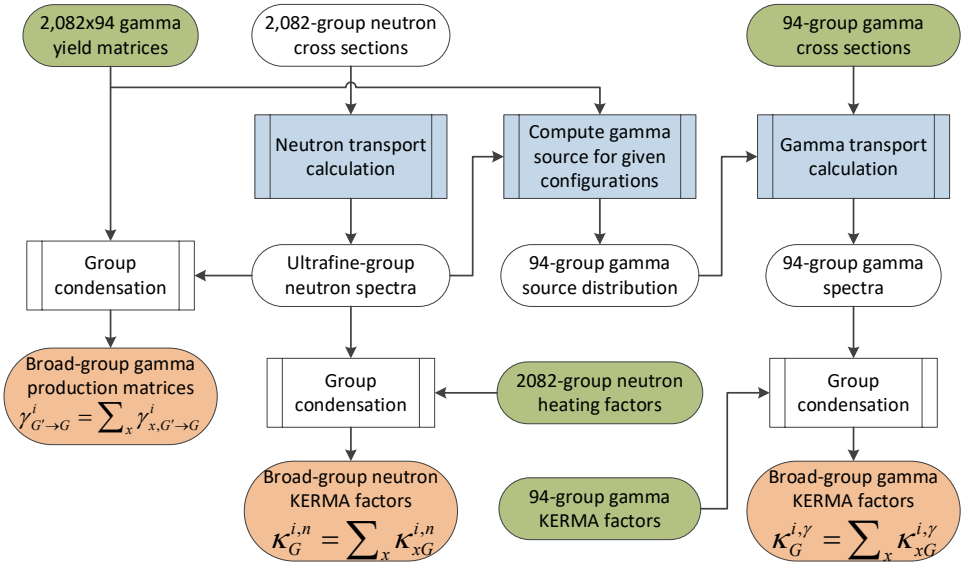

Fig. 3.3 Computational Procedure to Generate Broad-Group Gamma Production Matrices and KERMA Factors

3.2. Generation of Gamma Source Distribution for VARIANT Calculation

In the coupled neutron and gamma heating calculation, the transport of gamma rays or photons generated from neutron interactions is explicitly modeled. The photon productions from neutron interactions with nuclides are determined by the gamma production cross section

matrices that provide a set of probabilities of neutron in a neutron energy group to yield a photon in a photon energy group. Thus, the gamma source distribution in a medium can be determined by the product of the gamma production matrices, the nuclide densities in the medium, and the neutron flux.

3.2.1. Calculation of Intra-nodal Source Distribution

In the original DIF3D/GAMSOR/DIF3D scheme, the GAMSOR code generates the gamma source distribution in the format of the FIXSRC dataset [33]. For each triangular mesh k, the mesh-averaged gamma source density $\overline{S}_g^k$ is calculated as:

$$\overline{S}_g^k = \sum_{g'} \Gamma_{g'\to g}^k \overline{\phi}_{g'}^k \tag{3.9}$$

where $\Gamma_{g'\to g}^k$ is the macroscopic gamma production cross section of the neutrons in a neutron energy group g' to produce the photons in a gamma energy group g, and $\overline{\phi}_{g'}^k$ is the mesh-averaged neutron flux. The macroscopic production data is the summation of the products of nuclide densities and the isotopic gamma production matrices as:

$$\Gamma_{g'\to g}^k = \sum_i \gamma_{g'\to g}^i N_i^k \tag{3.10}$$

where $\gamma_{g'\to g}^i$ denotes the isotopic gamma production cross section provided in PMATRX and N_i^k is the nuclide density of isotope i in the mesh k. This mesh-averaged source is used as the source term in the finite difference diffusion equation in DIF3D.

On the other hand, VARIANT represents the flux distribution within a node with complete orthogonal polynomials in space and spherical harmonics in angle. In order to represent the fixed source distribution to be consistent with the intra-nodal flux distribution of VARIANT, a new fixed source dataset VARSRC has been defined [34]. The description of the VARIANT fixed source file VARSRC is provided in Appendix A. The angular distribution of gamma rays produced from neutron-induced reactions is isotropic for most reactions. The gamma source distribution can be calculated using the neutron flux distribution and the macroscopic gamma production cross sections. Denoting the basis polynomial by $f_m(\vec{r})$, the scalar neutron flux $\phi_g^k(\vec{r})$ of group g in node k can be written as:

$$\phi_g^k(\vec{r}) = \sum_m f_m(\vec{r}) \zeta_{g,m}^k \tag{3.11}$$

where $\zeta_{g,m}^k$ is the expansion coefficient (called the flux moment) corresponding to the basis polynomial $f_m(\vec{r})$. As a result, the emitted gamma source of group g at position $\vec{r}$ can be written as:

$$S_g^k(\vec{r}) = \sum_{g'} \Gamma_{g'\to g}^k \phi_{g'}^k(\vec{r}) = \sum_{g',m} \Gamma_{g'\to g}^k \zeta_{g',m}^k f_m(\vec{r}) = \sum_m Z_{g,m}^k f_m(\vec{r}) \tag{3.12}$$

where

$$Z_{g,m}^{k} = \sum_{g'} \Gamma_{g' \to g}^{k} \zeta_{g',m}^{k} \tag{3.13}$$

From the rightmost side of Eq. (3.12), it can be seen that $Z_{g,m}^{k}$ is the source moment corresponding to the basis polynomial $f_m(\vec{r})$, which can be calculated from the scalar flux moments and the macroscopic gamma production cross sections. The distribution of gamma source in a node is then represented using the same set of basis polynomials used for the flux distribution. The VARIANT solution representation is described in detail in Section 3.3 related to intra-nodal flux/power reconstruction.

3.2.2. Modified GAMSOR Code

The GAMSOR code has been extended to calculate the gamma source moments in each hexagonal prism node and to write them to the VARIANT fixed source file VARSRC. Specifically, a new module GENSRC to generate the VARSRC dataset has been added in parallel to the original module GENFIX that writes the FIXSRC dataset, as denoted by dashed red lines in Fig. 3.4. The modified GAMSOR first calculates the macroscopic gamma production matrices for each composition using the nuclide density and cross section reference file NDXSRF, the zone atom density file ZNATDN, and the production matrix file PMATRX. The resulting composition-dependent gamma production matrices are stored in a scratch array GAMMAC.

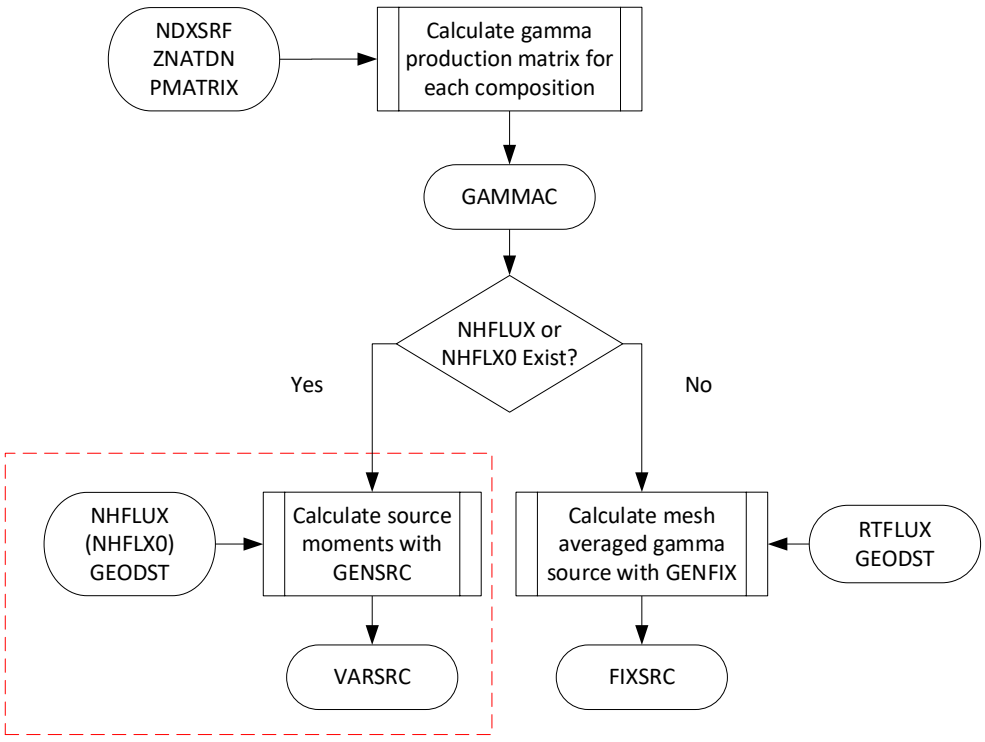

Fig. 3.4 Flow Diagram of Modified GAMSOR for Generation of Gamma Source Distribution

The gamma source in a spatial region is calculated by multiplying the neutron group fluxes of the region and the corresponding gamma production matrix, which is identified using the composition to region mapping stored in the NZNR array of the geometry description file GEODST. The modified GAMSOR generates the fixed source file FIXSRC or VARSRC, depending on the existence of the VARIANT flux solution file NHFLUX or NHFLX0. The NHFLX0 file contains only the spatial distribution of neutron flux. If neither NHFLUX nor NHFLX0 exists, it is assumed that the neutron flux calculation has been performed with the DIF3D finite-difference diffusion theory option. In this case, the module GENFIX is invoked to calculate the mesh-averaged gamma source in each triangular mesh using the neutron fluxes provided in the DIF3D output file RTFLUX and to generate the FIXSRC dataset.

If NHFLX0 exists, it is assumed that the neutron flux calculation has been performed with VARIANT. If NHFLX0 does not exist but NHFLUX does, NHFLUX is double-checked to make sure that it is generated from a VARIANT calculation since NHFLUX could also be generated by the DIF3D nodal diffusion theory option. If the VARIANT solution NHFLX0 or NHFLUX exists, the module GENSRC is invoked to calculate the gamma source moments using the neutron flux moments provided in NHFLX0 or NHFLUX and to write them in the format of VARSRC.

As an example, Fig. 3.5 compares the gamma source distributions of group 12 (out of 21 groups) calculated with DIF3D and VARIANT neutron flux solutions for a region composed of six fuel assemblies and one control assembly in the 1000 MWt Advanced Burner Reactor (ABR-1000) [37]. The left figure shows the gamma sources in triangular meshes obtained with the original GAMSOR code using the DIF3D neutron flux solution. The right figure shows the intra-nodal distributions of the gamma source calculated with the VARIANT neutron flux solution. It is apparent that the six triangular-mesh representation of intra-nodal gamma source distribution is too coarse. The difference in the gamma source distribution would result in a difference in the gamma flux distribution.

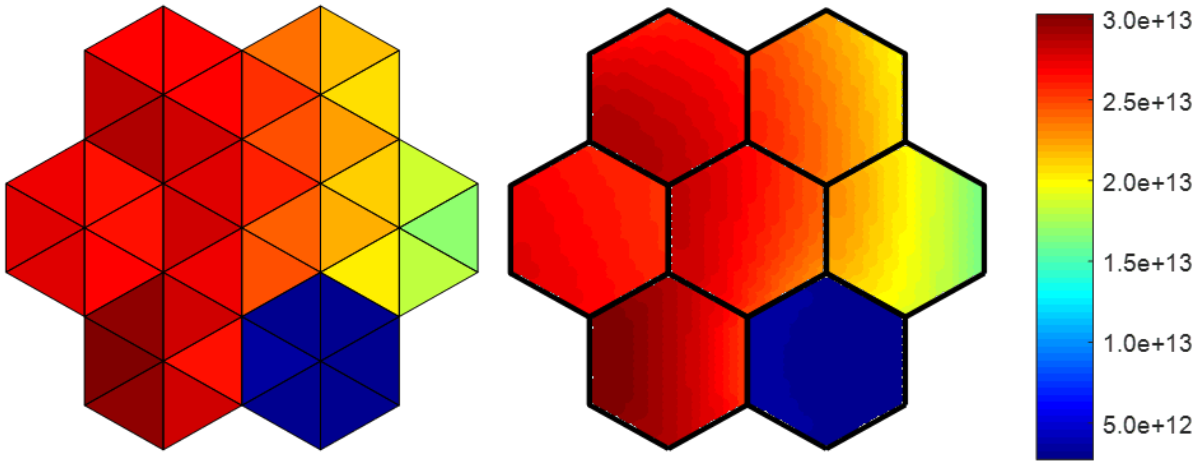

Fig. 3.5 Intra-nodal Gamma Source Distributions for DIF3D (Left) and VARIANT (Right) Calculations

3.3. Reconstruction of Pin Power Distribution from VARIANT Solution

As mentioned above, the previous SE2-ANL code utilized the DIF3D/GAMSOR/DIF3D procedure for coupled neutron and gamma heating calculations. Although an arbitrary fine mesh can be used in DIF3D, the existing heating calculation in SE2-ANL is limited to only six triangular meshes per hexagonal assembly. Furthermore, the pin power distributions are estimated very approximately the axial and the radial power profiles of each assembly are uniform in the xy-plane and in the z-direction, respectively. In each assembly, the axial power profile is obtained by averaging the fine-mesh power densities over six triangular meshes at each axial mesh interval. The radial power profile for fuel pins and assembly duct walls is evaluated at a single axial mesh by approximating the neutron and gamma fluxes by a linear or quadratic polynomial of two variables x and y, using six or 24 triangular mesh interval flux values.

Now that the heating calculation is upgraded with VARIANT transport calculations, it is natural to determine the pin power distribution directly based on the high-order intra-nodal neutron and gamma flux distributions, which are provided as the expansion coefficients of the basis polynomials in the VARIANT solutions. Since the local heterogeneity effect is small in fast reactors, the neutron and gamma heating rates in individual fuel pins and duct walls can be explicitly calculated using the fluxes evaluated at pin locations and along the duct mid-wall, the actual nuclide densities of each material, and the corresponding neutron and gamma KERMA factors. This pin power reconstruction scheme has been implemented into the CURVE (Computational Utility to Reconstruct VARIANT solution for power Evaluation) module of the SE2-UM code to eliminate the approximations in the existing heating calculation scheme.

3.3.1. Nodal Transport Solution of VARIANT

The VARIANT code developed at Argonne National Laboratory allows routine transport calculations for three-dimensional core configurations with homogenized assembly models. It is based on the variational nodal method that guarantees the nodal balance and permits refinement using hierarchical complete polynomial trial functions in space and spherical harmonics in angle. In the variational nodal method, the second-order form of the even-parity transport equation is solved in each node, and the even-parity fluxes of adjoining nodes are coupled through odd-parity fluxes at the interface.

The derivation of the second-order form of the even-parity transport equation starts with splitting the angular flux into even- and odd-parity components as:

$$\psi_g(\vec{r},\hat{\Omega}) = \psi_g^+(\vec{r},\hat{\Omega}) + \psi_g^-(\vec{r},\hat{\Omega}) \tag{3.14}$$

where $\psi_g^+(\vec{r},\hat{\Omega})$ and $\psi_g^-(\vec{r},\hat{\Omega})$ are the even- and odd-parity angular fluxes that satisfy the following properties:

$$\psi_g^+(\vec{r},-\hat{\Omega}) = \psi_g^+(\vec{r},\hat{\Omega}) \tag{3.15}$$

$$\psi_g^-(\vec{r},-\hat{\Omega}) = -\psi_g^-(\vec{r},\hat{\Omega}) \tag{3.16}$$

A coupled transport equation for even- and odd-parity angular fluxes is obtained by adding and subtracting Boltzmann transport equations for $\hat{\Omega}$ and $-\hat{\Omega}$ directions. By eliminating the odd-parity angular flux, the second-order form of the even-parity transport equation can be obtained as:

$$-\hat{\Omega}\cdot\vec{\nabla}\left[\frac{1}{\Sigma_{t,g}(\vec{r})}\hat{\Omega}\cdot\vec{\nabla}\psi_g^+(\vec{r},\hat{\Omega})\right]+\Sigma_{t,g}(\vec{r})\psi_g^+(\vec{r},\hat{\Omega})=\Sigma_{s,g\to g}(\vec{r})\phi_g(\vec{r})+Q_g(\vec{r},\hat{\Omega}) \tag{3.17}$$

It is noted that isotropic scattering is assumed in deriving Eq. (3.17) for simplicity while anisotropic scattering is treated in VARIANT as discussed in Ref. [2].

The variational nodal method is derived from the functional defined on nodal volumes and nodal interfaces, where the odd-parity flux is used as a Lagrange multiplier. Requiring this functional to be stationary with respect to variations of ψ_g^+ and ψ_g^- leads to the second-order form of the even-parity equation within each node, given in Eq. (3.17), and the odd-parity transport equation at the interfaces

$$\hat{\Omega}\cdot\vec{\nabla}\psi_g^+(\vec{r},\hat{\Omega})+\Sigma_{t,g}(\vec{r})\psi_g^-(\vec{r},\hat{\Omega})=0 \tag{3.18}$$

This functional is reduced to a quadratic form by expanding the even- and odd-parity fluxes in terms of complete polynomial trial functions in space and spherical harmonics in angle. The intra-nodal distribution of the even-parity angular flux of group g is expanded as:

$$\psi_g^+(\vec{r},\hat{\Omega})=\sum_{i,m}f_i(\vec{r})g_m(\hat{\Omega})\zeta_{gim}^+ \tag{3.19}$$

where $f_i(\vec{r})$'s are complete polynomial trial functions, $g_m(\hat{\Omega})$'s are even-order spherical harmonics, and ζ_{gim}^+ 's are the expansion coefficients called the flux moments. The odd-parity angular flux on each nodal interface γ is represented as:

$$\psi_{g\gamma}^-(\vec{r},\hat{\Omega})=\sum_{j,n}h_{\gamma j}(\vec{r})k_{\gamma n}(\hat{\Omega})\zeta_{g\gamma im}^- \tag{3.20}$$

where $h_{\gamma j}(\vec{r})$'s are polynomial trial functions and $k_{\gamma n}(\hat{\Omega})$'s are odd-order spherical harmonics.

The linear system of equations for the expansion coefficients or even- and odd-parity flux moments, ζ_{gim}^+ and $\zeta_{g\gamma im}^-$, are obtained by requiring the reduced functional to be stationary with respect to variations of these flux moments. Eventually, by applying a linear transformation of variables to the equations in ζ_{gim}^+ and $\zeta_{g\gamma im}^-$, a set of nodal response matrix equations are obtained for space-angle partial current moments for neutrons exiting and entering the node. The inter-nodal continuity conditions for the partial current moments are then used to solve the global equations iteratively.

Once the partial current moments are obtained, the nodal even-parity flux moments and hence the scalar flux distribution can be recovered. Using the isotropic components of the even-parity flux moments, the scalar flux distribution of group g within a node k can be obtained as:

$$\phi_{gk}(\vec{r}) = \int_{4\pi} \psi^{+}_{gk}(\vec{r},\hat{\Omega}) d\Omega = \sum_{i} f_i(\vec{r}) \zeta^{+}_{gi0,k} \tag{3.21}$$

The VARIANT code stores the flux moment solutions in the dataset NHFLUX [2], of which the latest file description is provided in Appendix B.

3.3.2. Flux Reconstruction Scheme

As shown in Eq. (3.21), the intra-nodal scalar flux distributions required for calculating the distributions of heat generation rates in fuel pins and duct walls can be obtained directly from the VARIANT solution. The expansion coefficients $\zeta^{+}_{gi0,k}$ in Eq. (3.21) are called the (scalar) flux moments and can be retrieved from the VARIANT solution file NHFLUX or NHFLX0. The NHFLX0 file contains only scalar flux moments in the exact format as NHFLUX. The even- and odd-parity flux moments in each node are stored in the 3D record of NHFLUX (NHFLX0).

For the user specified orders of polynomial and spherical harmonics, the number of spatial trial functions and the numbers of even- and odd-parity spherical harmonics are uniquely determined. Denoting the number of polynomial trial functions by N_S, the number of even-parity spherical harmonics by N_A^{+}, and the number of odd-parity spherical harmonics by N_A^{-}, the even-parity flux moments $\zeta^{+}_{gim,k}$ and the odd-parity flux moments $\zeta^{-}_{gim,k}$ of group g in node k are ordered as:

$$\begin{aligned} &\{\zeta^{+}_{\mu} = \zeta^{+}_{gim,k} \mid \mu = (m-1)N_S + i,\ 1 \le i \le N_S,\ 1 \le m \le N_A^{+}\}, \\ &\{\zeta^{-}_{\nu} = \zeta^{-}_{gin,k} \mid \nu = (n-1)N_S + i,\ 1 \le i \le N_S, 1 \le n \le N_A^{-}\} \end{aligned} \tag{3.22}$$

where i is the index for spatial trial functions, m is the index for the even-parity spherical harmonics, n is the index for the odd-parity spherical harmonics, μ is the sequential number for even-parity flux moments, and ν is the sequential number for odd-parity flux moments.

The polynomial trial functions of VARIANT are internally generated to evaluate the coefficient matrices, but they are not stored in any output file. Therefore, in order to reconstruct intra-nodal flux distributions, the polynomial trial functions should be re-generated using the same procedure used in the VARIANT code. To build the required polynomial trial functions, a set of monomials are prepared in the same sequence and up to the same expansion order that was used in the foregoing VARIANT calculation. Using the Gram-Schmidt orthogonalization method, these monomials are transformed into a set of orthogonal polynomials in the order consistent with the flux moments. For a user specified polynomial order N, the set of monomials are constructed in the following order:

$$\{x^{l-m-n} y^{m} z^{n} \mid\ 0 \le m \le l-n, 0 \le n \le l, 0 \le l \le N\} \tag{3.23}$$

For example, the monomials for a specified polynomial order of three are ordered as:

$$\{1, x, y, z, x^2, xy, y^2, xz, yz, z^2, x^3, x^2y, xy^2, y^3, x^2z, xyz, y^2z, xz^2, yz^2, z^3\} \tag{3.24}$$

In typical reactor systems, the axial distribution of flux is generally smoother than its radial distribution. Therefore, VARIANT allows the order reduction in z direction, which leads to

an incomplete set of polynomials in z under a specified approximation order. If the reduced order in the axial direction is R, the incomplete set of monomials is given by:

$$\begin{aligned}&\{x^{l-m-n}y^m z^n \mid 0\le m\le l-n, 0\le n\le l, 0\le l\le N-R\}\\&\quad\bigcup\{x^{l-m}y^m \mid 0\le m\le l, N-R+1\le l\le N\}\end{aligned} \tag{3.25}$$

For example, the monomials for a specified polynomial order of three with one order reduction in z direction are ordered as:

$$\{1, x, y, z, x^2, xy, y^2, xz, yz, z^2, x^3, x^2y, xy^2, y^3\} \tag{3.26}$$

It is noted that among the third order monomials in (3.24), those including the axial variable z are eliminated.

From the prepared set of monomials, the spatial trial functions are generated by the Gram-Schmidt orthogonalization procedure as illustrated in Fig. 3.6. To eliminate the dependency of trial functions on the node size, a dimensionless, local reference frame is adopted. By scaling x and y coordinates by the hexagonal pitch p and by scaling z coordinate by the node height Δz, the problem domain of a hexagonal prism node can be cast into the following dimensionless coordinates $(\tilde{x}, \tilde{y}, \tilde{z})$:

$$\begin{aligned}\tilde{x} &= \frac{x^*}{p} \in \left[-\frac{1}{2}, \frac{1}{2}\right]\\ \tilde{y} &= \frac{y^*}{p} \in \left[-\frac{1}{\sqrt{3}}\left(1-|\tilde{x}|\right), \frac{1}{\sqrt{3}}\left(1-|\tilde{x}|\right)\right]\\ \tilde{z} &= \frac{z^*}{\Delta z^*} \in \left[-\frac{1}{2}, \frac{1}{2}\right]\end{aligned} \tag{3.27}$$

where x^*, y^* and z^* are the physical coordinates from the origin at the node center. In this coordinate system, the volume of a hexagonal prism node becomes:

$$\int_{V_{node}} dV = \int_{-1/2}^{1/2} d\tilde{x} \int_{-(1-|\tilde{x}|)/\sqrt{3}}^{(1-|\tilde{x}|)/\sqrt{3}} d\tilde{y} \int_{-1/2}^{1/2} d\tilde{z} = \frac{\sqrt{3}}{2} \tag{3.28}$$

Further scaling of $\tilde{x}$ and $\tilde{y}$ by a factor $\sqrt{2}/3^{1/4}$ makes the node volume unity. With this scaling, the local coordinates become:

$$\begin{aligned}x &= \frac{\sqrt{2}x^*}{3^{1/4}p} \in \left[\frac{-1}{\sqrt{2}3^{1/4}}, \frac{1}{\sqrt{2}3^{1/4}}\right]\\ y &\in \left[\frac{-1}{\sqrt{3}}\left(\frac{\sqrt{2}}{3^{1/4}}-|x|\right), \frac{1}{\sqrt{3}}\left(\frac{\sqrt{2}}{3^{1/4}}-|x|\right)\right]\\ z &= \frac{z^*}{\Delta z^*} \in \left[-\frac{1}{2}, \frac{1}{2}\right]\end{aligned} \tag{3.29}$$

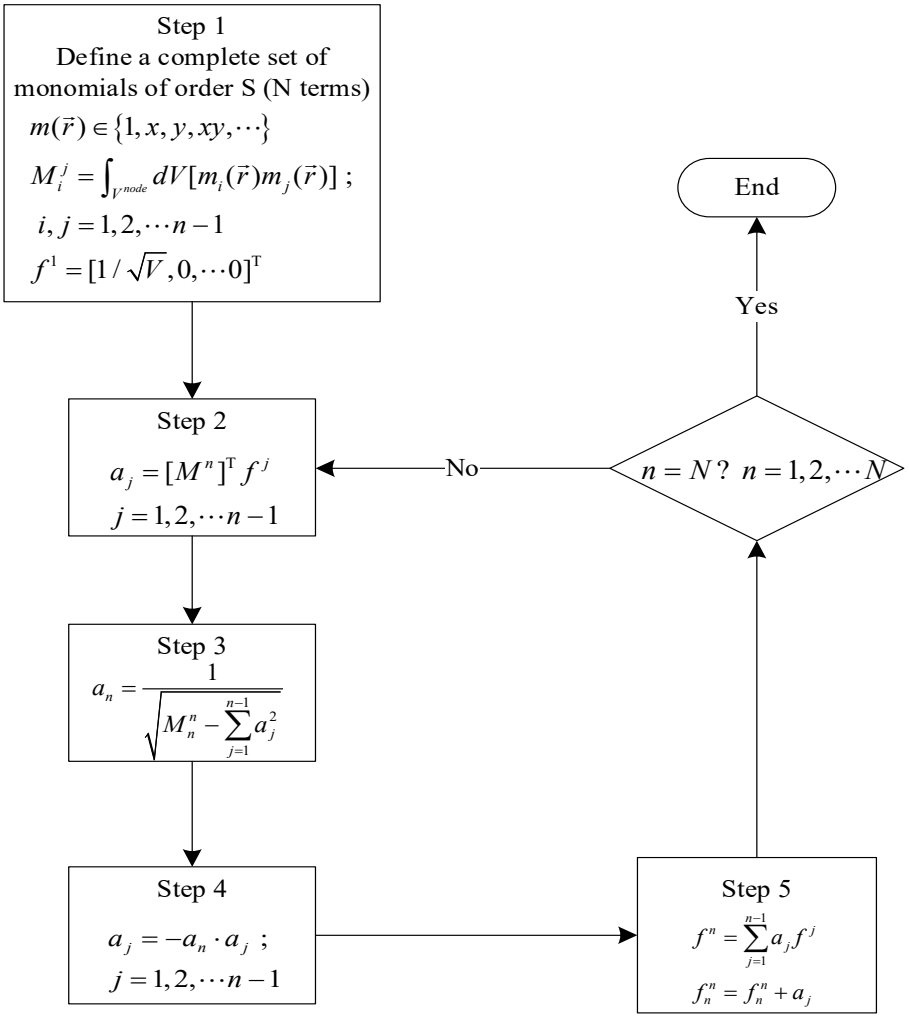

Fig. 3.6 Flow Diagram of Gram-Schmidt Orthogonalization Procedure [34]

Using the flux expansion coefficients and the polynomial trial functions, the intra-nodal flux distribution can be retrieved using Eq. (3.21). Since the local heterogeneity effect is small in fast reactor systems due to long neutron mean free paths, the flux distribution within a homogenized node can be directly used in calculating fuel pin and duct powers without employing local form functions as used in thermal reactor analysis. To calculate the power densities in individual fuel pins and assembly duct walls, the retrieved flux distributions are then evaluated along each pin and the mid-wall of the assembly duct. For each pin, the average flux over the pin cross-sectional area is calculated by default. Meanwhile, the intra-pin flux distribution can be approximated by the flux along the pin centerline according to the user specification. Because of the small spatial self-shielding effect within a fuel pin and the small pin radius in fast reactors, this approximation would not lead to a significant loss of accuracy.

As illustrated in Fig. 3.7-(A), the fuel pins are arranged in a triangular lattice. Therefore, the centerline positions of fuel pins are determined in the local coordinate system shown in Fig. 3.7-(B), using the following assembly design parameters: the assembly pitch (p), the pin pitch (pp), the number of fuel pin rings, the duct wall thickness (t), and the inner flat-to-flat distance

(L) of duct wall. In Fig. 3.7-(B), the red dashed line defines the six surfaces of a hexagonal node. The surfaces of hexagonal node are numbered counterclockwise.

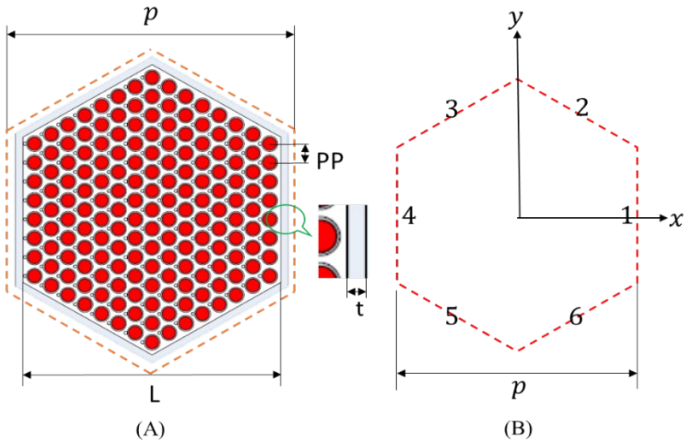

Fig. 3.7 Assembly Design Parameters and Local Coordinate System

As shown in Fig. 3.8-(A) with blue hexagons, the fuel pins arranged in a triangular lattice form hexagonal rings of fuel pins. Therefore, each fuel pin can be identified by the hexagonal ring number and the position number within the hexagonal ring. The hexagonal rings are sequentially numbered from the innermost ring (i.e., the central pin) to the outmost ring. The fuel pins within a hexagonal ring are numbered counterclockwise, starting from the pin located at the x' axis in Fig. 3.8-(A). A hexagonal ring with a ring number r includes one pin for $r=1$ and $6(r-1)$ pins for $r\neq 1$, and the pin position number varies from 1 to $6(r-1)$. In the power density calculation for the assembly duct wall, the locations for the flux evaluations are selected at equal intervals according to the user-specified number of evaluation points, as shown in Fig. 3.8-(B). The evaluation positions are ordered counterclockwise starting from the first point on surface 1, which is marked as α in Fig. 3.8-(B). The last evaluation point is the intersection point of surfaces 1 and 6, labeled as β.

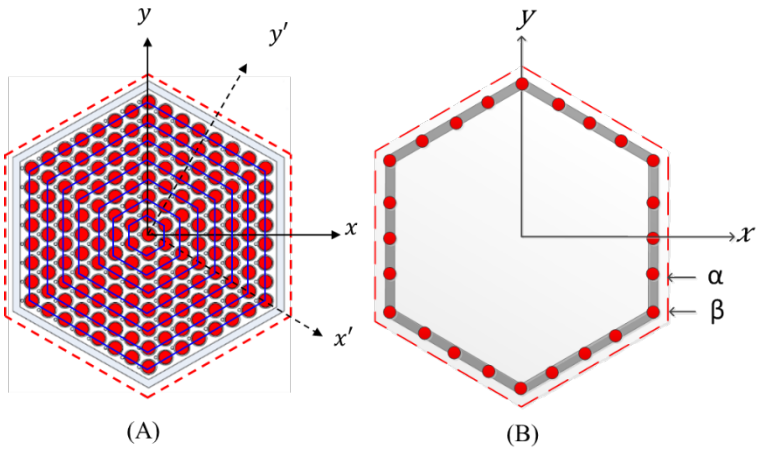

Fig. 3.8 Flux Evaluation Positions on Fuel Pins (A) and on Duct Wall (B)

3.3.3. Generation of Heat Source Distribution

Following the neutron and gamma flux calculations, the power densities in fuel pins and assembly duct walls are evaluated. The total heat generation rate at position $\vec{r}$ in node k from neutron and gamma contributions is calculated using the KERMA factors as:

$$P^k(\vec{r}) = \sum_g \phi^k_{gn}(\vec{r}) \left[\sum_i N^k_i(\vec{r}) \kappa^i_{n,g} \right] + \sum_{g'} \phi^k_{g'\gamma}(\vec{r}) \left[\sum_i N^k_i(\vec{r}) \kappa^i_{\gamma,g'} \right] \tag{3.30}$$

where $\kappa^i_{n,g}$ is the KERMA factor of nuclide i for neutron energy group g, $\kappa^i_{\gamma,g'}$ is the KERMA factor of nuclide i for gamma energy group g', $N^k_i(\vec{r})$ is the number density of nuclide i at position $\vec{r}$ in node k, $\phi^k_{gn}(\vec{r})$ is the neutron flux of neutron energy group g at position $\vec{r}$ in node k, and $\phi^k_{g'\gamma}(\vec{r})$ is the gamma flux of neutron energy group g' at position $\vec{r}$ in node k. The quantities in the first and second brackets of Eq. (3.30) are the power conversion factors at position $\vec{r}$ in node k for neutron and gamma fluxes, respectively.

In the CURVE calculation, the intra-nodal neutron flux distribution $\phi^k_{gn}(\vec{r})$ and gamma flux distribution $\phi^k_{g'\gamma}(\vec{r})$ are evaluated using Eq. (3.11) as we discussed in Section 3.3.2. In short, CURVE constructs the orthogonal basis polynomials in the same way as VARIANT does. The scalar flux moments are obtained from the VARIANT output file NHFLUX or NHFLX0. The neutron and gamma flux distributions are then evaluated along each fuel pin and the mid-wall of the assembly duct. In CURVE, the axial power shape is determined for individual fuel pin segments within each axial node of VARIANT separately, as illustrated in Fig. 3.9-(A). On the other hand, in the existing SE2-ANL heating calculation, a single axial power shape is used for all the pins and duct walls in an assembly as illustrated in Fig. 3.9-(B).

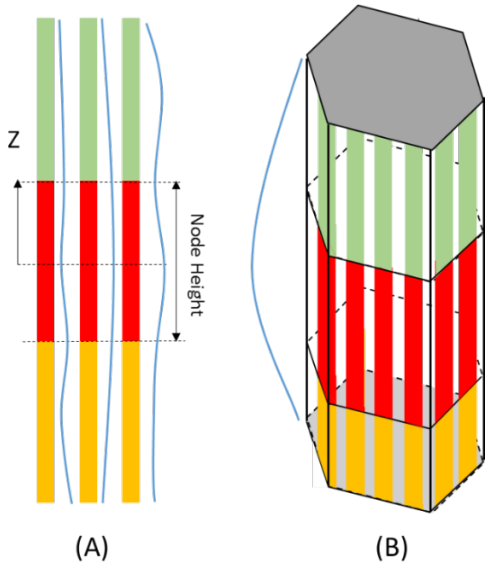

Fig. 3.9 Illustration of Axial Power Profiles Used in CURVE (A) and Existing SE2-ANL (B)

Specifically, the axial distribution of the group g flux along the i-th pin or duct segment within a VARIANT node is evaluated as:

$$\phi_{i,g}(z) = \sum_{n=0}^{N_Z} a_{gn}^{i} \cdot z^n, \quad -\frac{1}{2} \le z \le \frac{1}{2} \tag{3.31}$$

where a_{gn}^{i} is the n-th coefficient of the axial flux profile, and N_Z is the polynomial expansion order in the axial direction of the VARIANT solution. The range of variable z is due to the local coordinate frame used in VARIANT formulation, with $z = \pm 1/2$ representing the top and bottom surfaces of the node.

Although the VARIANT flux solution obtained with homogenized assembly models is directly used in pin flux reconstruction, the real heterogeneous configuration inside an assembly illustrated in Fig. 3.10 should be used to calculate the heating rates in different materials, which contain different nuclides with distinct KERMA factors. In addition, the atom densities can vary in different fuel pins of an assembly because of different burnup states. However, there is no capability to track the pin burnups in the current fuel cycle analysis based on VARIANT transport calculations. The capability to reconstruct the pin burnup characteristics of the RCT code [35] is available only for the fuel cycle analysis with the DIF3D nodal diffusion theory calculation. Therefore, for the moment, the pin power distributions are determined without considering the different burnup states of individual fuel pins. Instead, it is assumed that all the pin segments within a node have the same nuclide densities. In addition, the gamma heating in claddings and coolant inside the assembly duct is proportionally redistributed among the fuel pins within the node. This will result in a conservative estimation of fuel and cladding temperatures.

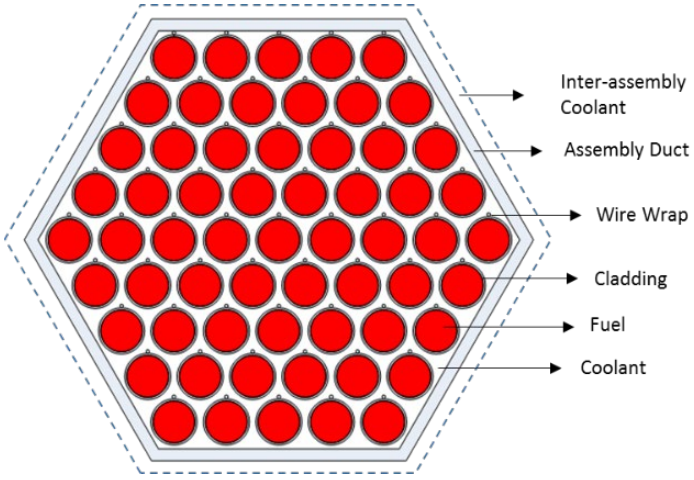

Fig. 3.10 Illustration of Material Distribution within Fuel Assembly

Under these approximations, the axial power shape of pin i in node k can be written as:

$$P_i^k(z) = \sum_{n=0}^{N_Z} b_{n,f}^{i,k} \cdot z^n + C \sum_{n=0}^{N_Z} b_{n,f}^{i,k} \cdot z^n, \quad -\frac{1}{2} \le z \le \frac{1}{2} \tag{3.32}$$

where the coefficient $b_{n,f}^{i,k}$ represents the shape of the heat generation rate due to fuel isotopes, and is calculated using the flux shape coefficients (i.e., a_{gn}^{i}'s in Eq. (3.31)), fuel nuclide densities, and KERMA factors. The second term in Eq. (3.32) represents the heating contribution of cladding and coolant isotopes that is assigned to pin i in proportion to the fuel linear power, with a scaling factor C. Meanwhile, for a specified duct material (e.g., HT-9 or SS-316), the total heating rate in the duct is explicitly calculated using the fluxes evaluated along the mid-wall of duct, the nuclide densities of the given material, and the corresponding KERMA factors. For the inter-assembly gap and the bypass gap between the inner and outer ducts of double-ducted control assemblies, the heat generation rates in the gaps are also explicitly calculated using the actual coolant nuclide densities and fluxes evaluated at the gaps.

The scaling factor C in Eq. (3.32) is determined to preserve the total power generation rate in the node. The total power P^k in node k can be determined using the node-averaged nuclide densities $\bar{N}_i^k$, the isotopic KERMA factors $\kappa_g^{i,n}$ and $\kappa_{g'}^{i,\gamma}$, the node-averaged neutron and gamma fluxes $\bar{\phi}_g^{k,n}$ and $\bar{\phi}_{g'}^{k,\gamma}$, and the node volume V^k as:

$$P^k = V^k \left(\sum_g \bar{\phi}_g^{k,n} \sum_i \bar{N}_i^k \kappa_g^{i,n} + \sum_{g'} \bar{\phi}_{g'}^{k,\gamma} \sum_i \bar{N}_i^k \kappa_{g'}^{i,\gamma} \right) \tag{3.33}$$

Therefore, the constant C can be determined by equating the sum of the integrated pin powers and the total heating in the duct walls and inter-assembly coolant gaps to the total power in the node given by Eq. (3.33),

$$P^k = \sum_i P_{pin}^{k,i} + P_{duct}^k + P_{gap}^k \tag{3.34}$$

The integrated power $P_{pin}^{k,i}$ of the i^{th} pin segment in node k can be simply calculated as:

$$P_{pin}^{k,i} = (1+C)\pi r_f^2 h_k \cdot \sum_{n=0}^{N_Z} \left(b_{n,f}^{i,k} \frac{z^{n+1}}{n+1} \Big|_{z=-1/2}^{z=1/2} \right) \tag{3.35}$$

where r_f is the fuel radius and h_k is the node height.

The heat generation rate in an assembly duct is calculated by evaluating the power densities along the vertical lines at the user-specified points on the duct mid-wall as illustrated in Fig. 3.11-(A) with red marks, where the grey hexagon represents the duct wall, and the dashed boundary is the hexagonal node boundary in the VARIANT model. The number of evaluation points per duct wall is specified by the user. Along each vertical line illustrated in Fig. 3.11-(B), the power shape is evaluated as a polynomial profile as in Eq. (3.32) but without the second term on the right hand side. By linear interpolation of these evaluated heating rates, the heating rate at an arbitrary position can be determined. The average power density over the six duct walls is approximately obtained by the average of the segment-averaged power densities at the user-specified evaluation points. Denoting the average power density in the duct of node k as $\bar{P}_{duct}^k$, the total duct power can be calculated as:

$$P_{duct}^{k} = \overline{P}_{duct}^{k} \cdot h_k \cdot \frac{\sqrt{3}}{2}\left[(L+t)^2 - L^2\right] \tag{3.36}$$

where h_k is the node height, L is the flat-to-flat distance of duct inner wall, and t is the duct thickness. The heat generation rate in the coolant gaps outside the pin bundle is determined in the same way by treating them as a duct filled with sodium coolant.

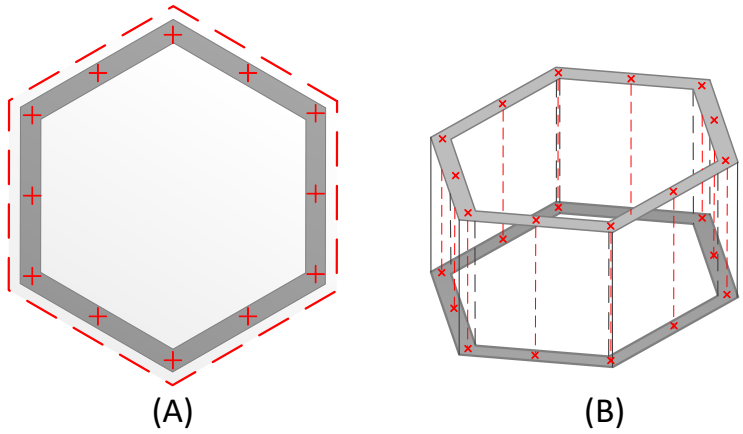

Fig. 3.11 Illustration of Evaluation Positions for Power Densities on Assembly Duct

In order to reduce the required memory, a user option to approximate the axial power shape in each axial segment of fuel pin or duct as a quadratic polynomial is allowed in CURVE. This approximation is based on the relatively smooth variation of flux along the axial direction in reactor core with extruded geometry. The coefficients of the quadratic polynomial are determined by preserving the power densities at the top and bottom boundaries of the segment as well as the segment-averaged power density.

The obtained polynomial power profiles for pin and duct segments are used to calculate the linear powers at fine-mesh points of each subchannel as required in the SE2-UM thermal-hydraulic calculations. The conventional subchannel definition and key geometrical parameters for wire-wrapped fuel and control assemblies are illustrated in Fig. 3.12. The inside of the duct wall (the inner duct for a double-ducted control assembly) is divided into interior, edge, and corner subchannels as divided by dashed lines in Fig. 3.12. The volumetric heat source in each subchannel includes the heats generated in the fuels and claddings contained in the subchannel in addition to the gamma heating in coolant. The heat generation rate in the claddings and coolant inside the duct wall is redistributed to fuel pins in proportion to their linear powers for a conservative estimation of fuel and cladding temperatures. The heat generation rate in an interior subchannel is determined by one sixth of the total linear powers of the three adjacent pins. For an edge subchannel, the heat generation rate is determined by one fourth of the total linear powers in the two adjacent pins. The heat generation rate in a corner subchannel is determined by one sixth of the adjacent pin linear power.

The linear power of a duct subchannel is calculated as the product of the average power density and the cross-sectional area of that channel. The average power density is determined using the duct power profiles evaluated along the user-specified vertical lines in the duct as

shown in Fig. 3.11. If necessary, a linear interpolation is performed using the power profiles evaluated at the nearby vertical lines. Again, the heat generation rates in the inter-assembly and bypass gaps are determined in the same way by treating them as a duct filled with sodium coolant.

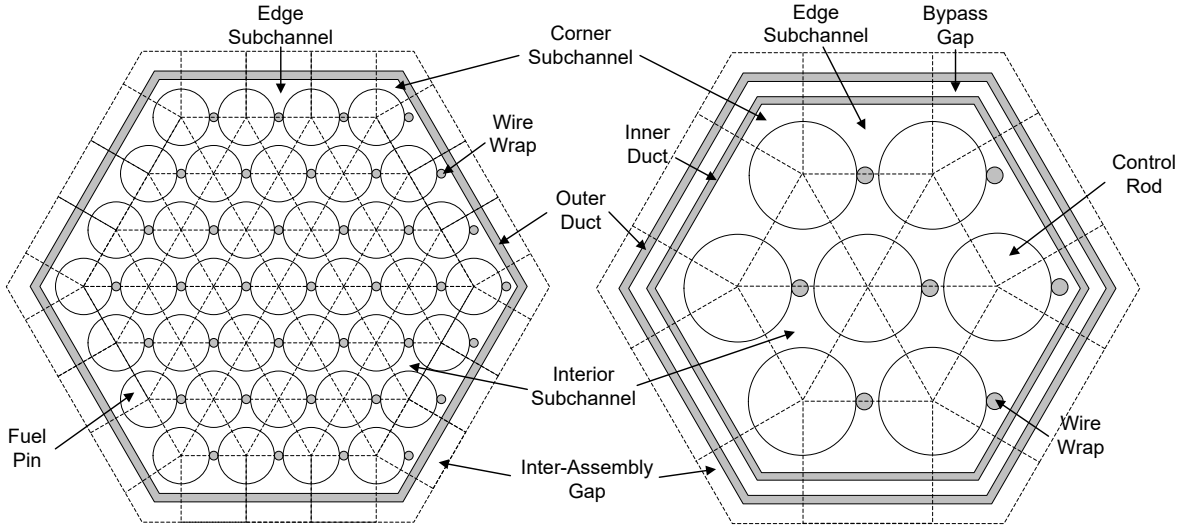

Fig. 3.12 Heterogeneous Pin Geometries in Fuel (Left) and Control (Right) Assemblies

3.3.4. Implementation of CURVE Code

3.3.4.1. Code Structure

The CURVE code was developed to reconstruct the intra-nodal flux distributions from VARIANT nodal transport solutions and to calculate the power distributions in fuel pins, assembly duct walls, and coolant gaps. Fig. 3.13 shows the code structure of CURVE. The CURVE code requires the following binary interface files generated in the coupled neutron and gamma transport calculations: NHFLUX (or NHFLX0), GHFLUX (or GHFLX0), GEODST, ZNATDN, and NDXSRF. It also requires the neutron and gamma KERMA factors stored in the PMATRX dataset. In addition, the assembly design parameters such as the number of fuel pins, pin pitch, and pin diameter are required to determine the pin positions and to retrieve the material nuclide densities.

To reconstruct the intra-nodal neutron and gamma flux distributions, a complete set of orthogonal polynomials for three-dimensional (3D) flux expansion is constructed using the Gram-Schmidt orthogonalization procedure, according to the spatial expansion order recorded in NHFLUX or NHFLX0. The flux reconstruction involves the evaluation of polynomial functions at many points, which requires substantial computing costs. In order to reduce the computational efforts, the polynomial basis functions are pre-evaluated and saved for each type of assemblies (e.g., fuel assemblies, control assemblies, reflectors, and shields). The 3D basis polynomials are pre-evaluated to compute the average value over the pin cross-sectional area (or at the pin centerline position if specified so) and along the mid-wall of assembly ducts to obtain a set of 1D polynomials, which are the basis functions for the axial flux distributions in each pin or duct wall and are stored in the data structure ZBASIS. The positions of pin centerlines and user-specified vertical lines along duct mid-walls are determined using the

assembly design parameters. To reduce the memory requirement to store the coefficients of the high-order polynomial for axial power profile representation, the axial power distribution can be further approximated as a quadratic polynomial for individual pin and duct segments. The coefficients of quadratic polynomials are determined to preserve the power densities at the top and bottom points of each segment and the segment-averaged power densities. For this, the 1D basis polynomials are evaluated at the top and bottom points of each pin and duct segment, and the average value over each segment are calculated. The evaluated 1D basis functions are stored in a data structure PINFILE for later use.

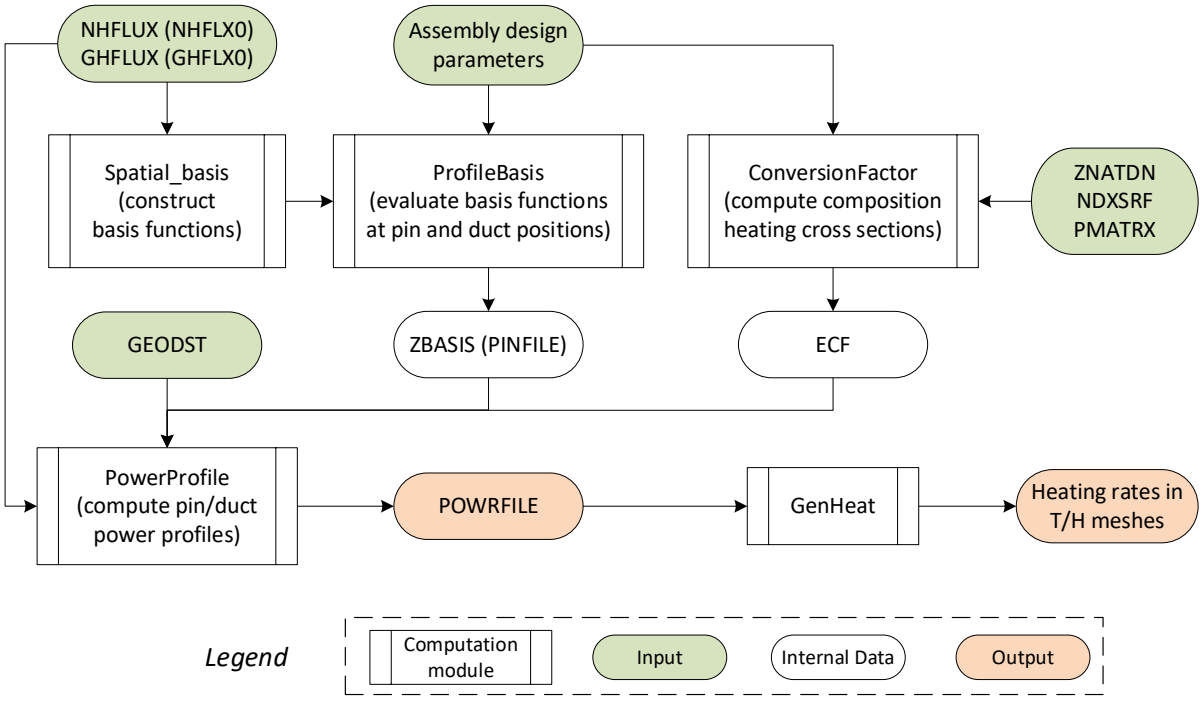

Fig. 3.13 Computational Flow and Data Transfer in CURVE

After processing the basis functions, the heating cross section (i.e. macroscopic KERMA factor) for each material (e.g., fuel, cladding, duct, and coolant) is prepared in the module ConversionFactor based on the heterogeneous assembly configuration. The nuclide densities of individual materials are obtained by unfolding the homogenized nuclide densities in ZNATDN using the specified assembly dimensions and the inter-assembly gap thickness. The isotopic neutron and gamma KERMA factors are obtained from the PMATRX dataset. The composition dependent heating cross sections are stored in a data structure ECF and can be mapped to specific nodes by the NZNR array in GEODST.

Using the pre-evaluated basis functions in ZBASIS (or PINFILE in the case of quadratic profiles), the macroscopic heating cross sections in ECF and the flux moments in NHFLUX, the module PowerProfile calculates the power profiles for every axial segment of fuel pin, duct wall, inter-assembly gap, and bypass gap within every hexagonal prism node of VARIANT. The coefficients of the polynomial profiles are written in a binary dataset POWRFILE, of which the data structure and contents are described in Appendix C.

The implementation of CURVE has been verified with multiple unit tests. The flux reconstruction scheme was tested using an artificial intra-nodal flux distribution. For the power evaluation, the quadratic polynomial approximation for the axial power profile in a prototype fast reactor fuel pin was examined. As a whole, the CURVE reconstruction scheme was verified using the ABR-1000 metal core design [36]. Additional discussions are provided in Appendix D.

3.3.4.2. Modules and Data Management

The CURVE program is well modularized consisting of six main modules. A brief description of each module is given in Table 3.1 below.

Table 3.1. Main Computational Modules of CURVE

Module Name	Function
Controls	Gets the assembly design parameters and user options for power evaluations from the SE2-UM input file.
Spatial_basis	Constructs polynomial basis functions according to the spatial expansion order and node geometry in the VARIANT calculation.
ConversionFactor	Calculates composition-dependent heating cross sections using the datasets ZNATDN, NDXSRF, and PMATRX as well as the assembly design parameters.
ProfileBasis	Determines the positions of individual pins and duct mid-walls. Pre-evaluate the basis functions for pin and duct segment within each VARIANT node.
PowerProfile	Evaluates the power profiles for fuel pins, duct walls, inter-assembly gaps and bypass gaps. Generates the interface dataset POWRFILE.
GenHeat	Uses power profiles in POWRFILE to calculate the heat source in thermal-hydraulic meshes defined in SE2-UM

Except for the binary interface files, the data transfer among modules in CURVE are mainly performed with the derived data structures in FORTRAN 90 standards, which can be dynamically allocated for large data storage. For instance, there is no separate input file for CURVE as a module of the SE2-UM code. The required input data for CURVE calculations are passed through the module Controls. All the control parameters of CURVE are stored in a derived data structure and can be accessed in any subroutine by using the module Controls. Other important data structures include ECF for macroscopic KERMA factors, ZBASIS and PINFILE for pre-evaluated basis functions, and PINPOWR for the coefficients of pin power profiles. The contents of PINPOWR are the same as the file POWRFILE, which is described in Appendix C. Descriptions of ECF, ZBASIS, and PINFILE are provided in Appendix E.

3.4. Verification of Heating Calculation Method

The newly developed coupled neutron and gamma heating calculation scheme based on VARIANT transport solutions was verified against Monte Carlo reference solutions using the

Advanced Burner Test Reactor (ABTR) [37] and Experimental Breeder Reactor II (EBR-II) [38] benchmark problems. For all the benchmark tests, the cross sections were generated using the ENDF/B-VII.0 library except for the delayed gamma production data. The reference Monte Carlo solutions were obtained using the MCNP6 code [39]. The coupled neutron and photon transport process was simulated explicitly, except that the photonuclear production of neutrons and the secondary photon production through fluorescence and bremsstrahlung radiation were not considered to make consistent comparisons with the deterministic MC^2-3/VARIANT calculations. That is, the photon transport was performed using the simple physics model of MCNP6 [40].

3.4.1. ABTR Benchmark Problem

The reference 250 MWt ABTR metal core configuration is shown in Fig. 3.14. It consists of 54 driver assemblies fueled with weapons-grade plutonium, 78 reflectors, 48 shields, 10 control, and 9 test assemblies. For the benchmark case, the three material test locations on the fourth ring are filled with reflector assemblies, and the six test-fuel locations are filled with driver fuel assemblies fueled with the TRU recovered from light water reactor (LWR) spent fuel instead of weapons-grade plutonium. The circular core barrel and surrounding sodium are represented by 54 background hexagonal assemblies (Barrel) without axial heterogeneity.

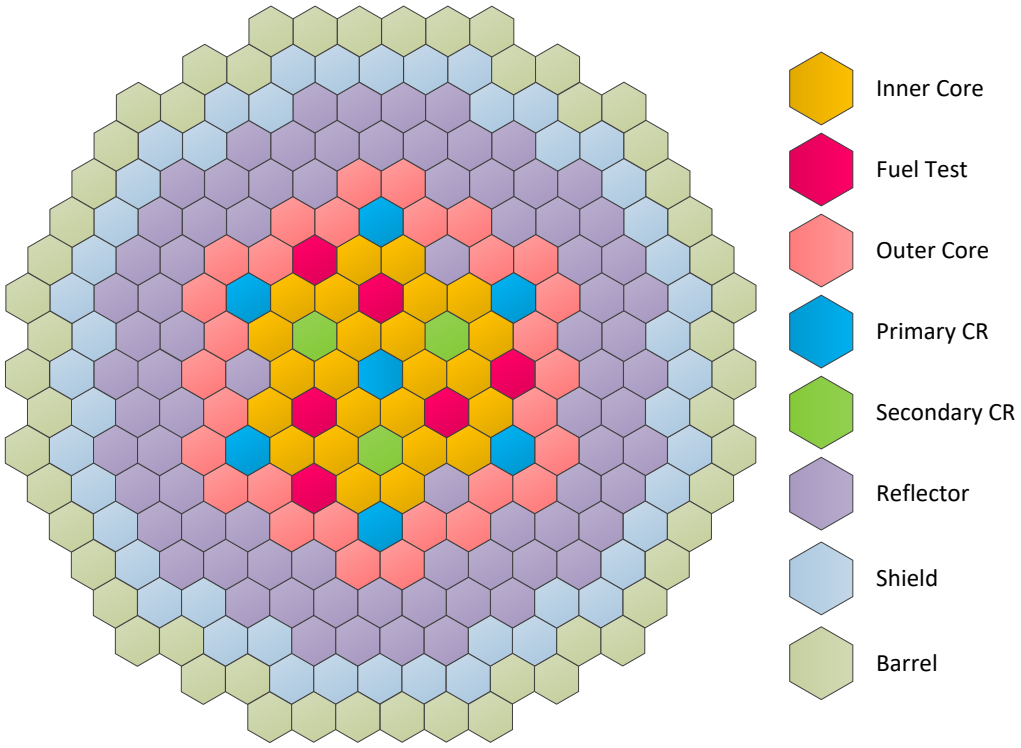

Fig. 3.14 Core Configuration of 250 MWt ABTR Benchmark Problem

The axial configurations for the four types of assemblies, i.e., driver assembly, control assembly, shield, and reflector are illustrated in Fig. 3.15. Each assembly except barrel is subdivided into 12 axial regions labelled as A ~ L in Fig. 3.15. The active core part of driver

assemblies is equally divided into five segments D ~ H. The control absorber is just positioned above the active core. The lift of control rods left an empty room filled with sodium.

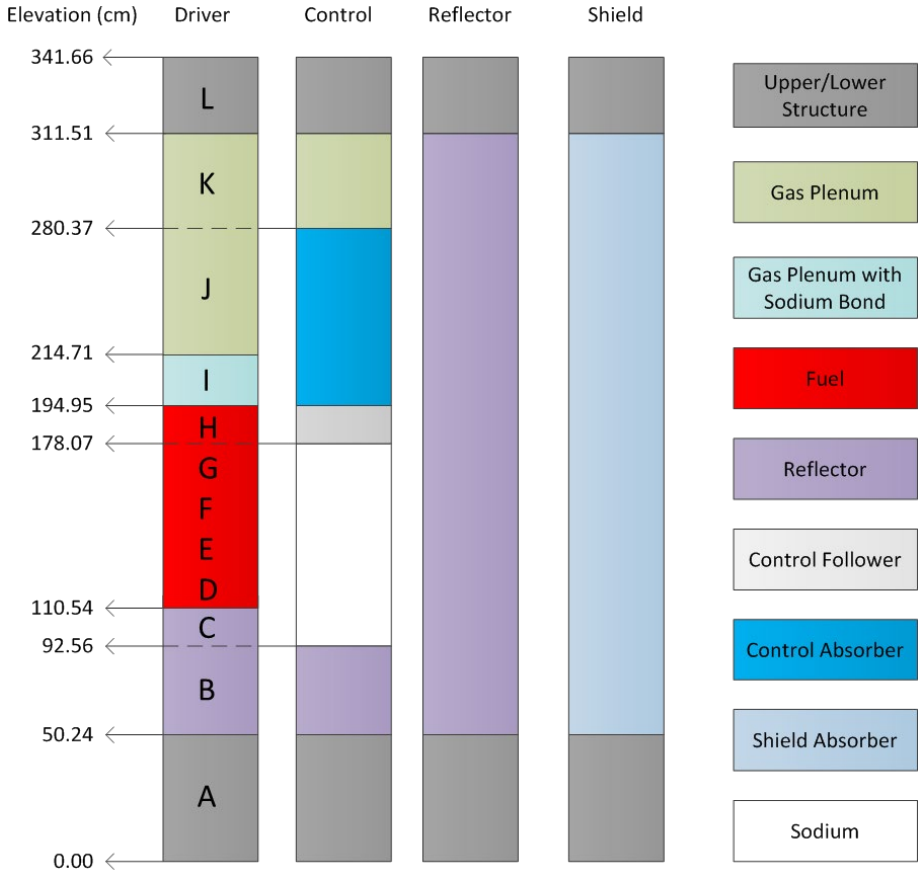

Fig. 3.15 Axial Layouts of Four Types of Assemblies in ABTR Benchmark Problem

In the Monte Carlo reference calculations, two MCNP6 models were made. One is made with homogenized assemblies just as in the VARIANT model. This calculation provides the reference assembly power distribution, which eliminates the local heterogeneity effect in modeling and can be used to verify the VARIANT flux solutions. The other MCNP6 model is made to represent the explicit intra-assembly pin geometries as shown in Fig. 3.16, except for the lower and upper structures, the lower reflector in control assembly, and the barrel assemblies. This calculation provides the reference solution of pin power distributions to verify the pin power reconstruction scheme. In MCNP6 simulations, coupled neutron and photon transport was considered, and the power distributions were estimated by F6 energy tallies. In the VARIANT/CURVE calculations, the energy deposited in the coolant inside the duct is redistributed to fuel pins, and thus the pin power tallies in MCNP6 are designated to fuel pin cells, instead of fuel pins plus claddings, for consistent comparisons. The effect of redistributing coolant heating to fuel pins was evaluted by comparing the results obtained with tallies set in fuel cells and in fuel pin plus cladding separately.

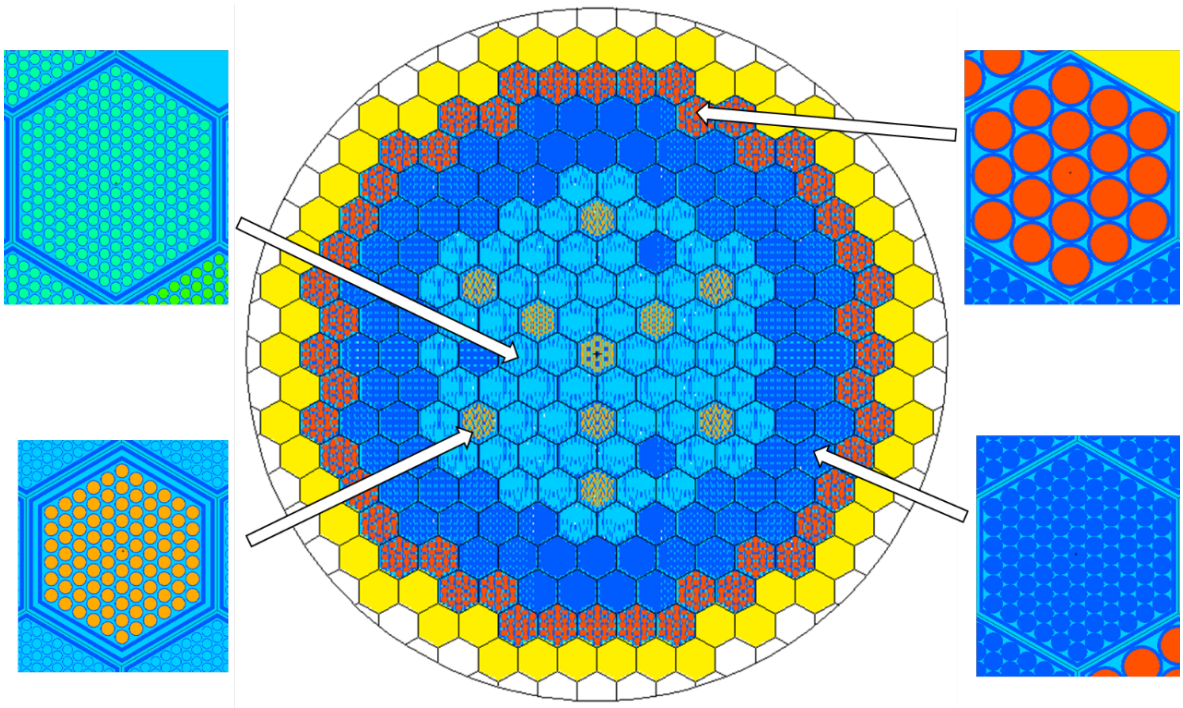

Fig. 3.16 Heterogeneous MCNP6 Model of ABTR Benchmark Problem

For the coupled neutron and gamma calculations with VARIANT, the MC^2-3 base libraries for gamma production matrices, heating cross sections, and gamma interaction cross sections were prepared in 2082 neutron groups and 94 photon groups as discussed in Section 3.1. The broad-group cross sections were generated in 33 neutron groups and 21 gamma groups, whose structures are shown in Appendix F, using the MC^2-3 code coupled with the TWODANT code. The TWODANT calculations were performed to account for the spectral transition effects using a full core R-Z model as shown in Fig. 3.17, which was converted from the hexagonal-z core model by preserving the volume and material mass of each region. For each region, 33-group neutron cross sections were generated by condensing the 2082-group cross sections in the MC^2-3 base library using the 2082-group neutron flux spectrum in that region determined from the TWODANT transport calculation. To generate broad-group gamma interaction cross sections, a 94-group photon spectrum was determined for each region by solving a fixed-source photon transport problem using TWODANT. The photon source in each region was calculated using the neutron flux obtained from the TWODANT calculation and the 2082 × 94 gamma production matrices. Using the resulting photon spectrum, the 94-group photon cross sections were condensed into broad-group constants. Since no delayed beta or gamma is included in the MCNP6 simulation, an option not to include delayed beta heating and delayed gamma production was used in the MC^2-3 calculations for consistency. In addition, both the MCNP6 and MC^2-3 calculations were performed with cross sections evaluated at the room temperature (293 K).

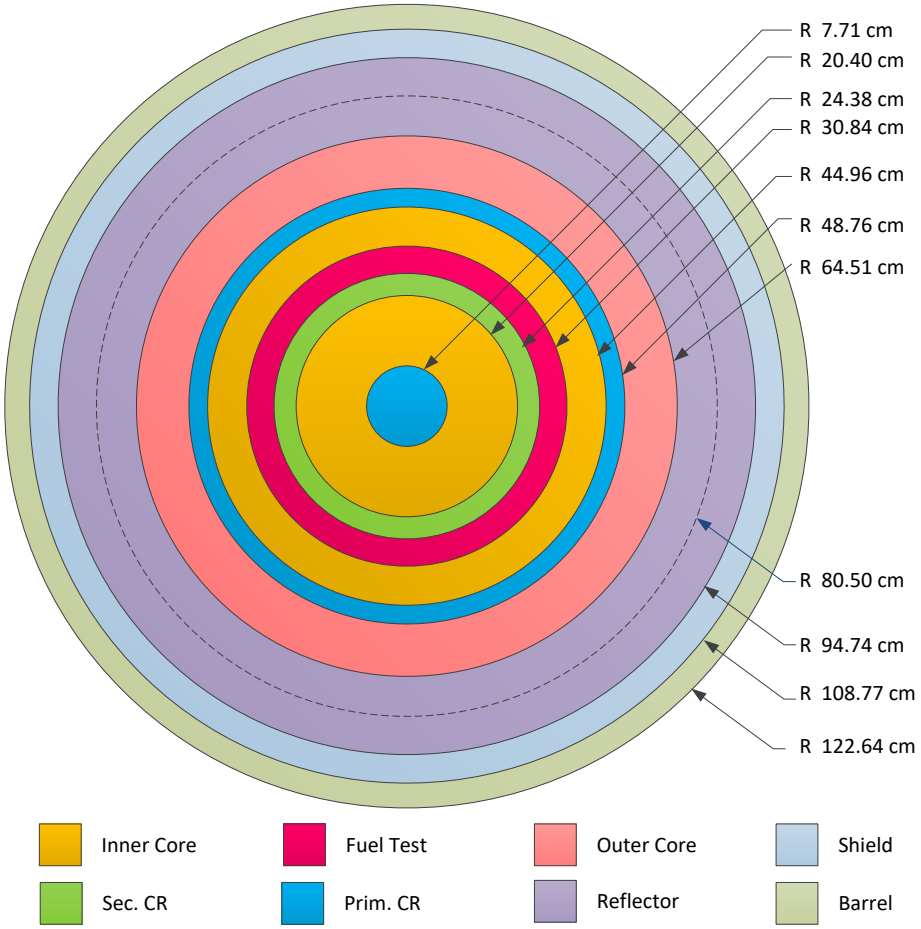

Fig. 3.17 R-Z Core Model of ABTR for Generation of Multigroup Cross Sections

3.4.1.1. Core Multiplication Factors

The core multiplication factors obtained from VARIANT and DIF3D calculations with different spatial and angular approximations are compared in Table 3.2 with the MCNP6 results. MCNP6 calculations were performed for the two core models: one with homogenized assemblies and the other with heterogeneous assemblies. The comparison of two MCNP6 results indicates that the local heterogeneity effect on the core multiplication factor is 522 pcm for the ABTR core. The VARIANT transport (P_5) solution agrees well with the MCNP6 result for the homogenized assembly model, with only 127 pcm difference in the multiplication factor. Comparatively, the VARIANT diffusion (P_1) solution underestimates the k-effective value by 1049 pcm since the diffusion approximation overestimates the neutron leakage. As expected, the DIF3D finite difference diffusion theory solution approaches the VARIANT P_1 solution with mesh refinement. It is also noted that the DIF3D finite difference diffusion solution with six meshes per hexagon agrees better with the Monte Carlo reference solution than the VARIANT P_1 solution due to error cancelation.

Table 3.2. Core Multiplication Factors from ABTR Benchmark Calculations

Code	Condition	k-effective	Difference from Ref.
MCNP	Homogenized assembly model (Ref.)	1.03561±0.00009	—
	Heterogeneous assembly model	1.04083±0.00010	0.00522
VARIANT	Homogenized assembly with P_5 angular approximation and sixth order spatial expansion	1.03688	0.00127
	Homogenized assembly with P_1 angular approximation and sixth order spatial expansion	1.02512	-0.01049
DIF3D	Finite difference diffusion option with 54 meshes per hexagonal assembly	1.02574	-0.00987
	Finite difference diffusion option with six meshes per hexagonal assembly	1.02884	-0.00677
	Nodal diffusion option with the same node sizes as in VARIANT calculations	1.02798	-0.00763

3.4.1.2. Assembly Power Distribution

The assembly total powers including both neutron and gamma heating contributions obtained from 33-group VARIANT calculations were compared to the reference MCNP6 results for the homogenized assembly model. Fig. 3.18 compares the assembly power distributions of VARIANT with the renormalized MCNP6 tallies according to the nominal total power. The statistical uncertainty of the MCNP6 results is below 0.1% in driver assemblies, and the maximum uncertainty over all assemblies is 0.28%. The relative deviations in assembly power distributions are shown in Fig. 3.19 and Fig. 3.20.

From Fig. 3.19 and Fig. 3.20, one can see that for most of the fuel assemblies, the assembly powers obtained from VARIANT calculations agree very well with the reference MCNP6 solution within 1% deviation. In the VARIANT transport (P_5) solution, only one fuel assembly in the outer core surrounded by four reflectors shows a deviation larger than 1% from the MCNP6 result. For all the fuel assemblies, except for the two fuel assemblies next to the reflector test assembly in the middle core, the VARIANT transport solution agrees better with the MCNP6 reference solution than the VARIANT diffusion (P_1) solution. The RMS error of the transport solution is 0.36% while the RMS error of the diffusion solution is 0.80%.

As expected, for all the control assemblies and the reflectors next to the outer core, the diffusion calculation overestimates the assembly power because it overestimates the leakage from fuel to non-fuel regions. Comparatively, the transport calculation improves the prediction accuracy of control assembly powers significantly. On the other hand, for the outer row of reflectors and shield assemblies, the transport solution gives comparable results with the diffusion solution. The underestimated assembly powers by ~2% at the periphery of the transport solution are due to the power normalization, and the larger relative errors are due to

the lower power level in reflectors and shields. The fluctuating relative errors in the diffusion solution also indicates error cancellations.

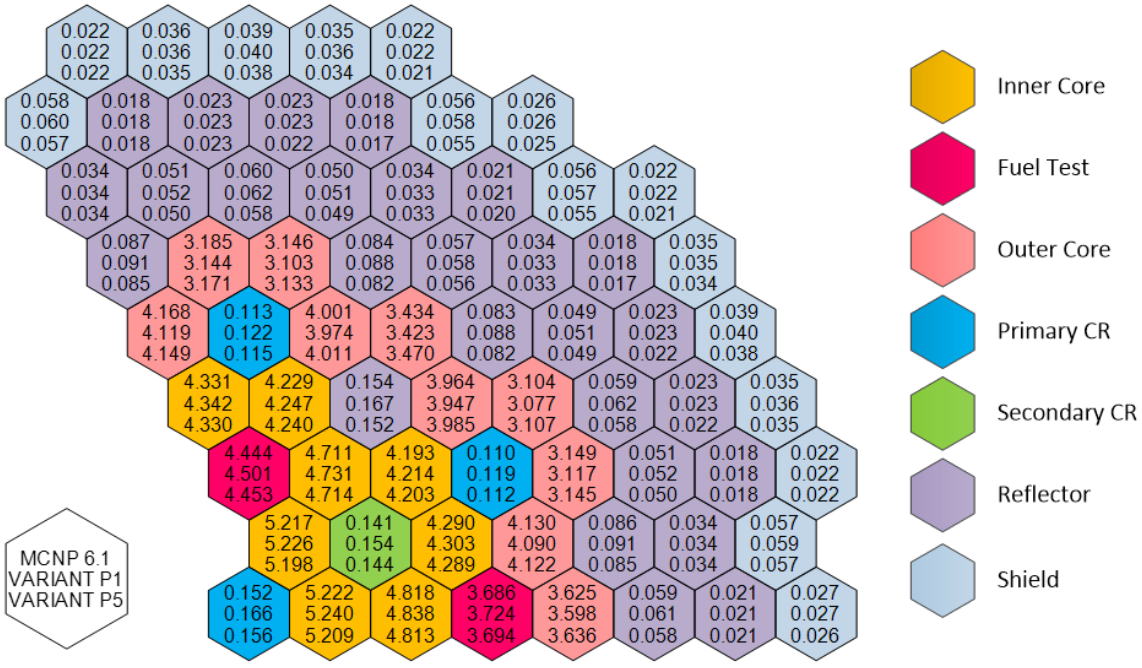

Fig. 3.18 Comparison of Assembly Power (MWt) Distributions (1/3 core) Obtained from VARIANT and MCNP6 Coupled Neutron and Gamma Heating Calculations

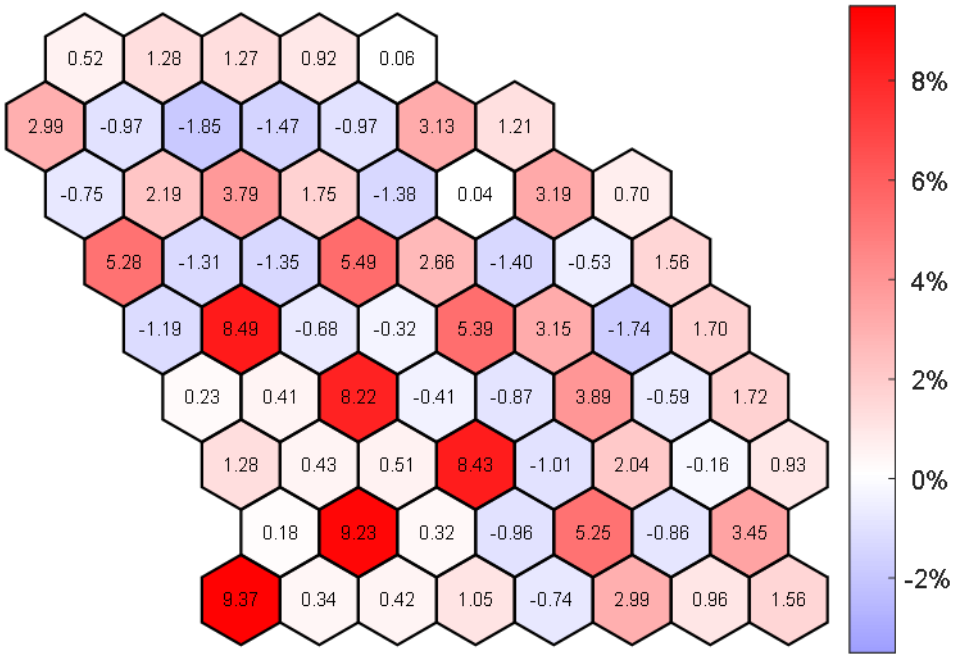

Fig. 3.19 Relative Deviation in Assembly Power Obtained with VARIANT P_1 Diffusion Calculations from MCNP6 Reference Solution

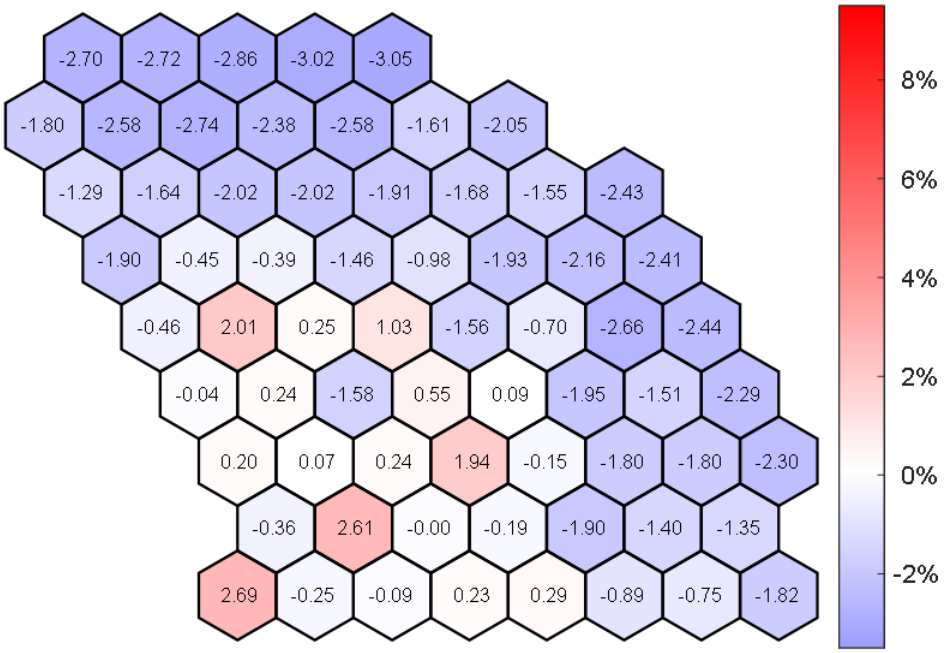

Fig. 3.20 Relative Deviation in Assembly Power Obtained with VARIANT P_5 Transport Calculations from MCNP6 Reference Solution

It is also noted that the assembly powers are significantly improved for the reflector and shield assemblies, compared to the previous results shown in the FY 2016 annual report [13]. This is mainly due to the missing gamma production data for inelastic scattering reactions and for boron-10 reactions in the previous gamma library of MC^2-3. In addition, incorrect group indexing was observed in the gamma production matrices for low-energy groups. These errors in the previous gamma library led to ~5% underestimation of the gamma source in fuel and reflectors, and ~95% underestimation of the gamma source in shields. Since the gamma heating is dominant in reflectors, the maximum assembly power error in the previous calculation was ~20%. With the corrected gamma production cross sections in the updated gamma library, the reflector and shield assembly powers can be accurately calculated now.

Through the above comparisons, the coupled neutron and gamma heating calculation scheme based on VARIANT transport solutions shows promising improvements in power calculations compared to the existing scheme based on diffusion theory solutions. These improvements are achieved mainly by predicting the neutron flux and gamma source distribution more accurately with the transport calculation.

3.4.1.3. Pin Power Distribution for Selected Fuel Assemblies

Using the new pin power calculation scheme based on VARIANT solutions, detailed pin power distributions were calculated for three fuel assemblies of the ABTR core: the inner core fuel assembly in the third assembly position of the third hexagonal ring (IC33), the fuel test assembly in the first assembly position of the fourth hexagonal ring (MC41), and the outer core fuel assembly in the second assembly position of the fifth hexagonal ring (OC52). The resulting pin powers were compared with the MCNP6 reference solution for the heterogeneous assembly model.

The first three figures in Fig. 3.21 show the arrangements of the fuel assemblies IC33, MC41, and OC52 and their six neighboring assemblies, respectively. The active core is equally divided into five axial regions D, E, F, G, and H. In the MCNP6 calculation for the heterogeneous assembly model, the total energy deposition due to neutron and gamma heating was tallied for every fuel pin segment in each axial region. In order to estimate the effect of assigning coolant heating to fuel pin in DIF3D and VARIANT heating calculations, two F6 tallies were separately considered: one is for the hexagonal pin cell shown in the rightmost figure in Fig. 3.21, and the other is for the fuel slug and cladding only. It turned out that the fraction of heat generated in coolant is ~0.2%. That is, the assignment of coolant heating to fuel pin increases the heat generation rate in fuel pin by ~0.2%. The MCNP6 pin power tallies were renormalized such that the sum of assembly powers in the heterogeneous assembly model is equal to the nominal power.

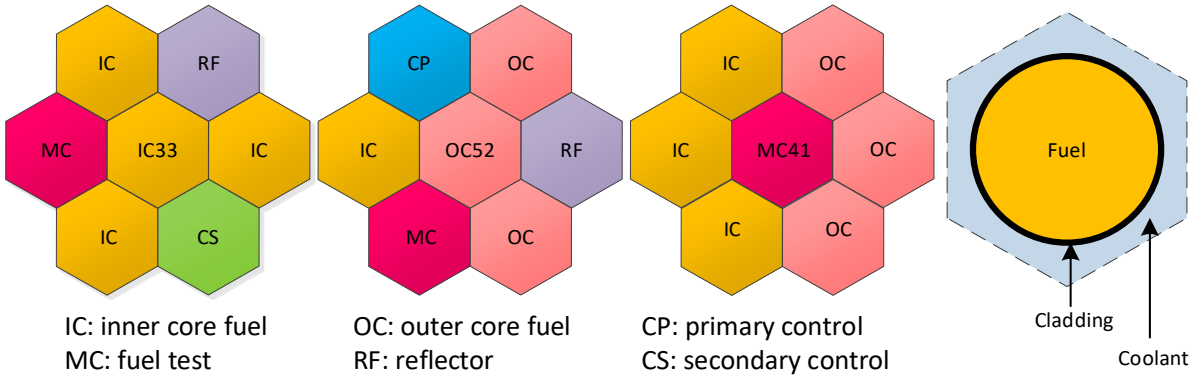

Fig. 3.21 Local Arrangements of Fuel Assemblies IC33, MC41, and OC52 and Their Six Neighbors and Schematic of Hexagonal Fuel Pin Cell in MCNP6 Model

The uncertainties in the MCNP6 results of a single calculation are typically underestimated because of the correlation between successive active cycles in MCNP criticality calculations. The fission source distribution of the current cycle is determined by the preceding cycle. The MCNP6 pin power results usually have larger uncertainties compared to the assembly power results. To estimate the realistic pin power uncertainty, the reference MCNP6 calculations were performed with five different random seed numbers, and the standard deviations in pin segment powers were estimated statistically. The resulting maximum uncertainty of pin power tallies is 1.68%, 1.63%, and 1.79% for fuel assemblies IC33, MC41, and OC51, respectively. As an example, Fig. 3.22 shows the normalized integral power of each pin segment within the axial region F at the core mid-plane of the assemblies IC33 and OC52. In both assemblies, the radial distributions of pin segment power are tilting to the neighboring reflectors. It is also observed that the assembly OC52, which is located at the boundary between core and reflectors, showed a steeper pin power gradient than the assembly IC33 that is located inside the core.

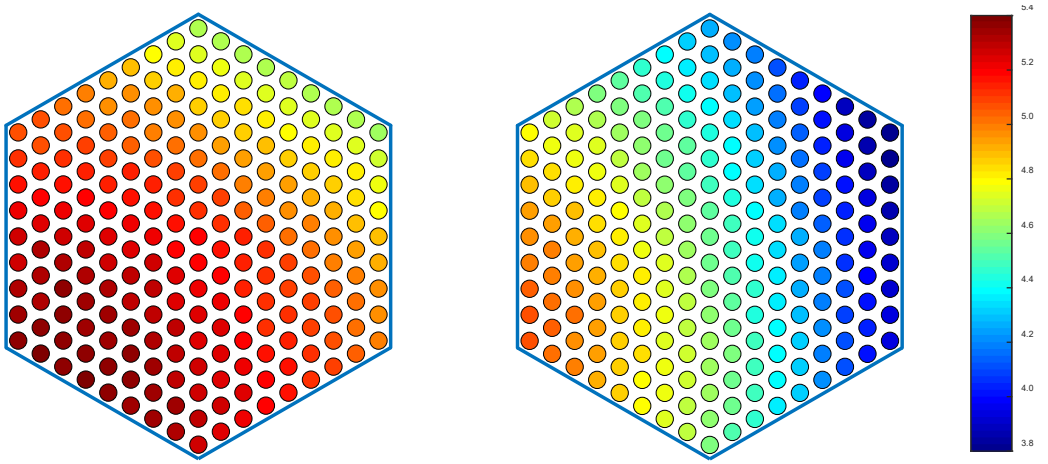

Fig. 3.22 Pin Segment Power (kW) in Axial Region F of IC33 (Left) and OC52 (Right)

The pin power calculation based on VARIANT solutions was performed with the average fluxes over the pin cross-sectional area. The axial pin power distribution in each pin segment was represented as sixth order polynomials. The integrated power in each pin segment was compared to the reference MCNP6 results for all the five axial regions in the active core. Table 3.3 and Table 3.4 show the maximum and RMS relative pin power deviations in each axial segment of the VARIANT solutions from the reference MCNP6 results. The maximum deviation in each assembly is marked with red color. Except for the axial region H of OC52, the maximum error in the pin segment powers of the VARIANT solution is below 4%, and the RMS error is ~1% for all axial regions. In addition, for all the axial regions of the three selected fuel assemblies, the VARIANT transport calculation produces more accurate pin power distributions than the diffusion solution, but the improvements made by transport calculations are marginal with the maximum improvement is ~1%.

Table 3.3. Maximum Deviations in Pin Powers Obtained from VARIANT Solutions from MCNP6 Results in Five Axial Regions of Fuel Assemblies IC33, MC41 and OC52 (Numbers in parentheses are corresponding MCNP6 results in kW at the pin with maximum error)

Assembly	Flux Calculation Option	D	E	F	G	H
IC33	VARIANT Diffusion (P_1)	2.70% (3.58)	2.72% (4.37)	2.72% (4.65)	2.72% (4.17)	-2.41% (3.13)
	VARIANT Transport (P_5)	2.18% (3.58)	2.07% (4.57)	2.51% (4.79)	2.45% (4.17)	-2.03% (3.01)
MC41	VARIANT Diffusion (P_1)	2.88% (2.91)	3.40% (3.74)	3.96% (4.30)	3.45% (3.82)	-2.07% (2.57)
	VARIANT Transport (P_5)	2.06% (2.91)	3.03% (3.36)	3.07% (4.30)	2.55% (3.82)	-1.95% (2.57)
OC52	VARIANT Diffusion (P_1)	-1.76% (3.33)	-2.33% (4.20)	-2.11% (4.53)	-2.55% (3.91)	-5.19% (2.61)
	VARIANT Transport (P_5)	-1.81% (3.54)	-1.46% (4.20)	1.58% (4.52)	-1.62% (3.91)	-4.15% (2.61)

Table 3.4. RMS Deviations in Pin Powers Obtained from VARIANT Solutions from MCNP6 Results in Five Axial Regions of Fuel Assemblies IC33 and OC52

Assembly	Flux Calculation Option	D	E	F	G	H
IC33	VARIANT Diffusion (P_1)	1.20%	1.20%	1.29%	1.34%	1.48%
	VARIANT Transport (P_5)	0.75%	0.87%	0.96%	0.94%	1.11%
MC41	VARIANT Diffusion (P_1)	1.82%	2.32%	2.44%	2.06%	1.13%
	VARIANT Transport (P_5)	0.96%	1.42%	1.53%	1.23%	0.96%
OC52	VARIANT Diffusion (P_1)	0.92%	1.30%	1.11%	1.35%	3.76%
	VARIANT Transport (P_5)	0.56%	0.69%	0.61%	0.72%	2.35%

The pin powers determined from VARIANT solutions have two major error sources. One is the inaccurate estimation of the power in each hexagonal prism node. Since the node power is preserved during the process of pin power evaluations, a node power error introduces a uniform bias in pin segment powers. The other is the distortion of intra-nodal flux distributions in the VARIANT solutions, which may further be attributed to the errors in cross sections and the angular and spatial approximations adopted in VARIANT calculations. Table 3.5 compares the node powers of the selected fuel assemblies between VARIANT and MCNP6 solutions. It is seen that the transport calculation yields more accurate node powers than the diffusion calculation. To eliminate the impact of node power on pin power distribution, the radial pin power skew in a node was determined by dividing individual pin segment powers by the averaged value in that node. Fig. 3.23 compare the radial pin power skew of the VARIANT solutions to the reference MCNP6 distribution for the axial node H of assembly OC52, which show the largest deviations in pin segment power of both the diffusion and transport solutions among all the axial nodes in the three selected fuel assemblies.

Table 3.5. Comparison of Node Powers (Watts) in Active Core of Selected Fuel Assemblies from MCNP6 (Heterogeneous Assembly Model) and VARIANT Solutions

Assembly	Node	MCNP	Std dev	VARIANT P_5	Diff.*	VARIANT P_1	Diff.*
IC33	D	8.320E+05	0.13%	8.368E+05	0.58%	8.413E+05	1.12%
	E	1.043E+06	0.14%	1.051E+06	0.76%	1.054E+06	1.12%
	F	1.108E+06	0.10%	1.117E+06	0.82%	1.121E+06	1.16%
	G	9.831E+05	0.18%	9.910E+05	0.81%	9.953E+05	1.25%
	H	6.927E+05	0.10%	6.857E+05	-1.00%	6.831E+05	-1.39%
MC41	D	6.346E+05	0.12%	6.402E+05	0.88%	6.459E+05	1.79%
	E	8.151E+05	0.16%	8.262E+05	1.36%	8.342E+05	2.34%
	F	8.689E+05	0.16%	8.814E+05	1.43%	8.898E+05	2.40%
	G	7.713E+05	0.28%	7.799E+05	1.12%	7.869E+05	2.02%
	H	5.422E+05	0.32%	5.379E+05	-0.79%	5.368E+05	-0.99%

* Both differences are relative to the MCNP6 results.

Table 3.5. Comparison of Node Powers (Watts) in Active Core of Selected Fuel Assemblies from MCNP6 (Heterogeneous Assembly Model) and VARIANT Solutions (Continued)

Assembly	Node	MCNP	Std dev	VARIANT P_5	Diff.*	VARIANT P_1	Diff.*
OC52	D	7.300E+05	0.41%	7.281E+05	-0.26%	7.244E+05	-0.77%
	E	9.200E+05	0.14%	9.173E+05	-0.30%	9.104E+05	-1.05%
	F	9.763E+05	0.07%	9.754E+05	-0.09%	9.677E+05	-0.88%
	G	8.710E+05	0.22%	8.673E+05	-0.42%	8.609E+05	-1.16%
	H	6.223E+05	0.16%	6.085E+05	-2.23%	5.995E+05	-3.67%

* Both differences are relative to the MCNP6 results.

It is shown in Fig. 3.23 that the VARIANT transport and diffusion solutions yield comparable intra-nodal pin power distributions that both agree well with the reference MCNP6 distribution. For the node H of OC52, among the maximum pin power error of -4.15% in the transport solution, ~2.25% error is due to the underestimated node power. Comparatively, among the maximum pin power error of -5.19% in the diffusion solution, more than half (3.67%) is due to the underestimated node power. These observations indicate that the improved pin segment powers of the transport solution presented in Table 3.5 are mainly due to the more accurate node power calculation.

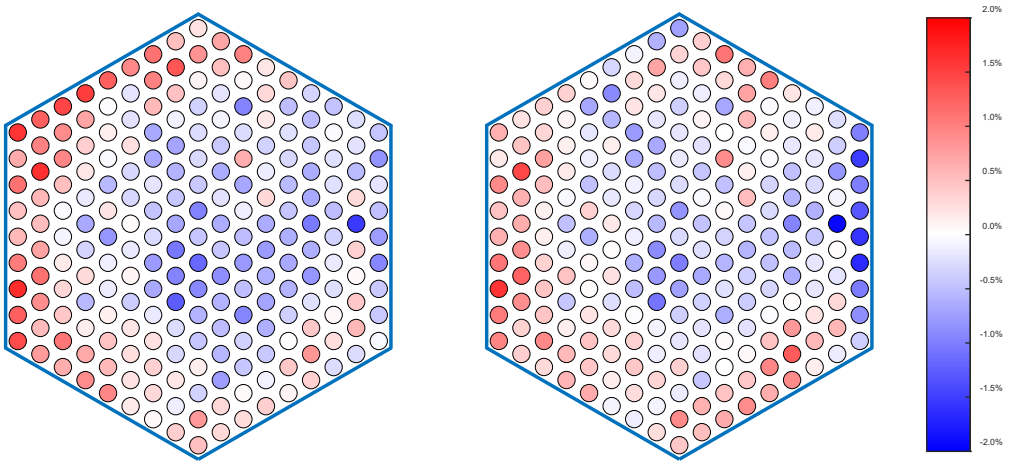

VARIANT P_1 vs MCNP6 VARIANT P_5 vs MCNP6

Fig. 3.23 Comparison of Radial Pin Power Skew between VARIANT and MCNP6 Solutions for Node H of Assembly OC52

3.4.1.4. Local Heterogeneity Effect in Pin Power Calculation

As we discussed in Section 3.3.3, the CURVE calculation neglects the local heterogeneity effects in power evaluation. To justify this approximation, the pin power form functions are determined as the pin power ratio relative to the average pin power in a node from the MCNP6 solution obtained with a heterogeneous single-assembly model and reflective boundary conditions. Fig. 3.24 shows the pin power form functions in the node F and H of assembly

OC52. It is seen that the radial pin power distribution is practically flat within a node. The local heterogeneity effect is mainly caused by the assembly duct and inter-assembly gap. At the core mid-plane (i.e., node F), the maximum pin power deviation from the average value is ~0.6%, including ~0.1% uncertainties in the MCNP tallies. At the top of active core (node H), the maximum deviation reaches 1%. After applying the form functions to the pin segment powers in node H of assembly OC52, the pin power skews of VARIANT solutions are compared to the MCNP6 reference results in Fig. 3.25. It is noted that the form functions do not make noticeable improvements in the predicted pin power distributions, which confirms that the neglect of the local heterogeneity of the fast reactor fuel assembly would not introduce significant errors in the pin power evaluation.

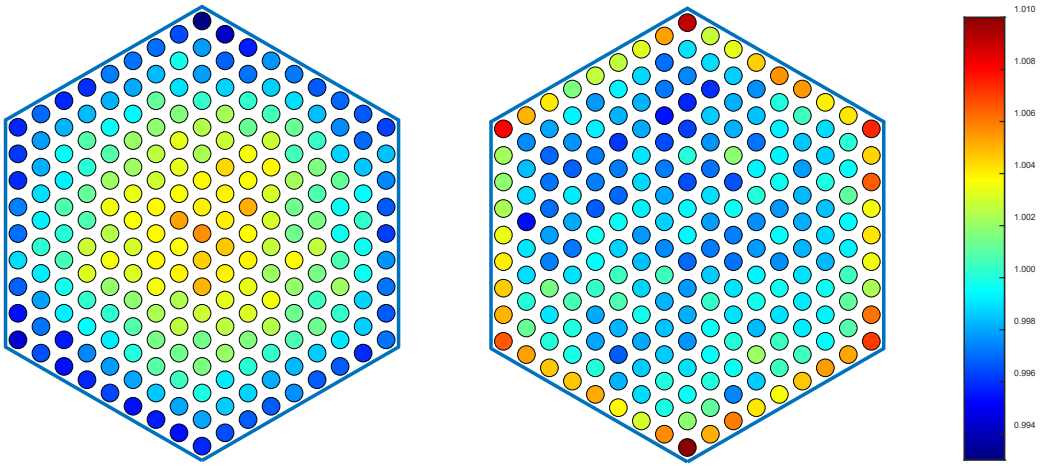

Fig. 3.24 Pin Power Form Functions in Node F (Left) and H (Right) of Assembly OC52 from MCNP6 Heterogeneous Assembly Calculation

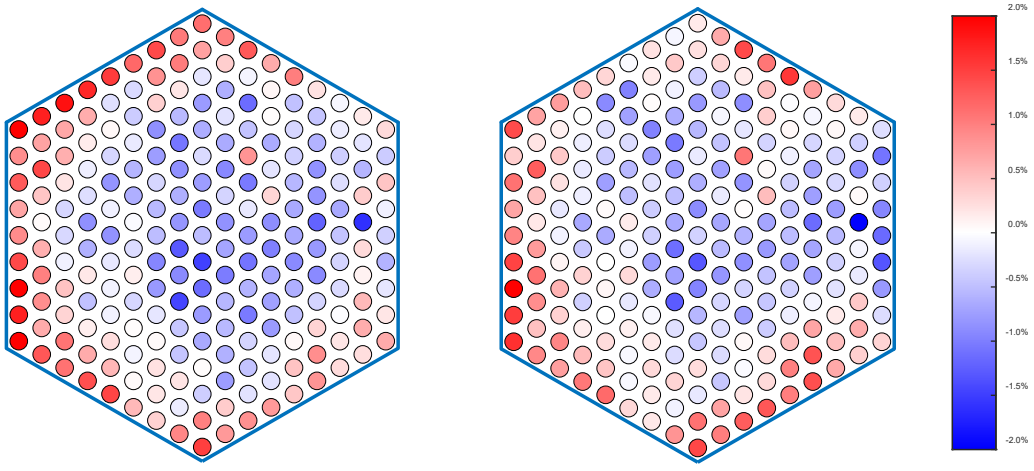

VARIANT P_1 vs MCNP6 VARIANT P_5 vs MCNP6

Fig. 3.25 Comparison of Radial Pin Power Skew between VARIANT and MCNP6 Solutions for Node H of Assembly OC52 after Applying Power Form Functions

3.4.1.5. Impact of Flux Reconstruction Option in CURVE Calculation

There are two user options in the CURVE pin power calculation to simplify the flux evaluation and reduce the required memory to save the pin power profiles. One is to evaluate the VARIANT flux solution along the pin centerline instead of calculating the averaged fluxes over the pin cross-sectional area. The other is to approximate the axial power profile in each pin segment as a quadratic polynomial. For the calculation of pin segment integral powers, the latter approximation would not make any difference since the average power density in a segment is preserved to determine the quadratic polynomial. As an example, the pin segment powers for assemblies IC33, MC41, and OC52 obtained with the default option and the user option to evaluate the VARIANT transport flux solution at pin center line are compared in Table 3.6. It is confirmed that the two flux evaluation options yield practically the same pin power results.

Table 3.6. Relative Difference (%) in Pin Segment Powers Introduced by Evaluating VARIANT Flux at Pin Centerline in CURVE Calculation

	D	E	F	G	H
IC33	0.0013	0.0005	0.0005	0.0005	0.0003
MC41	0.0012	0.0012	0.0012	0.0012	0.0011
OC52	0.0016	0.0010	0.0010	0.0010	0.0011

In addition, the pin power distributions obtained with the default option and the quadratic approximation option are compared at the core mid-plane (node F) and the top of active core (node H) for all fuel assemblies. It is seen from Fig. 3.26 that the quadratic approximation would not introduce a linear power difference larger than 0.1% at the core mid-plane. However, the difference could exceed 1% at the top (and bottom) of active core in some assemblies as shown in Fig. 3.27. This is because the flux distribution is not sooth enough to be represented by low-order polynomials at the core axial boundaries.

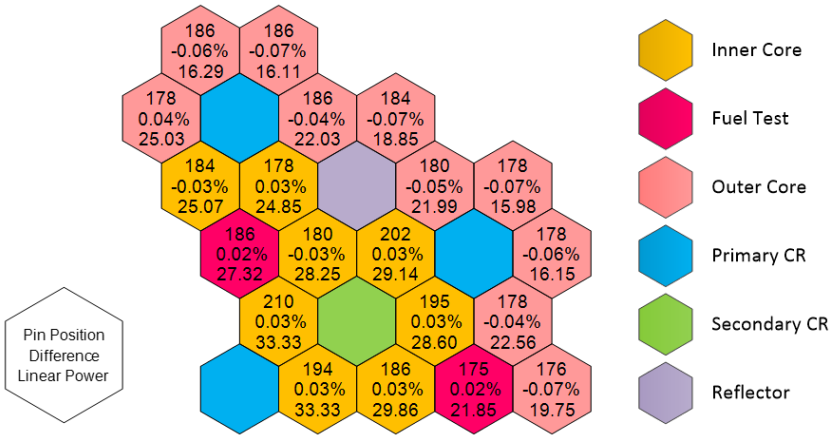

Fig. 3.26 Maximum Error (%) in Pin Linear Power in Node F of Fuel Assemblies Caused by Approximating Axial Power Profiles as Quadratic Polynomials and Corresponding Pin Number and Linear Power (kW/m)

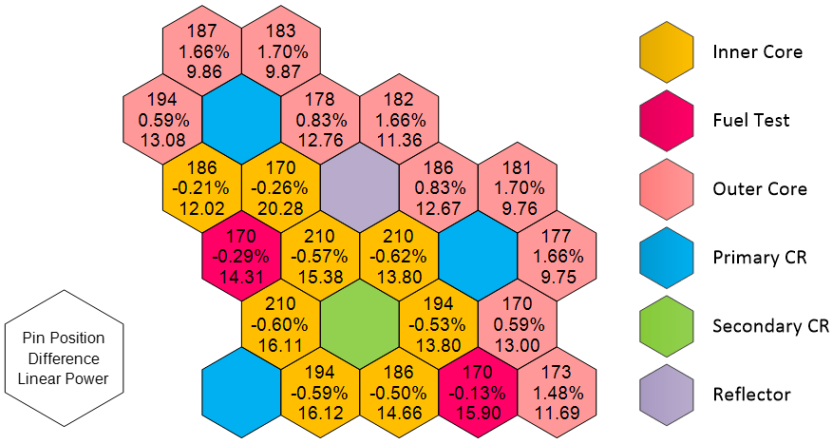

Fig. 3.27 Maximum Error (%) in Pin Linear Power in Node H of Fuel Assemblies Caused by Approximating Axial Power Profiles as Quadratic Polynomials and Corresponding Pin Number and Linear Power (kW/m)

3.4.1.6. Impact of TWODANT Gamma Spectrum Calculation

For the coupled neutron and gamma transport calculations with VARIANT, by default, the broad group gamma cross sections are generated with the 94-group region dependent gamma spectra obtained in a TWODANT full core transport calculation as described in Section 3.1.2. Meanwhile, since the gamma cross sections are relatively smooth, the gamma spectrum can be simply determined in a zero-dimensional (0D) slowing down calculation for each homogeneous composition, with the fixed gamma source calculated using the neutron spectrum and gamma production matrix for that composition.

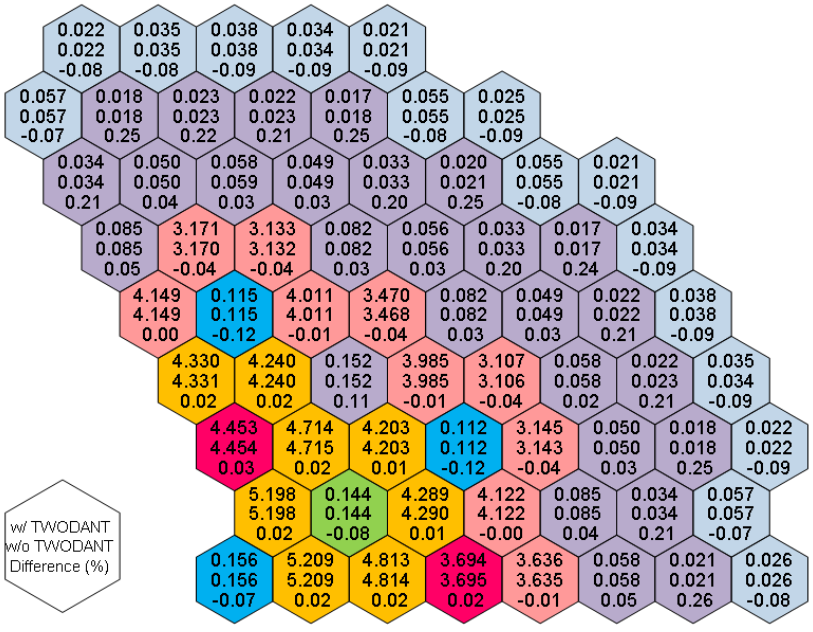

Fig. 3.28 ABTR Assembly Total Powers Obtained with Gamma Cross Sections Generated with or without TWODANT Spectrum Calculation

Here we tested the impact of gamma spectrum calculation option on the coupled heating calculation by comparing the assembly powers of VARIANT transport solutions using the gamma cross sections generated with the two different gamma spectrum calculation options. As shown in Fig. 3.28, the TWODANT full core gamma transport calculation of region dependent gamma spectra makes negligible differences in the resulting assembly powers. For all the fuel assemblies, the difference is less than 0.05%. For reflector assemblies, where the major source photons are produced in fuel assemblies and transported outwards, the difference in assembly power can be larger as ~0.25%. This is because the gamma heating becomes dominant in reflectors.

3.4.1.7. Contribution of Delayed Gamma and Delayed Beta Heating

The above analyses of the ABTR benchmark problem were all performed without considering the delayed gamma and delayed beta production in the heating calculations, because the MCNP6 reference calculations cannot handle the production of delayed photons and beta particles. Now with the VARIANT transport calculations, the heating contributions of delayed gamma and delayed beta are quantified for the ABTR reference metal core design. The assembly total powers including the contributions of delayed gamma and beta heating are shown in Fig. 3.29.

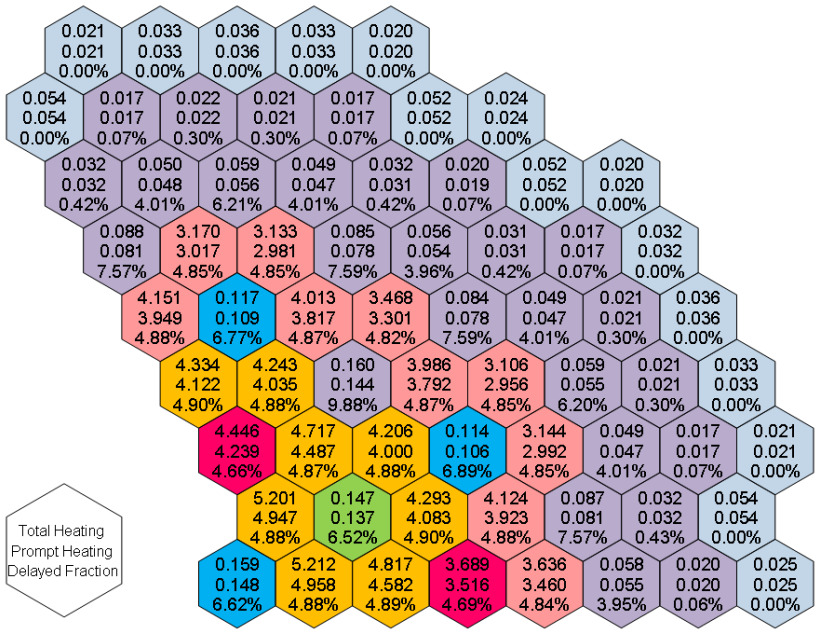

Fig. 3.29 ABTR Assembly Total Powers (MW) w/ and w/o Delayed Gamma and Beta Heating Contributions along with Power Fraction of Delayed Heating

Here the prompt heating means the assembly power neglecting the delayed heating contribution. It is seen that the delayed heating makes up ~5% of the total power in fuel assemblies. For the control and reflector assemblies next to fuel assemblies, the delayed heating fraction can be greater than 6%, which are mainly due to the delayed photons produced in fission and transported to the neighboring non-fuel regions. For the radial reflector

assemblies next to shields, the delayed photons from fuel regions did not contribute much to the total heating because they were mostly absorbed before reaching the core periphery. In addition, since the dominant heating in control absorbers is from the (n, α) reaction, the delayed gamma heating is negligible in the shield assemblies.

3.4.2. Comparison of Heating Calculation Methods Based on VARIANT and DIF3D Flux Solutions

Using the ABTR benchmark problem, the performance of the new heating calculation scheme based on VARIANT transport calculations was compared to that of the existing heating calculation scheme based on DIF3D finite difference diffusion calculations. Fig. 3.30 compares the assembly power distribution of the DIF3D diffusion solution with six triangular meshes per hexagon and the VARIANT P_5 transport solution with the reference MCNP6 results for the homogenized assembly model. It is seen that the VARIANT transport solution agrees better with the reference MCNP6 solution than the DIF3D coarse-mesh finite difference diffusion solution, except for the two outer core fuel assemblies near the material test assembly on the fourth row. The more accurate assembly powers of DIF3D in the outer core appear to be due to error cancelation as we saw in the comparison between VARIANT P_1 diffusion and P_5 transport solutions in Section 3.4.1.2. The DIF3D solution would approach the VARIANT P_1 diffusion solution with mesh refinement. However, due to the error cancellation in the coarse mesh finite difference approximation, the assembly power error of the DIF3D solution is less than that of the VARIANT P_1 diffusion solution, especially for the control assemblies.

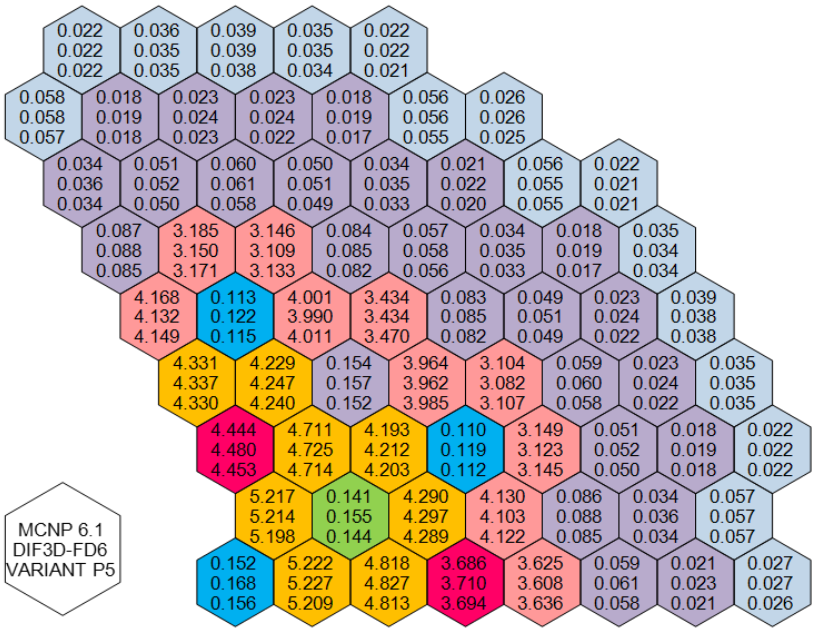

Fig. 3.30 Comparison of Assembly Power (MW) Distributions of DIF3D Diffusion and VARIANT Transport Solutions with Reference MCNP6 Solution

Using the existing pin power reconstruction scheme in the existing SE2-ANL code, the intra-nodal pin power distribution was calculated for the inner core fuel assembly IC33 and the outer core fuel assembly OC52. The neutron and gamma flux distributions of the DIF3D

coarse-mesh finite difference diffusion solutions were assumed to be separable in the planar and axial directions within an assembly. Furthermore, the heat generation rate outside the pin bundle is not explicitly considered. For a consistent comparison of pin powers, the fraction of assembly power generated outside the pin bundle obtained from the VARIANT transport solutions was applied in the existing SE2-ANL procedure. The pin bundle power was obtained by subtracting the power deposited outside the pin bundle from the assembly power. The pin segment powers were then calculated from the separable radial and axial power profiles of each assembly. Table 3.7 and Table 3.8 show the maximum and RMS relative errors in the pin segment powers determined from DIF3D and VARIANT solutions from the MCNP6 reference results.

Table 3.7. Maximum Deviations in Pin Powers Obtained with DIF3D and VARIANT Solutions from MCNP6 Results in Five Axial Regions of Fuel Assemblies IC33 and OC52

Assembly	Flux Calculation Option	D	E	F	G	H
IC33	DIF3D-FD Diffusion	-4.53%	3.82%	3.38%	3.83%	-4.02%
	VARIANT Diffusion (P_1)	2.70%	2.72%	2.72%	2.72%	-2.41%
	VARIANT Transport (P_5)	2.18%	2.07%	2.51%	2.45%	-2.03%
OC52	DIF3D-FD Diffusion	-6.45%	-3.57%	4.99%	3.48%	-5.68%
	VARIANT Diffusion (P_1)	-1.76%	-2.33%	-2.11%	-2.55%	-5.19%
	VARIANT Transport (P_5)	-1.81%	-1.46%	1.58%	-1.62%	-4.15%

Table 3.8. RMS Deviations in Pin Powers Obtained with DIF3D and VARIANT Solutions from MCNP6 Results in Five Axial Regions of Fuel Assemblies IC33 and OC52

Assembly	Flux Calculation Option	D	E	F	G	H
IC33	DIF3D-FD Diffusion	1.46%	1.17%	1.20%	1.26%	1.69%
	VARIANT Diffusion (P_1)	1.20%	1.20%	1.29%	1.34%	1.48%
	VARIANT Transport (P_5)	0.75%	0.87%	0.96%	0.94%	1.11%
OC52	DIF3D-FD Diffusion	2.62%	1.52%	1.57%	1.35%	3.96%
	VARIANT Diffusion (P_1)	0.92%	1.30%	1.11%	1.35%	3.76%
	VARIANT Transport (P_5)	0.56%	0.69%	0.61%	0.72%	2.35%

It is seen that the pin powers obtained with the existing SE2-ANL method based on DIF3D solutions deviate more from the MCNP6 pin powers than those obtained with the new method based on the VARIANT diffusion solution. On the other hand, as shown in Table 3.9, the DIF3D solution yields less accurate results than the VARIANT transport solution but more accurate node powers than the VARIANT diffusion solution, due to error cancelation as mentioned above.

Table 3.9. Comparison of Nodal Powers (Watts) of VARIANT and DIF3D Solutions with MCNP6 Solution for Five Axial Nodes of Fuel Assemblies IC33 and OC52

Assembly	Node	VARIANT P_5	diff.*	VARIANT P_1	diff.*	DIF3D-FD	diff.*
IC33	D	8.368E+05	0.58%	8.413E+05	1.12%	8.382E+05	0.74%
	E	1.051E+06	0.76%	1.054E+06	1.12%	1.053E+06	0.97%
	F	1.117E+06	0.82%	1.121E+06	1.16%	1.119E+06	1.05%
	G	9.910E+05	0.81%	9.953E+05	1.25%	9.943E+05	1.15%
	H	6.857E+05	-1.00%	6.831E+05	-1.39%	6.848E+05	-1.14%
OC52	D	7.281E+05	-0.26%	7.244E+05	-0.77%	7.241E+05	-0.82%
	E	9.173E+05	-0.30%	9.104E+05	-1.05%	9.129E+05	-0.77%
	F	9.754E+05	-0.09%	9.677E+05	-0.88%	9.709E+05	-0.55%
	G	8.673E+05	-0.42%	8.609E+05	-1.16%	8.639E+05	-0.81%
	H	6.085E+05	-2.23%	5.995E+05	-3.67%	6.034E+05	-3.05%

The existing heating calculation method distorts the radial pin power distribution because of the separability approximation, especially in the fuel assemblies next to reflector or control assemblies. Fig. 3.31 shows the radial pin power distribution in the axial node F of assembly IC33 obtained with the new heating calculation scheme based on the VARIANT transport calculation. Fig. 3.32 shows the distortion in the radial pin power distribution by the existing heating calculation scheme based on the DIF3D calculations relative to the pin power distribution in Fig. 3.31. The existing scheme overestimates the pin power for those pins next to the reflector and control assemblies because of the separability assumption, which is not valid in this assembly.

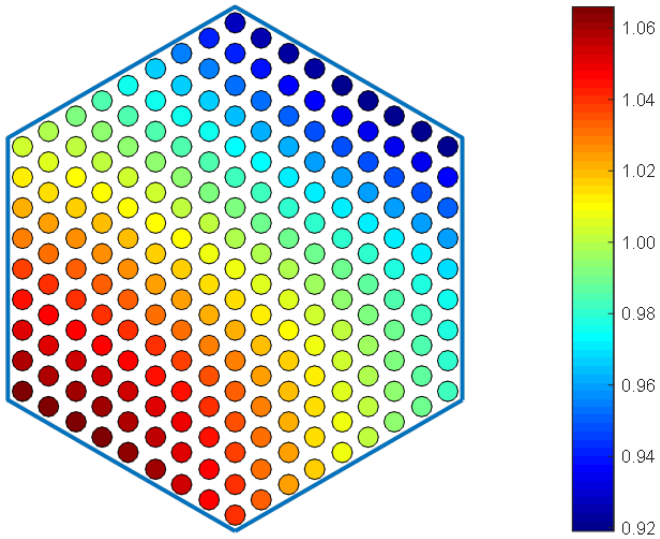

Fig. 3.31 Radial Pin Power Distribution in Node F of Assembly IC33 of ABTR Core

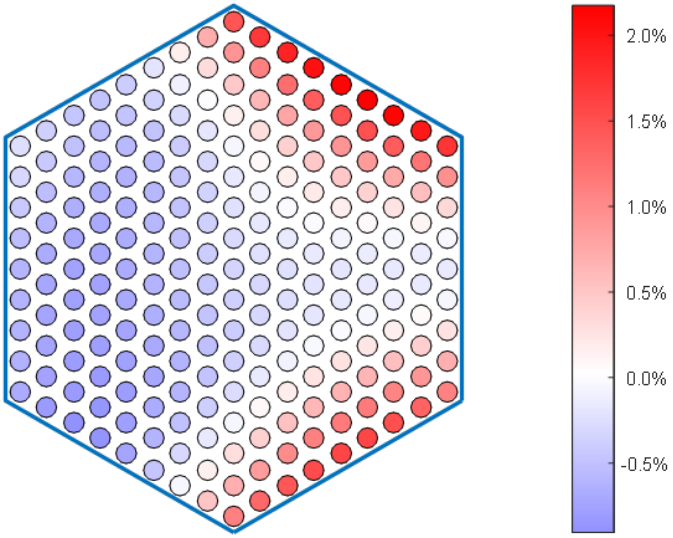

Fig. 3.32 Difference in Pin Power Distribution between Existing and New Heating Calculation Procedures for Node F of Fuel Assembly IC33 of ABTR Core

The results in Table 3.8 show that the improvement in segment-integrated pin power by transport calculation is not significant. However, larger discrepancies are expected in pointwise power distribution. Using the existing and new heating calculation schemes, the linear power was evaluated at fine-mesh points along each fuel pin in each fuel assembly of the ABTR core. The resulting fine-mesh values showed that the discrepancy could reach 9% in the assemblies near reflectors. As an example, the maximum differences in fine-mesh linear powers in the axial node F (i.e., the core mid-plane) of each fuel assembly along with the corresponding pin positions and linear powers are shown on the left-hand-side in Fig. 3.33. The fuel pins are arranged in a triangular lattice and numbered as illustrated on the right-hand-side in Fig. 3.33, where we just show the first four rings of fuel pins. It is noted that the maximum deviations in the outer core assemblies occur in the outermost ring of pins, facing the reflectors.

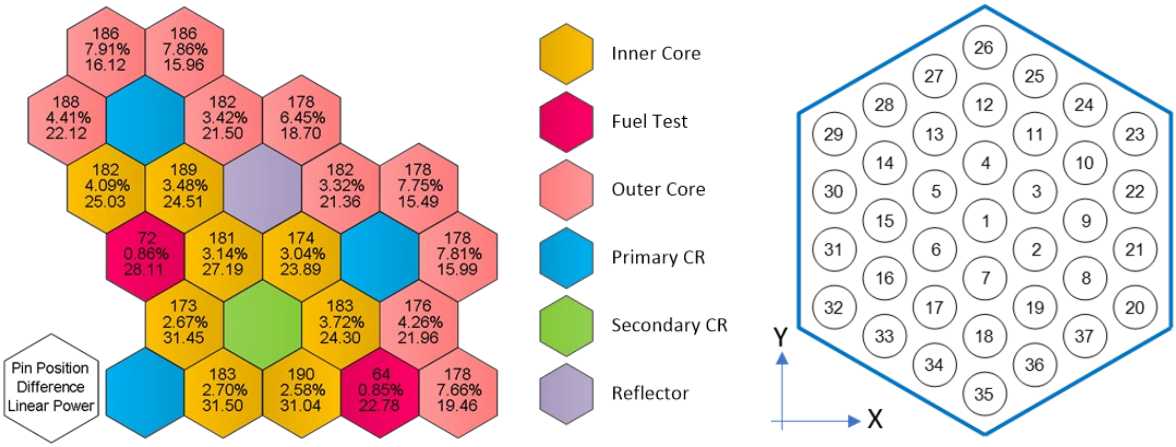

Fig. 3.33 Left: Maximum Difference (%) in Linear Power in Node F of Fuel Assemblies between Existing and New Heating Calculation Procedures and Corresponding Pin Number and Linear Power (kW/m); Right: Pin Numbering Scheme in CURVE Pin Power Evaluation

3.4.3. EBR-II Run 138B Benchmark Problem

The performance of the new heating calculation scheme based on VARIANT transport calculations was further tested using the EBR-II Run 138B benchmark problem. The EBR-II benchmark problem is based on the core configuration of Run 138B, which consists of 71 regular driver fuel assemblies, 13 half-worth (HW) fuel driver assemblies, 10 control and safety assemblies, six structural assemblies (steel dummy), and six experimental assemblies (including three material test assemblies and three fuel test assemblies). The detailed core specifications can be found in Ref. [41]. The core layout for EBR-II Run 138B is shown in Fig. 3.34. One driver assembly and one blanket assembly, respectively labeled as A and B in Fig. 3.34, are selected for verification tests of the pin power reconstruction scheme of CURVE.

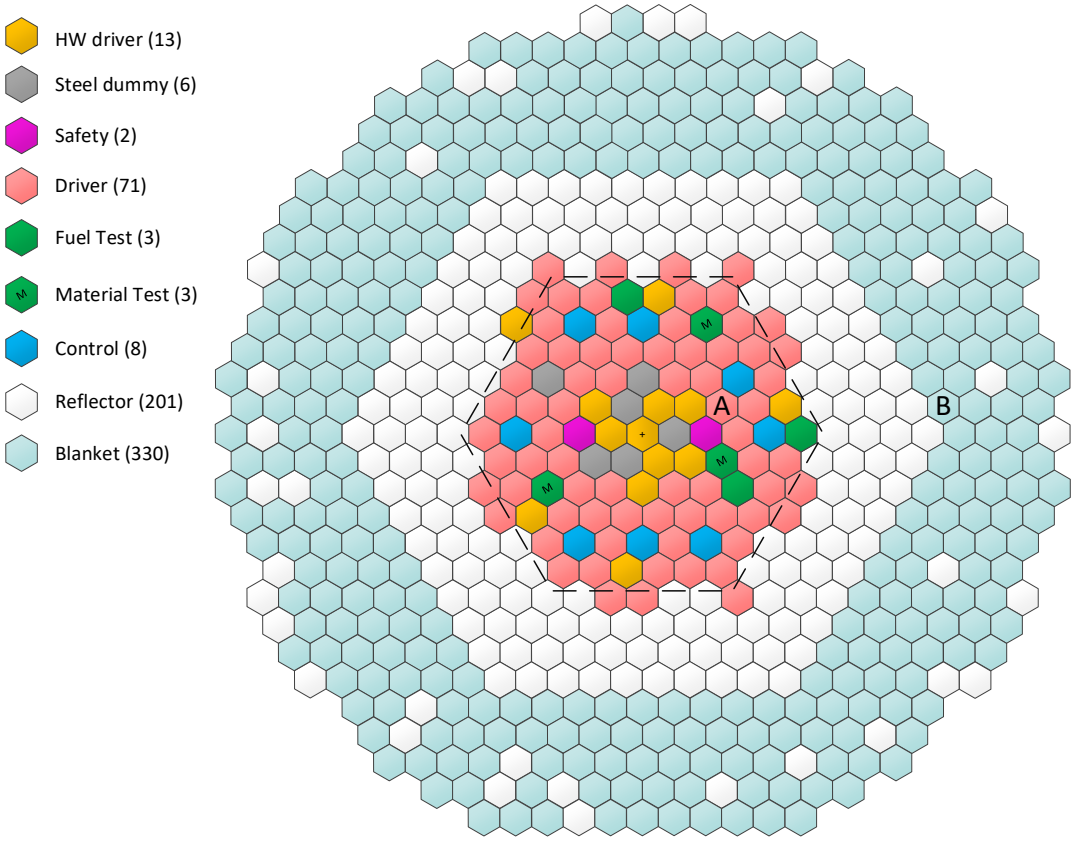

Fig. 3.34 EBR-II Core Loading Pattern for Run 138B

The coupled neutron and gamma heating calculations were performed based on the VARIANT transport and diffusion flux solutions, and the assembly power distributions were compared with the Monte Carlo reference solution. For the VARIANT calculations, a set of 33-group neutron and 21-group photon cross sections were generated using the MC^2-3 code based on the ENDF/B-VII.0 library. The VARIANT transport calculation was performed with P_3 angular approximation and sixth order polynomial expansion for spatial approximation. The Monte Carlo reference solution was obtained from an MCNP6 calculation for the homogenized assembly model using the ENDF/B-VII.0 library. The coupled neutron and gamma transport were simulated with 100,000 histories per cycle and 380 active cycles in total. Since no delayed

beta and delayed gamma is included in the MCNP6 simulation, an option not to include delayed beta heating and delayed gamma production was used in the MC^2-3 calculations for consistency.

Fig. 3.35 compares the integrated assembly powers for the innermost six rings of hexagonal assemblies, i.e., within the black dashed hexagon in Fig. 3.34. The statistical uncertainties of MCNP6 results are less than 0.2%. Fig. 3.36 and Fig. 3.37 show the relative deviations in the assembly powers of the VARIANT diffusion and transport solutions from the reference MCNP6 values, respectively. With the diffusion calculation, the maximum error is 2.26% for fuel assemblies and 11.70% for structural assemblies. With the transport calculation, the maximum errors in assembly powers are significantly reduced. The maximum error is reduced to 0.68% for fuel assemblies and to 4.05% for structure assemblies. A clear comparison between diffusion and transport calculations is given in Table 3.10 for each assembly type.

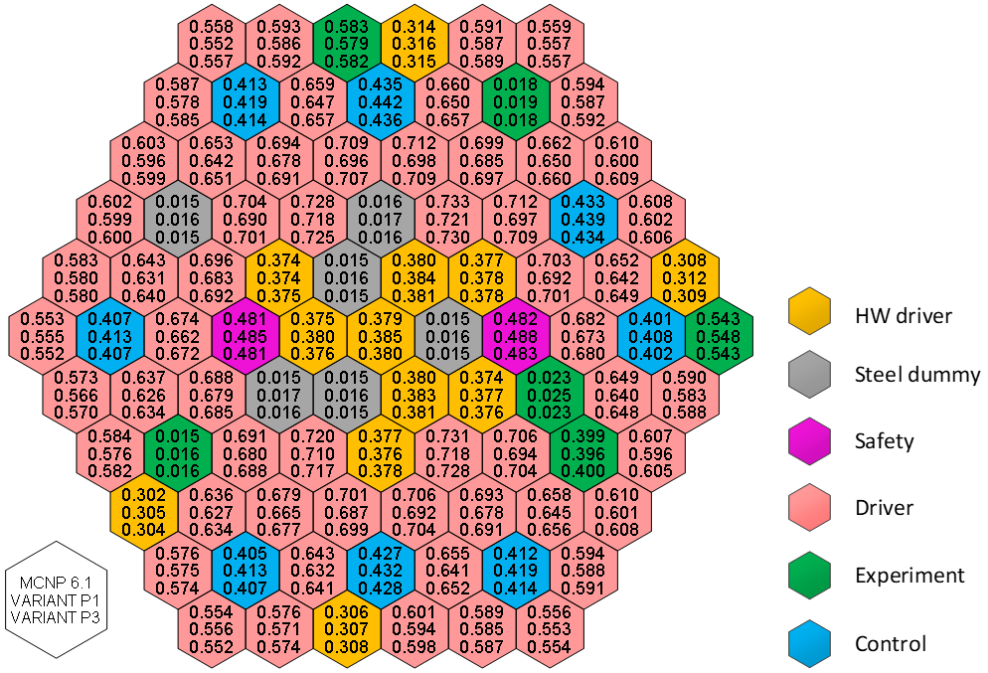

Fig. 3.35 Assembly Powers (MW) of EBR-II Run 138B Obtained with Coupled Neutron and Gamma Heating Calculations with VARIANT and MCNP6

Table 3.10. Relative Errors in Assembly Powers of VARIANT Diffusion (P_1) and Transport (P_3) Solutions from MCNP6 Reference Results for Different Assembly Types

Assembly Type		Fuel	Structure	Reflector	Blanket
Maximum uncertainty in MCNP results		0.11%	0.14%	1.68%	0.71%
RMS Error	VARIANT P_1	1.36%	10.33%	4.27%	6.27%
	VARIANT P_3	0.34%	3.37%	4.62%	3.00%
Max. Error	VARIANT P_1	-2.86%	11.70%	9.20%	9.10%
	VARIANT P_3	0.68%	4.05%	-7.19%	4.67%

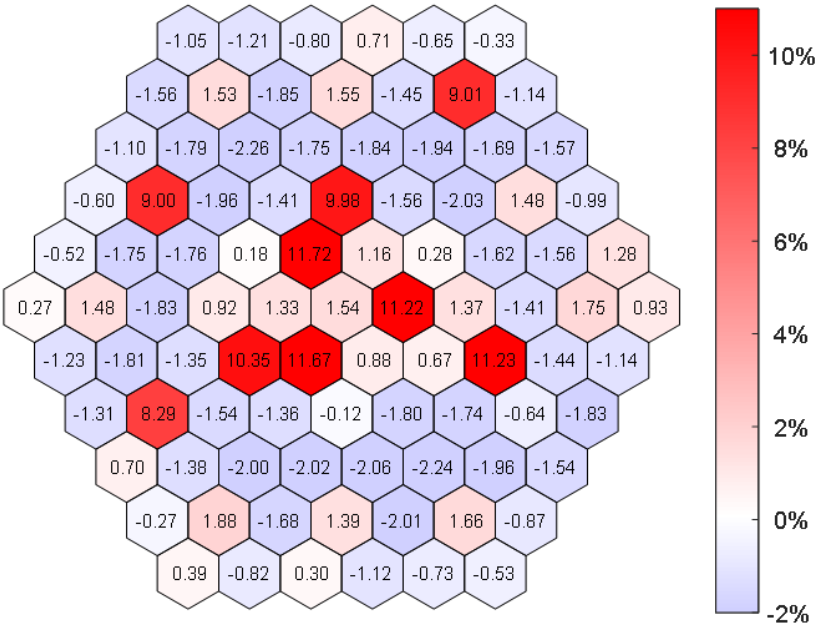

Fig. 3.36 Deviation in Assembly Power of VARIANT Diffusion Solution from Reference MCNP6 Solution for EBR-II Run 138B

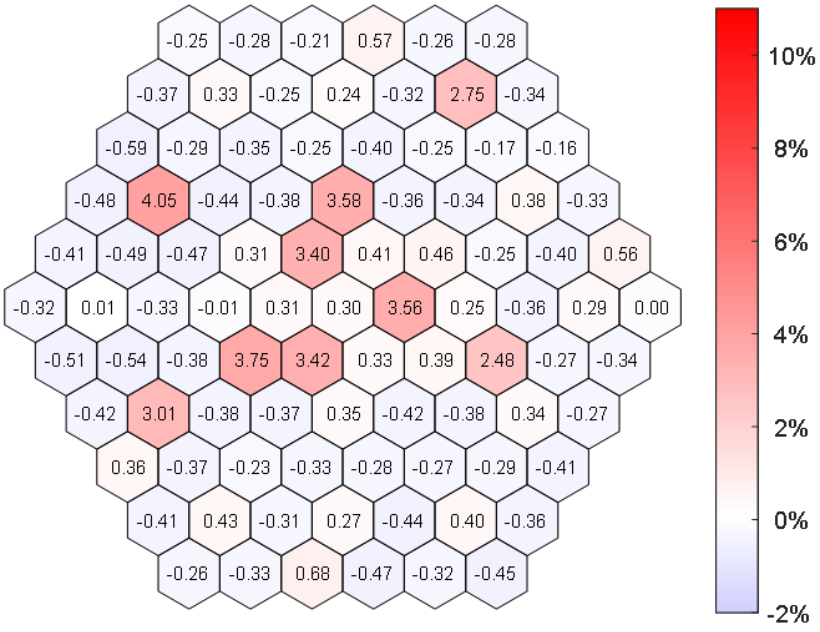

Fig. 3.37 Deviation in Assembly Power of VARIANT Transport Solution from Reference MCNP6 Solution for EBR-II Run 138B

The transport effects are pronounced in the small EBR-II core, and hence the VARIANT transport calculation improves the accuracy of assembly powers significantly. The gamma flux solution of diffusion calculation has relatively large errors both from the diffusion approximation for gamma transport and from the gamma source error caused by the neutron diffusion calculation. As a result, the relatively large errors in assembly powers are observed

in structure assemblies. The VARIANT transport results reduce the errors in structure assembly powers significantly but still show noticeable relative errors, which are mainly due to the small power level of structure assemblies. Compared with the previous results in Ref. [40], which were obtained with the 21-group gamma cross sections generated with NJOY, the new heating calculation based on the 94-group gamma library and VARIANT transport solutions improves the prediction accuracy for assembly powers. Especially for structure assemblies (including steel dummy and material test assemblies), the new gamma library helped reduce the assembly power errors to <4% from ~9%.

Using the EBR-II Run 138B benchmark problem, the CURVE pin power calculation scheme was tested by comparing the evaluated pin segment powers in two selected assemblies to the reference results obtained with MCNP6 simulations in a heterogeneous assembly model. Table 3.11 summarizes the relative errors in the CURVE calculated pin segment powers from the MCNP6 results. It is seen that for the driver assembly, the pin powers agree well with the reference results, with comparable relative errors to those of reconstructed pin powers in the ABTR benchmark problem. Larger relative errors are observed in the blanket assembly, which are mainly due to the inaccurate node power results in the VARIANT/CURVE calculation. For assembly B, the assembly power is overestimated by 5.88% compared with the MCNP6 result obtained with the heterogeneous assembly model.

Table 3.11. Relative Errors in Pin Segment Powers of CURVE Solution from Reference MCNP6 Results for Two Selected Assemblies in EBR-II

Assembly	Node Position	MCNP6 Uncertainty	RMS Error		Maximum Error	
			Diffusion	Transport	Diffusion	Transport
A (Driver)	Mid-Plane	0.5%	1.34%	0.76%	-2.88%	1.95%
	Top of Core	1.0%	2.14%	2.15%	-4.12%	-4.36%
B (Blanket)	Mid-Plane	1.8%	10.61%	7.31%	12.98%	9.67%
	Top of Core	2.6%	8.90%	5.38%	15.28%	11.38%

4. Steady-State Thermal-hydraulic Analysis Method

The multi-assembly, steady-state subchannel analysis code SE2-ANL has been widely used in thermal-hydraulic analysis of SFR design. It was developed by interfacing the SUPERENERGY-2 code [42] with ANL's steady-state heating calculation performed with the DIF3D and GAMSOR codes. SUPERENERGY-2 is a multi-assembly, steady-state code for wire-wrapped SFR core thermal-hydraulic analysis. For given power and flow distributions, it calculates the detailed core-wide coolant temperature profiles based on the ENERGY model. At ANL, reactor hot spot analysis methods as well as fuel and cladding temperature calculation models were added to the original version of SUPERENERGY-2. Both nominal and two-sigma temperatures are calculated for the fuel and cladding.

The new, coupled neutron and gamma heating calculation scheme based on VARIANT transport calculations described in Section 3 has been incorporated into the SE2-ANL code. In addition, several improvements have been made on the computational methods and models. First, the Cheng-Todreas correlations [18] have been implemented for better prediction of the mixing parameters. The limit on the axial mesh size due to the numerical instability problem of the current explicit difference scheme for axial discretization has also been eliminated by replacing the explicit difference scheme with the θ-method of the SLTHEN code [19]. This allows the use of the inter-assembly gap flow model with much smaller number of axial meshes. Furthermore, an automated flow allocation scheme has been implemented to determine assembly flow rates such that the peak cladding mid-wall temperatures of individual orifice zones are equalized over the burn cycle. To incorporate these improvements, the SE-ANL code has been restructured, and a large fraction of it has been completely rewritten, resulting in a new version named SE2-UM.

4.1. Review of ENERGY Model and Existing SE2-ANL Methods

4.1.1. ENERGY Model

In order to enhance the computational efficiency, the simplified energy equation mixing model called ENERGY was developed in mid 1970s specifically for SFRs. The simplicity of the model results from the replacement of the exact momentum coupling between subchannels with approximations appropriate for wire-wrapped SFR assemblies. The conventional subchannel definition and key geometrical parameters for wire-wrapped LMR assemblies illustrated in Fig. 3.12 are repeated in Fig. 4.1. As shown in Fig. 4.1, the subchannels in wire-wrapped assemblies can be divided into three regions: interior subchannels, edge subchannels, and corner subchannels. A bulk average value characterizes each of the hydrodynamic and thermal coolant conditions in every axial control volume of each subchannel.

Instead of considering every subchannel explicitly, the derivation of the model starts by dividing the rod array of an SFR assembly into two predominant regions, the central and wall regions, and by assuming characteristic flows in each region. The central region includes the interior subchannels, and the wall region includes the edge and corner subchannels. To reduce the computational time, the flow split models are used instead of solving the momentum equations. In the central region, the flow pattern is approximated by a uniform average axial flow and enhanced eddy diffusivity. The enhanced eddy diffusivity models the oscillatory lateral flows between subchannels due to the presence of wire wraps and the natural turbulence

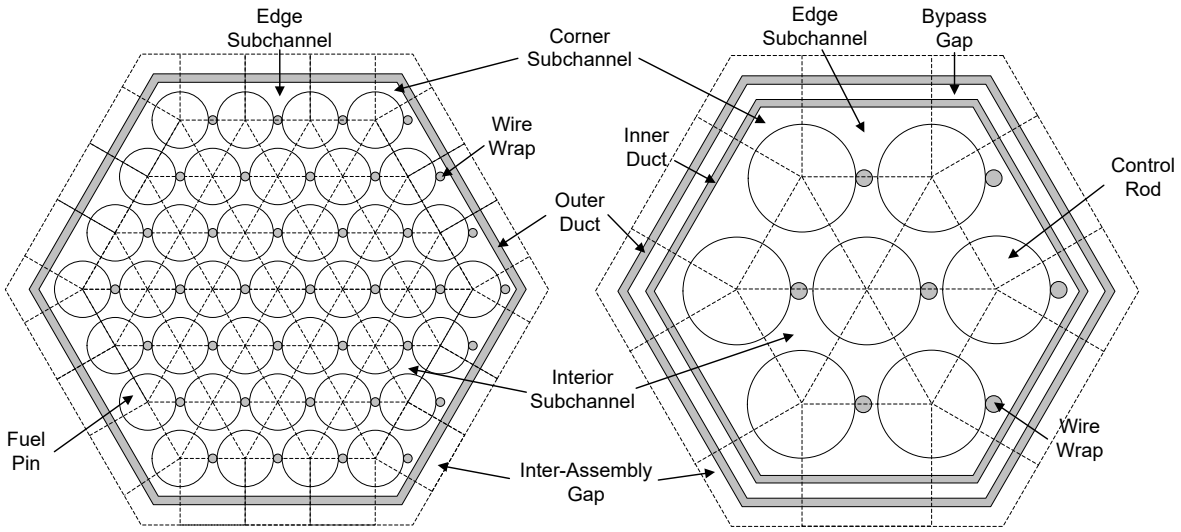

Fig. 4.1 Pin Geometries and Flow Subchannels in Single (Left) and Double (Right) Duct Assemblies

mixing. In the wall region, the velocity field is approximated by a uniform axial and a uniform circumferential component. The circumferential component represents the unidirectional cross flow along the duct wall induced by wire-wraps. The mixing between subchannels is again modeled using the enhanced eddy diffusivity as in the central region. Energy transport equations are then derived based on these four parameters: two axial velocities in the central and peripheral regions (U_{z1} and U_{z2}, respectively), one circumferential velocity in the wall region (U_s), and one enhanced eddy diffusivity for heat (ε). The resulting equations for subchannels in the central and wall regions are respectively given by

$$\rho c_p U_{z1} \frac{\partial T}{\partial z} = \left(\rho c_p \varepsilon_1 + \zeta k\right)\left(\frac{\partial^2 T}{\partial x^2} + \frac{\partial^2 T}{\partial y^2}\right) + Q, \tag{4.1}$$

$$\rho c_p U_s \frac{\partial T}{\partial s} + \rho c_p U_{z2} \frac{\partial T}{\partial z} = \left(\rho c_p \varepsilon_n + \zeta k\right)\frac{\partial^2 T}{\partial n^2} + \left(\rho c_p \varepsilon_s + \zeta k\right)\frac{\partial^2 T}{\partial s^2} + Q, \tag{4.2}$$

where T, ρ, c_p, and k represent the temperature, density, specific heat, and thermal conductivity of the coolant, respectively. The terms on the left represent the axial convection and the lateral convection due to circumferential swirl flow. The first terms on the right side of the equations represent the lateral heat exchange with neighboring subchannels due to conduction and wire-wrap sweeping flows (represented by the enhanced eddy diffusivity for heat). The volumetric heat source from the fuel is given by Q. The factor ζ (< 1) that multiplies the conductivity accounts for the winding (and hence lengthened) path between fuel pins followed by the sodium as energy is conducted in the direction transverse to the bulk flow. The heat transfer from the duct wall in the wall region is accounted by the boundary condition.

The flow split between the central and peripheral regions are derived from the equal pressure drop and continuity conditions. In the existing SE2-ANL code, there are two built-in flow split models: Novendstern model [43] and MIT turbulent flow split model (Chiu-

Rohsenow-Todreas correlations) [44]. In the MIT turbulent flow split model, the equal pressure drop condition are written as:

$$\frac{f_b}{De_b} = \frac{f_1}{De_1} X_1^2 = \frac{f_2}{De_2} X_2^2 \tag{4.3}$$

where subscript *b* represents the bundle average, subscript 1 is for the interior subchannel and 2 is for the edge subchannel, *f* is the friction factor, *De* is the equivalent hydraulic diameter, and *X* is the flow split parameter. Using these flow split parameters, the continuity condition can be expressed as:

$$S_1 X_1 + S_2 X_2 = 1.0 \tag{4.4}$$

where $S_1 = N_1 A_1 / A_b$, $S_2 = (N_2 A_2 + N_3 A_3) / A_b$, N_i is the number of subchannels of type i in the bundle, the subscript 3 is for the corner subchannel, and A_i is the axial average flow area of subchannel type i. Providing any two values of f_b, f_1, f_2, X_1, and X_2, the other three values can be calculated with Eq. (4.3) and Eq. (4.4). Hawley utilized the phenomenological models developed by Chiu [44] to determine the friction factors f_1 and f_2. Then the other three parameters were computed with known f_1 and f_2. The numerical coefficients in the final formulas of flow split parameters are fit with experimental flow split data. The expressions for MIT turbulent flow split model used in SUPERENERGY-2 are [42]

$$X_1 = \frac{A_1 N_1 + A_2 N_2 + A_3 N_3}{A_1 N_1 + (A_2 N_2 + A_3 N_3)\left(\frac{De_2}{De_1}\right)^{0.714} \alpha^{0.571}} \tag{4.5}$$

$$X_2 = \frac{A_1 N_1 + A_2 N_2 + A_3 N_3}{A_1 N_1 \left(\frac{De_1}{De_2}\right)^{0.714} \left(\frac{1}{\alpha}\right)^{0.571} + (A_2 N_2 + A_3 N_3)} \tag{4.6}$$

where

$$\alpha = \frac{2200\left(\frac{De_1}{H}\right)\left(\frac{Ar_1}{As_1}\right)\left(\frac{P}{\sqrt{\pi^2 P^2 + H^2}}\right)^2 + 1}{1.2\left[1 + (1.9 n C_{1L})^2\right]^{1.375}} \tag{4.7}$$

$$n = \frac{(P - D)\frac{P}{2}}{\left(P - \frac{D}{2}\right)\frac{P}{2} - \frac{\pi D^2}{16}} \tag{4.8}$$

$$A_{s1} = \frac{\sqrt{3}}{4} P^2 - \frac{\pi}{8} D^2 \tag{4.9}$$

$$A_{r1} = \frac{\pi}{6}\left(P - \frac{D}{2}\right)^2 - \frac{\pi}{24}D^2 \tag{4.10}$$

and P and D are the pin pitch and diameter, respectively.

In order to consider the thermal mixing effect introduced by wire wraps, two mixing parameters ε_{1L}^* and C_{1L} are used, where ε_{1L}^* is the dimensionless effective eddy diffusivity and C_{1L} is the ratio of the swirl velocity to the periphery axial velocity. Chiu, Rohsenow and Todreas correlated these two mixing parameters with the local subchannel velocity [45]. The Chiu-Rohsenow-Todreas correlations used in SE2-ANL are:

$$\varepsilon_{1L}^* = 0.128\left(\frac{P}{P-D}\right)^{0.5}\left(\frac{A_{r1}}{A_{s1}}\right)^{0.5}\frac{(D+D_w)P^2}{\sqrt{\pi^2(D+D_w)^2+H^2}}\left(\frac{1}{A_{s1}}\right) \tag{4.11}$$

$$C_{1L} = 10.5\left(\frac{P-D}{P}\right)^{0.35}\left(\frac{A_{r2}}{A_{s2}}\right)^{0.5}\frac{D+D_w}{\sqrt{\pi^2(D+D_w)^2+H^2}} \tag{4.12}$$

where

$$A_{s2} = P\left(\frac{D}{2}+D_w\right) - \frac{\pi}{8}D^2 \tag{4.13}$$

$$A_{r2} = \frac{\pi}{4}\left(\frac{D}{2}+D_w\right)^2 - \frac{\pi}{16}D^2 \tag{4.14}$$

and D_w is the wire-wrap diameter.

4.1.2. Subchannel Geometry and Axial Discretization of Energy Equation

There are mainly two types of assembly geometries to be considered for SFR subchannel analysis: single duct wire-wrap fuel pin assembly and double duct bypass assembly. They are shown in Fig. 4.2 and Fig. 4.3, respectively. A double duct bypass type assembly contains two duct walls and a bypass gap between these two walls. The interior subchannels are numbered sequentially in a counter-clockwise outward spiral starting with the two o'clock node neighboring the center pin [42]. Then the edge and corner subchannels are numbered in the same order. Duct and inter-assembly gap nodes are also numbered with the same pattern. If the assembly is the double duct type, the nodding will have two more rings as shown in Fig. 4.3.

To solve the energy equations numerically, the control volume method is applied to get the finite difference form equations. In the current version of SE2-ANL, the heat balance equations in Eq. (4.1) and Eq. (4.2) are axially discretized using the explicit differencing scheme. As a result, for a given set of inlet temperatures and radial boundary conditions, the coolant temperature distribution in the core is determined by marching in the axial direction from the bottom to the top of the core. However, the explicit scheme requires relatively small meshes to satisfy the stability criteria, and hence makes it impractical to model the axial convection

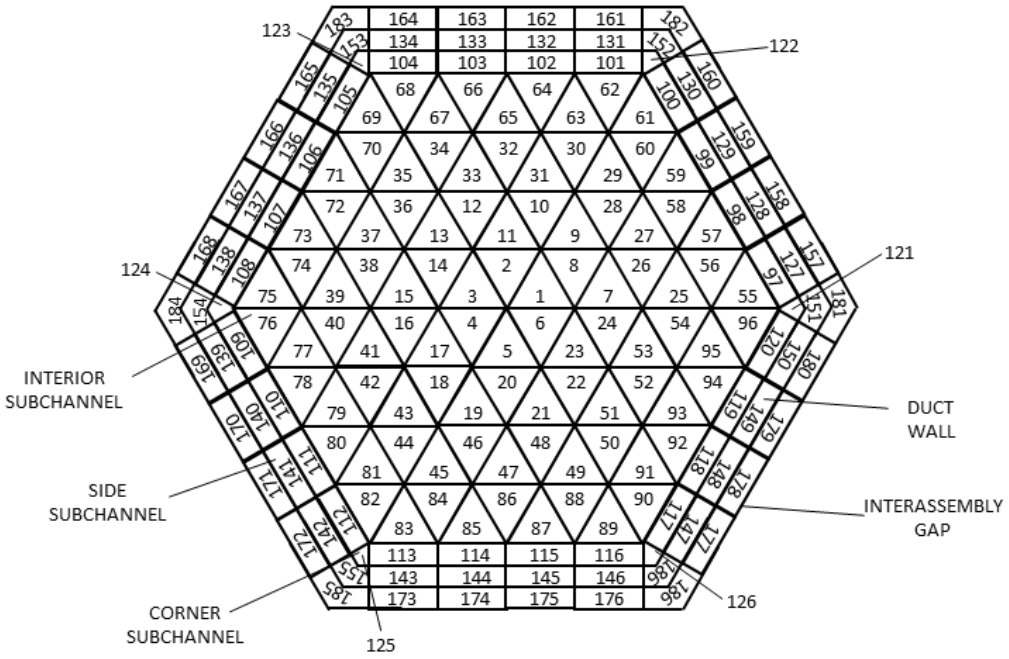

Fig. 4.2 Subchannel Numbering for 61-Pin Single Duct Assembly

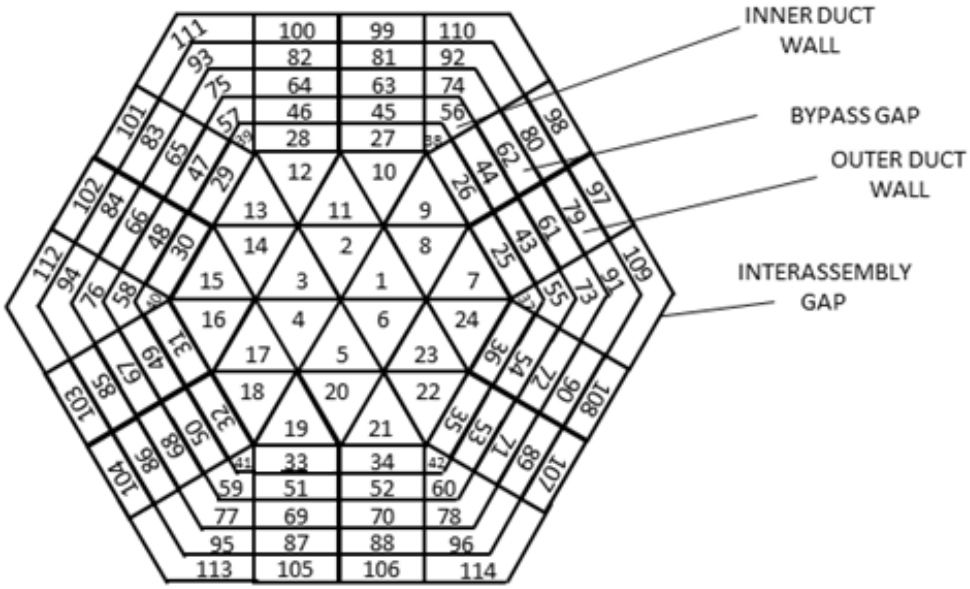

Fig. 4.3 Subchannel Numbering for 19-Pin Double Duct Assembly

due to the inter-assembly gap flow, which is generally very small. To represent the inter-assembly heat transfer in the case of a small inter-assembly gap flow, therefore, a one-dimensional conduction model is used by assuming that the inter-assembly gap sodium is stagnant. The temperature equation of a typical control volume can be written as:

$$\frac{dT}{dz} = \sum_{i=1}^{I} c_i (T_i - T) - c_q q' \tag{4.15}$$

where T is the temperature of a certain mesh, T_i are the temperature of the adjacent mesh, and q' is the linear heat generation rate in this mesh.

A detailed example is given for the interior subchannels. There are two different configurations for an interior subchannel, as shown in the Fig. 4.4. In one configuration, the interior subchannel of interest is surrounded by three interior subchannels. In the other configuration, it is surrounded by two interior subchannels and an edge subchannel.

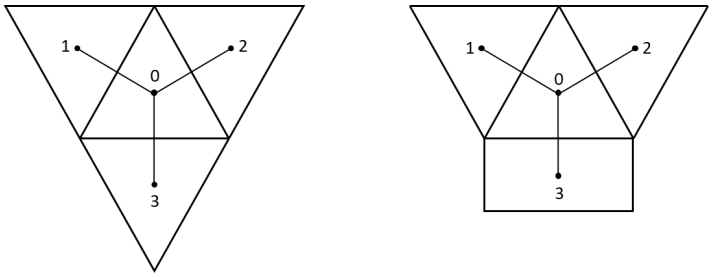

Fig. 4.4 Interior subchannel Configurations

Denoting the interior subchannel of interest by the subchannel 0 and the three adjacent subchannels by 1, 2, and 3, the general energy balance equation for the interior subchannel can be written as:

$$m_1 c_P \frac{dT_0}{dz} = q_0' + PC_\varepsilon \left(\frac{T_1 + T_2 - 2T_0}{\eta_1} + \frac{T_3 - T_0}{\eta_x} \right) \tag{4.16}$$

where T_i is the temperature of subchannel i, $C_\varepsilon = \zeta k + \rho c_P \varepsilon$, and η_i is the distance between the subchannel 0 and an adjacent subchannel i with $x = 1$ for an interior subchannel 3 and $x = 2$ for an edge subchannel 3, which are explicitly given by:

$$\eta_1 = \frac{P}{\sqrt{3}} \tag{4.17}$$

$$\eta_2 = \frac{1}{2}\left(\frac{P}{\sqrt{3}} + g + \frac{D}{2} \right) \tag{4.18}$$

With the explicit axial differencing scheme used in the existing SE2-ANL, the temperature at an axial mesh $n+1$ can be solved in terms of the temperatures at the axial mesh n as:

$$T_0^{n+1} = T_0^n + \frac{\overline{q}_{0n}' \Delta z^n}{m_1 c_p} + \frac{PC_\varepsilon \Delta z^n}{m_1 c_p} \left(\frac{T_1^n + T_2^n - 2T_0^n}{\eta_1} + \frac{T_3^n - T_0^n}{\eta_x} \right) \tag{4.19}$$

4.1.3. Hot Channel Analysis

To assure safe and reliable reactor operation, the impacts of uncertainties in theoretical and experimental analyses, instrumentation accuracy, manufacturing tolerances, properties, and correlations must be considered in the prediction of fuel assembly temperatures. In SE2-ANL, these uncertainties are treated through the use of hot channel factors. With the hot channel factors, nominal and 2σ values are calculated for peak cladding and fuel temperatures. The semi-statistical method is utilized in determining the hot channel factors in SE2-ANL. The semi-statistical method is a hybrid method of the earlier deterministic and statistical methods. It was used in the analysis of Clinch River Breeder Reactor (CRBR) by Westinghouse [46].

In the semi-statistical method, it is assumed the temperature T_M at location M is affected by the uncertainties as:

$$T_M(\boldsymbol{\alpha},\boldsymbol{\varepsilon}) = T_0 + \varepsilon_1 + \sum_{i=1}^{M} \Delta T_i(\boldsymbol{\alpha},\boldsymbol{\varepsilon}) \tag{4.20}$$

where T_0 is the nominal subchannel inlet temperature, and ΔT_i is the i-th temperature rise (e.g., subchannel coolant, film, cladding, gap, or fuel temperature rise). In Eq. (4.20), $\boldsymbol{\alpha} = (\alpha_1,\cdots,\alpha_n)$ is a deterministic error vector, and $\boldsymbol{\varepsilon} = (\varepsilon_1,\cdots,\varepsilon_n)$ is a random error vector with zero mean and standard deviation $\boldsymbol{\sigma} = (\sigma_1,\cdots,\sigma_n)$. Assuming the effects of random variables on each temperature rise are additive, Eq. (4.20) can be written as:

$$T_M(\boldsymbol{\alpha},\boldsymbol{\varepsilon}) = T_0 + \varepsilon_1 + \sum_{i=1}^{M} \left\{ \Delta T_i(\boldsymbol{\alpha},0) + \sum_{j=1}^{n} \left[\Delta T_i(\boldsymbol{\alpha},\boldsymbol{\varepsilon}_j) - \Delta T_i(\boldsymbol{\alpha},0) \right] \right\} \tag{4.21}$$

where $\boldsymbol{\varepsilon}_j = (0,\cdots,0,\varepsilon_j,0,\cdots,0)$. The direct and statistical sub-factors are defined as:

$$f_{il}^{D}(\alpha_l) = \frac{\Delta T_i(\boldsymbol{\alpha}_l,0)}{\Delta T_i(0,0)}, \quad \boldsymbol{\alpha}_l = (0,\cdots,0,\alpha_l,0,\cdots,0) \tag{4.22}$$

$$f_{ij}^{S}(\varepsilon_j) = \frac{\Delta T_i(0,\boldsymbol{\varepsilon}_j)}{\Delta T_i(0,0)}, \quad \boldsymbol{\varepsilon}_j = (0,\cdots,0,\varepsilon_j,0,\cdots,0) \tag{4.23}$$

From the definition of the direct sub-factor, we have:

$$\Delta T_i(\boldsymbol{\alpha},0) = f_{i1}^{D}(\alpha_1) f_{i2}^{D}(\alpha_2)\cdots f_{ik}^{D}(\alpha_k)\Delta T_i(0,0) = \Delta T_i(0,0)\prod_{l=1}^{k} f_{il}^{D}(\alpha_l) \tag{4.24}$$

Assuming that the statistical sub-factors are independent from the direct uncertainties,

$$\frac{\Delta T_i(\boldsymbol{\alpha},\boldsymbol{\varepsilon}_j)}{\Delta T_i(0,0)} = \frac{\Delta T_i(0,\boldsymbol{\varepsilon}_j)}{\Delta T_i(0,0)} \tag{4.25}$$

we have:

$$\Delta T_i(\boldsymbol{\alpha},\boldsymbol{\varepsilon}_j) = f_{ij}^{S}(\varepsilon_j)\Delta T_i(\boldsymbol{\alpha},0) = f_{ij}^{S}(\varepsilon_j)\Delta T_i(0,0)\prod_{l=1}^{k} f_{il}^{D}(\alpha_l) \tag{4.26}$$

Inserting Eq. (4.24) and Eq. (4.26) into Eq. (4.21) yields:

$$T_M(\boldsymbol{\alpha},\boldsymbol{\varepsilon}) = T_0 + \varepsilon_1 + \sum_{i=1}^{M} \Delta T_i(0,0) \prod_{l=1}^{k} f_{il}^{D}(\alpha_l) \left[1 + \sum_{j=1}^{n} \left\{ f_{ij}^{S}(\varepsilon_j) - 1 \right\} \right] \tag{4.27}$$

In order to obtain the expression for the 2σ temperature, the mean and variance of Eq. (4.27) need to be evaluated. By approximating the statistical sub-factors with the second order Tayler series:

$$f_{ij}^{S}(\varepsilon_j) \approx f_{ij}^{S}(0) + f_{ij}^{S'}(0)\varepsilon_j + \frac{1}{2} f_{ij}^{S''}(0)\varepsilon_j^2 = 1 + f_{ij}^{S'}(0)\varepsilon_j + \frac{1}{2} f_{ij}^{S''}(0)\varepsilon_j^2 \tag{4.28}$$

its mean and variance can be obtained as

$$E\left[f_{ij}^{S}(\varepsilon_j) \right] \approx 1 + \frac{1}{2} f_{ij}^{S''}(0)\sigma_j^2 \tag{4.29}$$

$$V\left[f_{ij}^{S}(\varepsilon_j) \right] = E\left[\left\{ f_{ij}^{S}(\varepsilon_j) - \left(1 + \frac{1}{2} f_{ij}^{S''}(0)\sigma_j^2 \right) \right\}^2 \right] = E\left[\left\{ f_{ij}^{S'}(0)\varepsilon_j \right\}^2 \right] \approx \left[f_{ij}^{S'}(0) \right]^2 \sigma_j^2 \tag{4.30}$$

Since $f_{ij}^{s}(\varepsilon_j)$ is typically a smoothly increasing function of ε_j, its second derivative should be very small. If the second derivatives of statistical sub-factors are neglected, the mean value of $T_M(\boldsymbol{\alpha},\boldsymbol{\varepsilon})$ becomes:

$$\begin{aligned} E\left[T_M(\boldsymbol{\alpha},\boldsymbol{\varepsilon}) \right] &= T_0 + \sum_{i=1}^{M} \Delta T_i(0,0) \prod_{l=1}^{k} f_{il}^{D}(\alpha_l) \left[1 + \sum_{j=1}^{n} \left\{ \frac{1}{2} f_{ij}^{S''}(0)\sigma_j^2 \right\} \right] \\ &\approx T_0 + \sum_{i=1}^{M} \Delta T_i(0,0) \prod_{l=1}^{k} f_{il}^{D}(\alpha_l) \end{aligned} \tag{4.31}$$

Assuming that the statistical sub-factors are uncorrelated (i.e., independent), the variance of $T_M(\boldsymbol{\alpha},\boldsymbol{\varepsilon})$ can be calculated as:

$$\begin{aligned} V\left[T_M(\boldsymbol{\alpha},\boldsymbol{\varepsilon}) \right] &= \sigma_1^2 + \sum_{i=1}^{M} \sum_{j=1}^{n} \left\{ \Delta T_i(0,0) \prod_{l=1}^{k} f_{il}^{D}(\alpha_l) \right\}^2 V\left[f_{ij}^{S}(\varepsilon_j) - 1 \right] \\ &= \sigma_1^2 + \sum_{i=1}^{M} \sum_{j=1}^{n} \left\{ \Delta T_i(0,0) \prod_{l=1}^{k} f_{il}^{D}(\alpha_l) \right\}^2 \left[f_{ij}^{S'}(0) \right]^2 \sigma_j^2 \end{aligned} \tag{4.32}$$

By approximating the derivative $f_{ij}^{S'}(0)$ with first order differencing as:

$$f_{ij}^{S'}(0) \approx \frac{f_{ij}^{S}(\sigma_j) - f_{ij}^{S}(0)}{\sigma_j} = \frac{f_{ij1\sigma}^{S} - 1}{\sigma_j} \tag{4.33}$$

Eq. (4.32) can be rewritten as:

$$V\left[T_M(\boldsymbol{\alpha},\boldsymbol{\varepsilon}) \right] = \sigma_1^2 + \sum_{i=1}^{M} \sum_{j=1}^{n} \left\{ \Delta T_i(0,0) \prod_{l=1}^{k} f_{il}^{D}(\alpha_l) \right\}^2 V\left[f_{ij1\sigma}^{S} - 1 \right]^2 \tag{4.34}$$

In SE2-ANL, the 2σ temperature can be calculated by utilizing either horizontal or vertical form. With the mean value and variance of $T_M(\boldsymbol{\alpha},\boldsymbol{\varepsilon})$, the sum of squares form of 2σ temperature is defined as:

$$T_{M_{SS}}^{2\sigma}(\boldsymbol{\alpha},\boldsymbol{\varepsilon}) = E\left[T_M(\boldsymbol{\alpha},\boldsymbol{\varepsilon})\right] + 2\sqrt{V\left[T_M(\boldsymbol{\alpha},\boldsymbol{\varepsilon})\right]} = a + 2\left[\sigma_1^2 + \sum_{i=1}^{M}\sum_{j=1}^{n} b_i^2 c_{ij}^2\right]^{1/2} \tag{4.35}$$

where

$$a = T_0 + \sum_{i=1}^{M} b_i \tag{4.36}$$

$$b_i = \Delta T_i(0,0)\prod_{l=1}^{k} f_{il}^D(\alpha_l) \tag{4.37}$$

$$c_{ij}^2 = \left(f_{ij1\sigma}^S - 1\right)^2 \tag{4.38}$$

The horizontal form is obtained from the sum of squares form by redefining the variance term:

$$\begin{aligned} T_{M_H}^{2\sigma}(\boldsymbol{\alpha},\boldsymbol{\varepsilon}) &= a + 2\left[\sigma_1^2 + \sum_{j=1}^{n}\left(\sum_{i=1}^{M} b_i c_{ij}\right)^2\right]^{1/2} = T_0 + \left[\sum_{i=1}^{M}\Delta T_i(0,0)\prod_{l=1}^{k} f_{il}^D(\alpha_l)\right] \\ &+ 2\left[\sigma_1^2 + \sum_{j=1}^{n}\left\{\sum_{i=1}^{M}\left[\Delta T_i(0,0)\prod_{l=1}^{k} f_{il}^D(\alpha_l)\right](f_{ij1\sigma}^S - 1)\right\}^2\right] \end{aligned} \tag{4.39}$$

The vertical form is obtained from the horizontal form by redefining the variance term. In Eq. (4.39), the summation over j is rearranged as:

$$\begin{aligned} \sum_{j=1}^{n}\left(\sum_{i=1}^{M} b_i c_{ij}\right)^2 &= \sum_{j=1}^{n}\left(\sum_{i=1}^{M}(b_i c_{ij})^2 + 2\sum_{i=1}^{M}\sum_{k=i+1}^{M}(b_i c_{ij})(b_k c_{kj})\right) \\ &= \sum_{i=1}^{M} b_i^2 \sum_{j=1}^{n} c_{ij}^2 + 2\sum_{i=1}^{M}\sum_{k=i+1}^{M} b_i b_k \sum_{j=1}^{n} c_{ij} c_{kj} \end{aligned} \tag{4.40}$$

Using the equality

$$\left[\sum_{i=1}^{M} b_i \left(\sum_{j=1}^{n} c_{ij}^2\right)^{1/2}\right]^2 = \sum_{i=1}^{M} b_i^2 \sum_{j=1}^{n} c_{ij}^2 + 2\sum_{i=1}^{M}\sum_{k=i+1}^{M} b_i b_k \left(\sum_{j=1}^{n} c_{ij}^2\right)^{1/2}\left(\sum_{j=1}^{n} c_{kj}^2\right)^{1/2} \tag{4.41}$$

Eq. (4.40) can be written as:

$$\sum_{j=1}^{n}\left(\sum_{i=1}^{M} b_i\, c_{ij}\right)^2 = \left[\sum_{i=1}^{M} b_i \left(\sum_{j=1}^{n} c_{ij}^2\right)^{1/2}\right]^2 + 2\sum_{i=1}^{M}\sum_{k=i+1}^{M} b_i\, b_k \left[\sum_{j=1}^{n} c_{ij} c_{kj} - \left(\sum_{j=1}^{n} c_{ij}^2\right)^{1/2}\left(\sum_{j=1}^{n} c_{kj}^2\right)^{1/2}\right] \tag{4.42}$$

The vertical form can be calculated as:

$$T_{M_V}^{2\sigma}(\boldsymbol{\alpha},\boldsymbol{\varepsilon}) = a + 2\left\{\sigma_1 + \left[\sum_{i=1}^{M} b_i \left(\sum_{j=1}^{n} c_{ij}^2\right)^{1/2}\right]^2\right\} = T_0 + \left[\sum_{i=1}^{M} \Delta T_i(0,0)\prod_{l=1}^{k} f_{il}^{D}(\alpha_l)\right] + 2\left\{\sigma_1 + \left[\sum_{i=1}^{M}\left[\Delta T_i(0,0)\prod_{l=1}^{k} f_{il}^{D}(\alpha_l)\right]\left(\sum_{j=1}^{n}\left(f_{ij1\sigma}^{S} - 1\right)^2\right)^{1/2}\right]^2\right\} \tag{4.43}$$

If the *i*-th hot channel factor is defined as:

$$f_i = \prod_{l=1}^{k} f_{il}^{D}(\alpha_l)\left\{1 + 2\left[\sum_{j=1}^{n}\left(f_{ij1\sigma}^{S} - 1\right)^2\right]^{1/2}\right\} \tag{4.44}$$

The vertical form can be rewritten as:

$$T_{M_V}^{2\sigma}(\boldsymbol{\alpha},\boldsymbol{\varepsilon}) = T_0 + 2\sigma_1 + \sum_{i=1}^{M} f_i \Delta T_i(0,0) \tag{4.45}$$

The direct and statistical hot channel sub-factors for peak cladding and fuel temperatures are specified in the input dataset A.THINP. The method to calculate 2σ temperature is specified on the type 05 card. The collapsed hot channel factors based on the semi-statistical vertical method are specified on the type 09 cards for coolant, film, and cladding temperature rises. The hot channel factors for CRBR driver and blanket assemblies are available in the SE2-ANL code. The direct and statistical sub-factors for the semi-statistical horizontal method are provided on the type 10 cards. Eleven direct sub-factors and thirteen statistical sub-factors are available for coolant, file, and cladding temperature rises. The sub-factors for CRBR driver and blanket assemblies are also available in the code.

4.2. New Computational Models and Numerical Schemes in SE2-UM

4.2.1. Cheng-Todreas Correlations

The Cheng-Todreas correlations [18] for the flow split and two mixing parameters $\varepsilon_{1\eta}^{*}$ and C_{1L} have been implemented into SE2-UM while the Novendstern and Chiu-Rohsenow-Todreas turbulent flow models are retained as additional options. In the Cheng-Todreas correlations, the applicable range is extended to the pitch to diameter ratio (P/D) ≤ 1.07, which was not covered by the previous Novendstern and Chiu-Rohsenow-Todreas correlations. The mixing parameter models are reformulated to be consistent with the subchannel friction factor models. In the Cheng-Todreas correlations, the flow split parameters are calculated as:

$$X_2 = 1/[S_2 + (X_1/X_2)S_1 + (X_3/X_2)S_3] \tag{4.46}$$

$$\frac{X_1}{X_2} = \left(\frac{De_1}{De_2}\right)^{(1+m)/(2-m)} \left(\frac{C_{f2}}{C_{f1}}\right)^{1/(2-m)} \tag{4.47}$$

$$\frac{X_3}{X_2} = \left(\frac{De_3}{De_2}\right)^{(1+m)/(2-m)} \left(\frac{C_{f2}}{C_{f3}}\right)^{1/(2-m)} \tag{4.48}$$

where C_{f1}, C_{f2}, and C_{f3} are friction factor constants for the wire wrapped rod

$$C_{f1} = C'_{f1}\left(\frac{P'_{w1}}{P_{w1}}\right) + W_d\left(\frac{3A_{r1}}{A_1'}\right)\left(\frac{D_{el}}{H}\right)\left(\frac{D_{el}}{D_w}\right)^m \tag{4.49}$$

$$C_{f2} = C'_{f2}\left[1 + W_s\left(\frac{A_{r2}}{A_2'}\right)\tan^2\theta\right]^{(3-m)/2} \tag{4.50}$$

$$C_{f3} = C'_{f3}\left[1 + W_s\left(\frac{A_{r3}}{A_3'}\right)\tan^2\theta\right]^{(3-m)/2} \tag{4.51}$$

The primed quantities C'_{f1}, C'_{f2}, and C'_{f3} are the friction factor constants for bare rod, θ is the angle between the wire and the vertical axis, W_d is the wire drag constant, and W_s is the wire sweeping constant. In the Cheng-Todreas correlations, they are given as:

$$C'_{fi} = b_{i0} + b_{i1}(P/D - 1) + b_{i2}(P/D - 1)^2 \tag{4.52}$$

$$W_d = \left[29.5 - 140(D_w/D) + 401(D_w/D)^2\right](H/D)^{-0.85} \tag{4.53}$$

$$W_s = 20.0\log(H/D) - 7.0 \tag{4.54}$$

The coefficients for bare rod in Eq. (4.52) in the hexagonal array are shown in the Table 4.1.

Table 4.1 The Coefficients for Bare Rod in Hexagonal Array

Subchannel	1.0 ≤ P/D ≤ 1.1			1.1 ≤ P/D ≤ 1.5		
	b_0	b_1	b_2	b_0	b_1	b_2
Interior	0.09378	1.398	8.664	0.1458	0.03632	0.03333
Edge	0.09377	0.8732	3.341	0.1430	0.04199	0.04428
Corner	0.1004	1.625	11.85	0.1499	0.006706	0.009567

In this model, the dimensionless effective eddy diffusivity $\varepsilon^*_{1\eta}$ is calculated with the characteristic length η instead of the interior equivalent hydraulic diameter used in the Chiu-Rohsenow-Todreas correlations, as shown in the following equation:

$$\varepsilon^*_{1\eta} = \frac{\varepsilon}{V_1 \eta} \tag{4.55}$$

where the characteristic length η is the distance from subchannel centroid to centroid. V_1 is the axial velocity for the interior subchannel. The Cheng-Todreas correlations used in SE2-UM are:

$$\varepsilon^*_{1\eta} = C_m / (A_{r1} / A')^{1/2} \tan\theta \tag{4.56}$$

$$C_{1L} = C_s / (A_{r2} / A'_2)^{1/2} \tan\theta \tag{4.57}$$

where C_m and C_s are constants depending on the geometrical parameters as:

$$C_m = \begin{cases} 0.14(P/D-1)^{-0.5}, & N_P \geq 19 \\ 0.1(P/D-1)^{-0.5}, & N_P = 7 \end{cases} \tag{4.58}$$

$$C_s = \begin{cases} 0.75(H/D)^{0.3}, & N_P \geq 19 \\ 0.6(H/D)^{0.3}, & N_P = 7 \end{cases} \tag{4.59}$$

4.2.2. Axial Discretization of Energy Equation with θ-method

As discussed before, the explicit scheme used in SE2-ANL makes it impractical to model the axial convection due to small meshes required to satisfy the stability criteria. In order to accommodate the axial convection due to the inter-assembly gap flow and to enhance the computational efficiency, the θ-method is employed for discretizing the energy equations in the axial direction [19]. Using θ-method, the finite difference form of Eq. (4.15) is derived as:

$$(1+\sum_{i=1}^{I} c_i \theta \Delta z_n) T^{n+1} - \sum_{i=1}^{I} c_i \theta \Delta z_n T_i^{n+1} = T^n + \sum_{i=1}^{I} c_i (T_i^n - T^n)(1-\theta)\Delta z_n - c_q \overline{q}' \Delta z_n \tag{4.60}$$

where T^n and T^{n+1} are the bottom and top surface temperatures of the n-th axial mesh, Δz_n is the axial mesh size, and θ is a parameter between 0 and 1. For example, the finite difference form equation for the interior subchannel shown in Fig. 4.4 can be written as:

$$\left(1+\sum_{i=1}^{3} C_i \theta \Delta z^n\right) T_0^{n+1} = T_0^n + \sum_{i=1}^{3} C_i T_i^{n+1} \theta \Delta z^n + \sum_{i=1}^{3} C_i (T_i^n - T_0^n)(1-\theta)\Delta z^n + C_q \overline{q}'_{0n} \Delta z^n \qquad (4.61)$$

This method yields a general expression from the fully explicit scheme for $\theta = 0$ to the fully implicit scheme for $\theta = 1$. The implicit scheme ($\theta \neq 0$) results in a linear system of equations for every radial plane. This linear system of equations is solved iteratively using the Gauss-Seidel method.

4.2.3. Automatic Flow Allocation

The overall goal of the orifice zoning and flow allocation is to equalize the pin cladding damage accrual and thus pin reliability over the lifetime. However, the current version of SE2-ANL determines the flow rates at a time point for given power distribution and orifice zones in such a way that the peak cladding temperatures in individual orifice zones are equal to each other within the specified convergence limit. Therefore, the optimum flow rates over the burn cycle are determined by manual iterations to equalize the larger values of the peak cladding temperatures at both BOC and EOC in individual orifice zones.

An automated flow allocation scheme has been implemented in SE2-UM to eliminate the cumbersome manual iterations. Now SE2-UM supports five different types of calculations. The first one is to calculate the temperature field for given coolant inlet flow rates. In this calculation, no flow iteration is involved. The flow rates are not renormalized to match the total flow rates calculated from reactor total power. The second type is the "perfect orifice zoning" calculation, where each assembly is assigned to its own orifice zone. Using the initial guess for flow rates in proportion to assembly powers, each assembly flow rate is iteratively determined to equalize the 2σ maximum cladding temperatures of each fuel assembly. The third one is the flow iteration calculation for user specified orifice zones and initial flow rates. In this calculation, the flow rates of fueled orifice zones are iteratively determined to equalize the maximum fuel pin cladding damage of each orifice zone at both BOC and EOC. The detailed algorithm for flow calculation is described below. The flow rates for non-fueled orifice zones are determined by renormalizing the average flow rate of the assemblies in each zone.

The forth calculation type is the fully automatic orifice zoning and flow allocation for user specified numbers of total and fueled orifice zones. The fully automatic flow allocation calculation procedure is shown in Fig. 4.5. First, the "perfecting orifice zoning" flow rates at BOC and EOC are calculated separately using the power distributions at BOC and EOC, respectively, and the initial flow rate of each assembly is determined by the larger value of the "perfect" flow rates at BOC and EOC. Then, by sorting and clustering these initial assembly flow rates, the specified numbers of fueled and non-fueled orifice zones are determined, and the assembly flow rates are calculated by renormalizing the initial assembly flow rates to the total core flow rate determined from the core power and the temperature increase across the core. With the determined orifice zones and the corresponding flow rates, the problem is now reduced to the third type of problem. Thus, using the algorithm used for the third type calculation, the assembly flow rates can be determined iteratively to equalize the maximum cladding temperatures in individual fueled orifice zones throughout the cycle. The fifth calculation type is the automatic flow allocation for user-specified orifice zones. The

calculation procedure for this calculation is basically the same as the fourth type of problem, except that the orifice zones are specified by the user instead of being determined by the code.

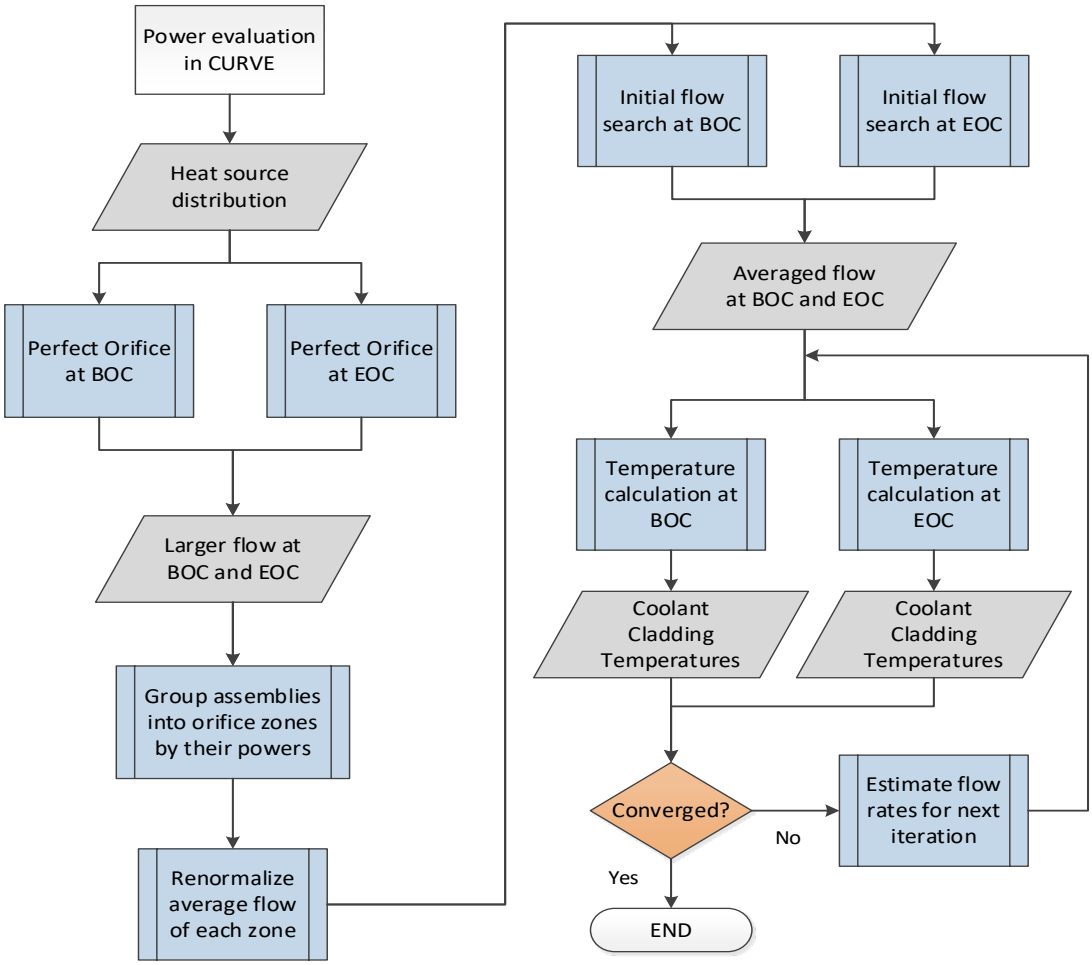

Fig. 4.5 Flow Diagram for Orifice Zoning and Flow Allocation Calculation

In the flow iteration calculation, the flow rates of the fueled orifice zones are determined iteratively to yield the same peak 2σ cladding mid-wall temperature in each orifice zone. With the calculated temperatures at BOC and EOC, the system equations to be solved can be formulated as:

$$\begin{aligned} &T_{m,1} = T_{m,2} = \cdots = T_{m,N-1} = T_{m,N} \\ &\sum_{n=1}^{N} w_n = w_t \end{aligned} \tag{4.62}$$

where w_n is the flow rate in the orifice zone n, $T_{m,n}$ is the larger value of the peak 2σ cladding middle wall temperatures at BOC and EOC in orifice zone n, and N is the number of fueled orifice zones. This system of nonlinear equations can be solved iteratively using the Newton-Raphson method as:

$$w_n^{(i+1)} = w_n^i + \delta w_n^{(i)}, \quad n = 1,2,\ldots,N \tag{4.63}$$

where $\delta w_n^{(i)}$ is determined by solving the system of linear equations

$$\begin{aligned} &\sum_{j=1}^{N} \frac{\partial}{\partial w_j}(T_{m,n} - T_{m,1})\delta w_j^{(i)} = T_{m,1}^{(i)} - T_{m,n}^{(i)}, \quad n = 2,3,\ldots,N \\ &\sum_{j=1}^{N} \delta w_j^{(i)} = 0 \end{aligned} \tag{4.64}$$

If the peak 2σ cladding middle wall temperature of the orifice zone n occurs at the axial height z_n of the fuel pin p of assembly h, $T_{m,n}$ can be represent as:

$$T_{m,n} = T_{c,n} + \overline{q}_h' r_{p,h} a_h(z_n)\left(\frac{1}{2\pi r_{o,h} h_h} + \frac{1}{2\pi k_h}\ln\frac{r_{i,h}}{r_{m,h}}\right) \tag{4.65}$$

$$T_{c,n} = T_{in} + \frac{\overline{q}_h' r_{p,h}}{c_{h,p} m_{p,h}(w_n)} \int_0^{z_n} a_h(z)dz \tag{4.66}$$

where

$T_{c,n}$ = coolant temperature corresponding to the peak 2- σ cladding middle wall temperature of the orifice zone n

$c_{p,h}$ = coolant specific heat for pin p of assembly h

$m_{p,h}$ = subchannel flow rate for pin p of assembly h

h_h = convection heat transfer coefficient of assembly h

k_h = cladding heat conductivity of assembly h

$r_{o,h}$ = cladding outer radius of assembly h

$r_{i,h}$ = cladding inner radius of assembly h

$r_{m,h}$ = cladding middle wall radius of assembly h

If the variations of the flow split parameters are neglected, the subchannel flow rate $m_{p,h}$ for pin p of assembly h is proportional to the flow rate of assembly h, and thus it can be written as:

$$m_{p,k} = \frac{c w_n}{n_n} \tag{4.67}$$

where n_n is the number of assemblies in orifice zone n, and c is a proportional constant. If the changes of heat transfer coefficient due to the flow rate variation are neglected, the derivatives in Eq. (4.64) can be calculated as:

$$\frac{\partial T_{m,n}}{\partial w_j} = \frac{\partial T_{c,n}}{\partial w_j} = -\delta_{nj} \frac{T_{c,n} - T_{in}}{m_{p,h}} \frac{dm_{p,h}}{dw_n} = -\delta_{nj} \frac{T_{c,n} - T_{in}}{w_n} \tag{4.68}$$

Combine the Eq. (4.64) and Eq. (4.68), the final form of system of linear equations can be written as:

$$\begin{bmatrix} T'_{c,1}/w_1 & -T'_{c,2}/w_2 & 0 & \cdots & 0 \\ T'_{c,1}/w_1 & 0 & -T'_{c,3}/w_3 & \cdots & 0 \\ \vdots & \vdots & \vdots & \ddots & \vdots \\ T'_{c,1}/w_1 & 0 & 0 & \cdots & -T'_{c,N}/w_N \\ 1 & 1 & 1 & \cdots & 1 \end{bmatrix} \begin{bmatrix} \delta w_1^{(i)} \\ \delta w_2^{(i)} \\ \vdots \\ \delta w_{N-1}^{(i)} \\ \delta w_N^{(i)} \end{bmatrix} = \begin{bmatrix} T_{m,1}^{(i)} - T_{m,2}^{(i)} \\ T_{m,1}^{(i)} - T_{m,3}^{(i)} \\ \vdots \\ T_{m,1}^{(i)} - T_{m,N}^{(i)} \\ 0 \end{bmatrix} \tag{4.69}$$

where $T'_{c,n} = T_{c,n} - T_{in}$. By solving the system of linear Eq. (4.69), $\delta w_n^{(i)}$ is determined and the flow rates for the next iteration are calculated with Eq. (4.63). With the new flow rates, the temperature calculations are repeated to get the peak 2σ cladding middle wall temperature and corresponding coolant temperature of the individual fueled orifice zones. This iteration will be continued until the convergence condition is satisfied, or the maximum iteration number is reached.

4.3. Computational Procedures and Modules of SE2-UM

4.3.1. I/O Information

SE2-UM utilizes NAMELIST as input card format instead of the old fixed format. There are mainly four blocks of input data: General Input Data, Assembly Type Data, Mixing Parameter Profiles, and Bundle Specific Data. Detailed input descriptions are provided in Appendix G. In the General Input Data blocks, the calculation type, the core information such as the number of assemblies, the number of assembly types, and the number of orifice zones are specified. The number of axial meshes, fuel and cladding materials, and hot channel factors are also given in this block. The data for each assembly type such as the number of fuel pins and assembly geometry information are given in the Assembly Type Data block. If needed, the user can specify the flow split and mixing parameters in the Mixing Parameter Profiles block instead of using the embedded correlations in the code.

The last block is the Bundle Specific Data. The flow rate and orifice zone assignment for each assembly are given in this block. For the first type calculation of SE2-UM, only the flow rate for each assembly needs to be provided. For the second and fourth types of calculation, neither the flow rate nor the orifice zone assignment is needed. For the third type calculation, the orifice zone assignment and initial flow rate should be provided for each assembly. For the fifth type calculation, only the orifice zone assignment is specified for each assembly. The stage factors for each region are also given in Bundle Specific Data block. The stage factors are used to account for the discrete batch effects relative to the equilibrium cycle (batch-averaged) power and are derived from the REBUS-3 calculation results. In addition to these input data, the datasets NHFLUX, GHFLUX, GEODST, NDXSRF, ZNATDN, and LABELS from VARIANT calculations, and the production matrix file PMATRX from the MC^2-3 calculation are required as the input data for SE2-UM.

In the output file of SE2-UM, the summary of the general input data and assembly input data are printed out first. The output data unit is controlled by the input parameter JFORM. If the JFORM equals 0, the output data will be in international engineering (SI) units. If the JFORM equals 1, the output data will be in British engineering units. In the second part of the output file, the results of pin power reconstruction from VARIANT solutions are summarized. The assembly power, peak pin position, pin peaking factor, and peak linear power for each assembly before normalization are listed. The normalized node power from neutron and gamma heating are given for each assembly separately.

The third part of the output file is the flow rate and temperature information from the thermal hydraulic calculations. The flow rate for each assembly either from input or determined internally by the code is printed out. The calculated velocities in the interior, edge, corner subchannel from flow split model, the flow mixing parameters, and pressure drop of each assembly are given. Then the coolant temperature iterations in each axial position are summarized. If this axial position is included in the input parameter APRNT, the detailed coolant temperature maps and the assembly energy balance at this axial level are printed. If the axial position is included in the input parameter DPRNT, the duct wall temperatures of six faces are printed. For double-duct type assemblies, both the inner and outer duct temperatures are given. The nominal and 2σ temperatures information for coolant, cladding and fuel are given at different axial positions. These temperatures at height of peak 2σ cladding middle wall temperature, peak 2σ fuel centerline temperature, peak 2σ fuel surface temperature, and minimum 2σ margin to fuel melt are listed for each assembly. For the flow iteration calculations, the third part output information are repeated for each flow iteration calculation. After one temperature calculation for both BOC and EOC, the flow rates of fuel assemblies in the next iteration are printed.

4.3.2. SE2-UM Code Information

SE2-UM includes a driver routine STP01, which controls the whole flow iteration calculation process. STP01 loads modules CURVE and SE2. In addition to these two modules, there are several subroutines included in driver STP01. Brief descriptions of subroutines in STP01 are given in Table 4.2. CURVE is called to perform the flux evaluation and the power profile calculation using VARIANT flux solutions. SE2 calculates the temperature profile of each subchannel for given power distributions. The main subroutines in SE2 are described in Table. 4.3.

Table 4.2 Subroutines in STP01

Subroutines	Function
RDINPUT	Processes input data and sets up global arrays
INITFLOW	Calculates the initial flow rates for flow iteration after perfect orifice calculations
AVEFLOW	Calculates the average assembly flow rates of BOC and EOC
ORFDIVD	Determines the orifice zone number of each assembly
ITFLOW	Determines the flow rates of fueled orifice zones for next flow iteration

Table 4.3 Main Subroutines in SE2

Subroutines	Function
POWRD	Reads linear powers from interface file POWRFILE
CHNNUM	Numbers subchannels and identifies neighboring subchannel numbers of each subchannel for an assembly type
GEOMET	Sets up geometry parameters of an assembly type
CDPROP	Obtains material properties of coolant and duct
FSMIXP	Finds subchannel flowsplit and mixing parameters
GRASH	Finds the critical Gr number and determines if the flow in this assembly has exceeded the forced convection condition
TMCOEF	Calculates all the coefficients of heat balance equations
STBCHK	Finds limiting axial step size and changes input step size based on ISCHK if $\theta = 0$
FPINPA	Computes fuel pin parameters
SETMHC	Sets MHCON array to point to neighboring interior subchannels of each pin
WHEADR	Writes header record of duct and cladding temperature files
INITQT	Initializes temperature array and energy balance indicators
GENCCF	Generates the coupling coefficients
TMPCAL	Performs temperature calculations from core bottom to top
PRNTTF	Prints cladding and fuel peak 2σ temperatures
ORFFLO	Iterates orifice flow to get equal peak 2σ cladding temperatures at a certain time point

4.4. Verification and Validation Tests of SE2-UM

4.4.1. Comparison of SE2-UM and SE2-ANL Solutions for ABR-1000

4.4.1.1. Subchannel Analyses with Different Heating Calculation Schemes

Using the SE2-UM and SE2-ANL codes, full-core subchannel analyses were performed for the 1000 MWt ABR metal core design [36], of which the one-third core configuration is shown in Fig. 4.6. The fuel compositions were retrieved from REBUS-3 fuel cycle analysis for a one-year equilibrium cycle of the startup core. As shown in the vertical layout in the left figure of Fig. 4.7, the fuel cycle analysis was performed by dividing the active core part of each assembly into five axial depletion zones. Each fuel assembly has 271 fuel pins arranged in a triangular lattice as schematically shown in the right image of Fig. 4.7.

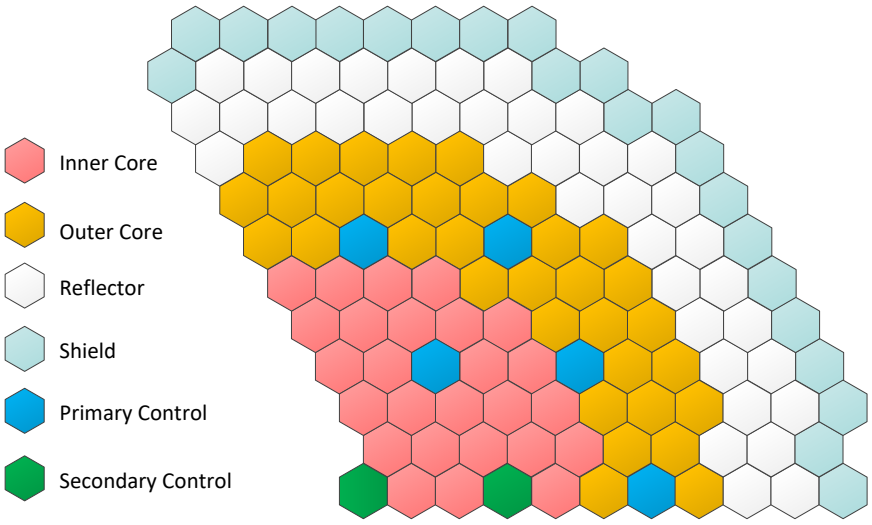

Fig. 4.6 Planar Layout of ABR-1000 Metal Core (1/3 Core Configuration)

The multigroup neutron and gamma cross sections, gamma production matrices, and isotopic neutron and gamma heating cross sections were generated with the MC^2-3 code. Initially, the region dependent 2082-group neutron spectra and 94-group gamma spectra were determined with full-core TWODANT transport calculations in the R-Z model. Then, the ultrafine group cross sections were condensed into 33 neutron and 21 gamma energy groups.

The coolant inlet and bulk outlet temperatures were assumed to be 355 °C and 510 °C, respectively. The total flow rate in the core was determined for a 155 °C temperature rise across the core. Hot channel factors were included in temperature predictions to account for core design analysis, fabrication, and operational uncertainties. The fuel assemblies were grouped into six orifice zones, and the non-fuel assemblies were grouped into four orifice zones. Fig. 4.8 shows the orifice zones and the corresponding assembly flow rates determined with the SE2-ANL. The same orifice zones and flow rates were used for the temperature calculations with the SE2-UM in order to isolate the impacts of the new heating calculation scheme based on VARIANT transport solutions.

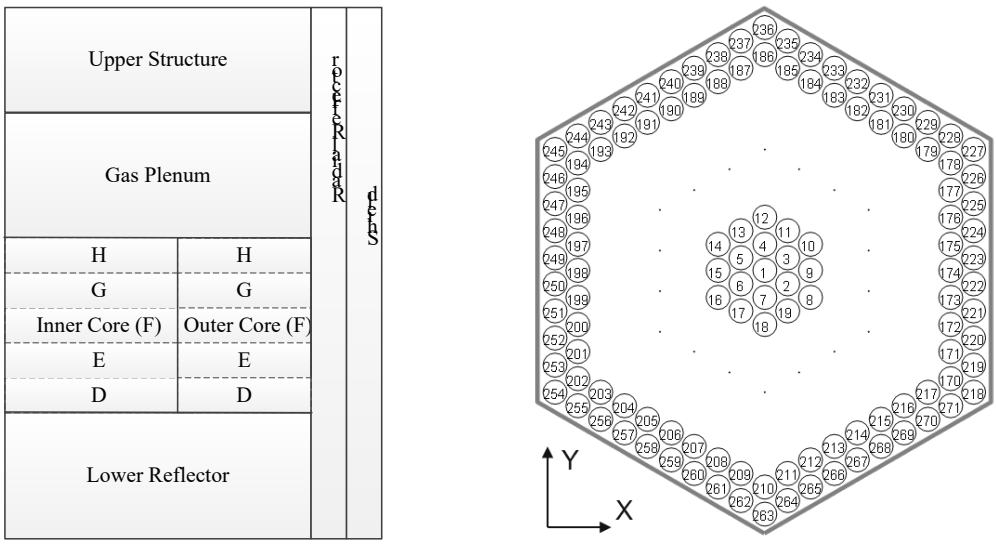

Fig. 4.7 Vertical Layout of ABR-1000 Metal Core (Left) and Pin Numbering Scheme within Fuel Assembly (Right)

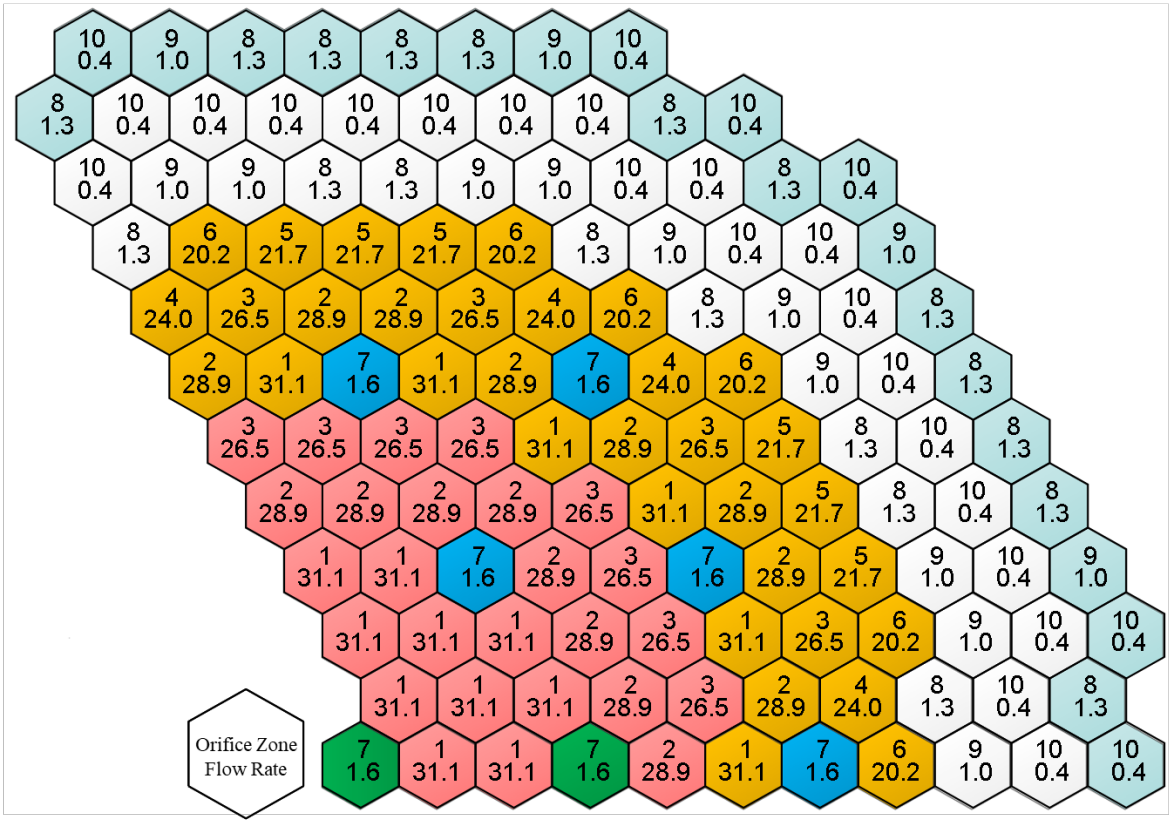

Fig. 4.8 Orifice Zones and Assembly Flow Rates (kg/s) of 1000 MWt ABR Problem

The integrated assembly powers at beginning of equilibrium cycle (BOEC) of SE2-ANL obtained from DIF3D finite-difference diffusion calculation and of SE2-UM obtained from VARIANT nodal transport calculation are shown in Fig. 4.9. The relative differences between the DIF3D and VARIANT solutions are shown in Fig. 4.10. Large relative deviations are

observed in reflector, shield, and control assemblies compared to driver assemblies. It can also be seen that relative to the VARIANT transport solution, the DIF3D diffusion solution overestimates the heating rates in the inner core assemblies, control assemblies, and reflectors, while it underestimates the heating rates in the outer core assemblies and the shields. As a result, the radial power distribution of the DIF3D diffusion theory solution is slightly steeper in the active core region near the outer boundary than that of the transport theory solution. This is expected since the diffusion theory tends to overestimate the leakage from the active core to the non-fueled region and the leakage from the outer boundary, which leads to the larger flux gradients over there.

Fig. 4.11 compares the peak 2σ cladding inner wall temperatures of fuel assemblies calculated with SE2-ANL and SE2-UM. The SE2-ANL calculation yields a maximum value of 617.2 °C in the second and twelfth assemblies of the seventh ring. On the other hands, the SE2-UM calculation yields a maximum value of 620.1 °C in the first and eighth assemblies of the eighth ring. These two maximum temperatures are lower than the design limit of 650 °C used for the ABR-1000 design. However, significant increases in the peak cladding inner wall temperature are observed in the fuel assemblies at the core periphery. The maximum increase is 8.6 °C, which also occurs at the third and eleventh assemblies of the ninth ring. These temperature increases are mainly due to the increased peak linear power with the new heating calculation method. The resulting peak 2σ fuel centerline temperatures are compared in Fig. 4.12. The maximum peak 2σ fuel centerline temperatures of SE2-ANL and SE2-UM are 812.8 °C and 818.8 °C, respectively, both of which occur in the first and sixth assemblies of the sixth ring. The maximum difference in the peak 2σ fuel centerline temperature between the SE2-ANL and SE2-UM results is 13.8 °C and occurs in the seventh and fifteenth assemblies of the ninth ring.

Fig. 4.13 compares the mixed mean coolant outlet temperatures of each assembly calculated with the SE2-UM and SE2-ANL codes. It is seen that the coolant outlet temperatures of fuel assemblies calculated with SE2-UM agree well with those of SE2-ANL. The maximum value of the mixed mean coolant outlet temperatures of SE2-ANL and SE2-UM are 519.3 °C and 519.1 °C, respectively. The maximum value occurs in the ninth assembly of the sixth ring in the SE2-ANL results and in the second assembly of the seventh ring in the SE2-UM results. However, non-negligible differences in the mixed mean coolant outlet temperatures are observed for reflector assemblies. The maximum difference in reflector assemblies is 14.3 °C, which occurs at the sixteenth assembly of the eleventh ring. These temperature differences are mainly due to the overestimated power in the reflector assemblies of SE2-ANL obtained from DIF3D diffusion calculation.

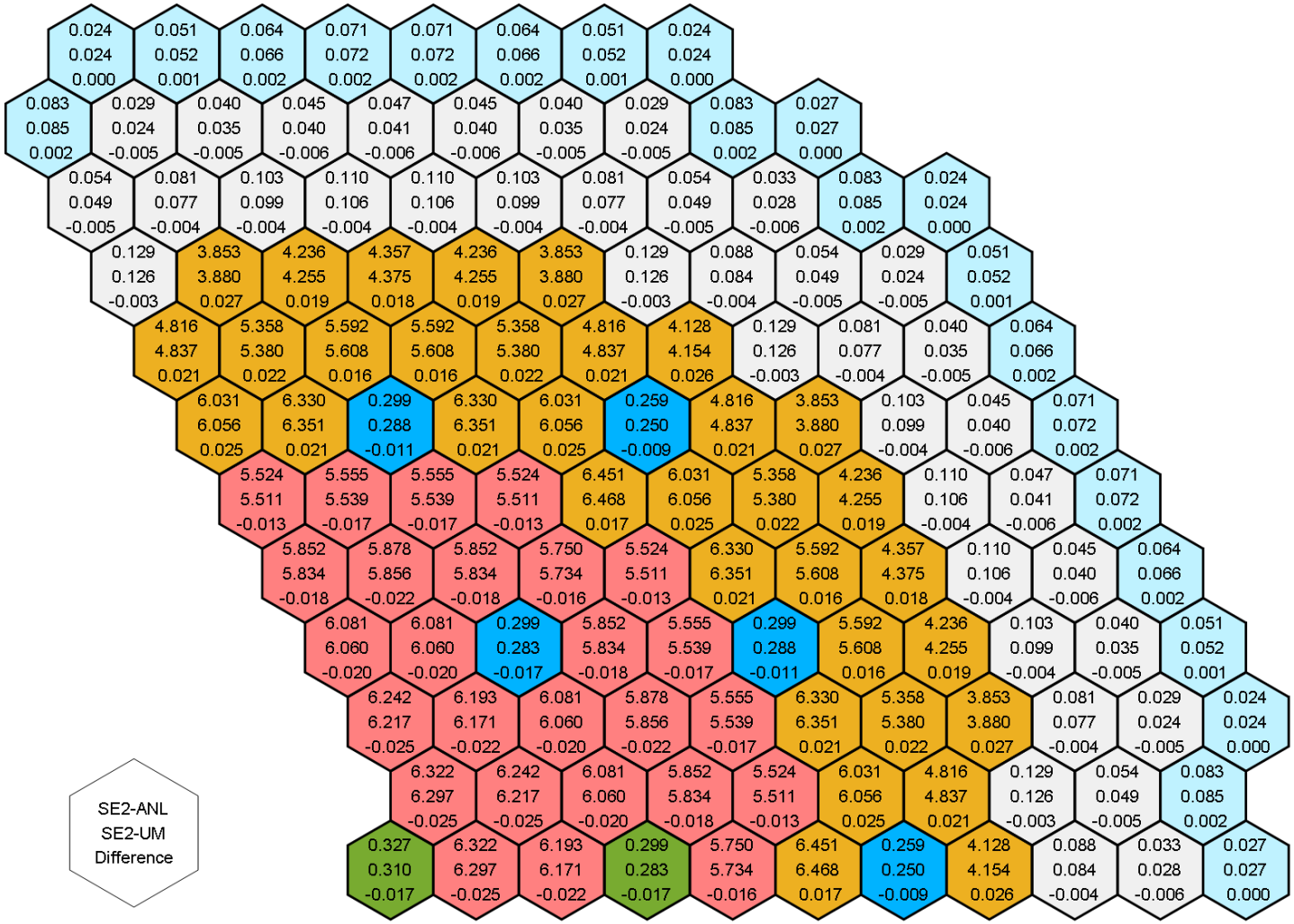

Fig. 4.9 Total Assembly Powers (MWt) of SE2-ANL and SE2-UM and Their Difference

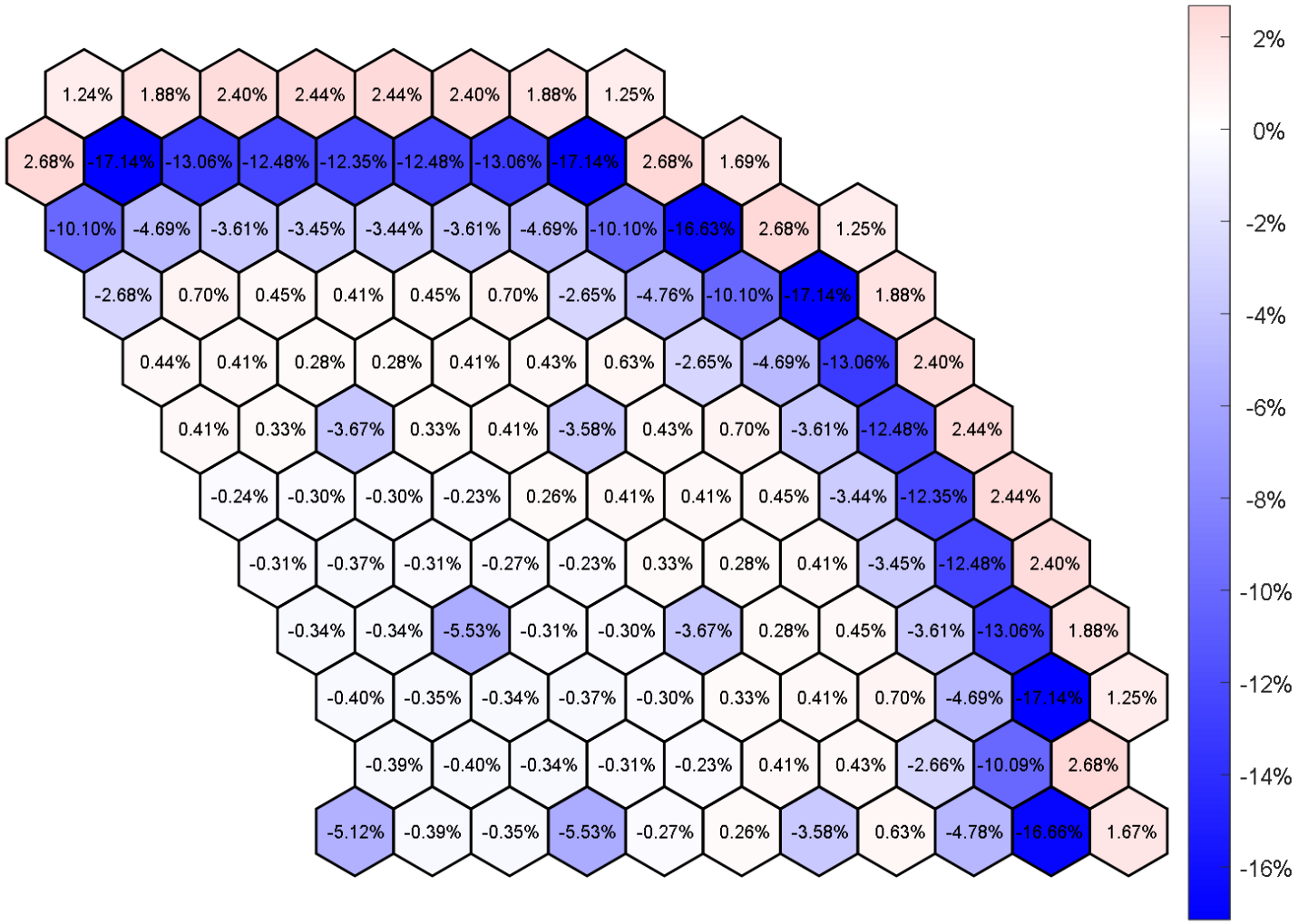

Fig. 4.10 Relative Differences of Total Assembly Powers (MWt) of SE2-ANL from SE2-UM Results

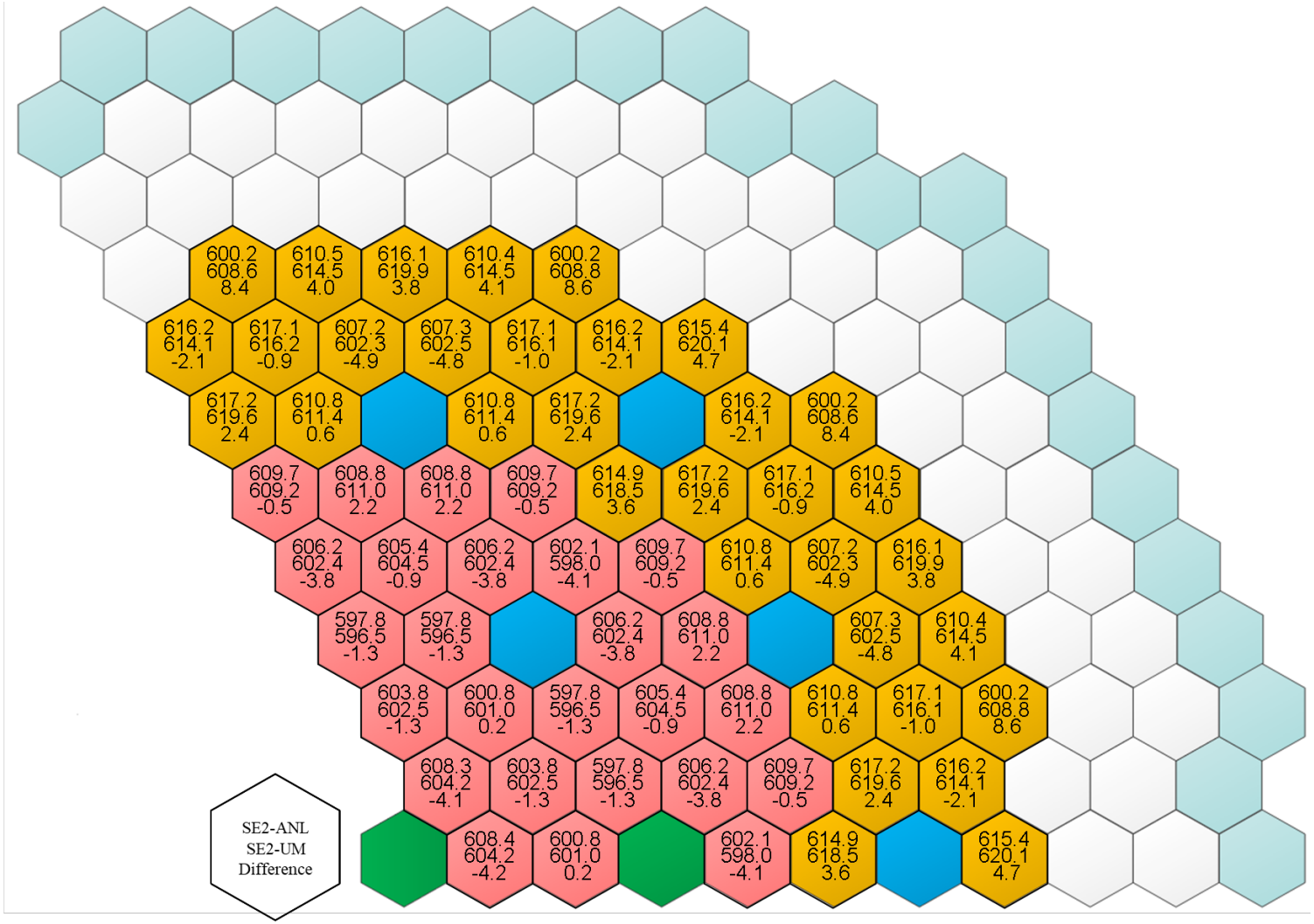

Fig. 4.11 Peak 2σ Cladding Inner Wall Temperatures (°C) of SE2-ANLand SE2-UM and Their Differences

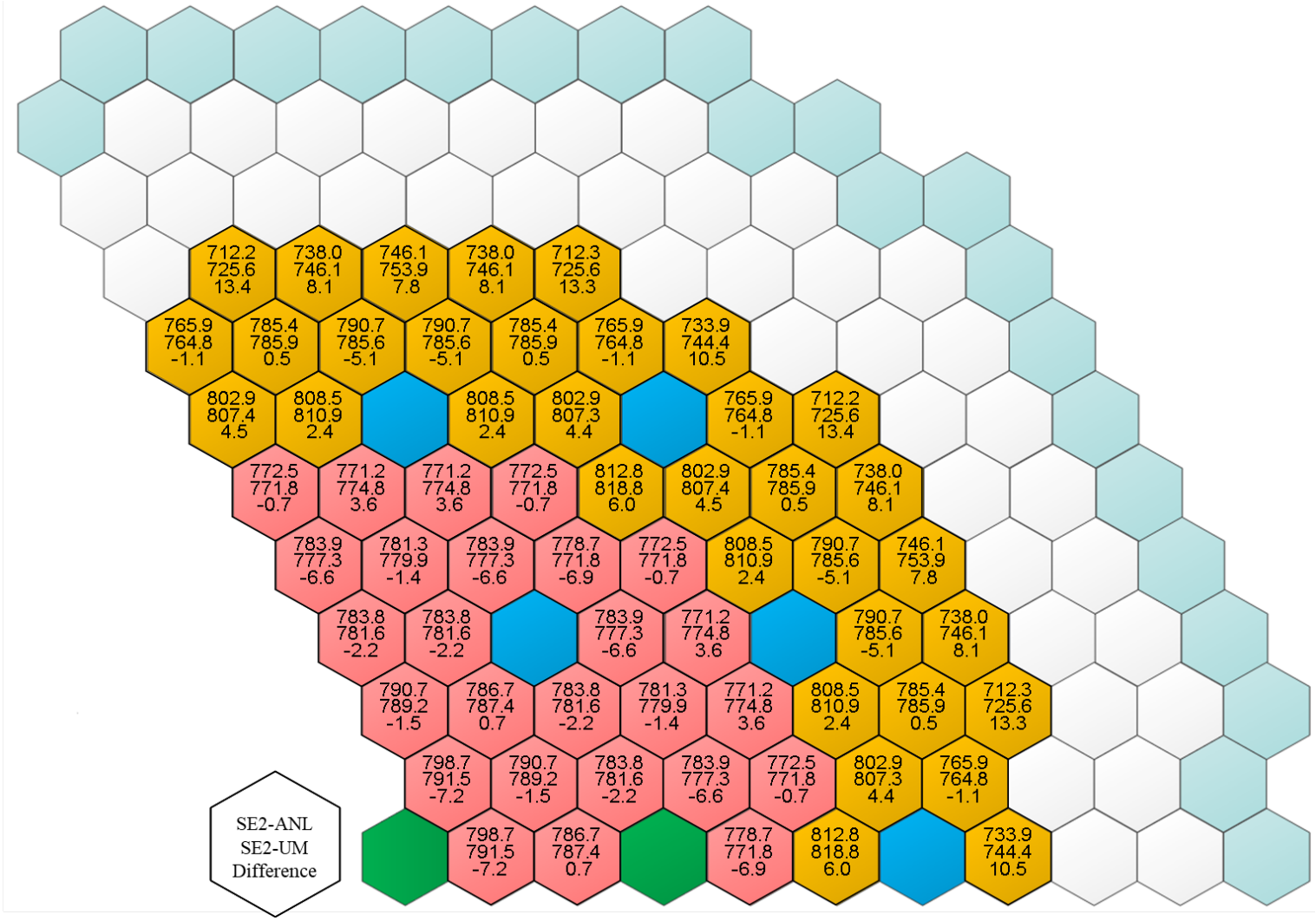

Fig. 4.12 Peak 2σ Fuel Centerline Temperatures (°C) of SE2-ANL and SE2-UM and Their Differences

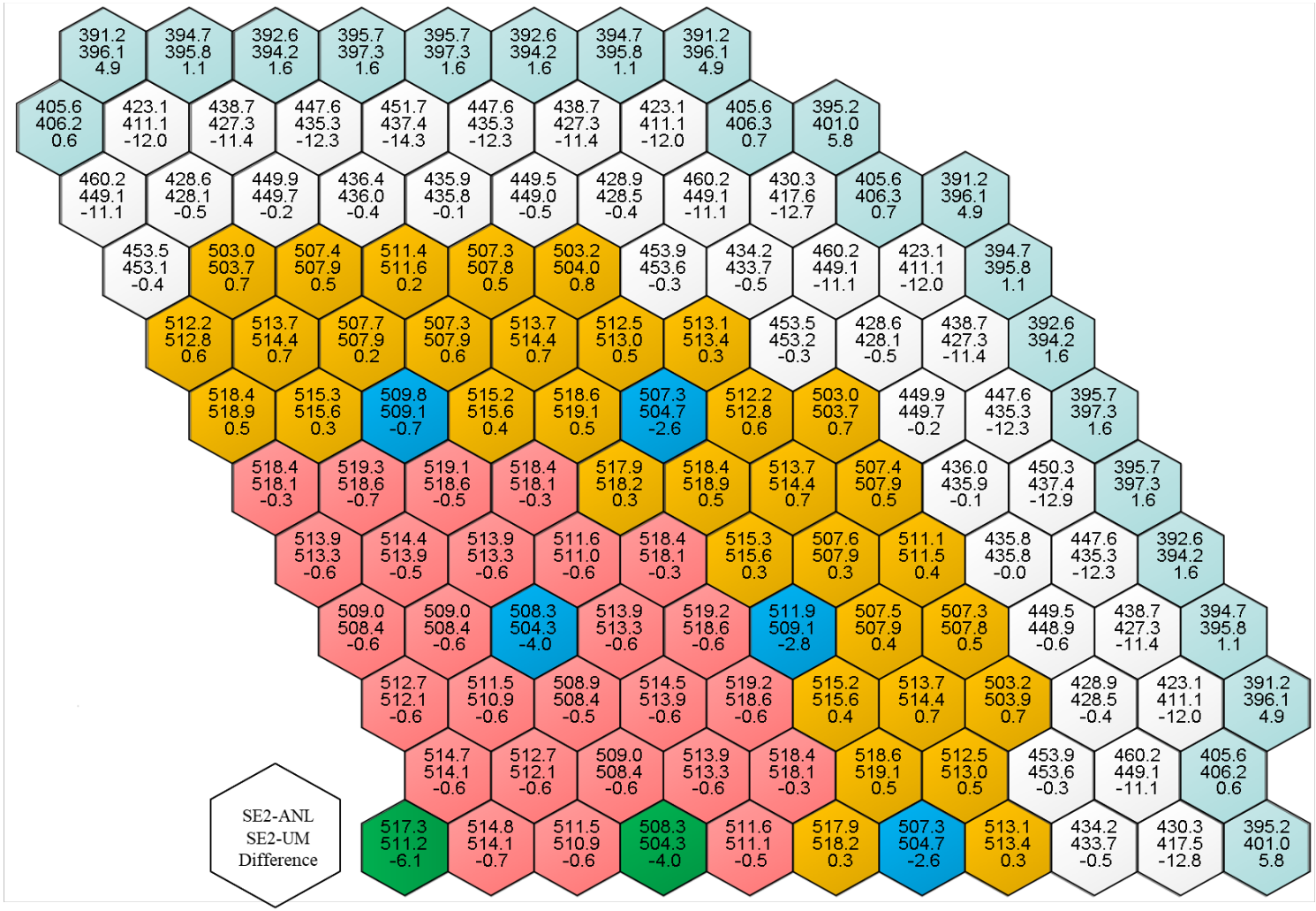

Fig. 4.13 Mixed Mean Coolant Outlet Temperatures (°C) of SE-ANL and SE2-UM and Their Difference

4.4.1.2. Temperature Calculation for Given Heat Source Distribution

To investigate the observed differences between the SE2-UM and SE2-ANL solutions for the ABR-1000 problem, SE2-UM and SE2-ANL subchannel analyses were repeated with the same heat source distribution obtained from DIF3D calculations. Furthermore, in order to eliminate the impacts of the differences in power distributions and in the inter-assembly heat transfer models, SE2-ANL subchannel analyses were performed with both the inter-assembly conduction model and the inter-assembly gap flow model. For the inter-assembly gap flow model, SE2-ANL requires a huge number of axial meshes to satisfy the numerical stability condition of the explicit difference scheme, and thus the inter-assembly gap flow rate was increased from 1.0 lbm/ft^2-hr to 10 lbm/ft^2-hr to reduce the computational time. However, the required number of axial meshes to satisfy the stability criterion was still 1,909,992. The SE2-UM calculation and the SE2-ANL calculation with inter-assembly conduction model were performed with 300 axial meshes as in the previous calculations.

Fig. 4.14 compares the mixed mean coolant outlet temperatures of the SE2-UM and SE2-ANL solutions. The SE2-UM solution was obtained with the inter-assembly gap flow model, while the SE2-ANL solution was obtained with the conduction model. By comparing to the results in Fig. 4.13, it can be seen that the differences between SE2-UM and SE2-ANL solutions are reduced when the same heat source distribution is used in both SE2-UM and SE2-ANL calculations. The maximum difference in fuel assemblies is only 0.3 °C, which occurs at the first assembly of the eighth ring. The maximum difference in control assemblies is 2.1 °C at the tenth assembly of the seventh ring. The maximum difference of reflector assemblies is 2.7 °C, occuring at the sixteenth assembly of the eleventh ring. The temperature differences in the reflector assemblies are mainly due to the conduction model utilized in the SE2-ANL calculation. Comparison of the results in Fig 4.13 with the results in Fig 4.14 indicates that the observed differences in the mixed mean outlet temperature in Fig. 4.13 are mainly due to the different power distributions between the DIF3D diffusion calculation of SE2-ANL and the VARIANT transport calculation of SE2-UM.

When the inter-assembly gap flow model is used for both SE2-UM and SE2-ANL calculations, the differences in the coolant outlet temperatures are further reduced, as shown in Fig. 4.15. The maximum temperature differences among the fuel and reflector assemblies are 0.2 °C and 1.8 °C, respectively. However, there are relatively large differences between SE2-UM and SE2-ANL results in two control assemblies, which are the first assembly of the first ring and the tenth assembly of the seventh ring. These differences are due to the influence of inconsistent boundary conditions in two models. For example, the control assembly at the tenth of seventh row is located at the boundary at the SE2-ANL model. There are three fuel assemblies around it in the SE2-ANL model and the adiabatic boundary condition is applied in the other three boundary surfaces, while there are six fuel assemblies around it in the SE2-UM model.

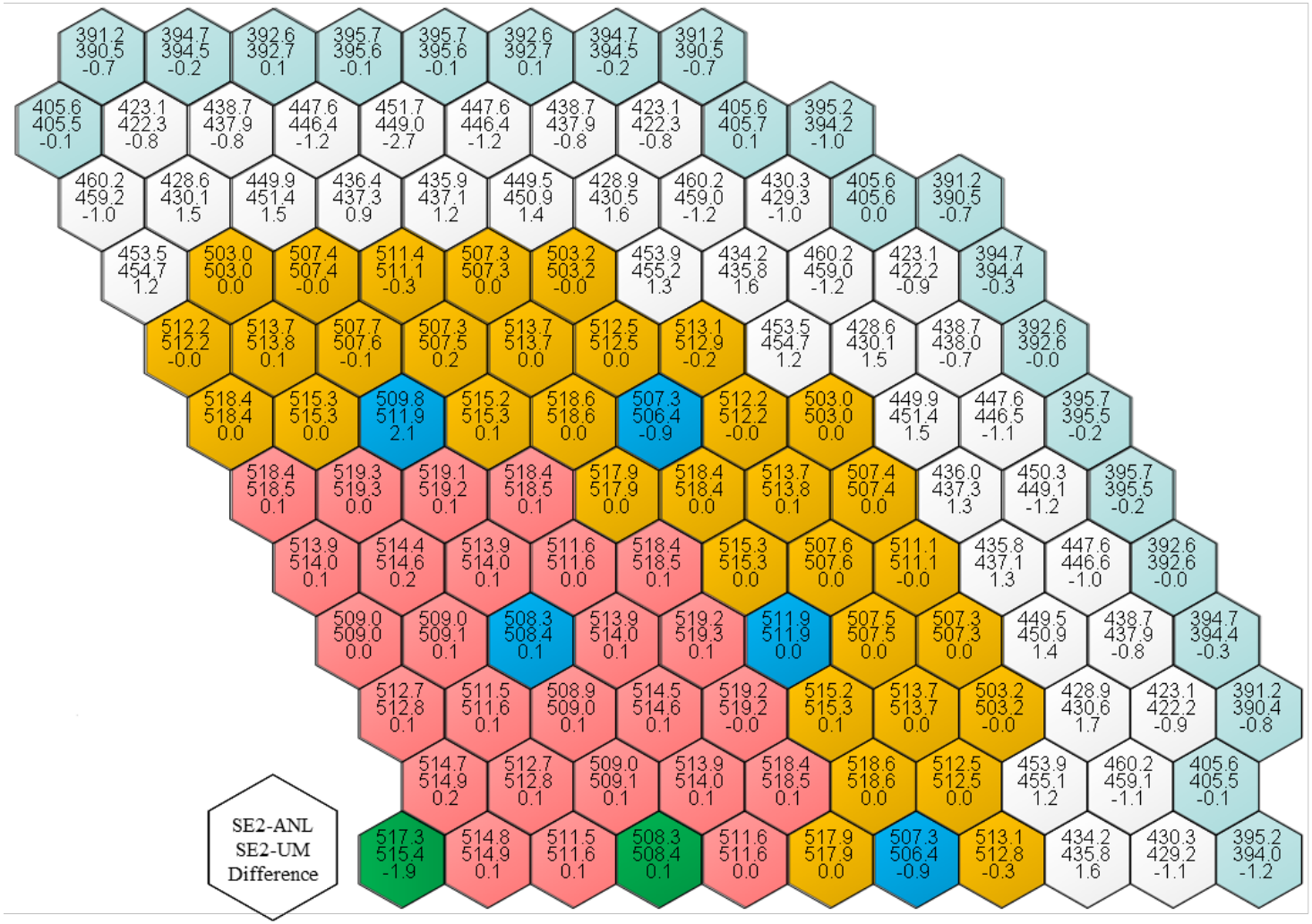

Fig. 4.14 Mixed Mean Coolant Outlet Temperatures (°C) of SE-ANL (with Inter-assembly Gap Conduction Model) and SE2-UM (with Inter-assembly Flow Model) for Given Power Distribution and Their Differences

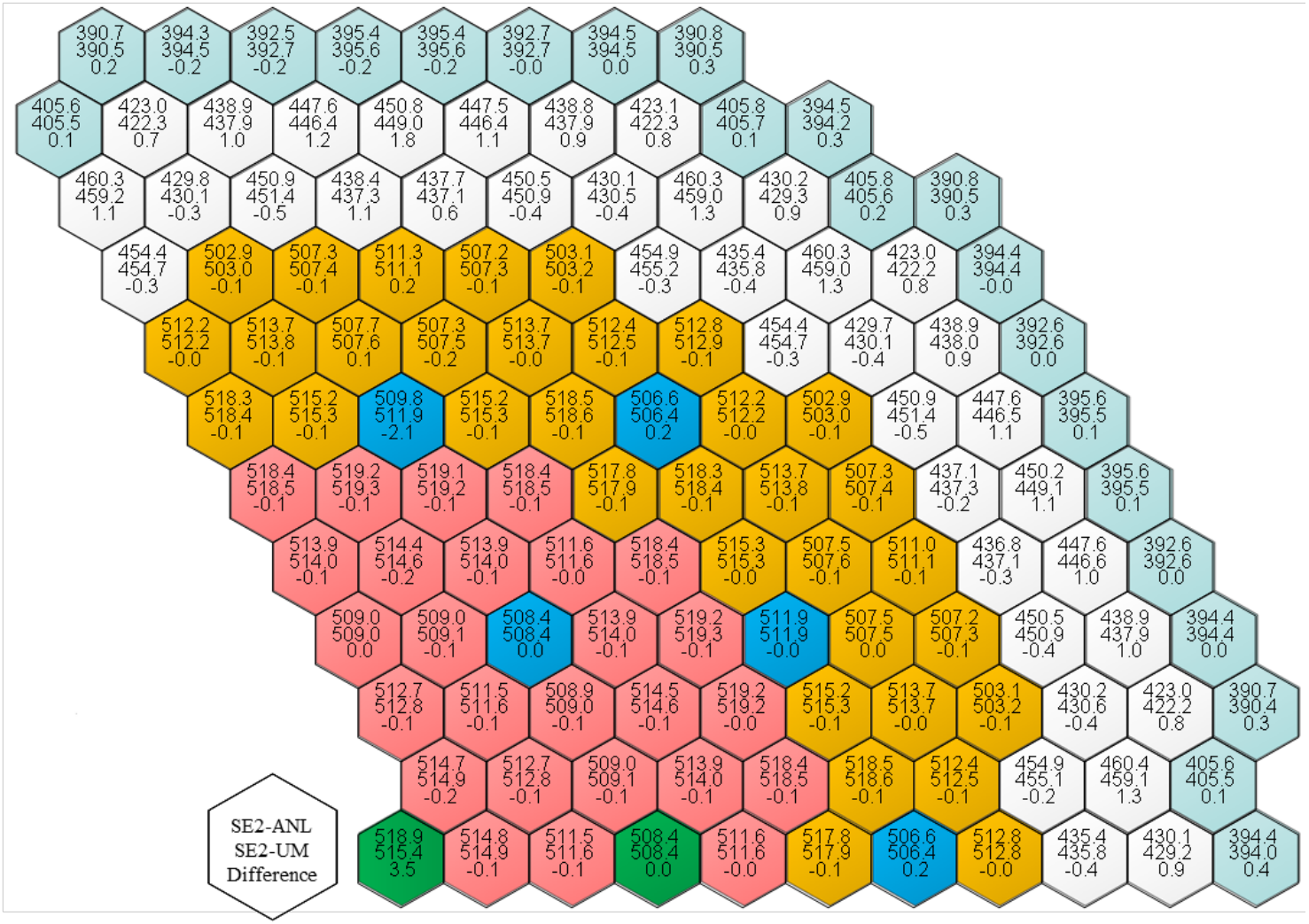

Fig. 4.15 Mixed Mean Coolant Outlet Temperatures (°C) of SE-ANL and SE2-UM Obtained with Inter-assembly Gap Flow Model for Given Power Distribution and Their Differences

4.4.2. Validation of SE2-UM with EBR-II Coolant Outlet Temperatures

In order to validate the SE2-UM code, the coolant outlet temperatures of the EBR-II reactor were calculated for three cycles of Run 163A, Run 164A, and Run 165A and compared with the measured values. EBR-II was a small sodium-cooled fast reactor with 637 subassemblies. The core configuration for Run 163A is shown in Fig. 4.16. The first seven rows are mainly driver assemblies with some additional experimental, structural and control assemblies. The stainless steel reflector assemblies are located in the rows 8 to 10. Then the depleted uranium blanket assemblies are located in the rows 11 to 16. Some stainless steel assemblies are also located in this region. The vertical layout of EBR-II Run 163A is shown in Fig. 4.17. Below the core, there are lower axial reflector and lower grid. Above the core, there are fission gas plenum, sodium gap above plenum (upper grid), and upper axial reflector. The detailed geometry information is obtained from Ref. [47].

The heating calculation of SE2-UM is based on the neutron and gamma fluxes calculated using the variational nodal transport code VARIANT and the modified GAMSOR code discussed in Section 3.2.2, while the heating calculation of the existing SE2-ANL is performed with the DIF3D finite difference diffusion theory code the original GAMSOR code. For the VARIANT and DIF3D calculations, a set of 33-group neutron and 21-group photon cross sections were generated using the MC^2-3 code based on the ENDF/B-VII.0 data. DIF3D finite-difference diffusion theory calculations were performed with six triangular meshes per hexagon. VARIANT nodal transport calculations were performed with P_5 angular approximation and sixth order polynomial expansion for spatial approximation.

To perform the subchannel analysis for EBR-II, the flow rate of each assembly is determined by the EBRFLOW code [48]. All the assemblies in EBR-II core are sorted into 11 different geometry types. Among these 11 types, there are two types of double-ducted bypass assemblies. The active length of the cold and un-irradiated driver subassemblies is 13.5 inches. However, the active core height used in this calculation is 14.4 inches to account for the effects of temperature expansion and irradiation growth. The coolant inlet and bulk outlet temperatures are assumed to be 371 °C and 469 °C, respectively.

A couple of approximations were used in this subchannel analysis. The first approximation is the neglect of the axial heterogeneity of the assembly in the thermal-hydraulic model of EBR-II. The pin geometry is extended from the assembly bottom to top. Another approximation is the introduction of very thin wire wraps to the assembly of bare rods, since the existing correlations for mixing parameters of SE2-ANL are limited to the wire-wrapped pin bundle whose pin pitch-to-diameter ratio ranges from 1.067 to 1.25. In the assemblies of rod pitch-to-diameter ratio of one, wire wraps of 0.001 inch diameter were artificially added.

To take into consideration of the inter-assembly heat transfer above the pin bundle, the top end portion of upper shield region, which is neglected in the neutronics model, is explicitly considered in the thermal-hydraulic model. Because the temperature at the top of pin of adjacent assemblies can be very different, the neglect of the top end portion of upper shield region could cause a noticeable error in the assembly outlet temperature. In the thermal-hydraulic model, extra zero power nodes were put at the top of the neutronics model in order to maintain the same total heat generation rate.

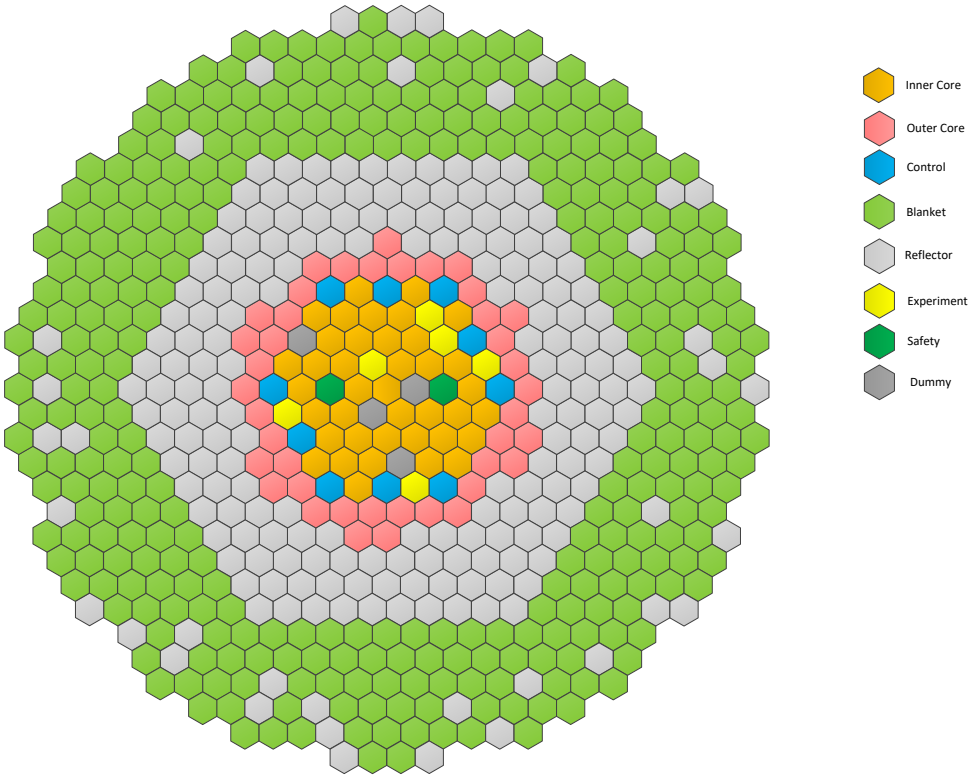

Fig. 4.16 EBR-II Core Loading Pattern for Run 163A

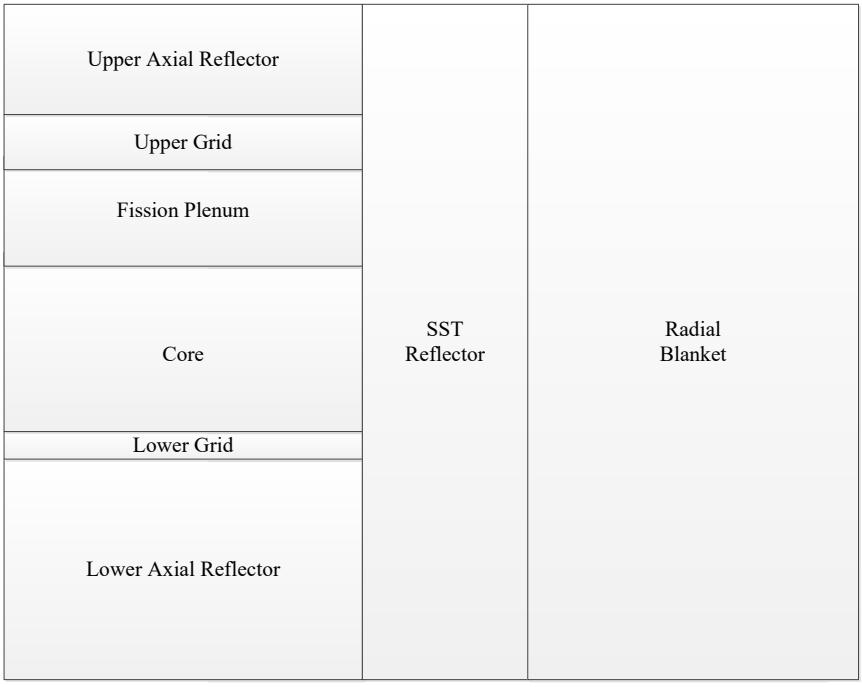

Fig. 4.17 Vertical Layout of EBR-II Run 163A

With the computational procedure and models mentioned above, the assembly outlet temperatures were calculated. The assembly flow rates from EBRFLOW were obtained from Ref. [47], which are shown in Fig. 4.18 to Fig. 4.20. The assembly mixed mean outlet temperatures calculated with SE2-UM are compared with the recorded plant data [49], which were measured with the coolant outlet thermocouples installed in the upper plenum, a quarter inch above the assembly outlet. Initially the thermocouples were in 26 different assemblies, but only 21 of these thermocouples functioned. Another assembly outlet temperature in position 5A3 was obtained by using the measured inlet temperatures of the breached fuel test facility (BFTF) since the temperature change between the assembly outlet and the BFTF inlet was expected to be small. Table 4.4, Table 4.5, and Table 4.6 show the measured sodium outlet temperatures, calculated outlet temperatures and the deviations of the SE2-UM results from the measured values in these 22 assemblies at Run 163A, 164A, and 165A, respectively.

The results show that the coolant outlet temperatures calculated with SE2-UM and SE2-ANL match well. In Run 163A, the maximum difference between these two calculation results is -11.0 °C, which occurs at the assembly 16E9. In driver assemblies, the maximum difference between these two results is only 2.4 °C, which occurs at the assembly 6C4. The maximum difference between SE2-UM and SE2-ANL results at Run 164A and 165A are 10.0 °C at the assembly 2B1 and -5.1 °C at the assembly 12E6, respectively. It is noted that there are large deviations between calculated and measured values in four assemblies in grid positions 2B1, 7A3, 7D4, and 16E9. Except for these four assemblies, the root mean square deviations of the calculated temperatures with SE2-UM from the measured values are all 7.0 °C for Run 163A, 164A, and 165A. Except for these four assemblies, the maximum differences between the calculated temperatures with SE2-UM and the measured values are 12.1 °C, 12.7 °C, and 11.2 °C in Run 163A, 164A, and 165A, respectively.

As mentioned in Ref. [9], the large differences between the SE2-UM results and the measured values in the above four assemblies appear to be due to either biased thermocouple readings or flow mixing effects. The thermocouples for the assemblies 2B1, 7A3, and 7D4 are believed to be biased based on the inconsistency of the thermocouple readings with the power-to-flow balances. Fig. 4.21 shows the measured and calculated outlet temperatures and the power-to-flow ratios of the assembly 2B1 and its surrounding assemblies in Run 163A. Because assembly 2B1 is a non-fueled experimental assembly and its surrounding assemblies are all fuel driver assemblies, the calculated power-to-flow ratio in the assembly 2B1 is much lower than the power-to-flow ratios of its surrounding assemblies. The outlet temperature of 2B1 is expected to be lower than the outlet temperatures of its surrounding assemblies. However, the measured results show that the outlet temperature of assembly 2B1 is higher than the outlet temperatures of its neighboring assemblies. These results indicate that the measured coolant outlet temperature for the assembly 2B1 is not correct due to biased thermocouple readings.

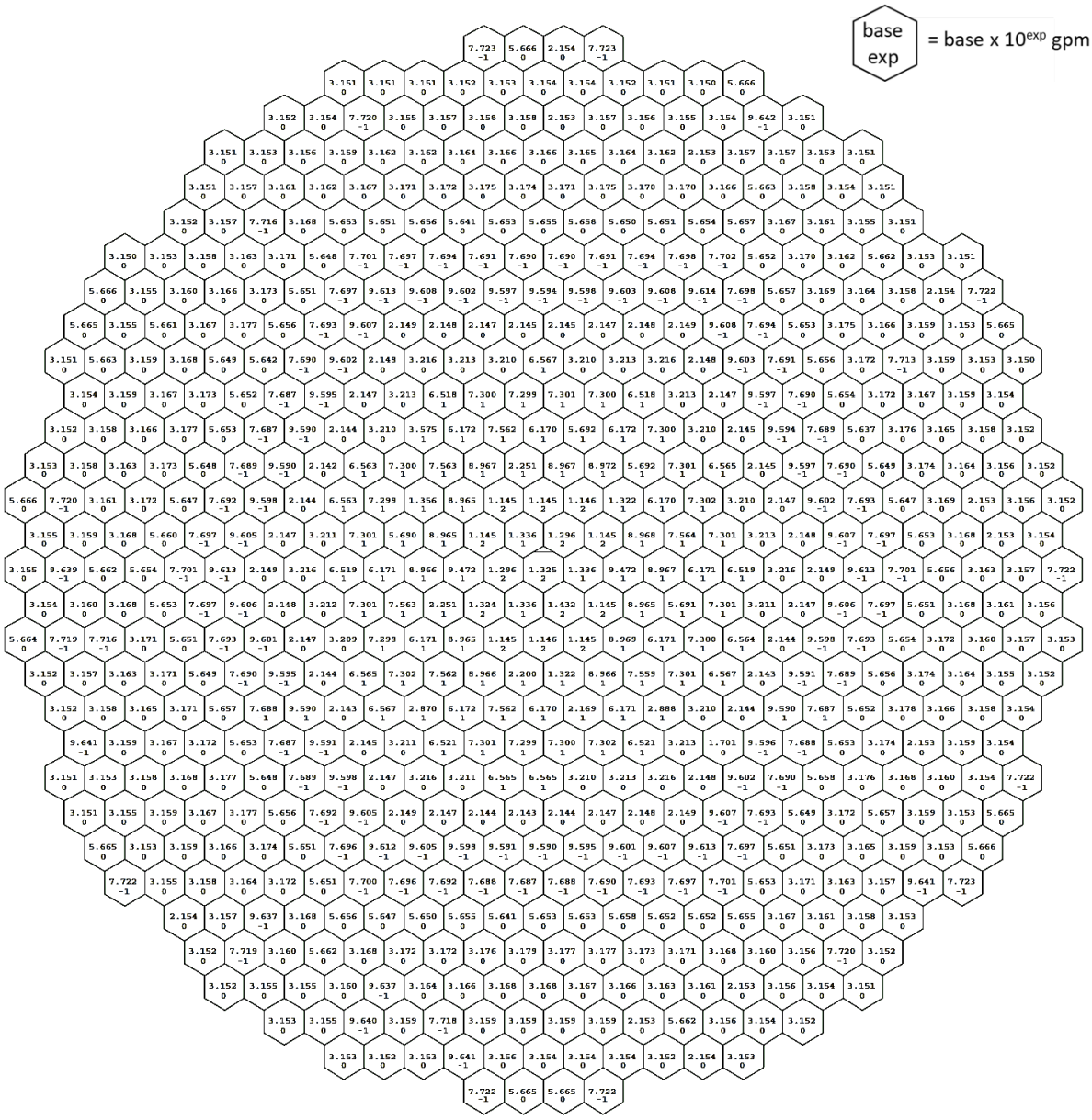

Fig. 4.18 Assembly Flow Rates (in gpm of 800 °F Na) Predicted by EBRFLOW for Run 163A

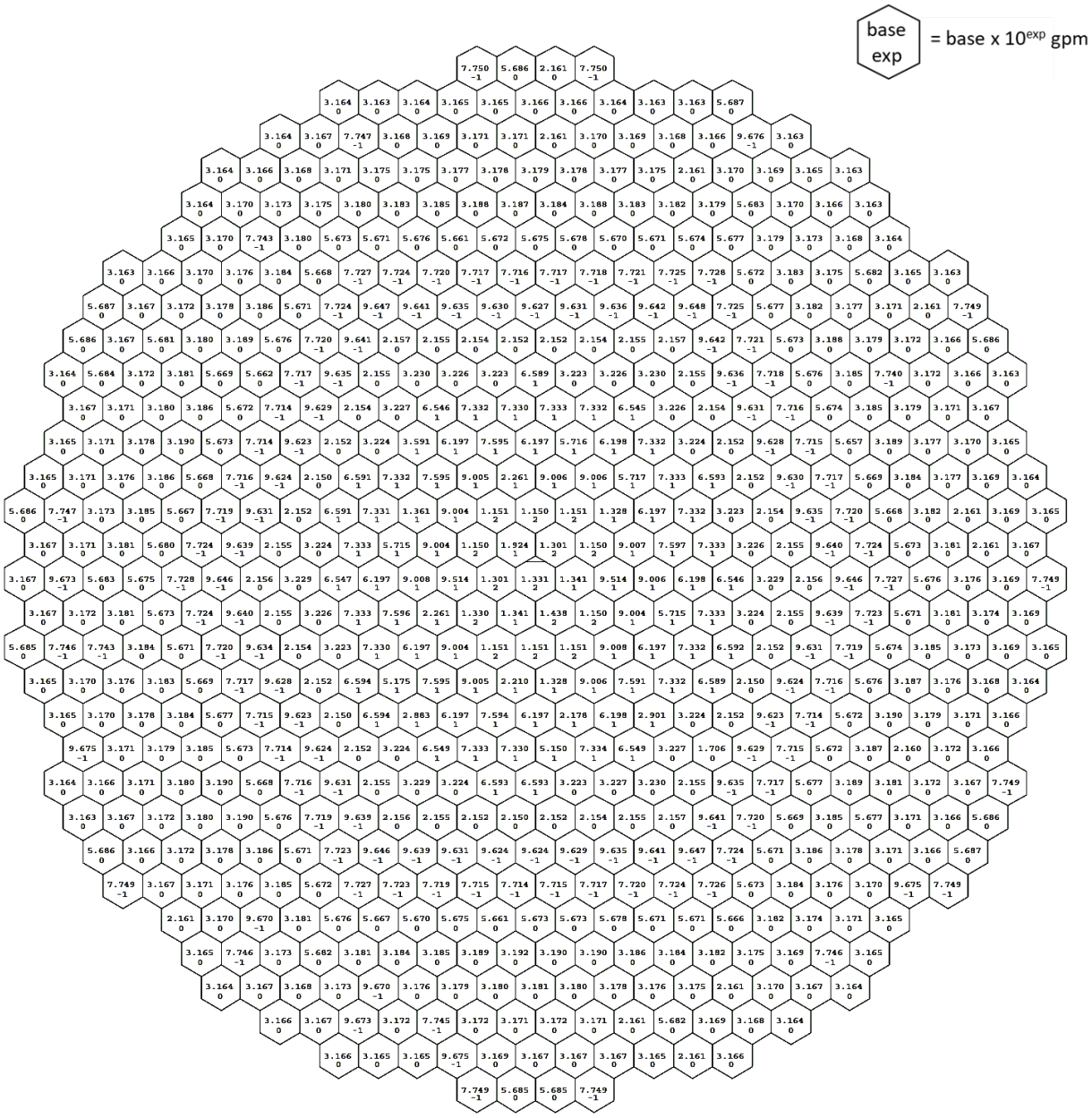

Fig. 4.19 Assembly Flow Rates (in gpm of 800 °F Na) Predicted by EBRFLOW for Run 164A

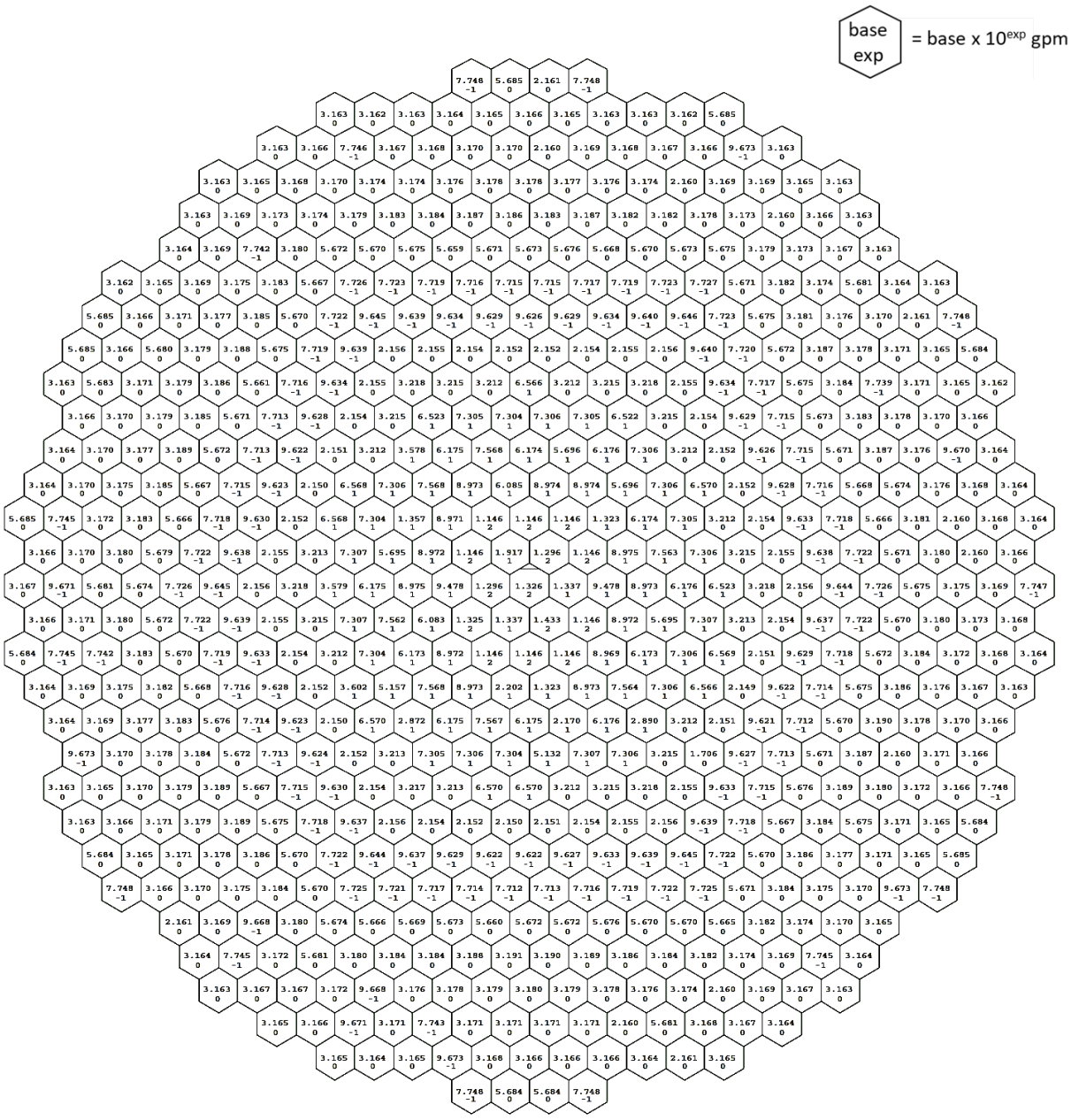

Fig. 4.20 Assembly Flow Rates (in gpm of 800 °F Na) Predicted by EBRFLOW for Run 165A

Table 4.4 Comparison of Calculated Assembly Mixed Mean Outlet Temperatures (°C) with Measured Values at Run 163A

Assembly Position	Measured Value (MV)	SE2-UM	SE2-UM – MV	SE2-ANL	SE2-ANL – MV	SE2-UM – SE2-ANL
1A1	455.7	460.2	4.5	460.4	4.7	-0.2
2A1	450.1	458.2	8.1	458.2	8.1	0.0
2B1	476.9	440.6	-36.3	441.8	-35.1	-1.2
2C1	442.7	451.5	8.8	451.6	8.9	-0.1
2E1	458.5	458.3	-0.2	458.2	-0.3	0.1
2F1	449.0	439.4	-9.6	441.2	-7.8	-1.8
3B1	475.0	475.3	0.3	475.1	0.1	0.2
3C1	460.7	468.4	7.7	468.5	7.8	-0.1
3F1	465.2	474.4	9.2	473.9	8.7	0.5
4B1	479.1	491.2	12.1	490.9	11.8	0.3
4C3	473.1	481.9	8.8	482.4	9.3	-0.5
4E1	482.2	490.1	7.9	489.8	7.6	0.3
4F1	491.3	492.7	1.4	491.9	0.6	0.8
5A3	455.6	450.5	-5.1	452.4	-3.2	-1.9
5A4	487.8	492.2	4.4	492.2	4.4	0.0
5C2	455.7	458.7	3.0	459.2	3.5	-0.5
6C4	479.6	484.5	4.9	484.6	5.0	-0.1
7A3	452.6	496.6	44.0	494.2	41.6	2.4
7D4	436.2	486.3	50.1	484.4	48.2	1.9
9E4	456.7	454.8	-1.9	452.5	-4.2	2.3
12E6	518.1	507.3	-10.8	512.3	-5.8	-5.0
16E9	433.4	374.3	-59.1	385.3	-48.1	-11.0

Table 4.5 Comparison of Calculated Assembly Mixed Mean Outlet Temperatures (°C) with Measured Values at Run 164 A

Assembly Position	Measured Value (MV)	SE2-UM	SE2-UM – MV	SE2-ANL	SE2-ANL – MV	SE2-UM – SE2-ANL
1A1	455.1	459.3	4.2	458.9	3.8	0.4
2A1	449.2	457.2	8.1	456.7	7.5	0.5
2B1	486.8	441.6	-45.2	431.6	-55.3	10.0
2C1	443.0	450.8	7.8	450.3	7.3	0.5
2E1	457.4	457.3	-0.2	456.7	-0.7	0.6
2F1	447.6	438.7	-8.9	440.1	-7.4	-1.4
3B1	474.4	474.4	0.0	473.5	-0.9	0.9
3C1	460.5	468.1	7.6	467.7	7.2	0.4
3F1	463.1	473.2	10.1	472.3	9.2	0.9
4B1	477.8	490.5	12.7	489.7	11.9	0.8
4C3	473.3	481.1	7.7	481.1	7.8	0.0
4E1	481.2	488.6	7.4	487.8	6.6	0.8
4F1	489.8	491.7	1.9	490.3	0.5	1.4
5A3	455.5	449.9	-5.6	451.3	-4.2	-1.4
5A4	487.2	491.6	4.3	490.9	3.7	0.7
5C2	458.0	459.0	1.0	459.1	1.1	-0.1
6C4	484.6	491.2	6.6	490.8	6.2	0.4
7A3	452.2	495.7	43.6	492.8	40.6	2.9
7D4	433.4	499.8	66.3	496.8	63.3	3.0
9E4	462.6	455.3	-7.3	461.3	-1.3	-6.0
12E6	517.7	508.9	-8.7	513.2	-4.5	-4.3
16E9	430.5	383.2	-47.3	385.3	-45.2	-2.1

Table 4.6 Comparison of Calculated Assembly Mixed Mean Outlet Temperatures (°C) with Measured Values at Run 165 A

Assembly Position	Measured Value (MV)	SE2-UM	SE2-UM – MV	SE2-ANL	SE2-ANL – MV	SE2-UM – SE2-ANL
1A1	454.9	458.7	3.7	459.0	4.1	-0.3
2A1	451.2	459.1	7.9	459.3	8.1	-0.2
2B1	485.7	431.4	-54.3	432.8	-52.9	-1.4
2C1	449.7	460.8	11.2	461.0	11.3	-0.2
2E1	458.4	456.7	-1.7	456.7	-1.8	0.0
2F1	448.6	439.6	-9.0	441.5	-7.1	-1.9
3B1	465.3	472.0	6.7	471.9	6.7	0.1
3C1	460.1	467.5	7.4	467.6	7.6	-0.1
3F1	462.9	472.5	9.6	472.1	9.2	0.4
4B1	478.2	487.8	9.6	487.7	9.4	0.1
4C3	472.2	480.6	8.4	481.2	9.0	-0.6
4E1	481.8	488.3	6.5	488.1	6.3	0.2
4F1	488.1	490.3	2.2	489.6	1.4	0.7
5A3	454.6	448.6	-6.0	450.5	-4.1	-1.9
5A4	485.6	489.5	3.9	489.7	4.1	-0.2
5C2	457.0	458.1	1.1	458.6	1.6	-0.5
6C4	488.5	490.8	2.3	491.1	2.6	-0.3
7A3	449.5	492.8	43.3	490.7	41.2	2.1
7D4	432.1	498.9	66.8	496.7	64.6	2.2
9E4	460.0	454.5	-5.5	453.9	-6.1	0.6
12E6	519.7	509.1	-10.7	514.2	-5.5	-5.1
16E9	428.7	383.1	-45.6	385.4	-43.3	-2.3

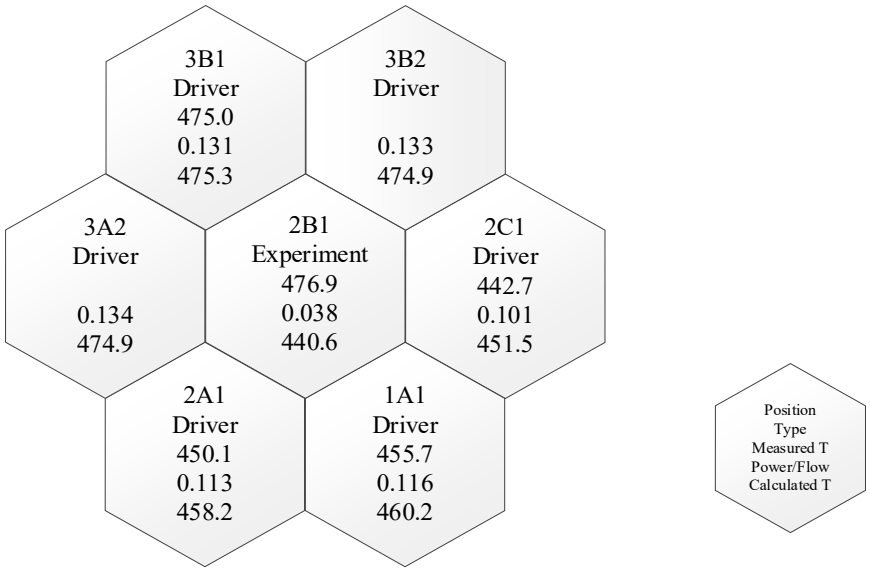

Fig. 4.21 Calculated and Measured Outlet Temperatures (°C) of Assembly 2B1 for Run 163A

Fig. 4.22 and Fig. 4.23 show the adiabatic assembly temperatures and the power-to-flow ratios for the assemblies 7A3 and 7D4 and their surrounding assemblies in Run 163A. Assemblies 7A3 and 7D4 are both fuel assemblies, surrounded by three fuel assemblies and three reflector assemblies. The power-to-flow ratios of assemblies 7A3 and 7D4 are much larger than the surrounding reflector assemblies. Thus, the outlet temperatures of these two assemblies should be much higher than the surrounding reflector assemblies. However, the measured outlet temperatures of these two assemblies are lower than the adiabatic outlet temperatures of the surrounding reflector assemblies. The measured values in 7A3 and 7D4 appear to be biased.

The difference between the SE2-UM result and the measured value in 16E9 is believed to be caused by the coolant mixing of the outflow from 16E9 and the low-pressure plenum region. Fig. 4.24 shows the adiabatic assembly temperatures, the power-to-flow ratios for the assembly 16E9 and its surrounding assemblies in Run 163A. Assembly 16E9 is a blanket assembly surrounded by three other blanket assemblies and one reflector assembly. However, the measured outlet temperature for the assembly 16E9 is higher than the adiabatic outlet temperatures for all the surrounding assemblies. The reason for this high measured temperature is very likely due to the biased thermocouple reading affected by the coolant from the low-pressure plenum region [49].

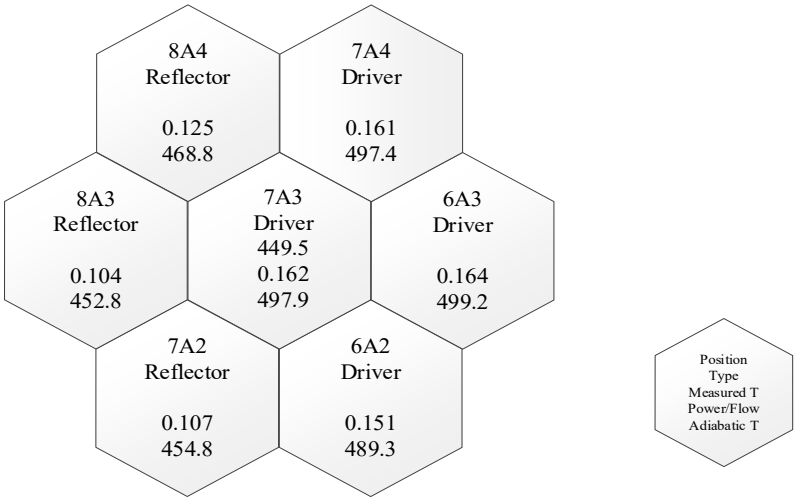

Fig. 4.22 Calculated and Measured Outlet Temperatures (°C) of Assembly 7A3 for Run 163A

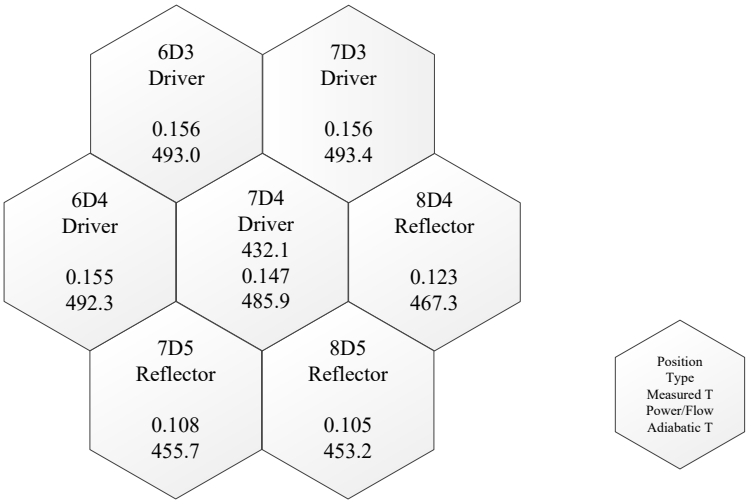

Fig. 4.23 Calculated and Measured Outlet Temperatures (°C) of Assembly 7D4 for Run 163A

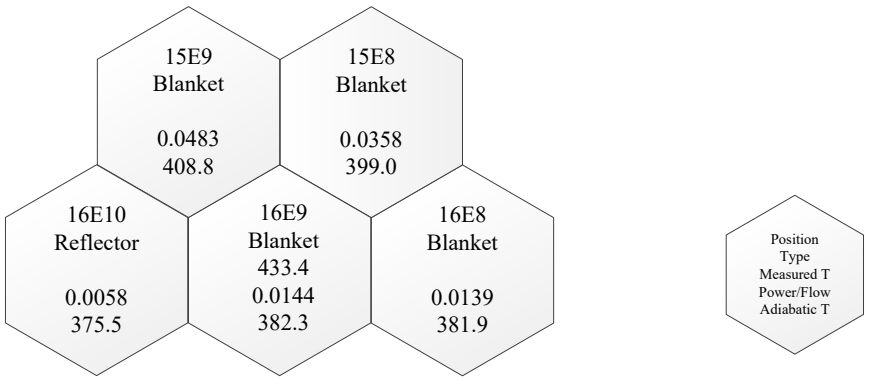

Fig. 4.24 Calculated and Measured Outlet Temperatures (°C) of Assembly 16E9 for Run 163A

4.4.3. Automatic Orifice Zoning and Flow Allocation Calculations with SE2-UM

Full-core subchannel analyses were performed for the 1000 MWt ABR metal core design with the fully automatic orifice zoning and flow allocation option of SE2-UM. The total number of orifice zones was 14, and the number of fueled orifice zones was 6, which were specified as input data. The stage factors obtained from the REBUS-3 equilibrium cycle calculation were also used in the temperature calculation, which are used to account for the discrete batch effects relative to the equilibrium cycle (batch-averaged) power. By applying the REBUS-3 stage factors, the assembly power used in the temperature calculation is the maximum power over the fuel residence time for every fuel assembly, which is the power of fresh fuel assembly. The batch-averaged power distributions and the fresh assembly power distributions at BOEC and EOEC are given in Fig. 4.25 and Fig. 4.26, respectively. Fig. 4.27 shows the orifice zones and the corresponding assembly flow rates determined using SE2-UM. The first six orifice zones are fuel orifice zones. The seventh orifice zone is for the control assemblies, and the other orifice zones are for the reflector and shield assemblies. The flow rates are converged at the third iteration under the criteria that the difference of maximum peak 2σ cladding middle wall temperature over the cycle between two different fueled orifice zones is less than 1 °C. The maximum peak 2σ cladding middle wall temperature for the six fueled orifice zones are 629.9 °C, 629.6 °C, 629.6 °C, 629.9 °C, 629.9 °C, and 629.9 °C, respectively. The maximum difference is 0.3 °C between each fueled orifice zones.

The peak 2σ cladding inner wall temperatures of individual assemblies are shown in Fig. 4.28. The maximum of peak 2σ cladding inner wall temperature at BOEC is 638.8 °C in the second assembly of the second ring. At EOEC, the maximum temperature position is shifyed to the outer core at the fifth and thirteenth assemblies of the ninth ring with the peak 2σ cladding inner wall temperature of 636.4 °C. Both the maximum temperatures are lower than the design limit of 650 °C, which is the fuel-cladding eutectic temperature for the typical ternary metal fuel [47]. Fig. 4.29 presents the peak 2σ fuel centerline temperatures. The maximum values of peak 2σ fuel centerline temperatures are 869.3 °C and 843.4 °C at BOEC and EOEC, respectively. The mixed mean outlet temperatures of each assembly are given in Fig. 4.30. Because the stage factors of REBUS-3 are applied in the temperature calculations, the coolant outlet temperatures are higher than the average core outlet temperature of 510 °C. The maximum mixed mean outlet temperatures at BOEC is 553.6 °C, which occurrs in the tenth assembly of the tenth ring. At EOEC, the maximum mixed mean outlet temperature is 528.4 °C, which occurrs in the fifth assembly of the seventh ring.

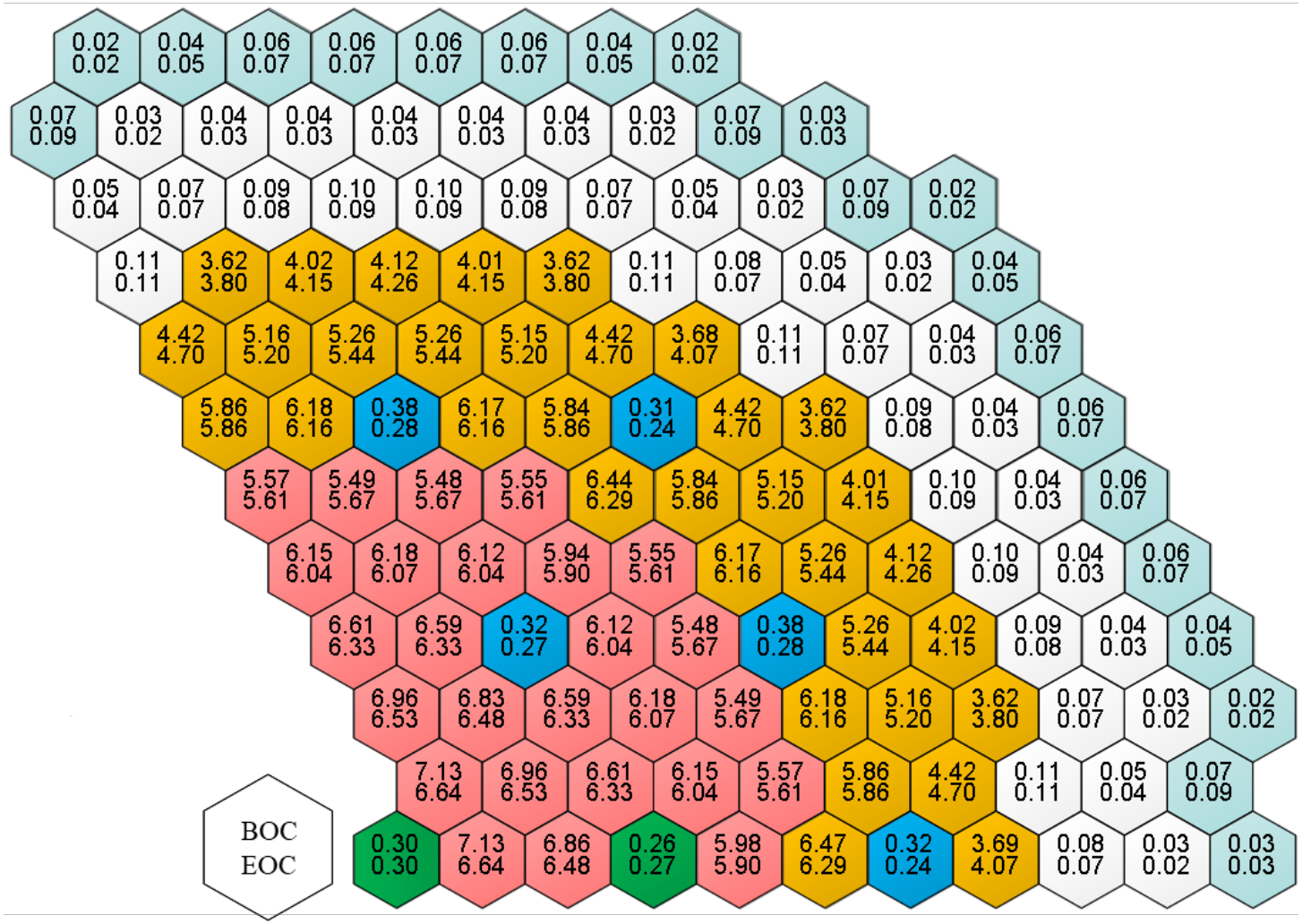

Fig. 4.25 Batch-averaged Assembly Power Distribution of 1000 MWt ABR

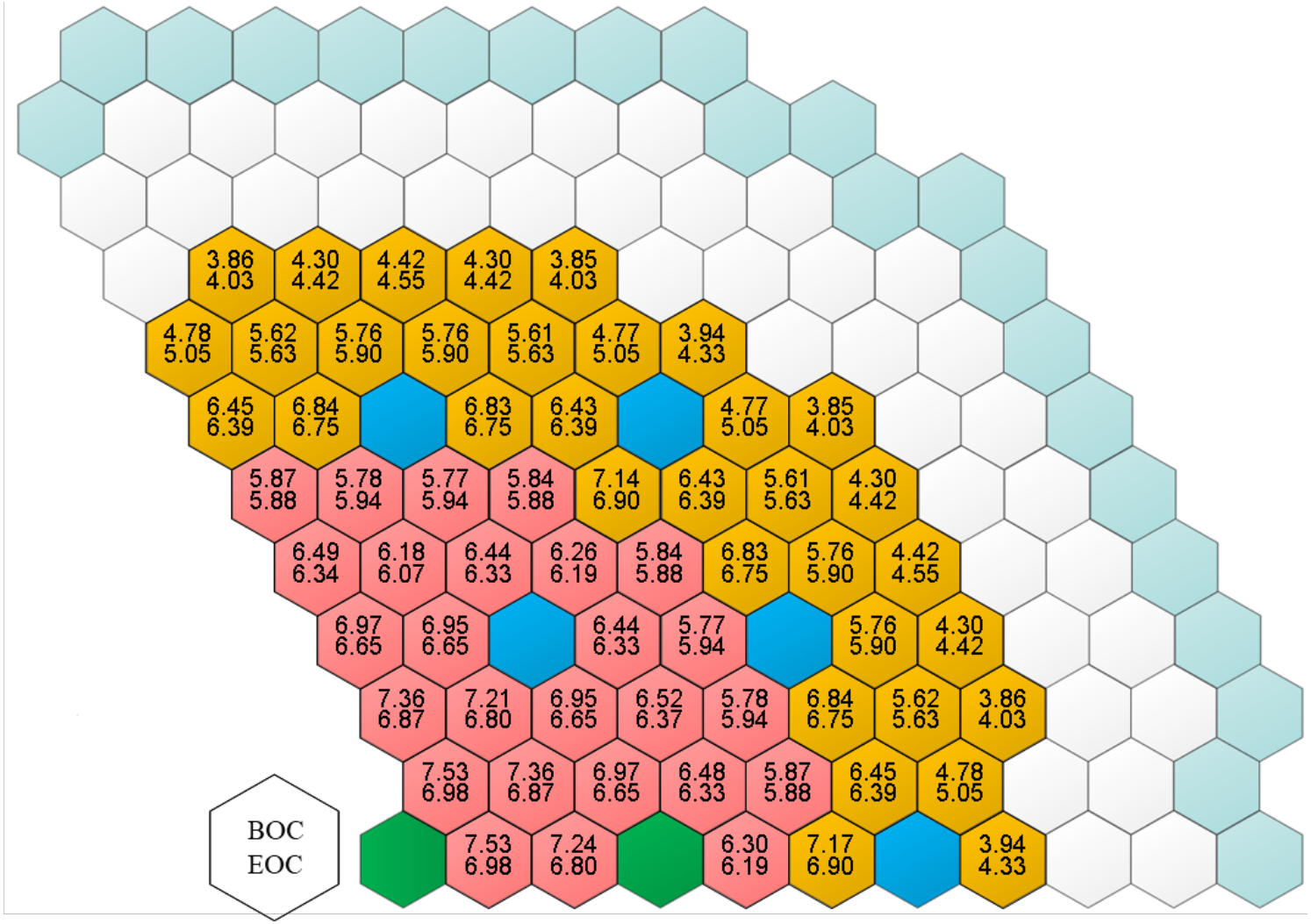

Fig. 4.26 Fresh Fuel Assembly Power Distribution of 1000 MWt ABR

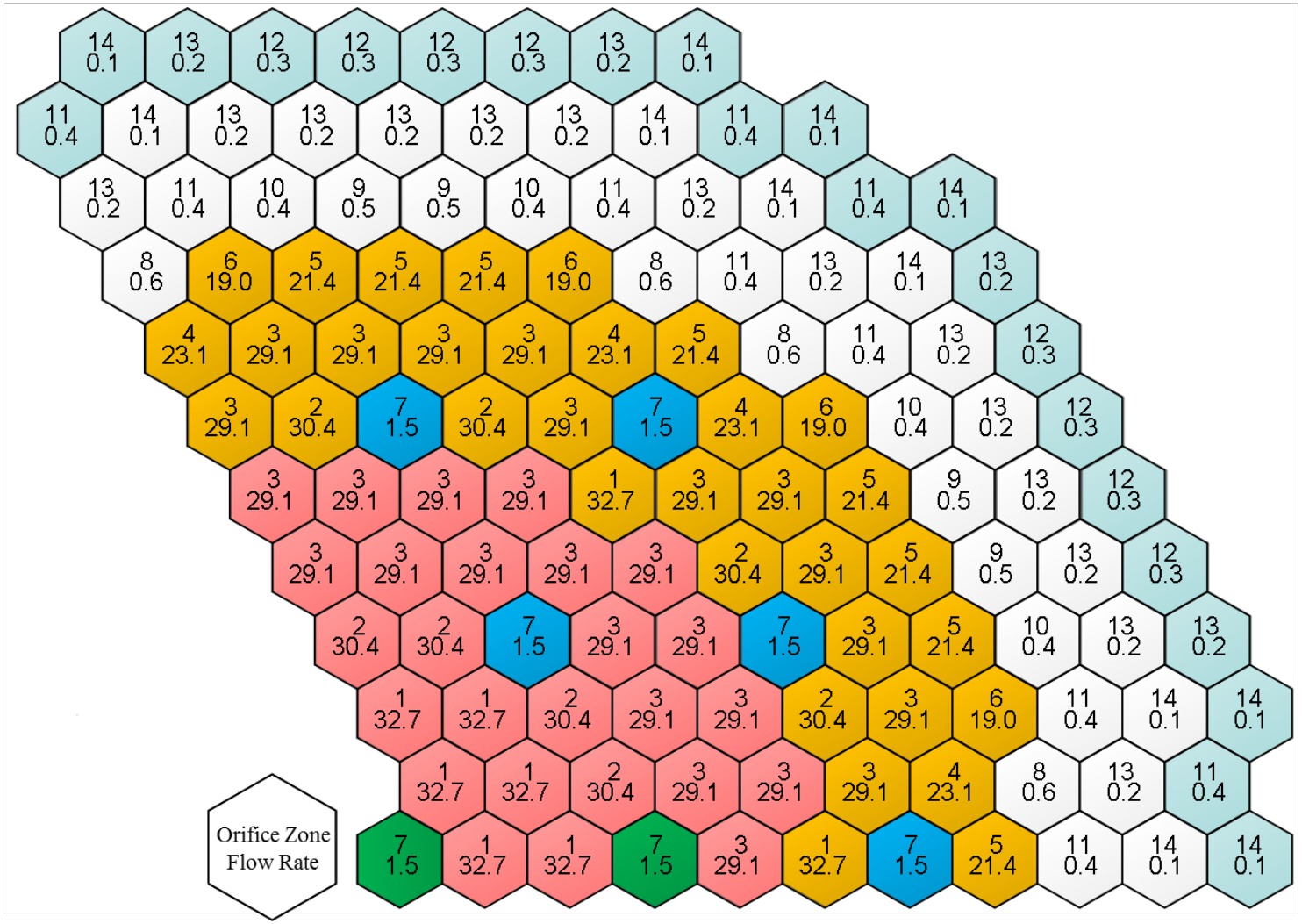

Fig. 4.27 Orifice Zones and Assembly Flow Rates (kg/s) of 1000 MWt ABR Obtained from SE2-UM Calculation

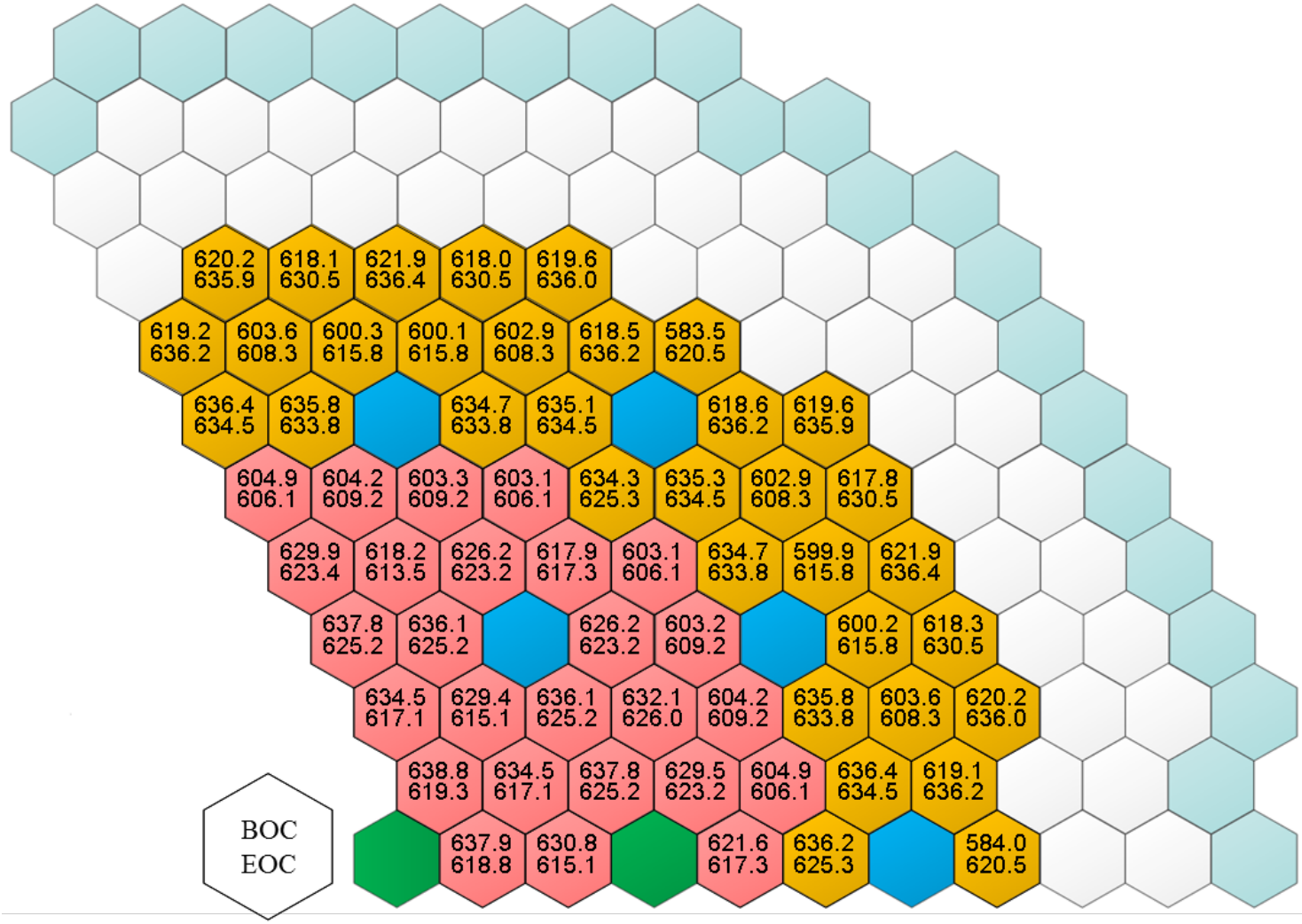

Fig. 4.28 Peak 2σ Cladding Inner Wall Temperatures (°C) at BOEC and EOEC of 1000 MWt ABR

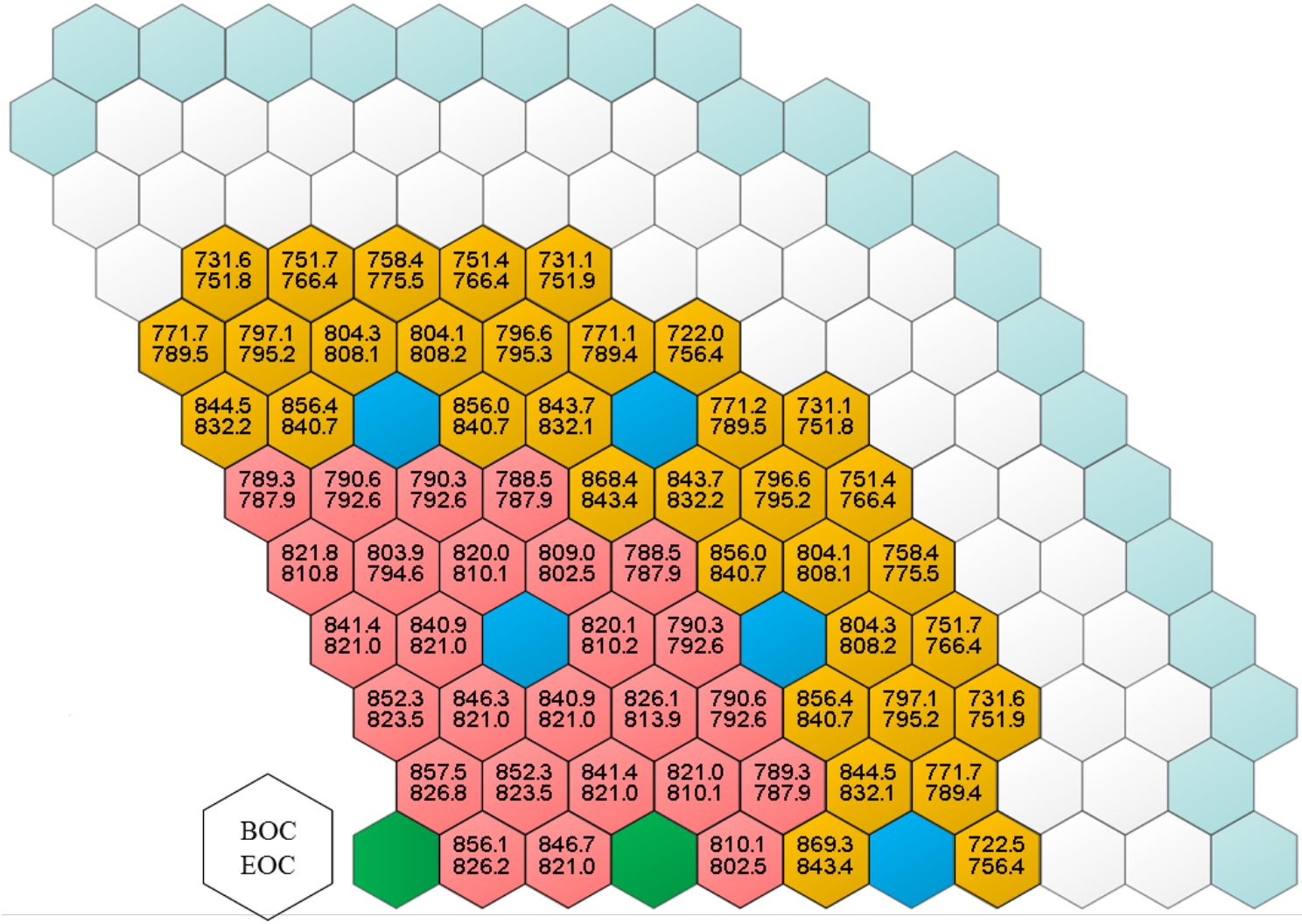

Fig. 4.29 Peak 2σ Fuel Centerline Temperatures (°C) at BOEC and EOEC of 1000 MWt ABR

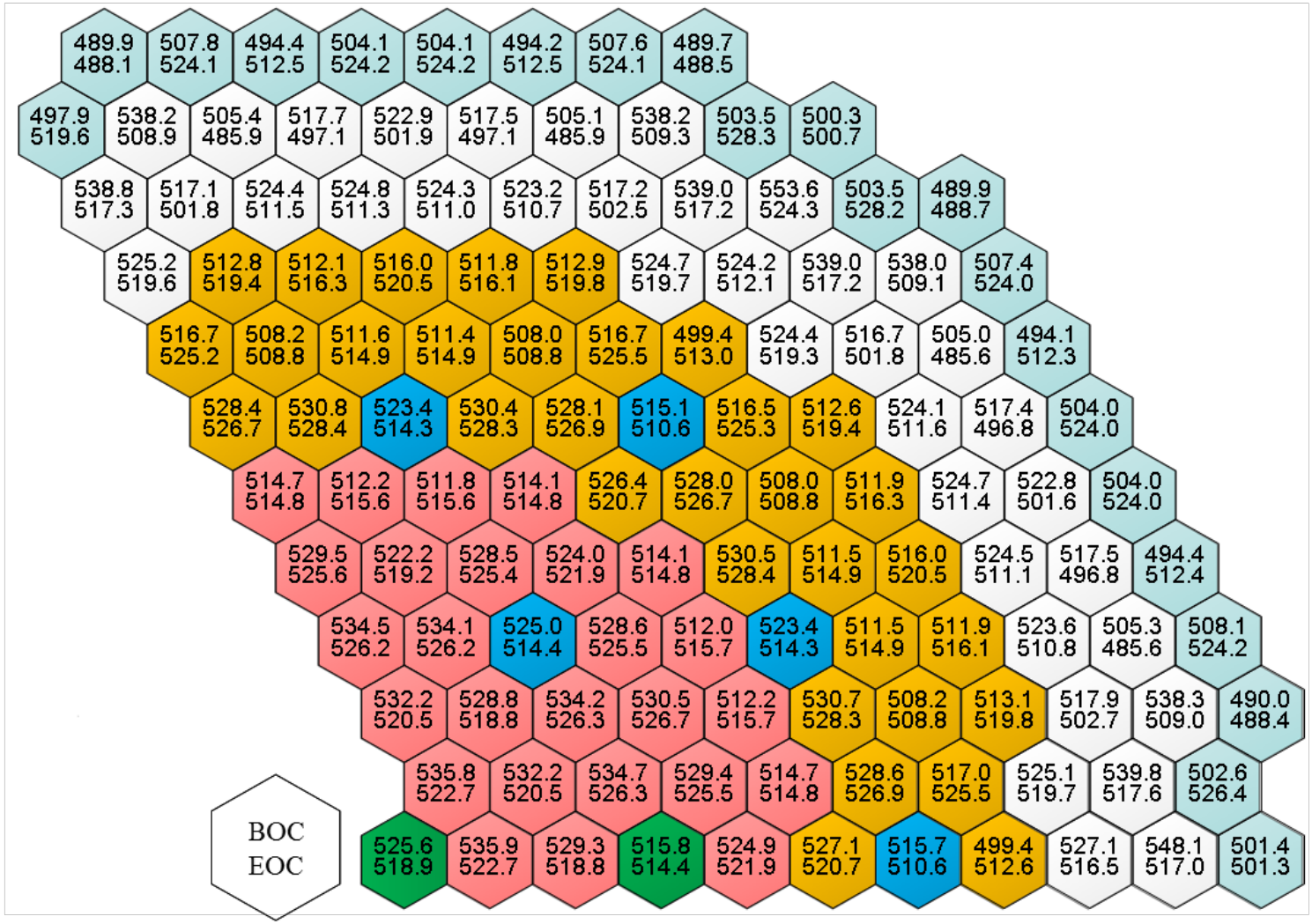

Fig. 4.30 Mixed Mean Outlet Temperatures (°C) at BOEC and EOEC of 1000 MWt ABR

5. Perturbation Theory Method for Bowing Reactivity Coefficient Calculation

In SFRs, the reactivity feedback due to core geometry deformation is one of the most important reactivity feedback phenomena [50]. The differential thermal expansion of duct induced by temperature gradients and the irradiation creep and swelling of duct due to neutron flux gradients lead to assembly bowing or core flowering, depending on the design of the core restraint system and differential displacements of the assembly support structure [51]. These geometrical deformations of the core perturb the neutron leakage from the core, thus leading to a change of reactivity.

In neutronics analyses, an assembly deformation can be modeled by dividing the assembly into fine axial segments and describing the corresponding nuclide density changes in the planar displacement of each axial segment. In the existing method, the reactivity worth of assembly displacement is evaluated using the perturbation theory code VARI3D and the triangular-z finite difference diffusion theory option of the DIF3D code with six triangular meshes per hexagonal assembly. For each hexagonal assembly, six perturbed cross sections are created by applying a correction factor to the so-called "triangular homogenization scheme," in which the cross sections for each triangular mesh are calculated by volume weighting of the cross sections of the homogenized assembly and the inter-assembly gap sodium. The correction factor is determined in such a way to preserve the mass displacement in each triangular mesh under the assumption that the unperturbed fluxes and adjoint fluxes are linear within the assembly [52]. The method to calculate the reactivity effects due to thermal expansion through "virtual density" changes in the diffusion equation [53] has also been revived recently [54]. However, this method has limitations in capturing the reactivity effects due to assembly displacements and in extending to the transport theory. Gentili et al. has also proposed a deterministic scheme for assembly bowing reactivity evaluation based on mesh projection method [55]. The main limitations of this method are that the assembly deformation due to thermal expansion cannot be treated simultaneously, and the assembly heterogeneity effect cannot be naturally taken into account.

In this study, a perturbation theory method for evaluating the reactivity changes due to assembly displacements has been developed by utilizing the heterogeneous real and adjoint flux distributions [20,21]. Forward and adjoint flux distributions in heterogeneous assemblies are reconstructed using the VARIANT transport solutions for homogenized-assembly core models and the PROTEUS-SN transport solutions for heterogeneous single-assembly models. A finite element mesh structure was superimposed on the heterogeneous assembly configuration, and the perturbation calculation was performed by following the material movement, which is analogous to the Lagrangian frame of reference in a fluid field. This scheme provides a unique convenience for modeling heterogeneous assembly displacements by eliminating the need to consider complex intersections of finite element meshes of PROTEUS-SN and shifted assemblies. Discretized formulation was derived based on the finite element method and the spherical harmonics method. Assembly bowing is modeled by shifting axially discretized assembly segments, and heterogeneous assembly configurations are represented by unstructured finite element meshes. The developed perturbation theory method has been implemented in a computer code named RAINBOW [22]. RAINBOW calculates the reactivity changes for the displacements of axial assembly segments in each of six directions normal to the duct wall surfaces.

5.1. Perturbation Theory Formulation

The λ-mode eigenvalue equation for neutron transport in a multiplying system can be written as

$$\begin{aligned}&\hat{\Omega}\cdot\nabla\psi_0(\vec{r},E,\hat{\Omega})+\Sigma_{0,t}(\vec{r},E)\psi_0(\vec{r},E,\hat{\Omega})\\&=\sum_{l=0}^{L}\sum_{k=-l}^{l}Y_{lk}(\hat{\Omega})\int dE'\Sigma_{sl}(\vec{r},E'\to E)\psi_{lk0}(\vec{r},E')+\frac{\lambda_0}{4\pi}\chi_0(E)\int dE'\nu\Sigma_{0,f}(\vec{r},E')\phi_0(\vec{r},E')\end{aligned} \tag{5.1}$$

with the vacuum boundary condition:

$$\psi_0(\vec{r},E,\hat{\Omega})=0,\quad \vec{r}\in\partial V,\quad \hat{\Omega}\cdot\hat{n}\le 0 \tag{5.2}$$

The adjoint equation of Eq. (5.1) is given by:

$$\begin{aligned}&-\hat{\Omega}\cdot\nabla\psi_0^*(\vec{r},E,\hat{\Omega})+\Sigma_{0,t}(\vec{r},E)\psi_0^*(\vec{r},E,\hat{\Omega})\\&=\sum_{l=0}^{L}\sum_{k=-l}^{l}Y_{lk}(\hat{\Omega})\int dE'\Sigma_{sl}(\vec{r},E\to E')\psi_{lk0}^*(\vec{r},E')+\frac{\lambda_0}{4\pi}\nu\Sigma_{0,f}(\vec{r},E)\int dE'\chi_0(E')\phi_0^*(\vec{r},E')\end{aligned} \tag{5.3}$$

with the vacuum boundary condition:

$$\psi_0^*(\vec{r},E,\hat{\Omega})=0,\quad \vec{r}\in\partial V,\quad \hat{\Omega}\cdot\hat{n}\ge 0 \tag{5.4}$$

where the subscript 0 refers to the original unperturbed system, V is the problem domain, ∂V is the domain boundary, $\hat{\boldsymbol{n}}$ is the unit normal vector at the boundary surfaces, $\psi(\vec{r},E,\hat{\Omega})$ and $\psi^*(\vec{r},E,\hat{\Omega})$ are the forward and adjoint neutron angular flux of energy E, position $\vec{r}$ and angle $\hat{\Omega}$, Σ_t is the total cross section, $\nu\Sigma_f$ is the number of neutron per fission multiplied by fission cross section, and χ is the fission spectrum. The scattering kernel is expanded using spherical harmonics $Y_{lk}(\hat{\Omega})$. ψ_{lk} and ψ_{lk}^* are the spherical harmonics moments of the forward and adjoint angular fluxes. Σ_{sl} is the scattering cross section for Legendre moment of order *l*.

It was shown that the fundamental eigenvalues of forward and adjoint transport equations must be equal [56]. Eq. (5.1) and Eq. (5.3) can be written in operator notation as:

$$\boldsymbol{A}_0\psi_0-\lambda_0\boldsymbol{F}_0\psi_0=0 \tag{5.5}$$

and

$$\boldsymbol{A}_0^*\psi_0^*-\lambda_0\boldsymbol{F}_0^*\psi_0^*=0 \tag{5.6}$$

where $\boldsymbol{A}_0$ and $\boldsymbol{F}_0$ are the neutron loss and migration operator and the fission operator, respectively. $\boldsymbol{A}_0^*$ and $\boldsymbol{F}_0^*$ are the adjoint operators of $\boldsymbol{A}_0$ and $\boldsymbol{F}_0$, respectively. The adjoint operators are defined by the following inner products:

$$\left\langle \boldsymbol{A}_0^*\psi_0^*,\psi_0\right\rangle=\left\langle \psi_0^*,\boldsymbol{A}_0\psi_0\right\rangle \tag{5.7}$$

and

$$\left\langle \boldsymbol{F}_0^* \psi_0^*, \psi_0 \right\rangle = \left\langle \psi_0^*, \boldsymbol{F}_0 \psi_0 \right\rangle \tag{5.8}$$

where the inner products indicate an integration over space, angle and energy domains.

Consider a perturbed system of which loss/migration and fission operators are given by:

$$\boldsymbol{A}' = \boldsymbol{A}_0 + \delta \boldsymbol{A} \tag{5.9}$$

and

$$\boldsymbol{F}' = \boldsymbol{F}_0 + \delta \boldsymbol{F} \tag{5.10}$$

The forward neutron transport equation for the perturbed system can be written as:

$$\boldsymbol{A}'\psi' - \lambda' \boldsymbol{F}'\psi' = 0 \tag{5.11}$$

with the perturbed eigenvalue and eigenfunction

$$\lambda' = \lambda_0 + \delta\lambda \tag{5.12}$$

and

$$\psi' = \psi_0 + \delta\psi \tag{5.13}$$

The vacuum boundary condition in Eq. (5.2) is also used for the perturbed system since the external boundary are unperturbed. Integrating the Eq. (5.11) with adjoint flux weighting over space, angle and energy domains yields:

$$\left\langle \psi_0^*, (\boldsymbol{A}' - \lambda' \boldsymbol{F}')\psi' \right\rangle = 0 \tag{5.14}$$

Inserting Eq. (5.9), Eq. (5.10) and Eq. (5.12) in Eq. (5.14) and using Eq. (5.7) and Eq. (5.8), we have:

$$\left\langle \psi_0^*, (\delta \boldsymbol{A} - \delta\lambda \boldsymbol{F}_0 - \delta \boldsymbol{F} \lambda_0 - \delta\lambda\delta \boldsymbol{F})\psi' \right\rangle = 0 \tag{5.15}$$

Therefore, the exact expression of the eigenvalue perturbation can be obtained as:

$$\delta\lambda = \frac{\left\langle \psi_0^*, (\delta \boldsymbol{A} - \lambda_0 \delta \boldsymbol{F})\psi' \right\rangle}{\left\langle \psi_0^*, (\boldsymbol{F}_0 + \delta \boldsymbol{F})\psi' \right\rangle} = \frac{\left\langle \psi_0^*, (\delta \boldsymbol{A} - \lambda_0 \delta \boldsymbol{F})(\psi_0 + \delta\psi) \right\rangle}{\left\langle \psi_0^*, (\boldsymbol{F}_0 + \delta \boldsymbol{F})(\psi_0 + \delta\psi) \right\rangle} \tag{5.16}$$

Neglecting the terms that are higher than first-order of the product of $\delta \boldsymbol{A}$, $\delta \boldsymbol{F}$, and $\delta\psi$, the eigenvalue perturbation $\delta\lambda$ can be obtained as:

$$\delta\lambda = \frac{\left\langle \psi_0^*, (\delta \boldsymbol{A} - \lambda_0 \delta \boldsymbol{F})\psi_0 \right\rangle}{\left\langle \psi_0^*, \boldsymbol{F}_0 \psi_0 \right\rangle} \tag{5.17}$$

The reactivity change $\delta\rho$ is defined by the change in the off-criticality between the unperturbed and perturbed system,

$$\delta\rho = \left(1 - \frac{1}{k'}\right) - \left(1 - \frac{1}{k}\right) = (1 - \lambda') - (1 - \lambda) = -\delta\lambda \tag{5.18}$$

Therefore, the first order perturbation formula for the reactivity can be obtained as:

$$\delta\rho = -\frac{\left\langle \psi_0^*, \left(\delta \boldsymbol{A} - \lambda_0 \delta \boldsymbol{F}\right)\psi_0 \right\rangle}{\left\langle \psi_0^*, \boldsymbol{F}_0 \psi_0 \right\rangle} \tag{5.19}$$

5.2. Lagrangian Scheme for Evaluating the Reactivity Worth of Material Movements

The proposed perturbation theory method focuses on evaluating the reactivity changes induced by the material movement of an assembly as shown in Fig. 5.1. The reactivity changes are determined by the differences in reaction rates before and after material relocations. Conceptually, the reaction rate is similar to some physical quantity of a material element in continuum mechanics that is subjected to a space-time-dependent velocity field. Therefore, the time rate of changes in reaction rate can be described by the substantial (or material) derivative. The physical meaning of the substantial derivative is the change rate of a quantity (reaction rate in this case) as experienced by an observer that is moving along with the flow (assembly material movement in this case). The observations made by a moving observer are affected by the stationary time rate of change of the property, which is zero in this case since the total amount of materials is conserved, and the microscopic cross sections are assumed unperturbed. What is observed also depends on where the observer goes as it floats along with the flow. If the flow takes the observer into a region where, for example, the local flux is higher, then the observed amount of reaction rate will be higher due to this change in location. The reaction rate change before and after material relocations can be obtained by integrating its substantial derivative over a period when the material movement goes on.

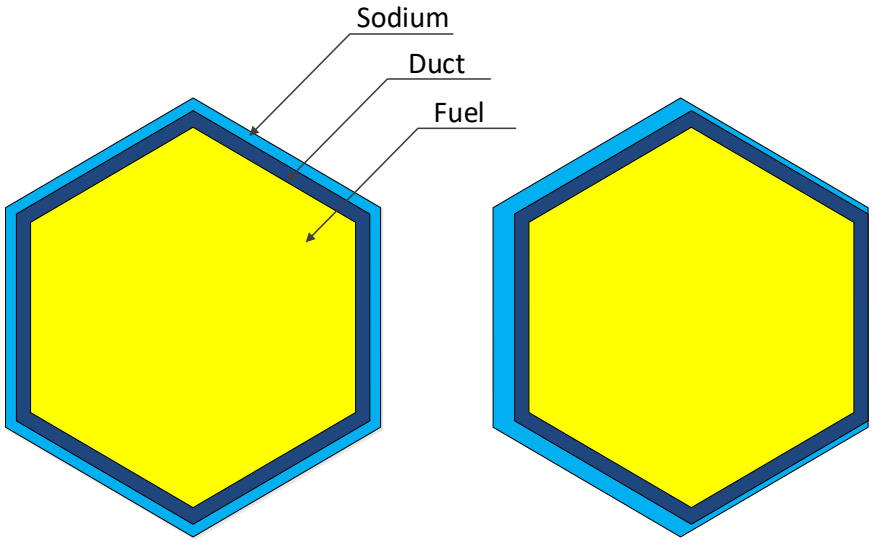

Fig. 5.1 Original (Left) and Displaced Assembly (Right) Configurations

The substantial derivative can be formulated based on Eulerian or Lagrangian types of descriptions of continuum deformation. It can be seen that the classical perturbation theory formulation in Eq. (5.19) is derived under the Eulerian frame. In the perturbed system, the materials are relocated in the spatial domain while the total mass of the materials are conserved. In addition, the microscopic cross sections are assumed unperturbed. By taking advantages of these properties, Eq. (5.19) is reformulated by using the Lagrangian frame of reference to simplify the numerical treatment of the perturbation with finite element spatial discretization.

In the Eulerian description, the focus is on the reference configuration, giving attention to what is occurring at a fixed point in space as time progresses, instead of giving attention to individual materials as they move through space and time. In Eulerian type of expression, the substantial derivative is:

$$\frac{\mathrm{D}}{\mathrm{D}t}q(x_0,t)=\frac{\partial}{\partial t}q(x_0,t)+\frac{dx_0}{dt}\nabla q(x_0,t) \tag{5.20}$$

In this particular case,

$$q(x_0,t)=\boldsymbol{M}(x_0,t)\psi(x_0) \tag{5.21}$$

where $\boldsymbol{M}$ is a reaction operator such as fission, capture, and scattering, and x_0 is a fixed point at the initial configuration such that $dx_0/dt=0$. Thus, the convection term is zero and the substantial derivative is only the time derivative of the reaction rate:

$$\frac{\mathrm{D}}{\mathrm{D}t}[\boldsymbol{M}(x_0,t)\psi(x_0)]=\frac{\partial}{\partial t}[\boldsymbol{M}(x_0,t)\psi(x_0)] \tag{5.22}$$

The total change in reaction rate at position x_0, $\delta R(x_0)$, can be obtained by integrating the equation over the time interval of material movement, that is:

$$\delta R(x_0)=\int_{t_1}^{t_2}\frac{\partial}{\partial t}[\boldsymbol{M}(x_0,t)\psi(x_0)]dt=\boldsymbol{M}(x_0,t)\psi(x_0)\Big|_{t_1}^{t_2}=\delta\boldsymbol{M}(x_0)\psi(x_0) \tag{5.23}$$

where $\delta\boldsymbol{M}(x_0)$ is the operator change at position x_0 before and after the assembly displacement. This reaction rate change yields Eq. (5.19) for the first order perturbation theory based on operator perturbation. Evaluation of Eq. (5.19) involves determining the material property changes at each spatial point. It is straightforward for the case that the material is stationary and changes are only in the local nuclide density or microscopic cross sections, such as for Doppler effects or coolant density coefficient. However, for the case of material movement, it becomes extremely difficult to determine the material property changes in each discretized spatial element, since the interface between different materials may intersect with the spatial element in the perturbed configuration.

In the Lagrangian description, the positions and reaction rates of the nuclides are described in terms of the material or referential coordinates and time. An observer standing in the referential frame of moving objective observes the changes in the position and reaction rates as the material body moves in space as time progresses. The substantial derivative in the Lagrangian type of expression is:

$$\frac{\mathrm{D}}{\mathrm{D}t}Q(x,t)=\frac{\partial}{\partial t}Q(x,t)+\frac{dx}{dt}\nabla Q(x,t) \tag{5.24}$$

where

$$Q(x,t)=\boldsymbol{M}(x)\psi(\chi^{-1}(x,t)) \tag{5.25}$$

and x is the spatial coordinate attached to the material. The coordinate x can be mapped to the initial coordinate x_0 as:

$$x = \chi(x_0, t) \tag{5.26}$$

Thus,

$$\frac{dx}{dt} = \frac{\partial}{\partial t}\chi(x_0, t) = v \tag{5.27}$$

is the velocity of material movement.

The substantial derivative of reaction rate for a material element is given by:

$$\frac{\mathrm{D}}{\mathrm{D}t}[\boldsymbol{M}(x)\psi(\chi^{-1}(x,t))] = \frac{\partial}{\partial t}[\boldsymbol{M}(x)\psi(\chi^{-1}(x,t))] + v\nabla[\boldsymbol{M}(x)\psi(\chi^{-1}(x,t))] \tag{5.28}$$

The first term in the right-hand side of the equation equals to zero since there is no production or destruction of material in the system and the microscopic cross sections of materials are constant with time. Integrating the equation over the time interval of material movement yields the reaction rate change before and after the assembly displacement. $\delta R(x)$ can be written as:

$$\delta R(x) = \int_{t_1}^{t_2} dt \frac{dx}{dt}\nabla[\boldsymbol{M}(x)\psi(\chi^{-1}(x,t))] = \boldsymbol{M}(x)\psi(\chi^{-1}(x,t))\Big|_{t_1}^{t_2} = \boldsymbol{M}(x)\delta\psi(x) \tag{5.29}$$

where $\delta\psi(x)$ is the difference in flux experienced by the material before and after assembly displacement. The above equation indicates that the calculation of the reaction rate change can be accomplished by evaluating the fluxes at different positions in the spatial domain, which is straightforward since the continuous flux distributions in polynomial forms are provided by the VARIANT calculations. Consequently, the reactivity change can be expressed as:

$$\Delta\rho = -\frac{\left\langle \psi^*, (\delta\boldsymbol{A} - \lambda\delta\boldsymbol{F})\psi \right\rangle}{\left\langle \psi^*, \boldsymbol{F}\psi \right\rangle} \Leftrightarrow -\frac{\left(\left\langle \tilde{\psi}^*, \boldsymbol{A}\tilde{\psi} \right\rangle - \left\langle \psi^*, \boldsymbol{A}\psi \right\rangle\right) - \left(\left\langle \tilde{\psi}^*, \lambda\boldsymbol{F}\tilde{\psi} \right\rangle - \left\langle \psi^*, \lambda\boldsymbol{F}\psi \right\rangle\right)}{\left\langle \psi^*, \boldsymbol{F}\psi \right\rangle} \tag{5.30}$$

where $\tilde{\psi}$ and $\tilde{\psi}^*$ are the forward and adjoint fluxes at the shifted position of a material element that was originally exposed to ψ and ψ^* at the base position.

5.3. Discretized Formulations of the Perturbation Theory Method

Eq. (5.30) requires evaluation of the two perturbation terms. The loss and migration terms are defined as:

$$\Delta I_A = \left\langle \psi^*, \delta\boldsymbol{A}\psi \right\rangle = \left\langle \tilde{\psi}^*, \boldsymbol{A}\tilde{\psi} \right\rangle - \left\langle \psi^*, \boldsymbol{A}\psi \right\rangle \tag{5.31}$$

Similarly, the fission term is defined as:

$$\Delta I_F = \left\langle \psi^*, \delta\boldsymbol{F}\psi \right\rangle = \left\langle \tilde{\psi}^*, \boldsymbol{F}\tilde{\psi} \right\rangle - \left\langle \psi^*, \boldsymbol{F}\psi \right\rangle \tag{5.32}$$

The inner product in the above equations denotes the integral over space, angle, and energy variables. Numerical evaluation of such integrals requires discretization on those variables. The discretization of the perturbation formula in space domain is based on unstructured finite

element meshes. Within each finite element, the flux is represented using its averaged value, and material homogenized cross sections are assumed constant.

Based on the spatially discretized formulation, the equivalence between the Lagrangian and Eulerian schemes can be further explained by the following example. Considering the fission term in Eq. (5.32), the integral over spatial domain can be approximated as the summation over all finite element meshes. Therefore, the fission term can be rewritten as:

$$\Delta I_F = \sum_{i=1}^{N} \psi_i^* \delta \boldsymbol{F}_i \psi_i = \sum_{i=1}^{N} \psi_i^* \left(\boldsymbol{F}_i^p - \boldsymbol{F}_i^b \right) \psi_i = \sum_{i=1}^{N} \psi_i^* \boldsymbol{F}_i^p \psi_i - \sum_{i=1}^{N} \psi_i^* \boldsymbol{F}_i^b \psi_i \tag{5.33}$$

where $\boldsymbol{F}_i^b$ and $\boldsymbol{F}_i^p$ represent the base and perturbed fission operator at mesh i. For sufficiently fine spatial discretization, the material shift from a mesh j to another mesh i can be defined by a mapping

$$i = I(j) \tag{5.34}$$

The perturbed fission operator at mesh i can be written as the unperturbed fission operator at mesh j as:

$$\boldsymbol{F}_i^p = \boldsymbol{F}_j^b = \boldsymbol{F}_{I^{-1}(i)}^b \tag{5.35}$$

Substituting Eq. (5.35) into Eq. (5.33) and changing the summation indices of the second term, we have:

$$\sum_{i=1}^{N} \psi_i^* \boldsymbol{F}_{I^{-1}(i)}^b \psi_i - \sum_{i=1}^{N} \psi_i^* \boldsymbol{F}_i^b \psi_i = \sum_{i=1}^{N} \psi_i^* \boldsymbol{F}_{I^{-1}(i)}^b \psi_i - \sum_{j=1}^{N} \psi_j^* \boldsymbol{F}_j^b \psi_j \tag{5.36}$$

In the first term of the right side of Eq. (5.36), the summation over mesh i attached to the fluxes can be converted to the summation over mesh j attached to the fission operator (i.e. material):

$$\sum_{i=1}^{N} \psi_i^* \boldsymbol{F}_{I^{-1}(i)}^b \psi_i = \sum_{j=1}^{N} \psi_{I(j)}^* \boldsymbol{F}_j^b \psi_{I(j)} \tag{5.37}$$

As a result, the fission term can be rewritten as:

$$\sum_{i=1}^{N} \psi_i^* \boldsymbol{F}_i^p \psi_i - \sum_{i=1}^{N} \psi_i^* \boldsymbol{F}_i^b \psi_i = \sum_{j=1}^{N} \psi_{I(j)}^* \boldsymbol{F}_j^b \psi_{I(j)} - \sum_{j=1}^{N} \psi_j^* \boldsymbol{F}_j^b \psi_j = \sum_{j=1}^{N} \boldsymbol{F}_j^b \left(\psi_{I(j)}^* \psi_{I(j)} - \psi_j^* \psi_j \right) \tag{5.38}$$

In general, the shifted finite element mesh may not overlap the finite element at the new location in the original mesh structure, thus the element-averaged forward and adjoint fluxes $\tilde{\psi}_j$ and $\tilde{\psi}_j^*$ at the new location would not be equal to the element-averaged fluxes $\psi_{I(j)}$ and $\psi_{I(j)}^*$ at the mesh i. Therefore, the element-averaged fluxes $\tilde{\psi}_j$ and $\tilde{\psi}_j^*$ are re-evaluated using the VARIANT and PROTEUS solutions. With the re-evaluated element-averaged fluxes, we have:

$$\left\langle \psi^*, \delta \boldsymbol{F} \psi \right\rangle = \sum_{i=1}^{N} \psi_i^* \delta \boldsymbol{F}_i \psi_i = \sum_{j=1}^{N} \boldsymbol{F}_j \left(\tilde{\psi}_j^* \tilde{\psi}_j - \psi_j^* \psi_j \right) \tag{5.39}$$

Similarly, the loss and migration term can be written as:

$$\left\langle \psi^*, \delta \boldsymbol{A} \psi \right\rangle = \sum_{i=1}^{N} \psi_i^* \delta \boldsymbol{A}_i \psi_i = \sum_{j=1}^{N} \boldsymbol{A}_j \left(\tilde{\psi}_j^* \tilde{\psi}_j - \psi_j^* \psi_j \right) \tag{5.40}$$

Fig. 5.2 illustrates a simple example where materials 2 to 4 are shifted in material 1. In this figure, an illustrative flux distribution is also given. The Eulerian scheme focuses on the material change in each spatial mesh to which a flux value is given, whereas the Lagrangian scheme focuses on the change in the flux exposed to each material. For example, with the Eulerian scheme, the perturbation of the fission term due to material displacement can be evaluated as:

$$\left\langle \psi^*, \delta \boldsymbol{F} \psi \right\rangle = [\psi_2^* (\boldsymbol{F}_1 - \boldsymbol{F}_2) \psi_2] + [\psi_3^* (\boldsymbol{F}_2 - \boldsymbol{F}_3) \psi_3] + [\psi_4^* (\boldsymbol{F}_3 - \boldsymbol{F}_4) \psi_4] + [\psi_5^* (\boldsymbol{F}_4 - \boldsymbol{F}_1) \psi_5] \tag{5.41}$$

On the other hand, with the Lagrangian scheme, the perturbation of the fission term can be equivalently written as:

$$\begin{aligned} \left\langle \psi^*, \delta \boldsymbol{F} \psi \right\rangle = & (\psi_3^* \boldsymbol{F}_2 \psi_3 - \psi_2^* \boldsymbol{F}_2 \psi_2) + (\psi_4^* \boldsymbol{F}_3 \psi_4 - \psi_3^* \boldsymbol{F}_3 \psi_3) \\ & + (\psi_5^* \boldsymbol{F}_4 \psi_5 - \psi_4^* \boldsymbol{F}_4 \psi_4) + (\psi_2^* \boldsymbol{F}_1 \psi_2 - \psi_5^* \boldsymbol{F}_1 \psi_5) \end{aligned} \tag{5.42}$$

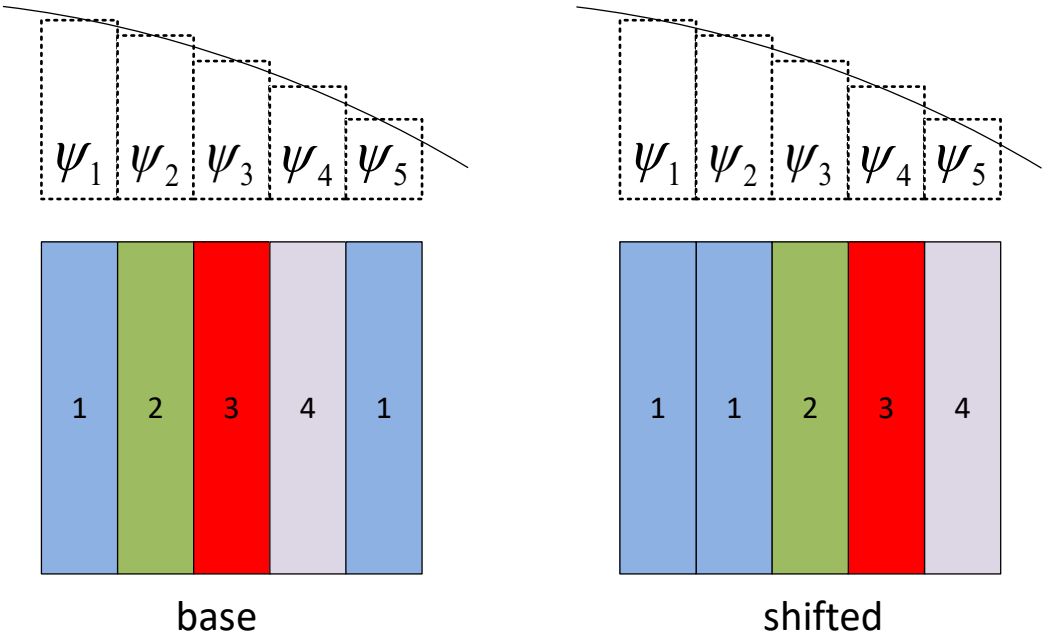

Fig. 5.2 Multi-mesh Example of Material Relocation

The spherical harmonic expansion for the angular variable are applied. Since the fission source is isotropic, the fission term ΔI_F can be written in terms of forward and adjoint scalar fluxes as:

$$\Delta I_F = \iiint dEdE'dV\,\chi(E)N(\vec{r})\nu\sigma_f(E')\left[\tilde{\phi}^*(\vec{r},E)\tilde{\phi}(\vec{r},E') - \phi^*(\vec{r},E)\phi(\vec{r},E')\right] \tag{5.43}$$

The integral over energy and space are numerically evaluated by a summation over the finite element mesh i and energy groups g and g':

$$\Delta I_F = \sum_g \chi(g)\sum_{g'}\sum_i N(i)\nu\sigma_f(i,g')\left[\tilde{\phi}(i,g')\tilde{\phi}^*(i,g) - \phi(i,g')\phi^*(i,g)\right]V_e(i) \tag{5.44}$$

where $V_e(i)$ is the volume of the finite element mesh i.

The loss and migration term ΔI_A can be expressed as the total reaction term minus the scattering source term:

$$\Delta I_A = \Delta I_T - \Delta I_S \tag{5.45}$$

where ΔI_T and ΔI_S are the total and scattering terms, which are defined as:

$$\Delta I_T = \iint dVdEN(\vec{r})\sigma_t(\vec{r},E)\int d\hat{\Omega}\left[\tilde{\psi}^*(\vec{r},E,\hat{\Omega})\tilde{\psi}(\vec{r},E,\hat{\Omega}) - \psi^*(\vec{r},E,\hat{\Omega})\psi(\vec{r},E,\hat{\Omega})\right] \tag{5.46}$$

and

$$\Delta I_S = \iint dVdE\sum_{l=0}^{L}\sum_{k=-l}^{l}\int dE'N(\vec{r})\sigma_{s,l}(\vec{r},E'\to E)\left[\tilde{\psi}^*_{lk}(\vec{r},E)\tilde{\psi}_{lk}(\vec{r},E') - \psi^*_{lk}(\vec{r},E)\psi_{lk}(\vec{r},E')\right] \tag{5.47}$$

For the scattering source term, the spatial and energy integration can be done in a similar manner to that of the fission term ΔI_F. By applying the space and energy discretization, we have

$$\Delta I_S = \sum_g\sum_{g'}\sum_i N(i)\sum_{l=0}^{L}\sigma_{s,l}(i,g'\to g)\sum_{k=-l}^{l}\left[\tilde{\phi}_{lk}(i,g')\tilde{\phi}^*_{lk}(i,g) - \phi_{lk}(i,g')\phi^*_{lk}(i,g)\right]V_e(i) \tag{5.48}$$

where $\phi_{lk}(i,g)$, $\phi^*_{lk}(i,g)$, $\tilde{\phi}_{lk}(i,g)$, and $\tilde{\phi}^*_{lk}(i,g)$ are discretized angular moments in space and energy. $\phi_{lk}(i,g)$ and $\tilde{\phi}_{lk}(i,g)$ can be obtained by evaluating the VARIANT solution stored in NHFLUX at the reference and shifted positions, while $\phi^*_{lk}(i,g)$ and $\tilde{\phi}^*_{lk}(i,g)$ can be obtained by evaluating the adjoint angular flux stored in NAFLUX at the reference and shifted positions.

The expression for the numerical evaluation of ΔI_T can be obtained in a similar way to derive ΔI_S. The angular fluxes $\psi(\hat{\Omega})$ and $\psi^*(\hat{\Omega})$ was expanded in terms of spherical harmonics as:

$$\psi(\vec{r},E,\hat{\Omega}) = \sum_{l=0}^{L}\sum_{k=-l}^{l}\psi_{lk}(\vec{r},E)Y_{lk}(\hat{\Omega}) \tag{5.49}$$

and

$$\psi^*(\vec{r},E,\hat{\Omega})=\sum_{l=0}^{L}\sum_{k=-l}^{l}\psi_{lk}^*(\vec{r},E)Y_{lk}^*(\hat{\Omega}) \tag{5.50}$$

Using the orthogonal relation of spherical harmonics

$$\int d\hat{\Omega}Y_{lk}(\hat{\Omega})Y_{l'k'}^*(\hat{\Omega})=\delta_{ll'}\delta_{kk'} \tag{5.51}$$

we have:

$$\begin{aligned}&\int d\hat{\Omega}\left[\tilde{\psi}^*(\vec{r},E,\hat{\Omega})\tilde{\psi}(\vec{r},E,\hat{\Omega})-\psi^*(\vec{r},E,\hat{\Omega})\psi(\vec{r},E,\hat{\Omega})\right]\\&=\sum_{l=0}^{L}\sum_{k=-l}^{l}\left[\tilde{\psi}_{lk}^*(\vec{r},E)\tilde{\psi}_{lk}(\vec{r},E)-\psi_{lk}^*(\vec{r},E)\psi_{lk}(\vec{r},E)\right]\end{aligned} \tag{5.52}$$

Inserting Eq. (5.52) into Eq. (5.46), we have:

$$\Delta I_T=\iint dVdE\sum_{l=0}^{L}\sum_{k=-l}^{l}N(\vec{r})\sigma_t(\vec{r},E)\left[\tilde{\psi}_{lk}^*(\vec{r},E)\tilde{\psi}_{lk}(\vec{r},E)-\psi_{lk}^*(\vec{r},E)\psi_{lk}(\vec{r},E)\right] \tag{5.53}$$

By applying the space and energy discretization, the total reaction term can be written as:

$$\Delta I_T=\sum_g\sum_i N(i)\sigma_t(i,g)\sum_{l=0}^{L}\sum_{k=-l}^{l}\left[\tilde{\phi}_{lk}(i,g)\tilde{\phi}_{lk}^*(i,g)-\phi_{lk}(i,g)\phi_{lk}^*(i,g)\right]V_e(i) \tag{5.54}$$

In summary, a set of discretized perturbation formula for calculation of the reactivity worth of shifting assembly n was obtained as:

$$\Delta\rho(n)=-\frac{\Delta I_A(n)-\Delta I_F(n)}{I_F} \tag{5.55}$$

$$\Delta I_A(n)=\Delta I_T(n)-\Delta I_S(n) \tag{5.56}$$

$$I_F=\left\langle\psi^*,F\psi\right\rangle \tag{5.57}$$

$$\begin{cases}\Delta I_T(n)=\sum_g\sum_i N(n,i)\sigma_t(n,i,g)\sum_{l=0}^{L}\sum_{k=-l}^{l}\left[\begin{matrix}\tilde{\phi}_{lk}(n,i,g)\tilde{\phi}_{lk}^*(n,i,g)-\\ \phi_{lk}(n,i,g)\phi_{lk}^*(n,i,g)\end{matrix}\right]V_e(n,i)\\ \Delta I_S(n)=\sum_g\sum_{g'}\sum_i N(n,i)\sum_{l=0}^{L}\sigma_{s,l}(n,i,g'\to g)\sum_{k=-l}^{l}\left[\begin{matrix}\tilde{\phi}_{lk}(n,i,g')\tilde{\phi}_{lk}^*(n,i,g)-\\ \phi_{lk}(n,i,g')\phi_{lk}^*(n,i,g)\end{matrix}\right]V_e(n,i)\\ \Delta I_F(n)=\sum_g\chi(n,g)\sum_{g'}\sum_i N(n,i)\nu\sigma_f(n,i,g')\left[\begin{matrix}\tilde{\phi}_{00}(n,i,g')\tilde{\phi}_{00}^*(n,i,g)-\\ \phi_{00}(n,i,g')\phi_{00}^*(n,i,g)\end{matrix}\right]V_e(n,i)\\ I_F=\sum_n\sum_g\chi(n,g)\sum_{g'}\sum_i N(n,i)\nu\sigma_f(n,i,g')\phi_{00}(n,i,g')\phi_{00}^*(n,i,g)V_e(n,i)\end{cases} \tag{5.58}$$

where N is the nuclide density, σ_t is the total cross section, σ_s is the scattering cross section, $\nu\sigma_f$ is the fission yield cross section, χ is the fission spectrum and V_e is the volume of the

finite element. ϕ_{lk} and $\tilde{\phi}_{lk}$ are the angular flux moments at the original and shifted locations. Similarly, ϕ^*_{lk} and $\tilde{\phi}^*_{lk}$ are the adjoint angular flux moments at the original and shifted locations. ϕ_{00} and ϕ^*_{00} are the forward and adjoint scalar fluxes. The indices n, g, i and l in Eq. (5.58) represent the node number, the energy group number, the finite element number, and the Legendre order, respectively. Equations (5.55) to Eq. (5.58) are the final expressions that are used in the numerical implementation of the first order perturbation method for calculating the reactivity worth of assembly displacement.

5.4. Development of RAINBOW Code for Bowing Reactivity Coefficient Calculation

5.4.1. RAINBOW Code Structure

The RAINBOW code structure and data flow are shown in Fig. 5.3. The RAINBOW code requires one general input file and four CCCC (Committee on Computer Code Coordination) binary interface files [33]. The four binary interface files are the microscopic cross section file ISOTXS, the geometry description file GEODST, the nodal flux solution file NHFLUX, and the nodal adjoint flux solution file NAFLUX that are obtained from VARIANT calculations.

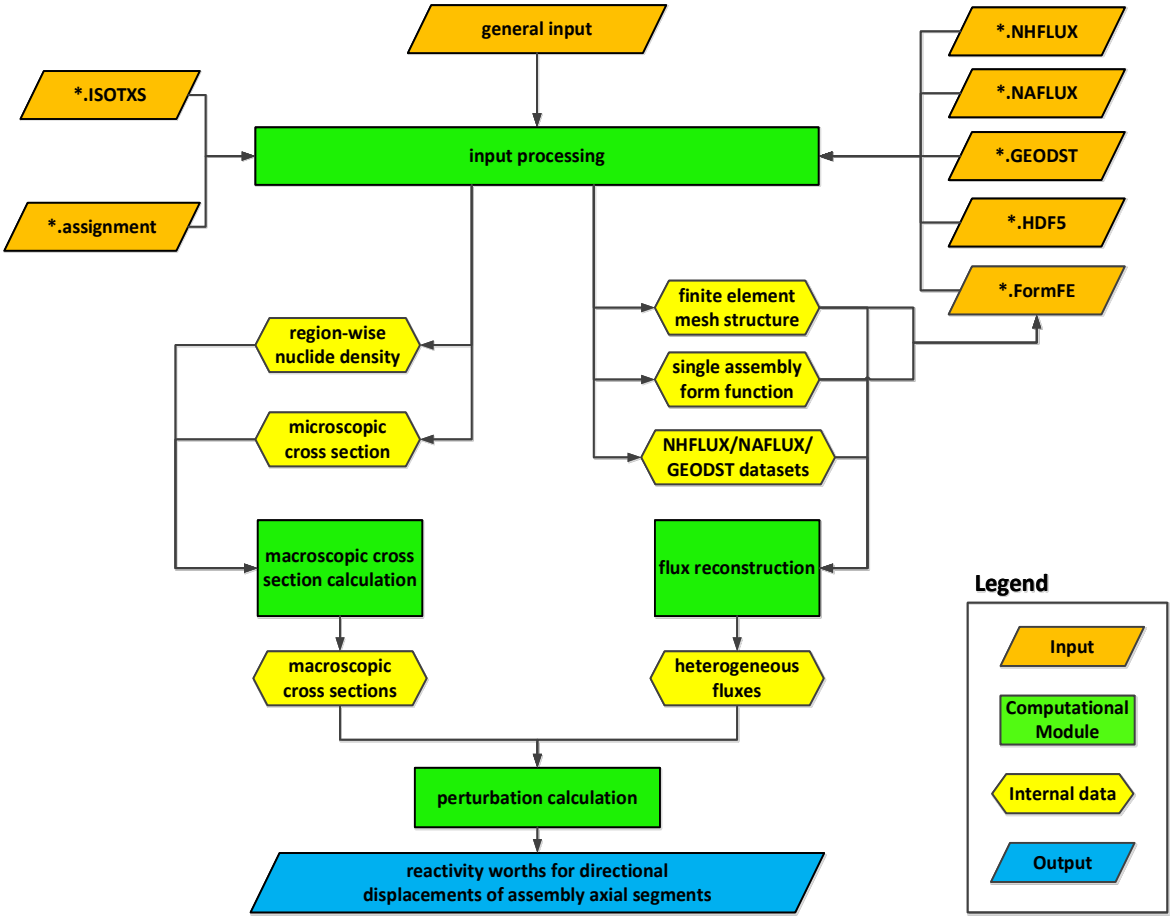

Fig. 5.3 RAINBOW Code Structure and Data Flow

It also requires assignment input and the files obtained by post-processing the HDF5 output files of the PROTUES-SN code. The RAINBOW code contains four main modules: the input processing module, the flux reconstruction module, the macroscopic cross section calculation module, and the perturbation calculation module.

5.4.2. Module Description

5.4.2.1. Input Processing Module

The input processing module preprocesses the interface files to extract the data for the subsequent computations. It adopts several I/O modules for CCCC interface files from the ARC (Argonne Reactor Computation) code package to preprocess the NHFLUX, NAFLUX, GEODST, and ISOTXS files. NHFLUX contains the spatial expansion coefficients for the forward scalar flux and higher order angular moments. The coefficients are extracted and stored into the variable USER_NHFLUX that is defined in a derived type following the NHFLUX file format. Since the adjoint flux is written in the same format in NAFLUX as the forward flux, it is treated in the same way and stored into the variable USER_NAFLUX. It is noted that NAFLUX contains the raw data generated by solving the adjoint neutron transport equation using forward neutron transport solver by reversing the energy group order and the angular direction. To evaluate the adjoint flux based on NAFLUX dataset, the energy group number should be reversed and the sign of odd-parity angular flux moments should be flipped. The GEODST file that contains the geometrical information of the core model is extracted into the variable USER_GEODST. The ISOTXS file that contains the microscopic cross sections for each isotope is read into the variable RAINBOW_ISOTXS.

The HDF5 output file of the PROTEUS-SN code is post-processed by a utility program to provide the heterogeneous forward and adjoint form functions of each single assembly. More information about the post-processing utility program is provided in Appendix H. The PROTEUS-SN solutions are defined in each finite element vertex. The intra-element flux distribution is determined by the vertex values combined with the shape function depending on the finite element type. The element-averaged flux is then obtained by integrating the intra-element flux distribution. Currently, the RAINBOW code accepts only two types of extruded finite elements based on three-node linear element and four-node bilinear element. The element types with more nodes and/or higher order could be included in the future development of RAINBOW code if necessary. The post-processing of the HDF5 file results in the following information: 1) assembly heterogeneous form functions of forward and adjoint fluxes in each finite element, 2) finite element vertex coordinates, and 3) global identification number for each finite element vertex that links the vertex identification number to the finite element identification number. The assembly form functions and the associate finite element mesh structure are fed into the input processing module and stored in the dataset PROTEUS_Solution. The datasets PROTEUS_Solution, USER_NHFLUX, USER_NAFLUX and USER_GEODEST are passed to the flux reconstruction module for computing the combined heterogeneous forward and adjoint fluxes used in the perturbation calculations.

The input processing module also adopts the assignment input file of the PROTEUS-SN code to obtain the compositions of heterogeneous assembly model. The assignment file provides three types of information, which are sufficient for calculating the homogenized nuclide densities for each heterogeneous block (e.g., regions such as fuel, duct, and coolant).

The MATERIAL_DEF card recursively defines the materials based on the isotopes appearing in the ISOTXS dataset, which are stored in the variable RAINBOW_Materials. The REGION_ALIAS card links a material to a block, which is stored in the variable RAINBOW_MaterialToBlock. The REGION_PROPERTY card assigns atom densities to a block, which is stored in the variable RAINBOW_MeshBlockProperties.

5.4.2.2. Macroscopic Cross Section Calculation Module

The HMG4C module of the VARIANT code generates the macroscopic cross section dataset COMPXS based on the data contained in the CCCC datasets ISOTXS, NDXSRF, ZNATDN, and DLAYXS. However, a heterogeneous assembly configuration is required to calculate the reactivity change due to assembly displacement. Thus, the macroscopic cross section dataset COMPXS from VARIANT calculation with fully homogenized-assembly model cannot be directly used in RAINBOW calculations. Instead, the perturbation calculations should be based on the heterogeneous assembly configuration used in PROTEUS-SN calculations. Therefore, the subroutines of the PROTEUS-SN code for calculating macroscopic cross sections of blocks are adopted in this module. The calculation procedure is shown in Fig. 5.4. The module accepts RAINBOW_Materials, RAINBOW_ALIAS, and RAINBOW_MeshBlockProperties together with RAINBOW_ISOTXS that are passed from the input processing module. The macroscopic cross sections for each block are finally calculated by multiplying the isotopic nuclide densities with associate microscopic cross sections and summing over all isotopes in the block.

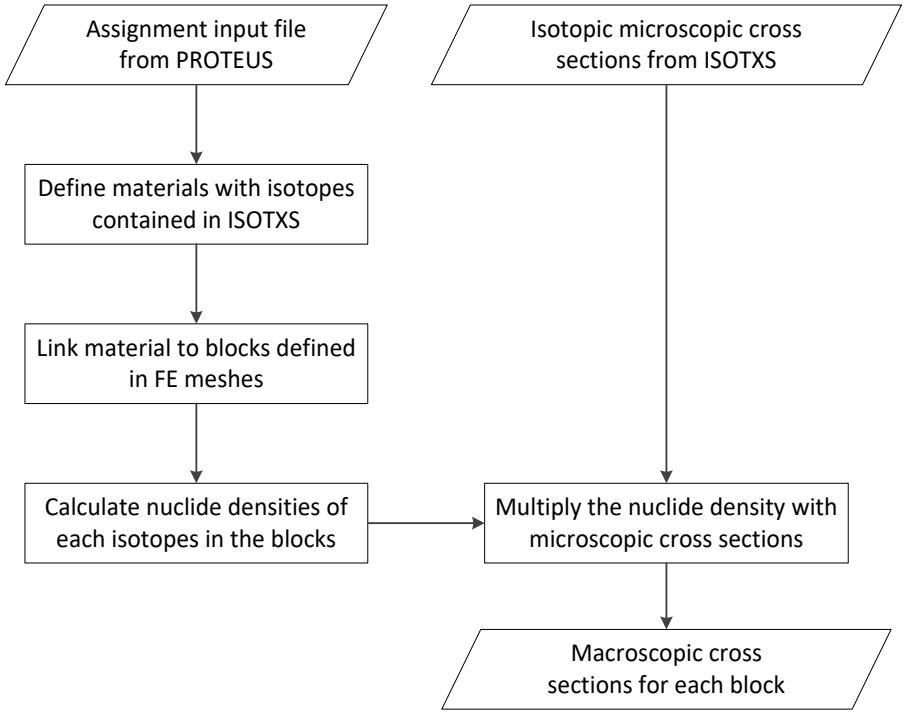

Fig. 5.4 Procedures for Calculating the Macroscopic Cross Sections for Each Block

5.4.2.3. Heterogeneous Flux Reconstruction Module

The heterogeneous flux reconstruction module contains the subroutines that produce the element-averaged forward and adjoint fluxes based on heterogeneous assembly configuration by combining the PROTEUS-SN single assembly solution and the VARIANT full core solution. The overall procedure of flux reconstruction is shown in Fig. 5.5.

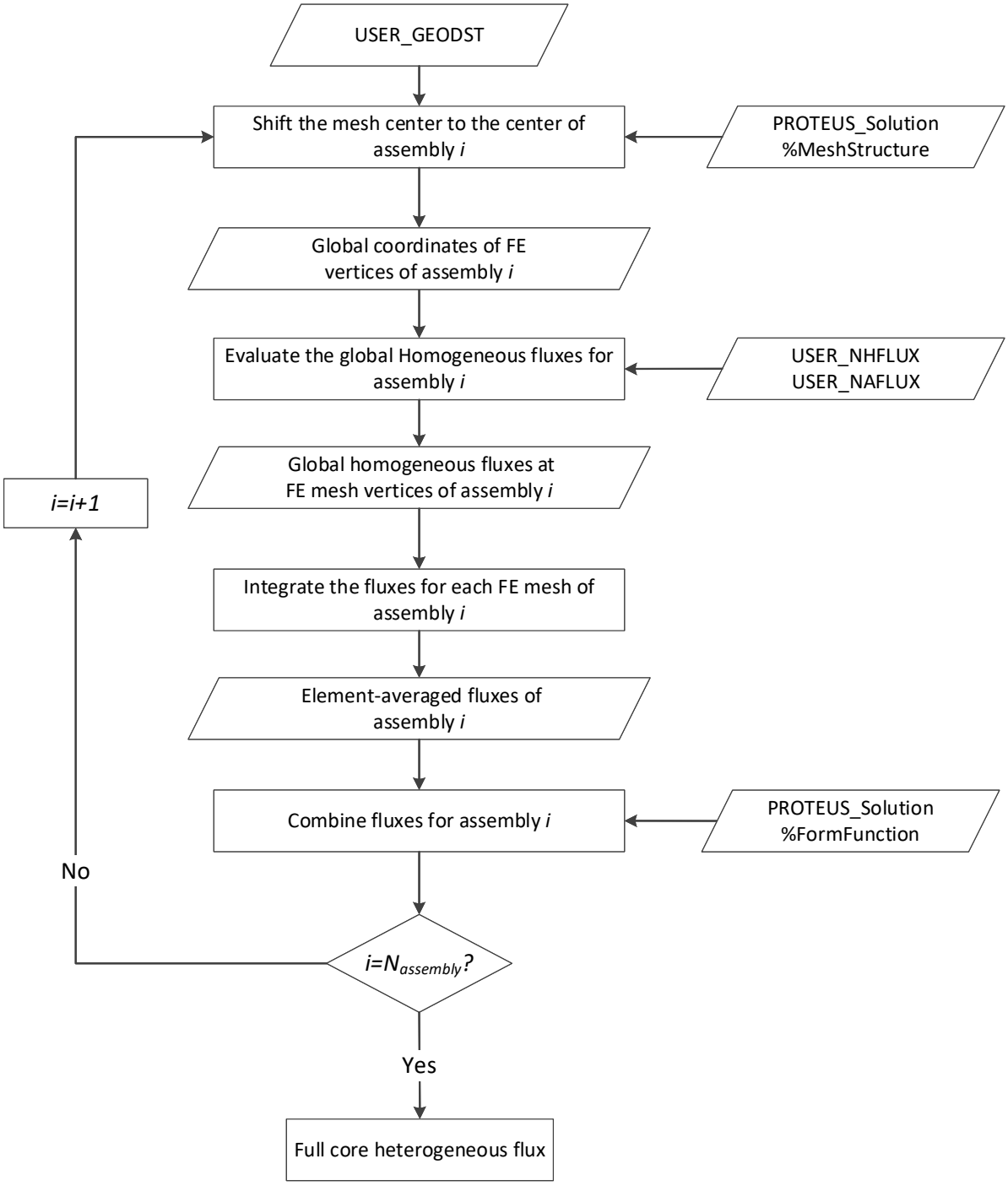

Fig. 5.5 Procedures for Reconstruction of Global Heterogeneous Flux

The finite element (FE) meshes are used for representing the spatial distribution of the heterogeneous flux within a fuel assembly. The finite element meshes used for the PROTEUS-SN code were superimposed on the VARIANT solution for each node (homogenized assembly). The global VARIANT solutions are processed node by node following the assembly ordering in the NHFLUX dataset as shown in Fig. 5.6 and Fig. 5.7. Fig. 5.6 and Fig. 5.7 also show the global frame of reference (X-Y), the origin of which is at the core center, and the local frame of reference (X'-Y'), the origin of which is at each assembly center.

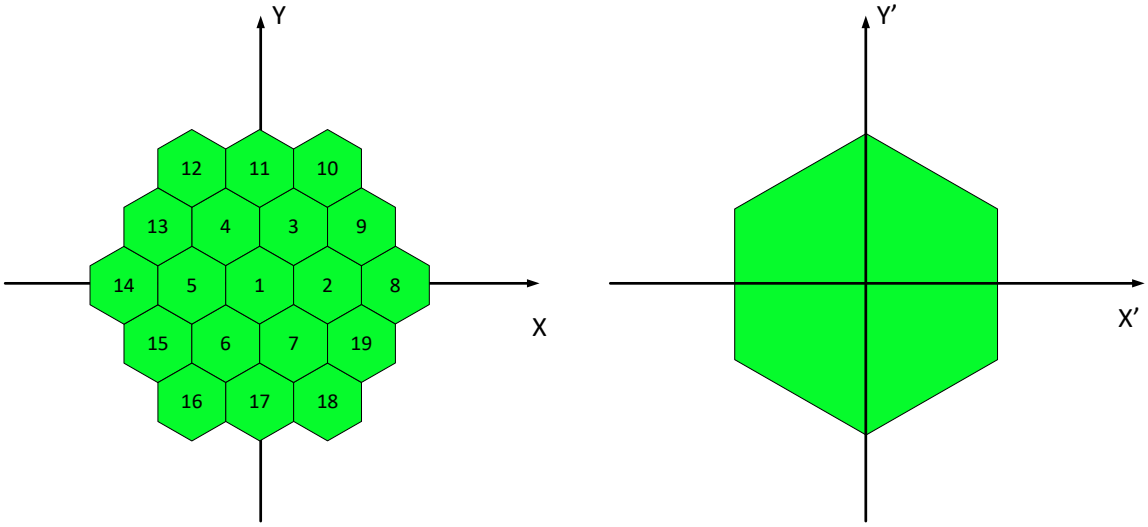

Fig. 5.6 Full Core Node Ordering in NHFLUX Dataset and Reference Frames for FE Meshes

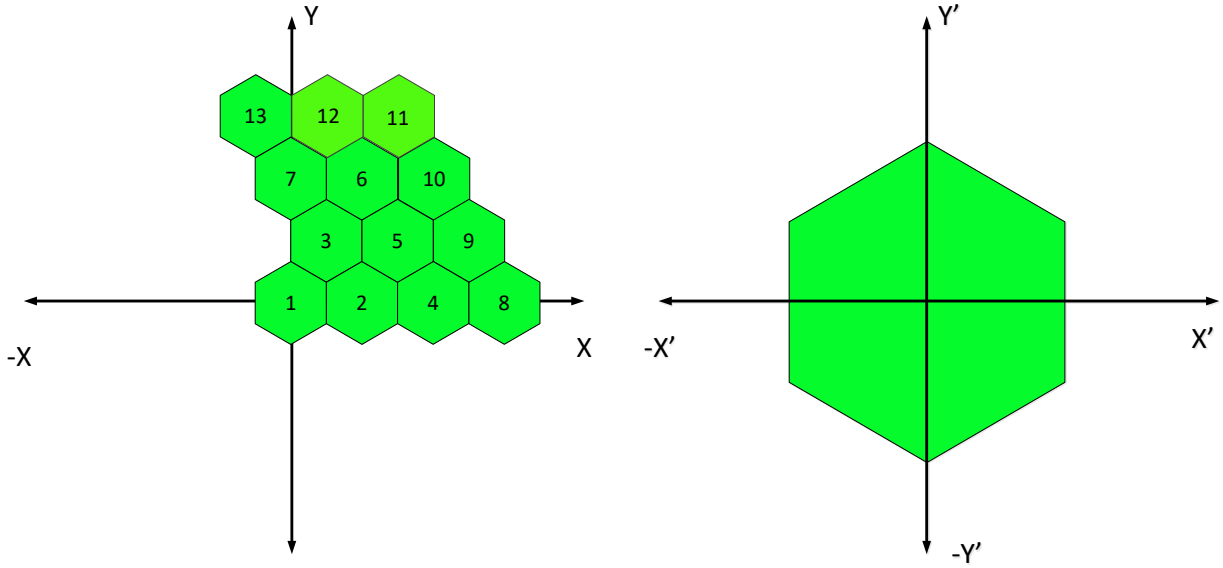

Fig. 5.7 One-third Core Node Ordering in NHFLUX Dataset and Reference Frames for FE

The flux evaluation subroutine takes the coordinates in the global frame of reference as input, while the FE meshes from PROTEUS-SN calculation are defined in the local frame of reference. The FE mesh coordinates at the global frame of reference for individual assembly are determined by adding the node center coordinates in the global frame of reference to the FE mesh local coordinates. The VARIANT global flux is evaluated at the vertices of each element. The element-averaged flux is determined following the same procedure used in evaluating the element-averaged flux of the PROTEUS-SN solution. The evaluated VARIANT and PROTEUS-SN solutions are then combined to yield a full core heterogeneous flux distribution based on the flux reconstruction method.

5.4.2.4. Perturbation Calculation Module

The designed perturbation calculation module in the RAINBOW code contains two procedures for thermal expansion and assembly displacement. Currently, the perturbation calculation for thermal expansion is under development, and thus this report is focused on the perturbation calculation for assembly displacement, which produces the reactivity change for a small shift of each axial segment of each assembly. The perturbation calculations are performed by shifting each assembly segment in each of six directions normal to the duct wall surfaces by a user-specified amount. Then, the reactivity change for assembly displacement in any given direction can be approximated by the linear combination of the reactivity changes in the selected six directions normal to duct wall surfaces.

The procedure for the perturbation calculations of the reactivity changes due to assembly displacements is shown in Fig. 5.8. The calculation starts from evaluating the bilinear-weighted fission production term I_F over the whole core, which provides the denominator of the perturbation formula. The numerator includes the perturbations of the fission production term and the loss and migration term. The loss and migration term equals to the absorption term plus the out-scattering term minus the in-scattering term, which is equivalent to the total reaction terms subtracting the scattering source term. The perturbations of the bilinear-weighted reaction rates and the reactivity changes are calculated by following the loops over the six directions, assembly axial segments, and assemblies. For each axial segment, the spatial integration of a bilinear-weighted reaction rate perturbation over the node is approximated by the production of the integrated value at the node mid-plane and the node height. The node height should be sufficiently small, and the bilinear-weighted reaction rate could be considered linear in axial direction such that its value at the node mid-plane provides an accurate approximation of the axially averaged quantity. This axial integration scheme of the bilinear-weighted reaction rate can be improved by analytically integrating the axial shapes of the bilinear-weighted reaction rates in each extruded finite element such that the limitations on the axial node size can be reduced.

5.4.3. I/O File Descriptions

5.4.3.1. Input File

The user-friendly NAMELIST input format is adopted in the RAINBOW code. There are three NAMELIST blocks: &ProblemSpecs, &AssemblySpecs, and &InterfaceFiles. The descriptions of the three NAMELIST blocks are shown in Table 5.1, Table 5.2, and Table 5.3.

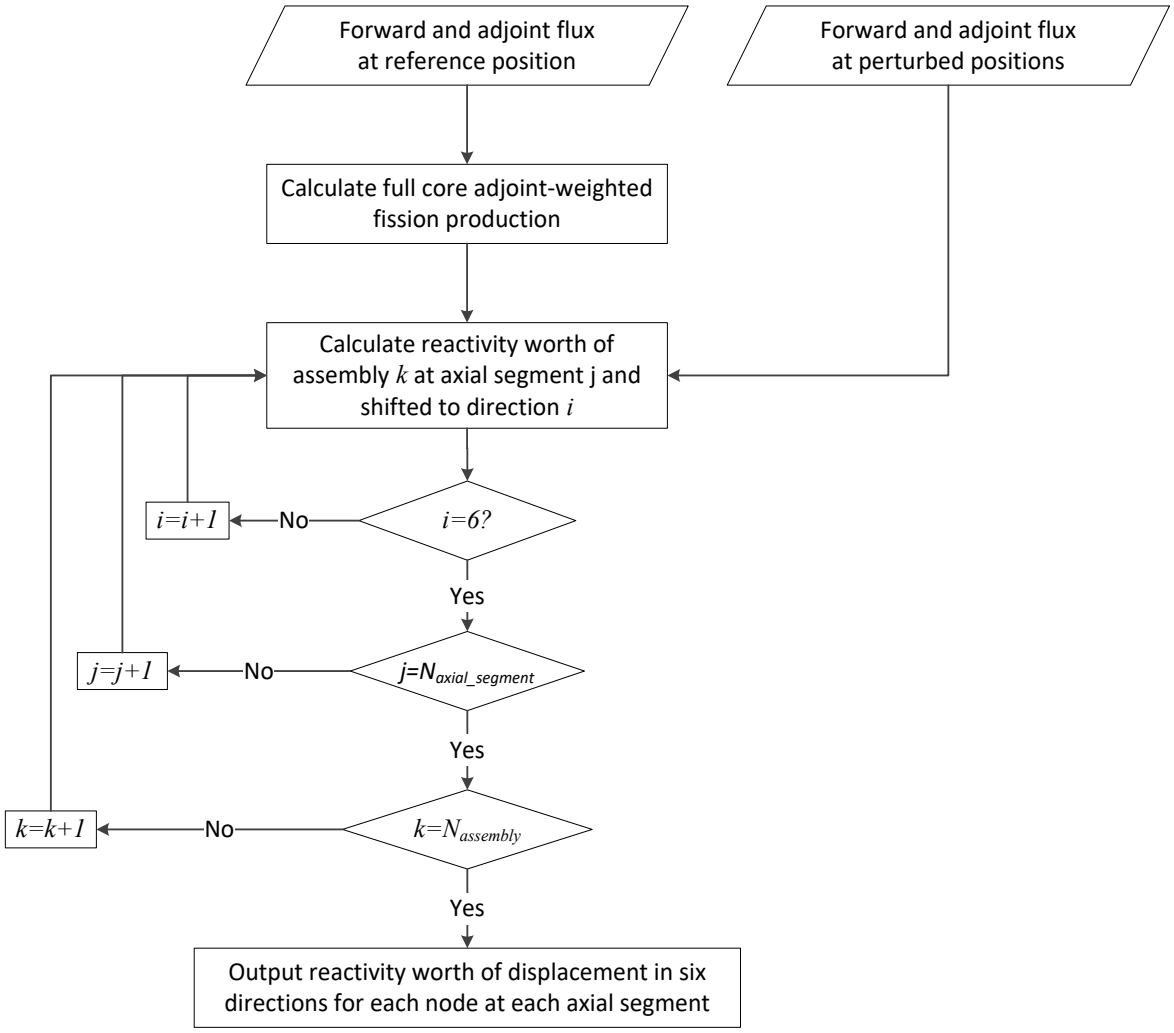

Fig. 5.8 Procedures for Perturbation Calculation of Reactivity Changes Due to Assembly Displacements

Table 5.1. Descriptions of the ProblemSpecs Block

Keyword	Type	Description
Problem%UseFormFunction	Logical	.TRUE. indicates the global flux will be corrected using local form functions. .FALSE. indicates use of global flux only (default)
problem%HexOption	Integer	=1 indicates one-third core model =0 indicates full core model
Problem%keffective	Real	Multiplication factor from VARIANT solution. (default=1.0)
Problem%NumGroup	Integer	Number of energy group
Problem%Dims	Integer	Number of problem dimension
Problem%NumMatZone	Integer	Number of material zones
Problem%ScatOrder	Integer	Legendre order used for expanding the scattering source
Problem%MomentOrder	Integer	Legendre order used for expanding the angular fluxes
Problem%NumAssembly	Integer	Total number of assemblies in the core module
Problem%NumActiveAssembly	Integer	Number of assemblies for perturbation calculations
Problem%NumAssemblyType	Integer	Number of difference assembly types
Problem%AssemblyMap(:,:)	Integer	The arrangement of active assemblies, inactive assemblies are specified as 0.

Table 5.2. Descriptions of the AssemblySpecs Block

Keyword	Type	Description
Shift	Real	Distance of each assembly segment being displaced (cm)
Axial Symmetry	Logical	.TRUE. indicates the core is axially symmetric and only half of the core will be calculated. .FALSE. indicates there is no axial symmetry and the calculation is performed for the full core (default)
NumSegments	Integer	Number of axial segments. If AxialSymmetry=.TRUE., The number of axial segments is for the one-half core
Zcenter(1:NumSegments)	Real	Axial coordinates for each axial segment
Zlength(1:NumSegments)	Real	Axial length of each axial segment
The following data repeats for each assembly type i		
Assembly(i)%Active	Logical	.TRUE. indicates the current assembly type is included in the perturbation calculations .FALSE. indicates skip the current assembly type, use only for non-fuel assembly. (such as control, reflector, etc)
Assembly(i)%NumElement	Integer	Number of finite element in the assembly
Assembly(i)%NumRegions	Integer	Number of regions in current assembly type, such as fuel, duct, gap sodium.
Assembly(i)%NumMoveRegions	Integer	Number of regions to be shifted, typically equals to Assembly(i)%NumRegions-1
Assembly(i)%NumVertex	Integer	Number of finite element vertices in the assembly
Assembly(i)%MatZone(1: NumSegments)	Integer	Assignment file identification for each axial segment. The value follows the order of assignment files specified in ASSIGNMENT_File in &InterfaceFiles Block

Table 5.3. Descriptions of the InterfaceFiles Block

Keyword	Type	Description
PROTEUS_Interface%ForwardFlux	Character	File name of form function of forward flux
PROTEUS_Interface%AdjointFlux	Character	File name of form function of adjoint flux
PROTEUS_Interface%GlobalID	Character	File name of globalid
PROTEUS_Interface%Mesh	Character	File name of Vetex position
PROTEUS_Interface%Assignment	Character	Assignment input file name adopted from PROTEUS calculation
VARIANT_Interface%ISOTXS	Character	File name for the ISOTXS dataset generated from MC^3-2 code
VARIANT_Interface%NHFLUX	Character	File name for the NHFLUX dataset generated from VARIANT code
VARIANT_Interface%NAFLUX	Character	File name for the NAFLUX dataset generated from VARIANT code
VARIANT_Interface%GEODST	Character	File name for the GEODST dataset generated from VARIANT code
ASSIGNMENT_File(1: problem%NumMatZone+1)	Character	Assignment file names for each material zones. The last assignment file specifies all regions filled with sodium.

5.4.3.2. Interface Files

The RAINBOW code inherent the material assignment file (*.assignment) from PROTEUS-SN calculation to define the core compositions. The material assignment file has three blocks. Table 5.4 presents a sample format of the material assignment file. The first block that starts with keyword 'MATERIAL_DEF' is used to define materials based on isotopes in ISOTXS file. The second block that starts with keyword 'REGION_ALIAS' associates the material defined in the first block to the corresponding blocks defined in the mesh files. The third block that starts with the keyword 'REGION_PROPERTY' gives the atom density to the materials defined in the first block in the unit of atoms/barn-cm with the keyword 'ATOM_DENSITY'. More detailed description of the material assignment file can be found in the User' manual of PROTEUS-SN code. [11]

The material assignment files used in the RAINBOW calculations are for individual assembly segments with different design or material compositions. One additional assignment file with all regions filled with sodium is also required for modeling the relocation of inter-assembly gap sodium as the assembly duct is shifted.

Table 5.4. Format of Material Assignment File

```
!************************************************************
! Definition of Materials/Compositions
!************************************************************
MATERIAL_DEF  FUEL              NA23IE   5.34303E-03
MATERIAL_DEF  FUEL              FE54IE   4.19650E-04
.                                 .          .
.                                 .          .
.                                 .          .
MATERIAL_DEF  FUEL              ZR96IE   1.28332E-04
MATERIAL_DEF  FUEL_DUCT         FE54IE   4.12729E-03
MATERIAL_DEF  FUEL_DUCT         FE56IE   6.47890E-02
.                                 .          .
.                                 .          .
.                                 .          .
MATERIAL_DEF  FUEL_DUCT         MO10IE   4.78009E-05
MATERIAL_DEF  FUEL_COOL         NA23IE   2.19776E-02
!************************************************************
! Assignment of Blocks to Materials
!************************************************************
REGION_ALIAS    REGION_000000001 FUEL
REGION_ALIAS    REGION_000000002 FUEL_DUCT
REGION_ALIAS    REGION_000000003 FUEL_COOL
!************************************************************
! Assignment of Material Property to Blocks
!************************************************************
REGION_PROPERTY  REGION_000000001    ATOM_DENSITY    3.41402E-02
REGION_PROPERTY  REGION_000000002    ATOM_DENSITY    8.25074E-02
REGION_PROPERTY  REGION_000000003    ATOM_DENSITY    2.19776E-02
```

The form functions are outputs from the utility program of post-processing of PROTEUS-SN HDF5 output file. The format of this file is shown in Table 5.5. The first column is

identification number of finite elements. The second column is the block number that the specific element is belongs. In the example shown in Table 5.5, there are three blocks representing fuel, duct and inter-assembly gap sodium. The following columns are averaged group-wise fluxes in each element. It is noted that even though the purpose of this file is to provide form functions, while no flux normalization is needed. The data in this file contains the absolute values of the element-averaged fluxes. The normalization is performed within the RAINBOW code.

Table 5.5. Format of Form Function File

ELEMENT	BLOCK	GROUP 1	GROUP 2	GROUP …	GROUP 33
1	1	4.33482E+06	7.85761E+07	…	8.07855E+08
2	1	4.34936E+06	7.88658E+07	…	8.09732E+08
3	1	4.42416E+06	8.02017E+07	…	8.17610E+08
.	.	.	.	.	.
.	.	.	.	.	.
.	.	.	.	.	.
1593	2	4.23590E+06	7.66593E+07	…	7.96168E+08
.	.	.	.	.	.
.	.	.	.	.	.
.	.	.	.	.	.
1881	3	4.23234E+06	7.65886E+07	…	3.20722E+03
.	.	.	.	.	.
.	.	.	.	.	.
.	.	.	.	.	.
2168	3	4.30825E+06	7.81620E+07	…	8.05504E+08

The vertex position file is also an output from the utility program of post-processing the PROTEUS-SN HDF5 output file. The format of this file is presented in Table 5.6. The x and y coordinates are defined in local reference of a single assembly. The origin is located at the center of an assembly. Fig. 5.9 displays one example of all the vertices of finite elements scattered within the domain of a single assembly. The connection information among these vertices are provided in the GlobalID file that will be described in the next section.

Table 5.6. Format of Vertex Position File

VertexID	x	y
1	6.21300E+00	5.47501E+00
2	5.88600E+00	5.66381E+00
3	5.85188E+00	5.29993E+00
.	.	.
1444	8.22940E+00	-4.35531E+00
1445	8.30880E+00	-4.39733E+00

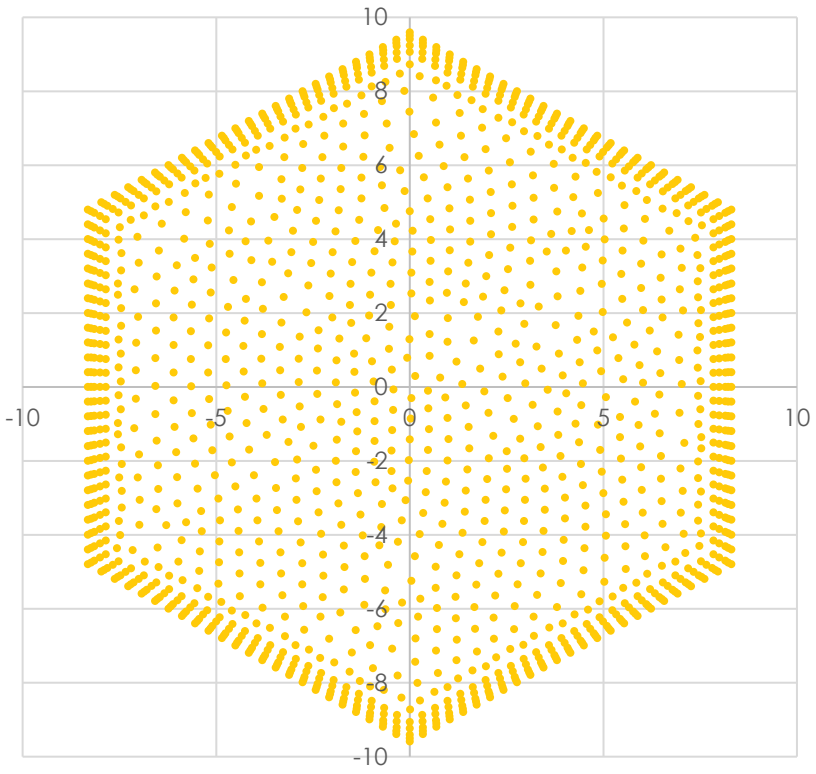

Fig. 5.9 Vertices of Finite Element Mesh for Single Assembly

Table 5.7. Format of GlobalID File

ELEMENT	NumVertex	VertexID			
1	3	25	26	27	
2	3	26	40	27	
3	3	60	61	62	
.	.	.	.	.	
.	.	.	.	.	
.	.	.	.	.	
1593	4	962	963	965	964
1594	4	964	965	967	966
.	.	.	.	.	.
.	.	.	.	.	.
.	.	.	.	.	.
2167	4	1403	1402	1404	1405
2168	4	1402	1115	1117	1404

5.4.3.3. Output File

The main output file contains the directional reactivity worth of each shifted assembly segment by a user specified distance. The numbering of the assembly follows the NHFLUX ordering as shown in Fig. 5.6 and Fig. 5.7 for full core and one-third core geometry. The reactivity maps repeat for each axial segment. The ordering of the axial segment is from the bottom level to the top level. The six directions of displacement are in counterclockwise ordering. The progress of execution of the RAINBOW code and the timing information are displayed on the screen. Table 5.9 shows a screen shot of such output.

Table 5.8. Format of Main Output File

```
          ************** DIRECTIONAL REACTIVITY WORTH OF ASSEMBLY DISPLACEMENT **************
SEGMENT 1
                   Direction 1    Direction 2    Direction 3    Direction 4    Direction 5    Direction 6
ASSEMBLY   1        0.00032        0.00031        0.00031        0.00032        0.00031        0.00031
ASSEMBLY   2       -0.00064       -0.00020        0.00069        0.00116        0.00069       -0.00020
ASSEMBLY   3       -0.00020       -0.00063       -0.00020        0.00069        0.00115        0.00069
ASSEMBLY   4        0.00062        0.00042        0.00003       -0.00015        0.00003        0.00041
ASSEMBLY   5        0.00002        0.00003        0.00023        0.00043        0.00043        0.00022
.
.
.
SEGMENT 2
                   Direction 1    Direction 2    Direction 3    Direction 4    Direction 5    Direction 6
ASSEMBLY   1       -0.00001       -0.00001       -0.00001       -0.00001       -0.00001       -0.00001
ASSEMBLY   2       -0.00357       -0.00169        0.00319        0.00627        0.00319       -0.00169
.
.
.
ASSEMBLY  72       -0.00000        0.00022        0.00023        0.00002       -0.00020       -0.00021
ASSEMBLY  73       -0.00006        0.00019        0.00026        0.00007       -0.00018       -0.00024
```

Table 5.9. Sample Output Displayed on Screen

```
Read RAINBOW input...
  Time used for reading input                              =    0.00 sec

Load VARIANT solutions NHFLUX and NAFLUX...
  Time used for loading NHFLUX/NAFLUX                      =    59.30 sec

Calculate macroscopic cross sections for each heterogeneous region...
 number of isotopes =        1136
  Time used for calculating macroscopic cross section      =    0.09 sec

Load PROTEUS-SN Solutions...
  Time used for loading PROTEUS-SN solutions               =    0.14 sec

 ---------------------
 SEGMENT           1
 ---------------------

Seg  1 ass   1 base flux evaluation ( 0.65 sec)
Seg  1 ass   1 dir 1 perturbed flux evaluation ( 0.66 sec)
Seg  1 ass   1 dir 1 bilinearly weight reaction rates calculation ( 0.52 sec)
Seg  1 ass   1 dir 2 perturbed flux evaluation ( 0.68 sec)
Seg  1 ass   1 dir 2 bilinearly weight reaction rates calculation ( 0.51 sec)
Seg  1 ass   1 dir 3 perturbed flux evaluation ( 0.65 sec)
Seg  1 ass   1 dir 3 bilinearly weight reaction rates calculation ( 0.51 sec)
Seg  1 ass   1 dir 4 perturbed flux evaluation ( 0.64 sec)
Seg  1 ass   1 dir 4 bilinearly weight reaction rates calculation ( 0.51 sec)
Seg  1 ass   1 dir 5 perturbed flux evaluation ( 0.64 sec)
Seg  1 ass   1 dir 5 bilinearly weight reaction rates calculation ( 0.51 sec)
Seg  1 ass   1 dir 6 perturbed flux evaluation ( 0.65 sec)
```

Table 5.9. Sample Output Displayed on Screen (continued)

```
Seg  1 ass   1 dir 6 bilinearly weight reaction rates calculation ( 0.51 sec)

Seg  1 ass   2 base flux evaluation ( 0.66 sec)
Seg  1 ass   2 dir 1 perturbed flux evaluation ( 0.68 sec)
Seg  1 ass   2 dir 1 bilinearly weight reaction rates calculation ( 0.51 sec)
Seg  1 ass   2 dir 2 perturbed flux evaluation ( 0.69 sec)
Seg  1 ass   2 dir 2 bilinearly weight reaction rates calculation ( 0.51 sec)
Seg  1 ass   2 dir 3 perturbed flux evaluation ( 0.68 sec)
Seg  1 ass   2 dir 3 bilinearly weight reaction rates calculation ( 0.52 sec)
Seg  1 ass   2 dir 4 perturbed flux evaluation ( 0.67 sec)
Seg  1 ass   2 dir 4 bilinearly weight reaction rates calculation ( 0.51 sec)
Seg  1 ass   2 dir 5 perturbed flux evaluation ( 0.65 sec)
Seg  1 ass   2 dir 5 bilinearly weight reaction rates calculation ( 0.51 sec)
Seg  1 ass   2 dir 6 perturbed flux evaluation ( 0.65 sec)
Seg  1 ass   2 dir 6 bilinearly weight reaction rates calculation ( 0.51 sec)
.
.
.

Calculate adjoint weighted fission production...
 Time used for calculating adjoint weighted fission production =    0.64 sec

---------------------
SEGMENT           2
---------------------

Seg  2 ass   1 base flux evaluation ( 0.66 sec)
Seg  2 ass   1 dir 1 perturbed flux evaluation ( 0.68 sec)
Seg  2 ass   1 dir 1 bilinearly weight reaction rates calculation ( 0.51 sec)
Seg  2 ass   1 dir 2 perturbed flux evaluation ( 0.68 sec)
Seg  2 ass   1 dir 2 bilinearly weight reaction rates calculation ( 0.51 sec)
Seg  2 ass   1 dir 3 perturbed flux evaluation ( 0.65 sec)
Seg  2 ass   1 dir 3 bilinearly weight reaction rates calculation ( 0.52 sec)
Seg  2 ass   1 dir 4 perturbed flux evaluation ( 0.64 sec)
Seg  2 ass   1 dir 4 bilinearly weight reaction rates calculation ( 0.51 sec)
Seg  2 ass   1 dir 5 perturbed flux evaluation ( 0.64 sec)
Seg  2 ass   1 dir 5 bilinearly weight reaction rates calculation ( 0.51 sec)
Seg  2 ass   1 dir 6 perturbed flux evaluation ( 0.65 sec)
Seg  2 ass   1 dir 6 bilinearly weight reaction rates calculation ( 0.51 sec)
.
.
.
Calculate bowing reactivity coefficients...
 Time used for calculating bowing reactivity coefficients =   0.00 sec

Write output...
 Time used for writing output =    0.00 sec

Job has completed successfully !
-----------------------------------------------------
Flux evaluation time                      = 4194.2 sec
Reaction rate integral calculation time   = 2560.8 sec
Total time                                = 6814.6 sec
```

5.5. Verification of RAINBOW Code

5.5.1. Mini-Core Problem

Benchmark calculations of the RAINBOW code for perturbation theory calculation of reactivity changes due to assembly displacements were performed using both 2D and 3D mini-core models. The reactivity change was calculated for an assembly (or an assembly axial segment) displacement by 2 mm in each of six directions normal to the duct wall surfaces. Reference solutions were obtained from MCNP6 Monte Carlo simulations by the difference in eigenvalue between the perturbed and unperturbed cases.

The mini-core models were derived from the ABTR design by reducing the number of assemblies. The 2D core models were obtained from the core configuration at the mid-plane. Two mini-core configurations were developed in this study as shown in Fig. 5.10. The mini-core model A consists of three rings of fuel assemblies, three rings of reflector assemblies and one ring of shield assemblies. The mini-core model B consists of four rings of fuel assemblies, two rings of reflector assemblies and one ring of shield assemblies. In the fuel region, three control assemblies are located in the third ring. A 3D mini-core model was developed by extruding the 2D mini-core model A in axial direction by 100 cm.

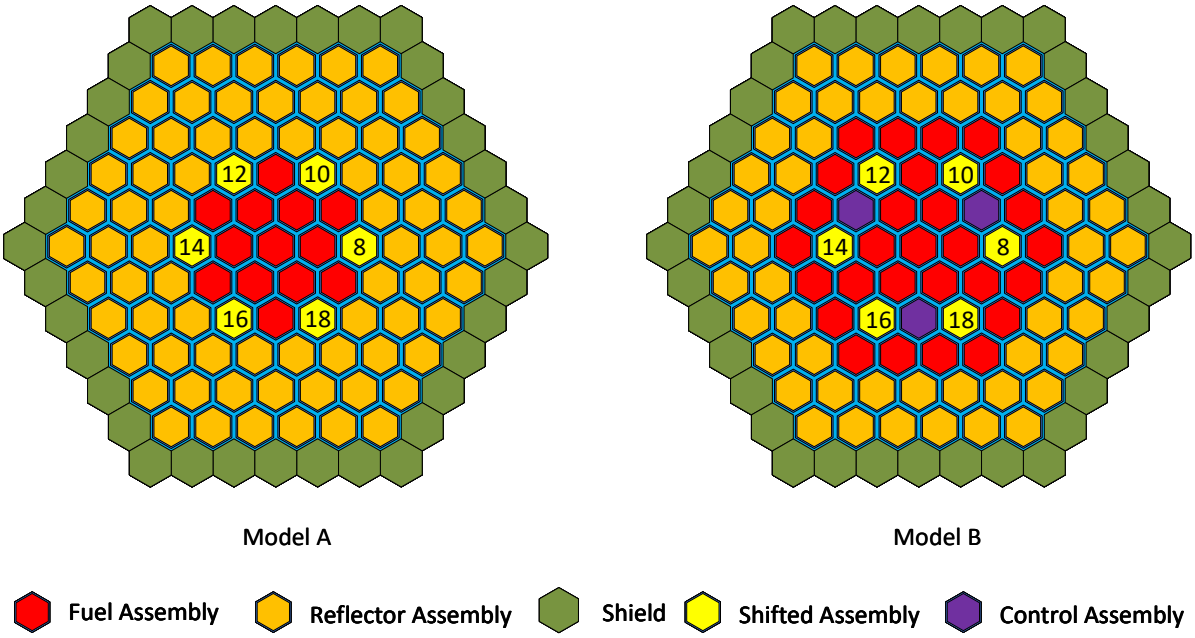

Fig. 5.10 Radial Layouts of Mini-core Models without (A) and with (B) Control Assemblies

Using the MC^2-3 code and the ENDF/B-VII.0 cross section library, a set of 33-group cross sections was generated for each of the mini-core model A, the mini-core model B with control assemblies in, and the mini-core model B with control assemblies out. In each MC^2-3 calculation, self-shielded 2082-group isotopic cross sections were first prepared for each region. Then, 2082-group transport calculations were performed for a whole-core R-Z geometry models (as shown in Fig. 5.11) using the discrete ordinate transport code TWODANT. For the case of mini-core model B with control assembly in or out, two separate TWODANT calculations were performed. In one calculation, the control absorber (or sodium

coolant) were homogenized with fuel to obtain accurate spectra for the fuel, reflector and shield regions. In the other calculation, the control absorber (or sodium) and fuel mixture region was filled with pure absorber (or sodium) to yield accurate spectrum for the control assembly region. Finally, region-dependent 33-group cross sections were determined by condensing the 2082-group cross sections of each region using the 2082-group TWODANT flux solutions.

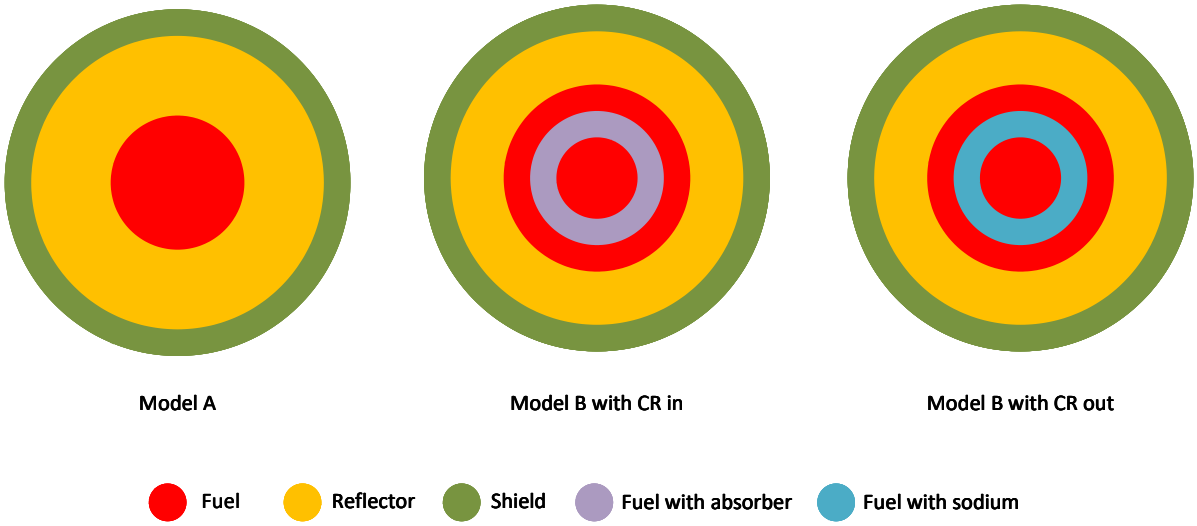

Fig. 5.11 TWODANT Models for Mini-core Models

The multiplication factors for the unperturbed base configurations of the mini-core models were calculated using the VARIANT code and compared with the reference MCNP6 results. Two cases were considered for the mini-core model B: one with three B_4C control assemblies in and the other with control assemblies out. In the case of control assemblies out, the control assembly positions are filled with sodium. The MCNP6 simulations were performed with 1,000,000 particles per cycle, and 800 inactive and 2000 active cycles. For each core configuration, two MCNP6 calculations were performed: one with homogenized assembly model and the other with the partially heterogeneous assembly model. One standard deviation of the resulting eigenvalue reported by the MCNP6 code was one pcm for all calculations. The VARIANT calculations were performed with 6th order polynomial approximations for the intra-nodal flux and source distributions and a quadratic polynomial approximation for the nodal interface current distribution. A P_5 angular approximation of flux was used with an anisotropic scattering order of 5.

The resulting multiplication factors for 2D and 3D mini-core models are summarized in Table 5.10. The difference in multiplication factor between the VARIANT and MCNP6 results is mainly due to the assembly heterogeneity effects, since the VARIANT calculations were performed with fully homogenized assemblies while MCNP6 calculations were done with partially homogenized assemblies where the assembly duct and the inter-assembly sodium are explicitly modeled. It is noted that the 3D mini-core models were deeply subcritical with original ABTR assembly composition due to large leakage. The Pu-239 faction in the fuel was increased from 14% to 19% to yield a critical 3D mini-core models. The multiplication factors for critical 3D mini-core models are summarized in Table 5.11.

Table 5.10 Multiplication Factors for Mini-core Models Calculated by VARIANT and MCNP6 with ABTR Assembly Composition

	VARIANT	MCNP6	Difference, pcm
2D Mini-core A	1.00419	1.00918±0.00001	-499
2D Mini-core B with CR in	0.99252	0.99281±0.00001	-29
2D Mini-core B with CR out	1.11077	1.11131±0.00001	-54
3D Mini-core A	0.85347	0.85512±0.00001	-165
3D Mini-core B with CR in	0.85578	0.85407±0.00001	171
3D Mini-core B with CR out	0.92119	0.91991±0.00001	128

Table 5.11 Multiplication Factors for Critical 3D Mini-Core Models Calculated by VARIANT and MCNP6

	VARIANT	MCNP6	
		Homogenous	Heterogeneous
3D Mini-Core A	1.00726	1.00691	1.00952
3D Mini-Core B with CR in	0.93539	0.93288	0.93568
3D Mini-Core B with CR out	1.00508	1.00427	1.00652

5.5.1.1. Perturbation Theory Calculation Results of 2D Problems

The first set of tests was performed using the mini-core model A. The displacement worth of the assembly 8 (according to the NHFLUX node ordering shown in Fig. 5.6) was calculated by shifting the assembly by 2 mm from its origin in each of the six directions normal to the duct wall surfaces (see Fig. 5.12). Table 5.12 compares the reactivity worths from RAINBOW perturbation calculation and MCNP6 eigenvalue subtractions.

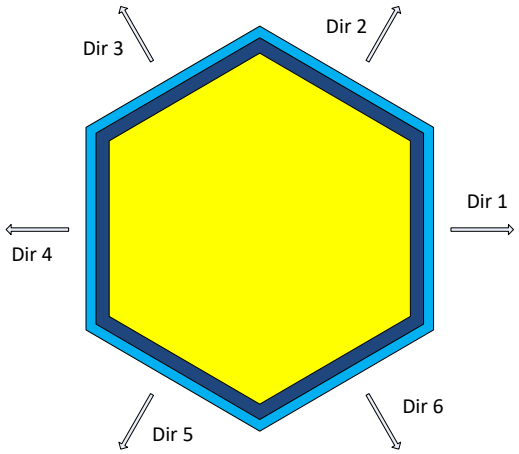

Fig. 5.12 Assembly Displacements in Six Directions

Table 5.12 Comparison of RAINBOW and MCNP6 Reactivity Changes of Fuel Assembly Displacements in the Third Ring of Mini-core Model (a)

Assembly Displacement	RAINBOW	MCNP6
Assembly 8 Shifted in Direction 1	-19.16	-15.71±1.4
Assembly 8 Shifted in Direction 2	-9.62	-7.86±1.4
Assembly 8 Shifted in Direction 3	9.53	11.78±1.4
Assembly 8 Shifted in Direction 4	19.15	19.63±1.4
Assembly 8 Shifted in Direction 5	9.53	11.78±1.4
Assembly 8 Shifted in Direction 6	-9.63	-7.86±1.4
Assemblies 8, 10, 12, 14, 16 and 18 Shifted Outwards	-114.94	-108.13±1.4
Assemblies 8, 10, 12, 14, 16 and 18 Shifted Inwards	114.89	112.79±1.4

It can be seen that the assembly displacement worths predicted by RAINBOW agree well with the MCNP6 results. The maximum reactivity worth in magnitude is obtained when the assembly is shifted in the direction 1 (outward from the core center) and in the direction 4 (inward toward the core center). The MCNP6 results show that the displacement worth for the inward direction is larger in magnitude than that for the outward direction by about 3 standard deviations, suggesting that the flux gradient in the inner side of the assembly 8 is larger than that in the outer side of the assembly 8. On the other hand, the RAINBOW results show similar magnitudes for these two directions.

To introduce a larger perturbation and thus reduce the MCNP6 statistical error, the reactivity worth was calculated by shifting the six assemblies at the third ring. As shown in Table 6.4, the MCNP6 result is -108.13±1.4 pcm for the outward shift and 112.79±1.4 pcm for the inward shift. The absolute values are very close to each other. This indicates that the observed difference in displacement worth between the inward and outward shifts of the assembly 8 resulted from the MCNP6 statistical error. The RAINBOW perturbation calculation result is -114.94 pcm for the outward shift and 114.89 pcm for the inward shift, which agree very well with the MCNP6 results. The perturbation calculation slightly overestimates the reactivity worth in magnitude due to the first order perturbation approximation under which the interaction effects of multiple assembly shifts were neglected.

Additional perturbation calculations were made with inward displacements of the assembly 8 by 1.2 mm, 1.6 mm and 2.0 mm. The reactivity worth results of MCNP6 and RAINBOW calculations are compared in Fig. 5.13. It can be seen that the RAINBOW results agree well with the MCNP6 results and that the reactivity worth of assembly displacement increases in proportional to the amount of displacement for these small perturbations.

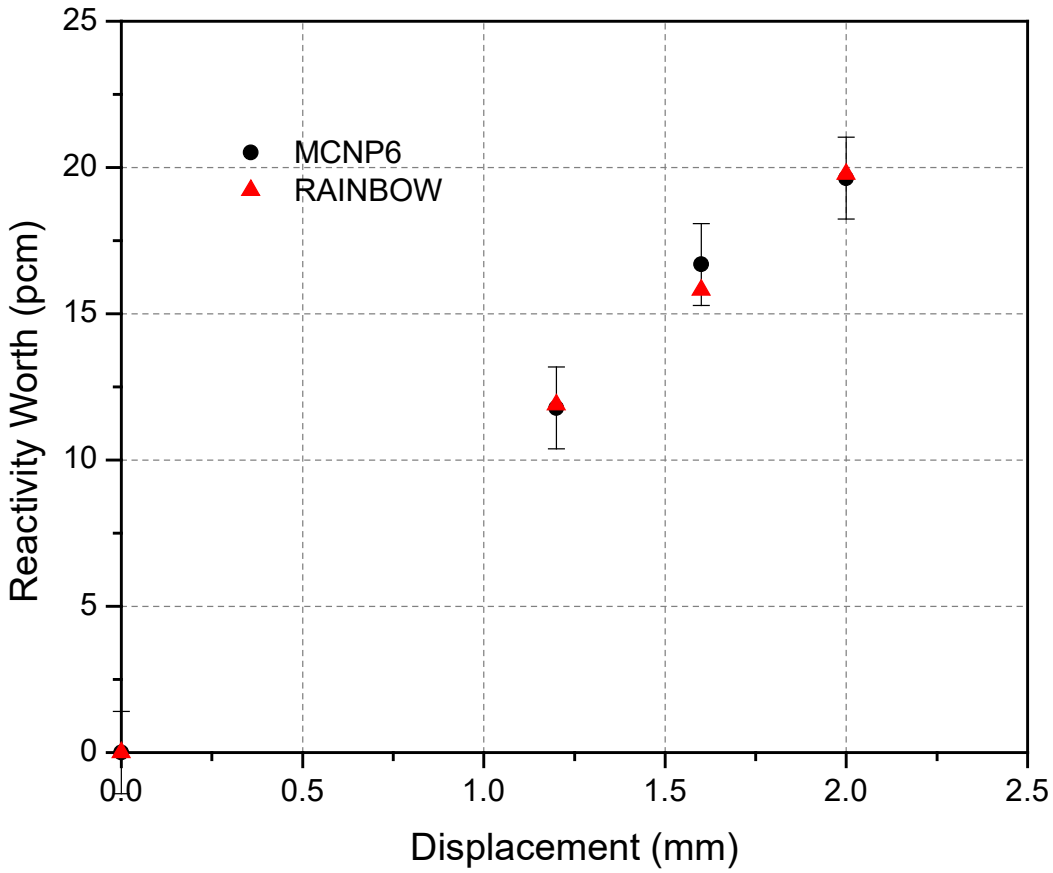

Fig. 5.13 Comparison between MCNP6 and RAINBOW Results with Different Amount of Displacements

A second set of tests were performed using the mini-core model B, which provides more heterogeneous configuration in the fuel region. Using the RAINBOW and MCNP6 codes, the reactivity change due to displacement was calculated for the assemblies 2, 8 and 20 (see the NHFLUX node ordering shown in Fig. 5.6) by displacing each of these assemblies by 2 mm. The MCNP6 solutions were obtained to yield one pcm standard deviation in the multiplication factor to minimize the effect of Monte Carlo statistical uncertainties. As a result, the standard deviation for the reactivity change is 1.4 pcm. Table 5.13 compares the reactivity changes due to assembly displacement obtained from RAINBOW and MCNP6 calculations for the configuration of control assemblies out. The three control assembly positions are filled with sodium. The RAINBOW results show good agreement with the MCNP6 results. For most of the cases, the difference from the MCNP6 result is within one or two standard deviation of the MCNP6 results.

Table 5.14 shows a statistical analysis of the results. Among the total 18 reactivity changes, 12 RAINBOW values (i.e., 67%) agree with the MCNP6 results within one standard deviation, 17 values (i.e., 94%) agree within two standard deviations, and all 18 values agree within three standard deviations. This distribution of the RAINBOW results is close to the normal distribution, indicating that the improved RAINBOW results are statistically consistent with the MCNP6 results.

Table 5.13 Comparison of RAINBOW and MCNP6 Reactivity Changes of Assembly Displacements in the Third Ring of Mini-core Model B with Control Assembly Out

Assembly	Method	Dir 1	Dir 2	Dir 3	Dir 4	Dir 5	Dir 6
2	MCNP6	-4.86	-1.62	4.86	6.48	2.43	-3.24
	RAINBOW	-4.99	-2.99	1.98	4.94	2.94	-2.02
8	MCNP6	-4.86	-3.24	1.62	7.29	4.05	-1.62
	RAINBOW	-5.59	-3.76	1.80	5.57	3.73	-1.88
20	MCNP6	-4.86	-4.86	3.24	8.10	4.05	-3.24
	RAINBOW	-6.26	-3.16	3.11	6.27	3.15	-3.12

Table 5.14 Statistical Analysis of RAINBOW Results with Respect to MCNP6 Standard Deviations for Mini-core Model B with Control Assembly Out

	< 1 sigma	< 2 sigma	< 3 sigma
Number of cases	12	17	18
Percentage of cases	67%	94%	100%
Probability in normal distribution	68%	95%	99%

The reactivity change due to assembly displacement was also calculated for the case with control rod inserted, which allows larger variations in the flux distributions. Table 5.15 compares the RAINBOW and MCNP6 results for the displacements of assemblies 2, 8 and 20. The RAINBOW results agree well with the MCNP6 results. Table 5.16 shows the statistical analysis of the RAINBOW results with respect to the MCNP6 standard deviations. Nine RAINBOW values (i.e., 50%) agree with the MCNP6 results within one standard deviation, 16 values (i.e., 89%) agree within two standard deviations, and all 18 values (i.e. 100%) agree within three standard deviations, indicating the RAINBOW results are statistically consistent with the MCNP6 results.

Fig. 5.14 shows the reactivity map of assembly displacement for all the fuel assemblies generated by RAINBOW calculations. It is noted that a negative reactivity is induced due to enhanced leakage and reduced fission productions when a fuel assembly is shifted outward from the core center. In general, the assembly displacement worth decreases (i.e., become more negative) as the location moves from the core center to the core periphery because the global flux gradient is larger near the core periphery. The variations in local flux distribution resulting from the control assemblies also affect the assembly displacement worth.

Table 5.15 Comparison of RAINBOW and MCNP6 Reactivity Changes of Assembly Displacements in the Third Ring of Mini-core Model B with Control Assembly In

Assembly	Method	Dir 1	Dir 2	Dir 3	Dir 4	Dir 5	Dir 6
2	MCNP6	-7.10	-3.04	6.09	9.13	5.07	-1.01
	RAINBOW	-8.02	-3.40	4.55	7.93	3.39	-4.61
8	MCNP6	-11.16	-7.10	3.04	10.14	8.12	2.03
	RAINBOW	-10.51	-9.05	1.53	10.61	8.98	-1.55
20	MCNP6	-8.12	-4.06	4.06	9.13	7.10	-2.03
	RAINBOW	-7.97	-5.58	2.36	7.97	5.58	-2.42

Table 5.16 Statistical Analysis of RAINBOW Results with Respect to MCNP6 Standard Deviations for Mini-core Model B with Control Assembly In

	< 1 sigma	< 2 sigma	< 3 sigma
Number of cases	9	16	18
Percentage of cases	50%	89%	100%
Probability in normal distribution	68%	95%	99%

5.5.1.2. Perturbation Theory Calculation Results of 3D Problems

Numerical tests were also performed for the 3D perturbation theory calculation capability of the RAINBOW code using a 3D configuration obtained by extruding the 2D mini-core A. The assembly was 100 cm in height and was divided into multiple axial segments as illustrated in Fig. 5.15. Based on the good linearity observed on the binearly-weighted reaction rates shown in Fig. 5.16, a relatively large axial mesh sized of 10 cm was selected for the perturbation calculations. The perturbation calculations were performed for the upper five axial segments of the assembly, since the results for the lower half of the assembly will be exactly the same as the upper one due to the symmetry.

Reactivity changes were calculated for the displacement of the upper five axial segments of one or six assemblies in the third ring (assemblies 8, 10, 12, 14, 16 and 18 in Fig. 5.4). Table 5.17 compares the reactivity changes obtained from RAINBOW perturbation calculations and MCNP6 eigenvalue calculations for assembly 8. The results show limited agreement with MCNP6 reference results mainly due to the MCNP6 statistical uncertainties since the displacement of single axial segment results in a tiny change in eigenvalue. As the distance of from the core center increases, the RAINBOW results decrease almost linearly due to the reduced fuel worth. However, this is hardly seen from the MCNP6 results since the reactivity change due to a single axial segment displacement is so small that it is comparable with MCNP6 standard deviations.

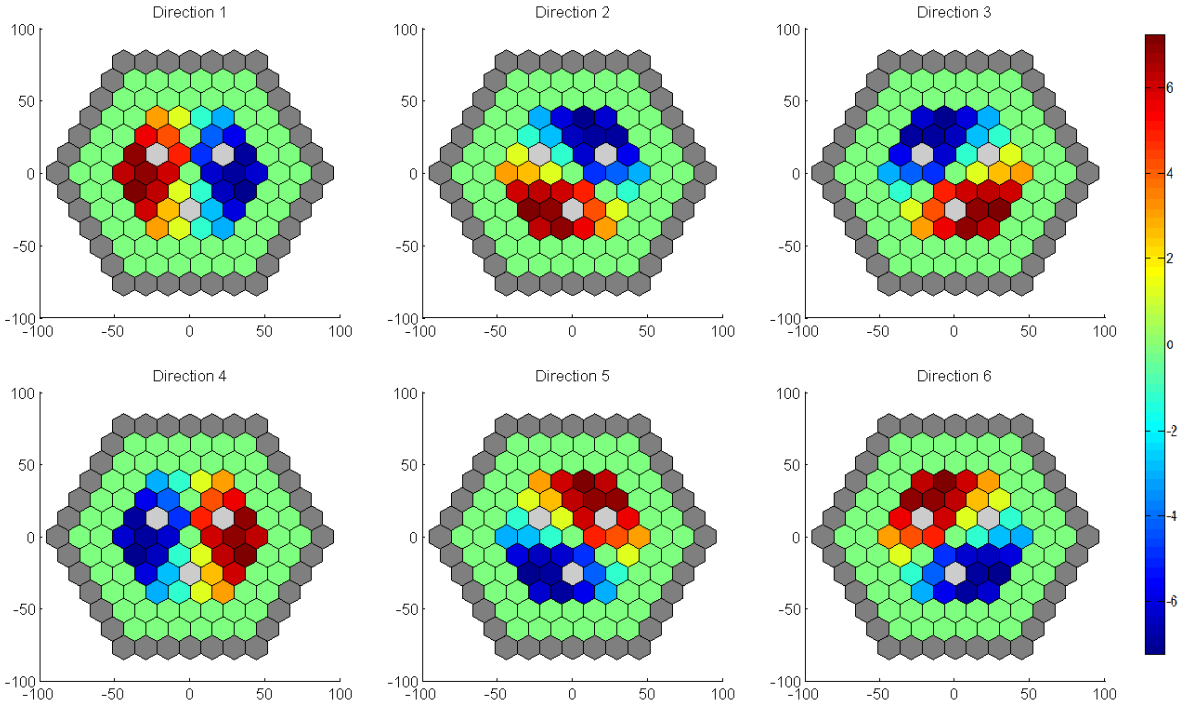

Fig. 5.14 Directional Reactivity Worth of Fuel Assemblies

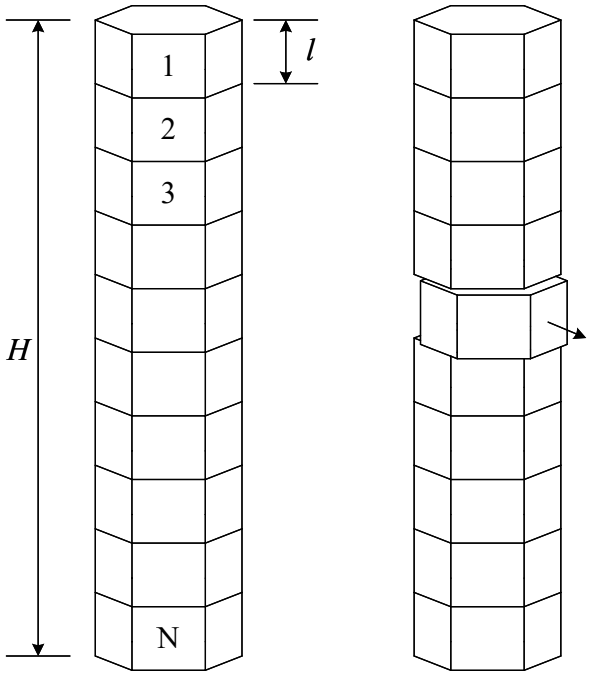

Fig. 5.15 Displacement of an Axial Segment of 3D Assembly Model

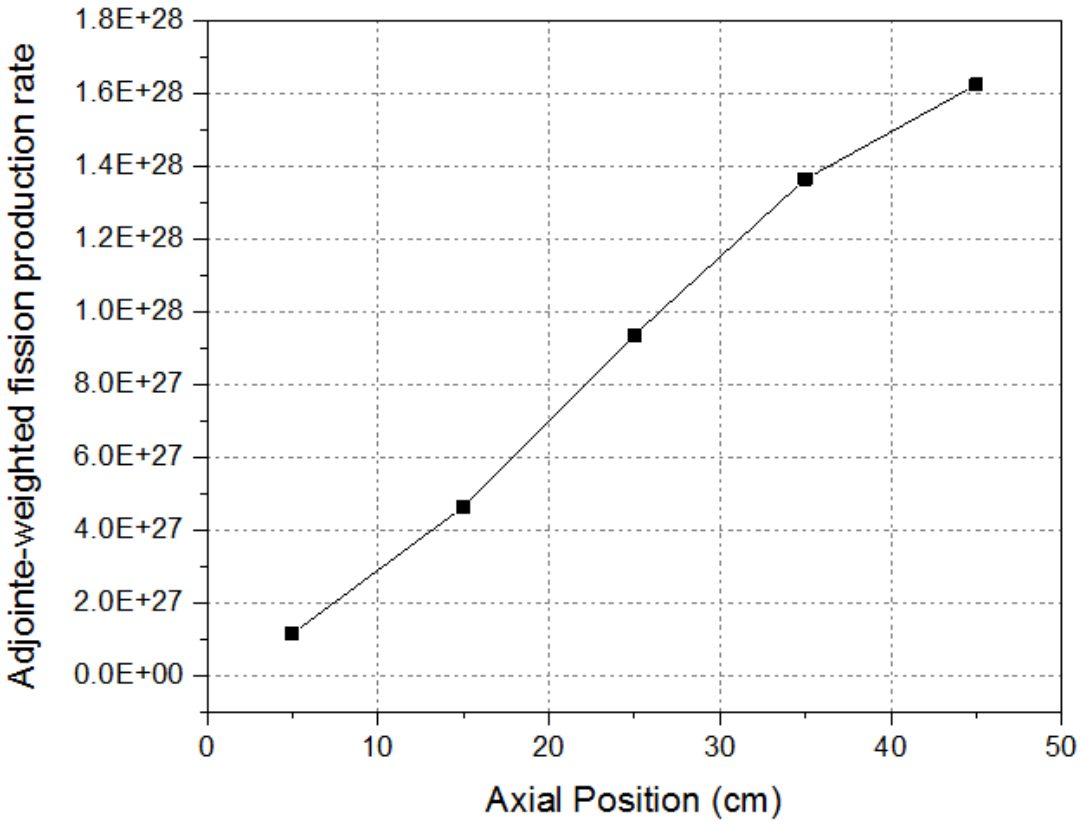

Fig. 5.16 Bilinear-weighted Fission Production Rate as a Function of Segment Axial Position

Table 5.17 Comparison of RAINBOW and MCNP6 Reactivity Changes of Single Assembly Axial Segment Displacements

	Assembly 8	
	RAINBOW	MCNP6
Segment 1	-1.31	-2.34±1.4
Segment 2	-2.24	1.17±1.4
Segment 3	-3.49	-3.51±1.4
Segment 4	-4.65	-3.51±1.4
Segment 5	-5.34	-4.68±1.4

In order to introduce a large perturbation relative to the standard deviation of MCNP6 results, the six assemblies were simultaneously shifted outward from the core center by 2 mm from their original positions. Table 5.18 to Table 5.20 compare the reactivity changes obtained from RAINBOW perturbation calculations with the MCNP6 results determined by the eigenvalue difference between the base and perturbed cases for the mini-core model A, the

mini-core model B with control assemblies in and the mini-core model B with control assemblies out, respectively. For most of the cases, the RAINBOW results agree with the reference MCNP6 results within two standard deviation of the MCNP6 results. However, the displacements of the segments 3 and 4 in the mini-core model B with control assemblies out show exceptionally large differences. These large errors appear to be due to the statistical uncertainties of the MCNP6 calculations since the MCNP6 results of these two cases deviate significantly from the linear trend of reactivity worth with respect to the distance from the core center as shown in Fig. 5.18, which can be deduced from the physical argument.

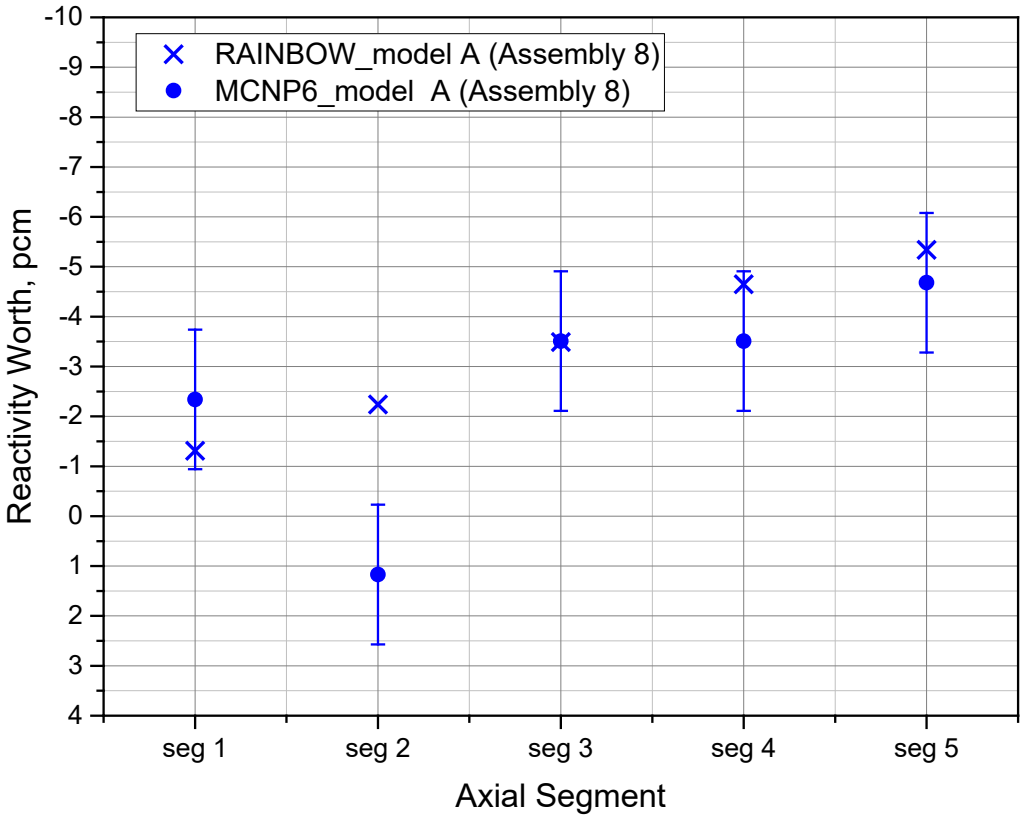

Fig. 5.17 Reactivity Worth Due to Displacement of Five Axial Segments

Table 5.18 Comparison of RAINBOW and MCNP6 Reactivity Changes for Axial Segment Displacements of Six Assemblies 8, 10, 12, 14, 16 and 18 in Mini-Core Model A

	RAINBOW, pcm	MCNP6, pcm	difference, pcm
Segment 1	-6.36	-7.85±1.40	-1.49
Segment 2	-10.98	-12.76±1.40	-1.78
Segment 3	-16.98	-17.67±1.40	-0.69
Segment 4	-22.62	-24.54±1.40	-1.92
Segment 5	-25.92	-23.56±1.40	2.36

Table 5.19 RAINBOW and MCNP6 Reactivity Changes for Axial Segment Displacements of Six assemblies 8, 10, 12, 14, 16 and 18 in Mini-Core Model B with Control Assemblies In

	RAINBOW, pcm	MCNP6, pcm	difference, pcm
Segment 1	-3.21	-4.57±1.51	-1.36
Segment 2	-6.23	-8.00±1.51	-1.76
Segment 3	-10.19	-11.42±1.51	-1.23
Segment 4	-13.90	-14.85±1.51	-0.95
Segment 5	-16.14	-15.99±1.51	0.14

Table 5.20 RAINBOW and MCNP6 Reactivity Changes for Axial Segment Displacements of Six assemblies 8, 10, 12, 14, 16 and 18 in Mini-Core Model B with Control Assemblies Out

	RAINBOW, pcm	MCNP6, pcm	difference, pcm
Segment 1	-3.87	-2.96±1.41	0.91
Segment 2	-5.73	-5.92±1.41	-0.19
Segment 3	-7.96	-4.94±1.41	3.02
Segment 4	-9.95	-5.92±1.41	4.03
Segment 5	-11.12	-10.86±1.41	0.26

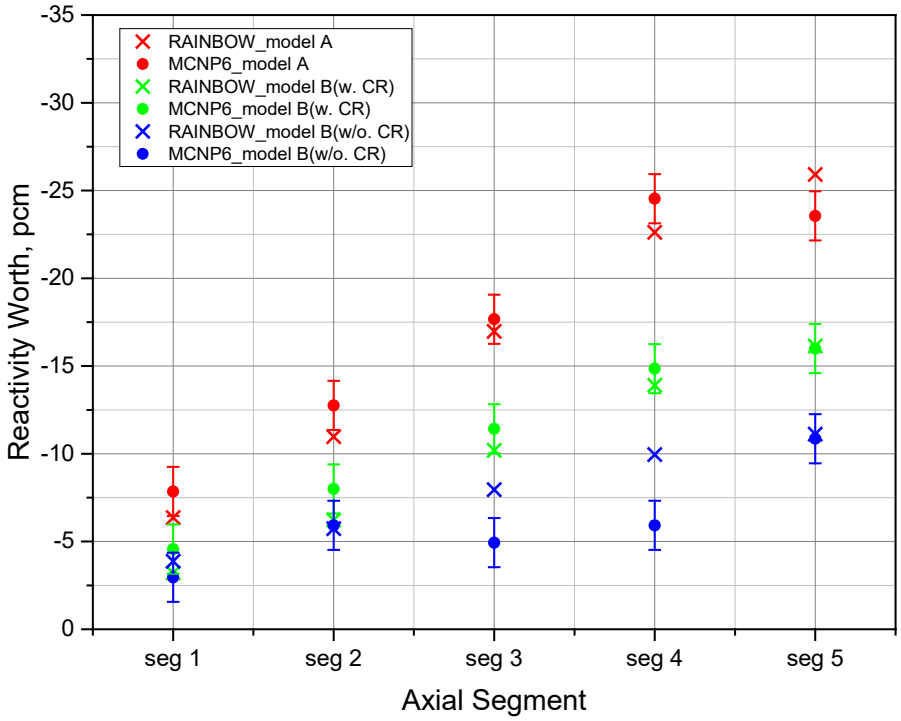

Fig. 5.18 Reactivity Worth Due to Displacement of Six Axial Segments

Table 5.21 shows a statistical analysis of RAINBOW results with respect to MCNP6 standard deviations. Among the total 15 reactivity changes, 8 RAINBOW values (i.e., 53%) agree with the MCNP6 results within one standard deviation, 13 values (i.e., 87%) agree within two standard deviations, and all 15 values agree within three standard deviations. This distribution of the RAINBOW results deviates somewhat from the normal distribution, indicating either a physical difference between the RAINBOW and MCNP6 results or the inaccurate uncertainties of the MCNP6 results.

Table 5.21 Statistical Analysis of RAINBOW Results with Respect to MCNP6 Standard Deviations

	<1 σ	<2 σ	<3 σ
Number of cases	8	13	15
Percentage of cases	53%	87%	100%
Probability in normal distribution	68%	95%	100%

Based on the fact that a Monte Carlo simulation yields an underestimated standard deviation of multiplication factor because of the neglect of the inter-cycle correlation of fission source, the observed inconsistency between the RAINBOW and MCNP6 results are likely due to the inaccuracy in the reported MCNP6 standard deviations. For further investigation, the standard deviations were estimated statistically for the base and perturbed cases of the three mini-core models by repeating the MCNP6 simulation five times with different random seed numbers.

Table 5.22, Table 5.23, and Table 5.24 show the eigenvalues of five independent MCNP6 simulations for the base and five perturbed cases. It can be seen that the statistically estimated standard deviations are 3.29 times larger in maximum than the reported MCNP6 standard deviation of 1 pcm.

Table 5.25, Table 5.26, and Table 5.27 compares the RAINBOW results with the MCNP6 reference solutions determined by the statistical average of five independent MCNP6 results. It can be seen that the RAINBOW results agree well with the MCNP6 reference results. In addition, the reactivity worth of axial segment displacements predicted by both RAINBOW and MCNP6 calculations show a linear dependence on the distance from the core center as shown in Fig. 5.19. For 14 cases out of 15, RAINBOW result agrees with the mean value of five MCNP results within one standard deviation. The remaining one case agrees within two standard deviations.

Table 5.22 Eigenvalues of Five Independent MCNP6 Simulations for Base and Five Perturbed Cases of Mini-core Model A

	Seed 1	Seed 2	Seed 3	Seed 4	Seed 5	Mean	STD, pcm
Base	1.00952	1.00951	1.00950	1.00944	1.00951	1.00950	3.21
Segment 1	1.00944	1.00944	1.00943	1.00943	1.00943	1.00943	0.55
Segment 2	1.00938	1.00940	1.00934	1.00939	1.00938	1.00938	2.28
Segment 3	1.00934	1.00935	1.00933	1.00934	1.00930	1.00933	1.92
Segment 4	1.00927	1.00930	1.00923	1.00927	1.00926	1.00927	2.51
Segment 5	1.00928	1.00926	1.00922	1.00920	1.00922	1.00924	3.29

Table 5.23 Eigenvalues of Five Independent MCNP6 Simulations for Base and Five Perturbed Cases of Mini-core Model B with Control Assemblies In

	Seed 1	Seed 2	Seed 3	Seed 4	Seed 5	Mean	STD, pcm
Base	0.93568	0.93568	0.93568	0.93568	0.93570	0.93568	0.89
Segment 1	0.93564	0.93564	0.93566	0.93566	0.93563	0.93565	1.34
Segment 2	0.93561	0.93563	0.93560	0.93562	0.93559	0.93561	1.58
Segment 3	0.93558	0.93559	0.93556	0.93560	0.93559	0.93558	1.52
Segment 4	0.93555	0.93555	0.93558	0.93557	0.93555	0.93556	1.41
Segment 5	0.93554	0.93553	0.93552	0.93554	0.93553	0.93553	0.84

Table 5.24 Eigenvalues of Five Independent MCNP6 Simulations for Base and Five Perturbed Cases of Mini-core Model B with Control Assemblies Out

	Seed 1	Seed 2	Seed 3	Seed 4	Seed 5	Mean	STD, pcm
Base	1.00652	1.00653	1.00651	1.00657	1.00653	1.00653	2.28
Segment 1	1.00649	1.00646	1.00649	1.00649	1.00648	1.00648	1.30
Segment 2	1.00646	1.00647	1.00647	1.00647	1.00647	1.00647	0.45
Segment 3	1.00649	1.00644	1.00643	1.00647	1.00645	1.00646	2.41
Segment 4	1.00646	1.00642	1.00641	1.00642	1.00643	1.00643	1.92
Segment 5	1.00641	1.00642	1.00640	1.00642	1.00645	1.00642	1.87

Table 5.25 Comparison of RAINBOW and Statistically Estimated MCNP6 Reactivity Changes for the Mini-Core Model A

	RAINBOW, pcm	MCNP6, pcm	difference, pcm
Segment 1	-6.36	-6.08±3.23	0.28
Segment 2	-10.98	-11.58±3.90	-0.60
Segment 3	-16.98	-16.10±3.71	0.88
Segment 4	-22.62	-22.57±4.04	0.05
Segment 5	-25.92	-25.52±4.55	0.40

Table 5.26 Comparison of RAINBOW and Statistically Estimated MCNP6 Reactivity Changes for the Mini-Core Model B with Control Assemblies In

	RAINBOW, pcm	MCNP6, pcm	difference, pcm
Segment 1	-3.21	-4.34±1.72	-1.13
Segment 2	-6.23	-8.45±1.94	-2.22
Segment 3	-10.19	-11.42±1.88	-1.23
Segment 4	-13.90	-14.17±1.79	-0.27
Segment 5	-16.14	-17.36±1.31	-1.23

Table 5.27 Comparison of RAINBOW and Statistically Estimated MCNP6 Reactivity Changes for the Mini-Core Model B with Control Assemblies out

	RAINBOW, pcm	MCNP6, pcm	difference, pcm
Segment 1	-3.87	-4.94±2.61	-1.06
Segment 2	-5.73	-6.32±2.31	-0.59
Segment 3	-7.96	-7.50±3.30	0.46
Segment 4	-9.95	-10.27±2.96	-0.31
Segment 5	-11.12	-11.06±2.93	0.06

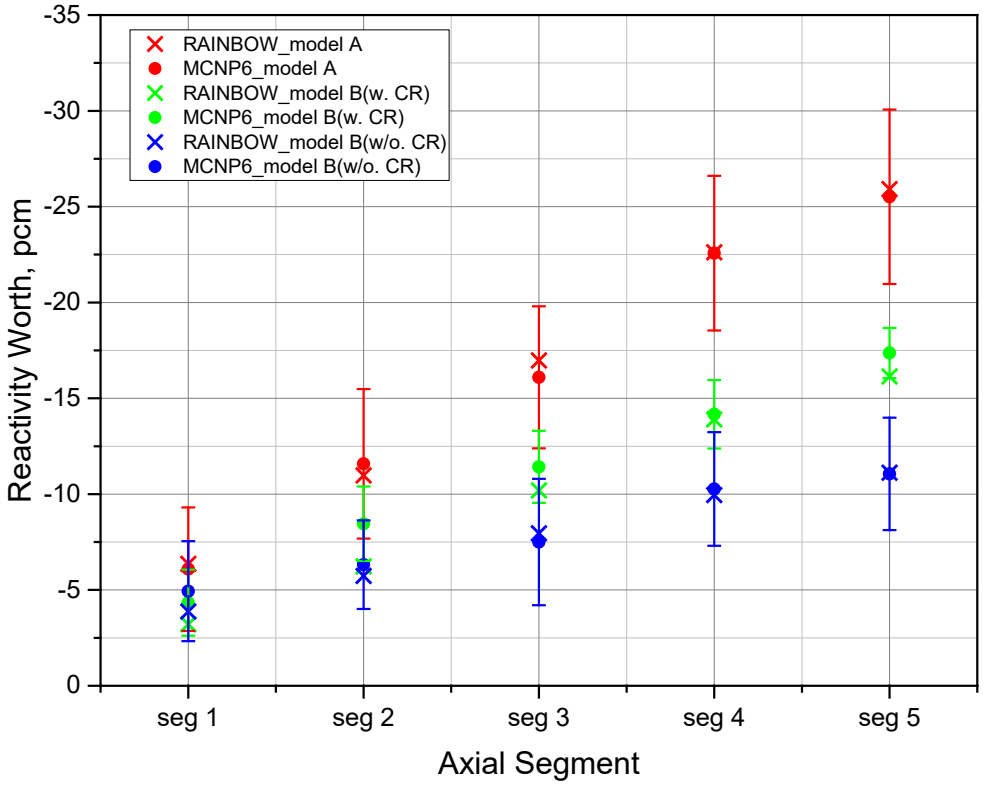

Fig. 5.19 Comparison of RAINBOW Reactivity Changes with MCNP6 Results Obtained by Statistical Average of Five Independent MCNP6 Simulations

5.5.2. AFR-100 Problem

The verification problem presented in this section is based on three-dimensional 100 MWe Advanced Fast Reactor (AFR-100) model [57]. The planar layout and the fuel enrichment map in the active core are shown in Fig. 5.20. The VARIANT calculations were performed using one-third core model. Each assembly excluding the lower and upper structures are axially divided into 10 segments in the RAINBOW model. The segmentation specifications are shown in Table 5.28.

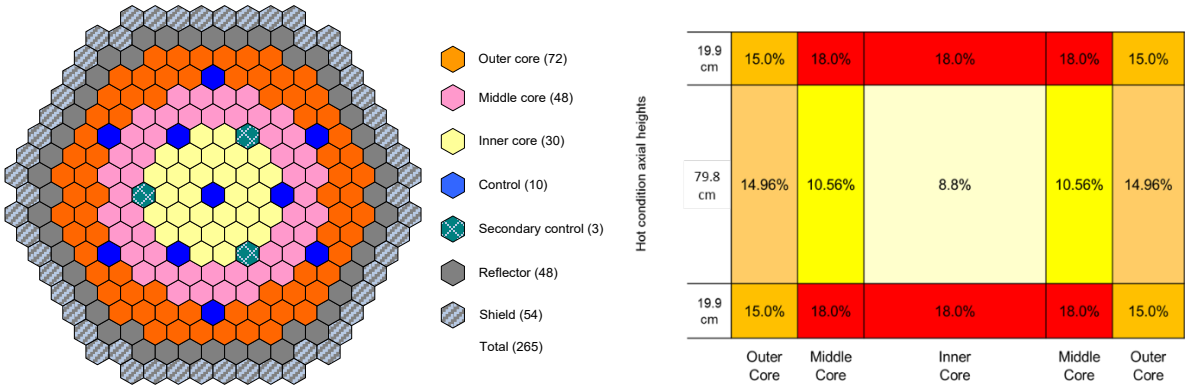

Fig. 5.20 Planar (Left) Layout of the AFR-100 Core Configuration and Fuel Enrichment Map (Right) in Active Core

Table 5.28. Axial Segmentation of AFR100 Fuel Assembly

Segment	Midplane elevation (cm)	Segment length (cm)	Regions
SEG1	46.82	33.2	Lower shield
SEG2	80.02	33.2	Lower reflector
SEG3	106.56	19.9	Lower fuel zone
SEG4	126.47	19.9	Mid-fuel zone 1
SEG5	146.40	19.9	Mid-fuel zone 2
SEG6	166.32	19.9	Mid-fuel zone 3
SEG7	186.27	20.0	Mid-fuel zone 4
SEG8	206.21	19.9	Top fuel zone
SEG9	229.73	27.2	Bond sodium
SEG10	253.03	19.4	Fission gas plenum

For transport calculations, the region dependent multigroup cross sections were generated using the MC^2-3 code. Initially, a 1041-group TWODANT transport calculation was performed in the RZ full-core model to account for the spectrum transition among different core regions. The ultrafine group cross sections were then collapsed into 33 neutron energy groups using the obtained 1041-group spectra. In the MC^2-3 calculations, specific composition temperatures were taken into account. A material temperature map is provided in Appendix I.

In the VARIANT transport calculations to determine the global distributions of forward and adjoint fluxes, the options of P_5 angular expansion and sixth order polynomial spatial expansion for intra-nodal flux distribution and linear expansion for surface leakage were chosen. The neutron anisotropic scattering order was approximated up to P_3 order. For the heterogeneous assembly model to determine the local flux form functions with PROTEUS-SN, the heterogeneous nuclide densities were retrieved from the VARIANT assembly homogenized model to ensure consistent comparisons based on the geometrical component volume fractions provided in Table 5.29. Using the forward and adjoint neutron flux distributions from VARIANT core calculation, and the form functions from PROTEUS-SN assembly calculations, the reactivity change due to displacements of individual assembly segments were calculated for the AFR-100 core using RAINBOW.

Table 5.29. Volume Fractions within Heterogeneous Assemblies of AFR-100

	Inter-Assembly Gap	Outer Duct	Sodium Bypass Channel	Inner Duct	Sodium Coolant	Cladding (include Smeared Wire Wrap)	Material Inside Cladding
Driver	0.03791	0.06995	-	-	0.21689	0.09071	0.58454
Reflector	0.03791	0.06995	-	-	0.10651	0.78563	0
Shield	0.03791	0.06995	-	-	0.12324	0.06050	0.70840
Control	0.03791	0.06995	0.08916	0.06379	0.15612	0.03216	0.55091

In the RAINBOW calculations, the reactivity worth of each segment due to directional displacement were computed by shifting each segment by 1.5 mm in six planar directions as illustrated in Fig. 5.12. The bowing reactivity coefficient is then deduced as the reactivity worth per millimeter of segment displacement. The bowing reactivity worth was evaluated for all the assemblies from the first row to the ninth row in 1/3 core geometry. The assembly numbering scheme is shown in Fig. 5.21. In Appendix J, the displacement reactivity coefficients in the unit of pcm/mm of individual segment of the 73 assemblies in 1/3 AFR-100 core are tabulated.

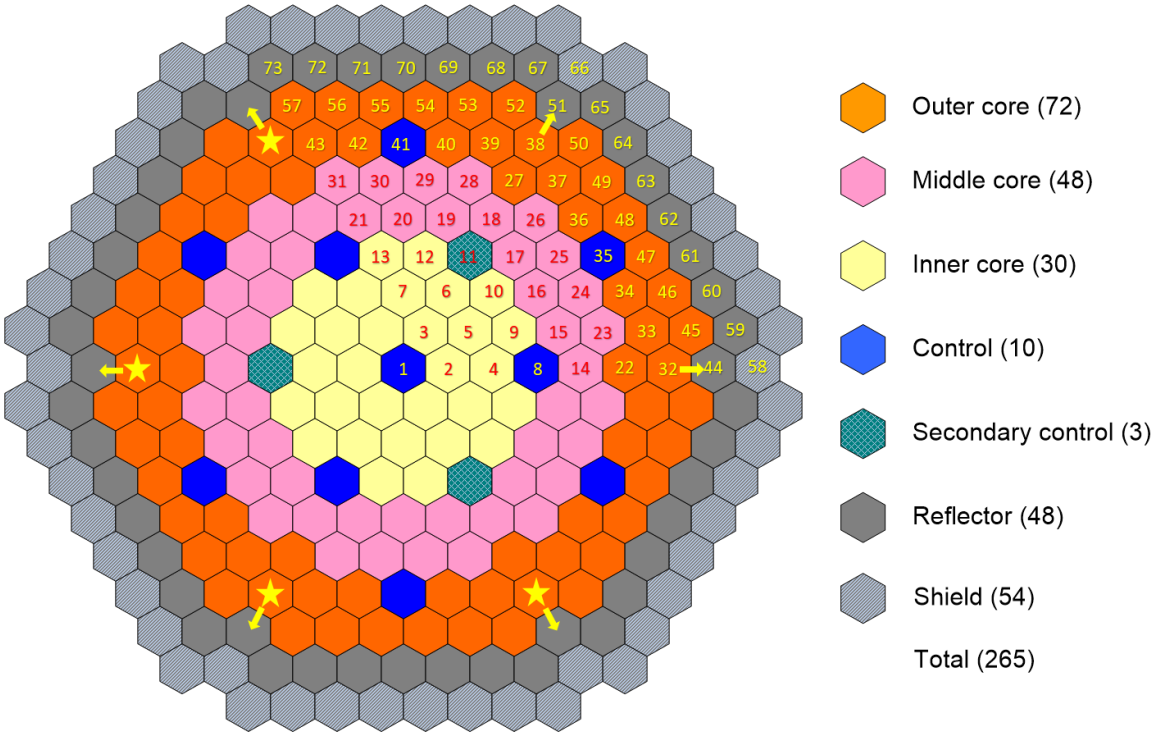

Fig. 5.21 Assembly Numbering Scheme in 1/3 Core RAINBOW Calculation and Positions and Directions of Six Shifted Assemblies in Verification Test

The RAINBOW calculation results were spot-checked by comparing the reactivity change due to six fuel assembly in the outer core shifting outwards, separately calculated by RAINBOW and MCNP6 simulations. Partially heterogeneous assembly model of AFR-100 was built with the MCNP6, in which the assembly duct and inter-assembly gap were explicitly modeled while all the pins and sodium coolant within duct (or the inner duct in the case of double-ducted control assembly) were homogenized. Because the MCNP6 library only provides neutron cross sections at limited number of temperatures. A separate set of 33-group neutron cross sections were generated for VARIANT and PROTEUS calculations using MC^2-3 at consistent material temperatures, which are the closest values in the available MCNP6 library to the real condition. The selected six assemblies are assemblies 32, 38, and the four starred assemblies in Fig. 5.21. For each of the six assemblies, the six segments in the active core were shifted by 2 mm in the direction towards the adjacent reflector assembly as shown by the yellow arrows in Fig. 5.21. The 2 mm displacement was selected to show a larger reactivity change since the costly reference MCNP6 calculation with 2300 active cycles and 500,000 particles per cycle resulted around one pcm uncertainty in the reactivity worth.

By comparing two MCNP6 simulation results separately obtained with unperturbed and shifted assemblies, the total reactivity change due to the 2 mm displacements in 36 segments of six fuel assemblies was -7.69 $\pm$ 1.36 pcm. Comparatively, the direction perturbation calculation with RAINBOW resulted in -6.14 pcm reactivity change, which is within 2σ uncertainty of the reference result. Considering that the MCNP6 uncertainty was underestimated because of the dependence of fission source distributions in successive cycles, the RAINBOW calculation agreed with the MCNP6 reference calculation statistically.

6. Conclusions

In order to overcome the limitations and to improve the accuracy of the existing method based on the diffusion theory calculations, we have developed a new coupled neutron and gamma heating calculation scheme based on VARIANT transport solutions and a perturbation theory method to calculate bowing reactivity coefficients based on the VARIANT core solutions and the PROTEUS-SN assembly solutions. The new heating calculation scheme has been incorporated into the SE2-ANL steady-state subchannel analysis code with improved numerical algorithms and additional capabilities for automatic flow allocation calculations, and the perturbation theory method has been implemented into a computer code named RAINBOW.

The coupled neutron and gamma heating calculation scheme based on VARIANT transport calculations has been developed to determine the pin power distributions more accurately by eliminating the limitations of the current procedure based on the DIF3D finite difference diffusion theory calculations. For this, the GAMSOR code has been extended to generate the VARIANT fixed source file VARSRC, and a new utility code CURVE has been developed to generate the heat source distributions in fuel pins and assembly duct walls. Using the neutron and gamma flux solutions obtained from VARIANT transport calculations, the intra-nodal distributions of neutron and gamma fluxes are reconstructed for each assembly. By evaluating the intra-nodal flux distributions, the flux values at the center of each fuel pin and along the centerline of each duct wall are calculated for the user-specified axial meshes. Heating rates are calculated using the reconstructed neutron and gamma fluxes and the corresponding KERMA factors. Verification tests of the new heating calculation method were performed for the ABTR benchmark problem by comparing the pin power and duct power distributions with the reference Monte Carlo solutions. The performances of the existing and new heating calculation schemes were also compared for the ABTR and EBR-II Run 138B problems. The results showed that the accuracy of pin and duct wall power distributions can be improved significantly by replacing the existing method based on DIF3D finite difference diffusion calculations and SE2-ANL reconstruction scheme with the new method based on VARIANT transport calculations and CURVE reconstruction scheme.

A new subchannel analysis code SE2-UM has been developed by restructuring and rewriting a large fraction of SE2-ANL to interface with the new heating calculation scheme based on the VARIANT transport calculations. The utility code CURVE to evaluate the VARIANT flux solution along each fuel pin and the duct mid-wall has been incorporated into SE2-UM. In addition, the explicit differencing scheme for discretizing the energy equation in the axial direction has been replaced with the θ-method. This allows the use of the inter-assembly gap flow model with much smaller number of axial meshes. The latest Cheng-Todreas correlations for the mixing parameters in wire-wrapped SFR assemblies have also incorporated. Furthermore, an automated flow allocation scheme has been implemented to determine the assembly flow rates in such a way that the peak cladding mid-wall temperatures of individual orifice zones are equalized over the burn cycle. As verification and validation tests of SE2-UM, the 1000 MWt ABR metal core design and three cycles of EBR-II (Run 163A, Run 164A, and Run 165A) were analyzed. The automatic orifice zoning and flow allocation capability of SE2-UM was also tested using the 1000 MWt ABR metal core design. The maximum difference in the mixed mean outlet temperature of the ABR core between SE2-

UM and SE2-ANL was 14.3 °C, which occurred in a reflector assembly. This difference is mainly due to the different heat source distributions obtained with the DIF3D diffusion calculations for SE2-ANL and with the VARIANT transport calculations for SE2-UM. In the EBR-II problem, except for four assemblies whose thermocouple readings appear to be biased, the root mean square deviations of the 18 calculated temperatures with SE2-UM from the measured values were all 7.0 °C for all three cycles.

A perturbation theory method for evaluating the reactivity worth of the assembly displacement has been developed based on the global VARIANT transport solutions with homogenized assembly models and the local PROTEUS-SN transport solutions with single heterogeneous assembly models. A new numerical scheme of perturbation calculation was developed by following the material movement, which is analogous to the Lagrangian frame of reference in a fluid field. This scheme provides a unique convenience for modeling heterogeneous assembly displacements by eliminating the need to consider complex intersections of finite element meshes of PROTEUS-SN and shifted assemblies. A computer code RAINBOW has been developed to calculate the reactivity changes due to assembly bowing in sodium-cooled fast rectors. Assembly bowing is modeled by shifting axially discretized assembly segments, and heterogeneous assembly configurations are represented by unstructured finite element meshes. RAINBOW calculates the reactivity changes per unit displacements of axial assembly segments in each of six directions normal to the duct wall surfaces. Benchmark calculation of the RAINBOW code were performed using 2D and 3D mini-core models that were derived from the ABTR core design and the AFR-100 design. The RAINBOW results agreed well with the MCNP6 reference solutions within two standard deviations.

References

1. K. L. Derstine, "DIF3D: A Code to Solve One-, Two-, and Three-Dimensional Finite-Difference Diffusion Theory Problems," ANL-82-64, Argonne National Laboratory, April (1984).
2. G. Palmiotti , E. E. Lewis and C. B. Carrico, "VARIANT : VARIational Anisotropic Nodal Transport for Multidimensional Cartesian and Hexagonal Geometry Calculation," ANL-95/40, Argonne National Laboratory (1995).
3. B. J. Toppel, "A User's Guide to the REBUS-3 Fuel Cycle Analysis Capability," ANL-83-2, Argonne National Laboratory (1983).
4. C. H. Lee and W. S. Yang, "MC^2-3: Multigroup Cross Section Generation Code for Fast Reactor Analysis," *Nucl. Sci. Eng.*, **187**, 268-290 (2017).
5. M. A. Smith, C. Adams, W. S. Yang, and E. E. Lewis, "VARI3D & PERSENT: Perturbation and Sensitivity Analysis," ANL/NE-13/8, Argonne National Laboratory (2013).
6. E. R. Shemon, C. H. Lee, M. A. Smith and A. Marin-Lafleche, "NEAMS Neutronics: Development and Validation Status," *Proc. ICAPP* 2014, Charlotte, North Carolina, April 6-9, 2014.
7. P. F. Fischer, J. W. Lottes, and S. G. Kerkemeier, "Nek5000 Webpage," http://nek5000.mcs.anl.gov (2008).
8. R. M. Ferencz, "Technical Spotlight: NEAMS Structural Mechanics with Diablo," LLNL-TR-645482, Lawrence Livermore National Laboratory (2013).
9. W. S. Yang and A. M. Yacout, "Assessment of the SE2-ANL Code Using EBR-II Temperature Measurements," Proc. 7th Int'l Mtg. on Nuclear Reactor Thermal Hydraulics, NUREG/CP-0142, Saratoga Springs, New York, September 10-15, 1995.
10. T. J. Moran, "Core Restraint Contributions to Radial Expansion Reactivity," *Proc. of Joint ASME/ANS Nuclear Power Conference*, Ju1y 20-23, 1986, Philadelphia, PA.
11. E. R. Shemon, M. A. Smith, and C. Lee, "PROTEUS-SN User Manual, Revision 3.0," ANL/NE-14/6 (Rev. 3.0), Argonne National Laboratory (2014).
12. Puran Deng, Won Sik Yang, and Gang Yang, "Coupled Neutron and Gamma Heating Calculation Based on VARIANT Nodal Transport Method," *Trans. Am. Nucl. Soc.*, **115**, 1303-1306 (2016).
13. W. S. Yang, et al., "FY 2016 Annual Report – Fuel Pin and Duct Wall Heating Calculation Based on Neutron and Gamma Transport Solutions," PU/NE-16/16, Purdue University, September 30, 2016.
14. C. G. Stenberg and C. H. Adams, "New ANL Heating Calculations," private communication, Argonne National Laboratory, August 20, 1986.
15. R. N. Hill, "Coupled Neutron-Gamma Heating Calculations," private communication, Argonne National Laboratory, February 2, 1988.

16. G. Yang, W. S. Yang, and P. Deng, "SE2-ANL Subchannel Analysis with New Heating Calculation Based on VARIANT Transport Code," *Trans. Am. Nucl. Soc*., **115**, 1315-1318 (2016).

17. G. Yang, P. Deng, and W. S. Yang, "Integration of Heating Calculation Based on VARIANT Transport Solutions and Enhanced Modeling Capabilities into SE2-ANL," UM/NRDSL-18/03, University of Michigan, June 30, 2018.

18. S. Cheng, N. E. Todreas, "Constitutive correlations for wire-wrapped subchannel analysis under forced and mixed convection conditions. Part 1.[LMFBR]," No. DOE/ET/37240-108-TR-Pt. 1. Massachusetts Institute of Technology, Cambridge, 1984.

19. W. S. Yang and H. G. Joo, "LMR Core Temperature Calculation Based on Implicit Formulation of the ENERGY Model and a Krylov Subspace Method," *Annals of Nuclear Energy*, **26**, 629, 1999.

20. T. Jing and W. S. Yang, "A Perturbation Theory Method for Evaluating Reactivity Worth of Assembly Displacements in Fast Reactors," *Trans. Am. Nucl. Soc*., **117**, 1407-1411 (2017).

21. T. Jing and W. S. Yang, "Development of RAINBOW Code to Calculate Reactivity Changes Due to Assembly Bowing in Sodium Fast Reactors," *Proc. of PHYSOR 2018*, Cancun, Mexico, April 22-26, 2018.

22. T. Jing, W. S. Yang, P. Deng, and G. Yang, "User's Manual of RAINBOW Code for Assembly Bowing Reactivity Worth Calculation," UM/NRDSL-18/08, University of Michigan, September 30, 2018.

23. The HDF Group, "Hierarchical Data Format, Version 5," http//www.hdfgroup.org/HDF5/, February 27, 2013.

24. H. Henryson II, B. J. Toppel, and C. G. Stenberg, "MC^2-2: A Code to Calculate Fast Neutron Spectra and Multigroup Cross Sections," ANL-8144, Argonne National Laboratory, June (1976).

25. R. E. Macfarlane and A. C. Kahler, "Methods for Processing ENDF/B-VII with NJOY," *Nuclear Data Sheet*, **111**, 2739 (2010).

26. C. H. Lee and W. S. Yang, "Development of Multigroup Cross Section Generation Code MC^2-3 for Fast Reactor Analysis," *International Conference on Fast Reactors and Related Fuel Cycles*, Kyoto, Japan, December 7-11, 2009, International Atomic Energy Agency (2012).

27. C. H. Lee and W. S. Yang, "MC^2-3: Multigroup Cross Section Generation Code for Fast Reactor Analysis," ANL/NE-11-41 (Rev.2), Argonne National Laboratory (2013).

28. B. K. Jeon, et al., "Improved Gamma Yield and Interaction Cross-Section Libraries of MC^2-3," *Trans. Am. Nucl. Soc.,* **115**, 1299 (2016).

29. Cross Section Evaluation Working Group, "ENDF-6 Formats Manual: Data Formats and Procedures for the Evaluated Nuclear Data Files ENDF/B-VI and ENDF/B-VII," BNL-90365-2009 Rev. 2, Brookhaven National Lab., December (2011).

30. J. Katakura, et al., "Estimation of Beta- and Gamma-ray Spectra for JENDL FP Decay Data File," *J. Nucl. Sci. Technol.*, **38**, 470 (2001).

31. J. Katakura, "JENDL FP Decay Data File 2011 and Fission Yields Data File 2011," JAEA-Data/Code 2011-025, Japan Atomic Energy Agency (2012).

32. R. E. Alcouffe, F. W. Brinkley, D. R. Marr, and R. D. O'Dell, "User's Guide for TWODANT: A Code Package for Two-Dimensional, Diffusion-Accelerated, Neutral-Particle Transport," LA-10049-M, Los Alamos National Laboratory (1990).

33. R. Douglas O'Dell, "Standard Interface Files and Procedures for Reactor Physics Code, Version IV," LA-6941-MS, Los Alamos Scientific Laboratory, September (1977).

34. M. A. Smith, E. E. Lewis, and E. R. Shemon, "DIF3D-VARIANT 11.0: A Decade of Updates," ANL/NE-14/1, Argonne National Laboratory (2014).

35. W. S. Yang, P. J. Flinck, and H. Khalil, "Reconstruction of Pin Power and Burnup Characteristics from Nodal Calculations in Hexagonal-Z Geometry," *Nucl. Sci. Eng.*, **111**, pp. 21-33 (1992).

36. T. K. Kim, W. S. Yang, C. Grandy, and R. N. Hill, "Core design studies for a 1000 MW_{th} Advanced Burner Reactor," *Annals of Nuclear Energy*, **36**, 331 (2009).

37. T. K. Kim, W. S. Yang, E. A. Hoffman, and R. N. Hill, "Core Design Studies for Advanced Burner Test Reactor," ANL-AFCI-169, Argonne National laboratory, June 30, 2006.

38. T. Sumner and T. Y. C. Wei, "Benchmark Specifications and Data Requirements for EBR-II Shutdown Heat Removal Tests SHRT-17 and SHRT-45R," ANL-ARC-226 (Rev. 1), Argonne National Laboratory, May 31, 2012.

39. T. Goorley, et al., "Initial MCNP6 Release Overview," *Nuclear Technology*, **180**, 298 (2012).

40. Denise B. Pelowitz, et al., "MCNP6^{TM} User's Manual Version 1.0," LA-CP-13-00634, Rev. 0, Los Alamos National Laboratory, May (2013).

41. T. Fei et al, "Calculation of Photon Heat Generation for EBR-II Using DIF3D/MC^2-3," ANS Winter Meeting, Anaheim, California, November 9-13, 2014.

42. K. L. Basehore and N. E. Todreas, "SUPERENERGY-2: A Multiassembly Steady-State Computer Code for LMFBR Core Thermal–Hydraulic Analysis," PNL-3379, Pacific Northwest Laboratory, 1980.

43. E. H. Novendstern, "Turbulent flow pressure drop model for fuel rod assemblies utilizing a helical wire-wrap spacer system," Nuclear Engineering and Design, 22(1): 28-42, 1972.

44. C. Chiu, W. M. Rohsenow, and N. E. Todreas, "Flow Split Model for LMFBR Wire Wrapped Assemblies," COO-2245-56TR, Massachusetts Institute of Technology, Cambridge, 1978.

45. C. Chiu, W. M. Rohsenow, and N. E. Todreas, "Turbulent sweeping flow mixing model for wire wrapped LMFBR assemblies," COO-2245-55TR, Massachusetts Institute of Technology, Cambridge, 1978.

46. R. B. Vilim, "Reactor Hot Spot Analysis," private communication, Argonne National Laboratory, August 1985.

47. L. L. Briggs, L. K. Chang, and D. J. Hill, "Safety Analysis and Technical Basis for Establishing an Interim Burnup Limit for Mark-V & Mark-VA Fueled Subassemblies in EBR-II," Version 1.2, Argonne National Laboratory, March 1995.

48. A. Gopalakrishnan and J. L. Gillette, "EBRFLOW – A Computer Program for Predicting Coolant Flow Distribution in the Experimental Breeder Reactor - II," Nucl. Tech., **17**, 205, 1973.

49. W. S. Yang, "Analysis of EBR-II Subassembly Outlet Temperatures Using SE2-ANL", private communication, Argonne National Laboratory, March 24, 1994.

50. R. A. Wigeland and T. J. Moran, "Radial Core Expansion Reactivity Feedback in Advanced LMRs: Uncertainties and Their Effects on Inherent Safety," *Proc. Topl. Mtg. on Safety of Next Generation Power Reactors*, April 1-5, 1988, Seattle, WA.

51. J. J. Grudzinski and C. Grandy, " Fuel Assembly Bowing and Core Restraint Design in Fast Reactors," *Proc. of the ASME 2014 International Mechanical Engineering Congress and Exposition*, November 14-20, 2014, Montreal, Quebec, Canada.

52. P. J. Finck, Private Communication, Argonne National Laboratory (1987).

53. B. D. Abramov, "Calculation of Reactivity Effects in Deformed Zones of Nuclear Reactors," *Atomic Energy*, **85**, 853 (1998).

54. M. Reed, K. Smith, and B. Forget, "The Virtual Density Theory of Neutronics: A Generic Method for Geometry Distortion Reactivity Coefficients," *Proc. PHYSOR 2014*, Kyoto, Japan, Sep. 28 – Oct. 3, 2014.

55. M. Gentili, B. Fontaine, and G. Rimpault, "Deformed Core Reactivity Evaluation with Mesh Projection-based Method," *Nuclear Technology*, **192**, 2 (2015).

56. E. E. Lewis and W. F. Miller, Jr. *Computational Methods of Neutron Transport*, Chapter 1, American Nuclear Society, Inc., La Grange Park, Illinois (1993).

57. C. Grandy, J. Sienicki, A. Moisseytsev, L. Krajtl, M. Farmer and T.K. Kim, "Advanced Fast Reactor – 100 (AFR-100) Report for the Technical Review Panel," ANL-ARC-288, Argonne National Laboratory (2014).

Appendix A. Description of VARIANT Fixed Source File VARSRC

```
C***********************************************************************
C           VARSRC FOR DIF3D-VARIANT                                   -
C              FIXED SOURCE FILE FORMAT FOR USE WITH VARIANT           -
C              CONTAINS VOLUMETRIC NODAL SOURCE MOMENTS                -
C              USED SPECIFICALLY FOR DIF3D 11.0 AND LATER              -
C                                                                      -
C              CARD 1D,3D FORMAT IS SAME SETUP AS NHFLUX_VARIANT       -
C              CARDS 1D,3D WITH IWNHFL=1 AND NSURF=1                   -
C                                                                      -
C***********************************************************************

C----------------------------------------------------------------------
CS          FILE STRUCTURE                                             -
CS                                                                     -
CS          RECORD TYPE                   RECORD    PRESENT IF         -
CS          ==========================    ======    ==========         -
CS          FILE IDENTIFICATION                     ALWAYS             -
CS          SPECIFICATIONS                  1D      ALWAYS             -
CS                                                                     -
CS  ***********(REPEAT FOR ALL GROUPS)                                 -
CS  *       FLUX MOMENTS                    3D      ALWAYS             -
CS  ***********                                                        -
C----------------------------------------------------------------------


C----------------------------------------------------------------------
C          FILE IDENTIFICATION                                        -
C                                                                     -
C    HNAME,(HUSE(I),I=1,2),IVERS                                      -
C                                                                     -
C    1+3*MULT=NUMBER OF WORDS                                         -
C                                                                     -
C    HNAME             HOLLERITH FILE NAME - NHFLUX - (A6)            -
C    HUSE(I)           HOLLERITH USER IDENTIFICATION (A6)             -
C    IVERS             FILE VERSION NUMBER                            -
C    MULT              DOUBLE PRECISION PARAMETER                     -
C                          1- A6 WORD IS SINGLE WORD                  -
C                          2- A6 WORD IS DOUBLE PRECISION WORD        -
C                                                                     -
C----------------------------------------------------------------------

C----------------------------------------------------------------------
C          SPECIFICATIONS     (1D RECORD)                             -
C                                                                     -
C    NDIM,NGROUP,NINTI,NINTJ,NINTK,ITER,EFFK,POWER,NSURF,             -
C    NMOM,NINTXY,NPCXY,NSCOEF,ITRORD,IAPRX,ILEAK,IAPRXZ,ILEAKZ,       -
C    IORDER,NPCBDY,NPCSYM,NPCSEC,IWNHFL,NMOMS (IDUM,I=1,6)            -
C                                                                     -
C    30 =NUMBER OF WORDS                                              -
C                                                                     -
C    NDIM              (not used)                                     -
C    NGROUP            NUMBER OF ENERGY GROUPS                        -
C    NINTI             (not used)                                     -
```

```
C    NINTJ             (not used)                                          -
C    NINTK             NUMBER OF PLANES                                    -
C    ITER              (not used)                                          -
C    EFFK              (not used)                                          -
C    POWER             (not used)                                          -
C    NSURF             NUMBER OF XY-PLANE SURFACES PER NODE                -
                         Must = 1 to read with NHFLUX reader               -
C    NMOM              NUMBER OF EVEN-PARITY FLUX MOMENTS IN VARIANT       -
C    NINTXY            NUMBER OF MESH CELLS (NODES) ON XY-PLANE            -
C    NPCXY             (not used)                                          -
C    NSCOEF            (not used)                                          -
C    ITRORD            (not used)                                          -
C    IAPRX             (not used)                                          -
C    ILEAK             (not used)                                          -
C    IAPRXZ            (not used)                                          -
C    ILEAKZ            (not used)                                          -
C    IORDER            (not used)                                          -
C    NPCBDY            (not used)                                          -
C    NPCSYM            (not used)                                          -
C    NPCSEC            (not used)                                          -
C    IWNHFL            NHFLUX CONTENT                                      -
C                        Must=1, SIGNIFIES ONLY FLUXES ARE PRESENT         -
C    NMOMS             NUMBER OF ODD-PARITY FLUX MOMENTS IN VARIANT        -
C    IDUM              (not used)                                          -
C                                                                           -
C---------------------------------------------------------------------------

C---------------------------------------------------------------------------
C          REGULAR SOURCE MOMENTS   (3D RECORD)                            -
C                                                                           -
C    ((SOURCE(I,J),I=1,NMOM),J=1,NINTXY),                                   -
C    ((SOURCE(NMOM+I,J), I=1,NMOMS),J=1,NINTXY) --SEE STRUCTURE BELOW---    -
C                                                                           -
C    (NMOM+NMOMS)*NINTXY*MULT = NUMBER OF WORDS                             -
C                                                                           -
C     DO K=1,NINTK                                                          -
C        READ(N)   *LIST AS ABOVE*                                          -
C     END DO                                                                -
C                                                                           -
C     SOURCE(I,J) IS THE INHOMOGENEOUS SOURCE MOMENT BY NODE FOR            -
C     THE PRESENT AXIAL PLANE AND THE PRESENT ENERGY GROUP                  -
C     WHOLE STRUCTURE:                                                      -
C     NMOM*NHEX | NMOMS*NHEX, NPLANE, NGROUP                                -
C                                                                           -
C---------------------------------------------------------------------------
```

Appendix B. Description of VARIANT Output File NHFLUX

```
C-----------------------------------------------------------------------
CS          FILE STRUCTURE                                             -
CS                                                                     -
CS          RECORD TYPE                    RECORD    PRESENT IF        -
CS          =========================      ======    ==========        -
CS          FILE IDENTIFICATION                      ALWAYS            -
CS          SPECIFICATIONS                   1D      ALWAYS            -
CS          INTEGER POINTERS                 2D      NSURF.GT.1        -
CS                                                                     -
CS  ***********(REPEAT FOR ALL GROUPS)                                 -
CS  *       FLUX MOMENTS                     3D      IWNHFL=0 OR 1     -
CS  *       XY-DIRECTED PARTIAL CURRENTS     4D      IWNHFL=0 OR 2     -
CS  *       Z -DIRECTED PARTIAL CURRENTS     5D      NDIM.EQ.3 AND     -
CS  *                                                IWNHFL=0 OR 2     -
CS  ***********                                                        -
C-----------------------------------------------------------------------


C-----------------------------------------------------------------------
CR          FILE IDENTIFICATION                                        -
C                                                                      -
CL    HNAME,(HUSE(I),I=1,2),IVERS                                      -
C                                                                      -
CW    1+3*MULT=NUMBER OF WORDS                                         -
C                                                                      -
CD    HNAME             HOLLERITH FILE NAME - NHFLUX - (A6)            -
CD    HUSE(I)           HOLLERITH USER IDENTIFICATION (A6)             -
CD    IVERS             FILE VERSION NUMBER (=4)                       -
CD    MULT              DOUBLE PRECISION PARAMETER                     -
CD                          1- A6 WORD IS SINGLE WORD                  -
CD                          2- A6 WORD IS DOUBLE PRECISION WORD        -
C                                                                      -
C-----------------------------------------------------------------------

C-----------------------------------------------------------------------
CR          SPECIFICATIONS     (1D RECORD)                             -
C                                                                      -
CL    NDIM,NGROUP,NINTI,NINTJ,NINTK,ITER,EFFK,POWER,NSURF,             -
CL    NMOM,NINTXY,NPCXY,NSCOEF,ITRORD,IAPRX,ILEAK,IAPRXZ,ILEAKZ,       -
CL    IORDER,NPCBDY,NPCSYM,NPCSEC,IWNHFL,NMOMS (IDUM,I=1,6)            -
C                                                                      -
CW    30 =NUMBER OF WORDS                                              -
C                                                                      -
CD    NDIM              NUMBER OF DIMENSIONS                           -
CD    NGROUP            NUMBER OF ENERGY GROUPS                        -
CD    NINTI             NUMBER OF FIRST DIMENSION FINE MESH INTERVALS  -
CD    NINTJ             NUMBER OF SECOND DIMENSION FINE MESH INTERVALS -
CD    NINTK             NUMBER OF THIRD DIMENSION FINE MESH INTERVALS. -
CD                      NINTK.EQ.1 IF NDIM.LE.2                        -
CD    ITER              OUTER ITERATION NUMBER AT WHICH FLUX WAS       -
CD                      WRITTEN                                        -
```

```
CD    EFFK              EFFECTIVE MULTIPLICATION FACTOR                -
CD    POWER             POWER IN WATTS TO WHICH FLUX IS NORMALIZED      -
CD    NSURF             NUMBER OF XY-PLANE SURFACES PER NODE.           -
CD    NMOM              NUMBER OF EVEN-PARITY FLUX MOMENTS IN VARIANT   -
CD    NINTXY            NUMBER OF MESH CELLS (NODES) ON XY-PLANE        -
CD    NPCXY             NUMBER OF XY-DIRECTED PARTIAL CURRENTS ON       -
CD                      XY-PLANE (also known as NPCHEX)                 -
CD    NSCOEF            NUMBER OF PARTIAL CURRENT MOMENTS PER NODE      -
CD                      SURFACE                                         -
CD    ITRORD            ORDER OF THE POLYNOMIAL APPROXIMATION OF THE    -
CD                      SOURCE WITHIN THE NODE                          -
CD    IAPRX             ORDER OF THE POLYNOMIAL APPROXIMATION OF THE    -
CD                      FLUXES WITHIN THE NODE                          -
CD    ILEAK             ORDER OF THE POLYNOMIAL APPROXIMATION OF THE    -
CD                      LEAKAGES ON THE SURFACES OF THE NODES           -
CD    IAPRXZ            ORDER OF THE PN EXPANSION OF THE FLUX           -
CD    ILEAKZ            ORDER OF THE PN EXPANSION OF THE LEAKAGE        -
CD    IORDER            DIF3D VERSION                                   -
CD                      =0, VERSION 8.0 OR PREVIOUS ONES                -
CD                      =2, VERSION 9.0                                 -
CD    NPCBDY            NUMBER OF OUTGOING PARTIAL CURRENTS ON OUTER    -
CD                      XY-PLANE BOUNDARY.                              -
CD    NPCSYM            NUMBER OF OUTGOING PARTIAL CURRENTS ON          -
CD                      SYMMETRIC XY-PLANE BOUNDARY. HEXAGONAL          -
CD                      GEOMETRY ONLY.                                  -
CD    NPCSEC            NUMBER OF OUTGOING PARTIAL CURRENTS ON          -
CD                      SECTOR XY-PLANE BOUNDARY. HEXAGONAL GEOMETRY    -
CD                      ONLY.                                           -
CD    IWNHFL            NHFLUX CONTENT                                  -
CD                      =0, BOTH FLUXES AND PARTIAL CUURENTS ARE        -
CD                          PRESENT IN THE FILE                         -
CD                      =1, ONLY FLUXES ARE PRESENT                     -
CD                      =2, ONLY PARTIAL CURRENTS ARE PRESENT           -
CD    NMOMS             NUMBER OF ODD-PARITY FLUX MOMENTS IN VARIANT    -
CD    IDUM              RESERVED FOR FUTURE USE                         -
C                                                                       -
C-----------------------------------------------------------------------

C-----------------------------------------------------------------------
CR          INTEGER POINTERS   (2D RECORD)                              -
C                                                                       -
CC          PRESENT IF NSURF.GT.1                                       -
C                                                                       -
CL    (IPCPNT(I,J),I=1,NSURF),J=1,NINTXY),(IPCBDY(I),I=1,NPCBDY),       -
CL    (ITRMAP(I),I=1,NINTXY),(IPCSYM(I),I=1,NPCSTO),                    -
CL    (IPCSCP(I),I=1,NPCSTO)                                            -
C                                                                       -
CW    NSURF*NINTXY + NPCBDY + NINTXY + 2*NPCSTO =NUMBER OF WORDS        -
C                                                                       -
CD    IPCPNT(I,J)       POINTERS TO INCOMING XY-PLANE PARTIAL CURRENTS.-
CD    IPCBDY(I)         POINTERS TO OUTGOING PARTIAL CURRENTS ON OUTER -
CD                      XY-PLANE BOUNDARY.                              -
CD    ITRMAP(I)         TRANSFORMATION MAP BETWEEN NODAL AND GEODST     -
CD                      MESH CELL ORDERINGS.                            -
CD    IPCSYM(I)         POINTERS TO OUTGOING PARTIAL CURRENTS ON        -
```

```
CD                      SYMMETRIC AND SECTOR XY-PLANE BOUNDARY.         -
CD                      HEXAGONAL GEOMETRY ONLY.                        -
CD    IPCSTO(I)         POINTERS TO INGOING PARTIAL CURRENTS ON         -
CD                      SYMMETRIC AND SECTOR XY-PLANE BOUNDARY.         -
CD                      HEXAGONAL GEOMETRY ONLY.                        -
CD    NPCSTO            = NPCSYM + NPCSEC                               -
CD    NPCXY             = NSURF*NINTXY + NPCBDY + NPCSTO                -
C                                                                       -
C-----------------------------------------------------------------------

C-----------------------------------------------------------------------
CR          REGULAR FLUX MOMENTS   (3D RECORD)                          -
C                                                                       -
C     FLUX(NMOM*NINTXY+NMOMS*NINTXY) IS THE ARRAY SIZE AND SETUP        -
C     (NMOM*NINTXY+NMOMS*NINTXY)*MULT = NUMBER OF WORDS                 -
C                                                                       -
C     EMOM=NMOM*NINTXY                                                  -
C     OMOM=NMOMS*NINTXY                                                 -
C     DO K=1,NINTK                                                      -
C        READ(N) (FLUX(I),I=1,EMOM),(FLUX(EMOM+I),I=1,OMOM)             -
C     END DO                                                            -
C     FLUX(I,J)  REGULAR FLUX MOMENTS BY NODE FOR THE PRESENT GROUP     -
C                                                                       -
C-----------------------------------------------------------------------

C-----------------------------------------------------------------------
CR          REGULAR XY-DIRECTED PARTIAL CURRENTS   (4D RECORD)          -
C                                                                       -
CD                                                                      -
CL    ((PCURRH(M,I),M=1,NSCOEF),I=1,NPCXY) ----SEE STRUCTURE BELOW----  -
C                                                                       -
CW    NPCXY*NSCOEF*MULT = NUMBER OF WORDS                               -
C                                                                       -
C     DO 1 K=1,NINTK                                                    -
C   1 READ(N)   *LIST AS ABOVE*                                         -
C                                                                       -
CD    PCURRH(M,I)       OUTGOING XY-DIRECTED PARTIAL CURRENTS           -
CD                      ACROSS ALL XY-PLANE SURFACES FOR THE            -
CD                      THE PRESENT GROUP                               -
C                                                                       -
CD    ================================================================  -
C                                                                       -
CN    ELEMENTS I=1,NSURF*NINTXY OF EACH VECTOR PCURRH(M,.) MAP TO       -
CN    SURFACE S OF NODE N WHERE S = MOD(I-1,NSURF)+1 AND                -
CN    N = (I-1)/NSURF + 1. M INDEX OF PARTIAL CURRENT MOMENT.           -
CN                                                                      -
CN    THE REMAINING ELEMENTS (PCURRH(M,I),I=NSURF*NINTXY+1,NPCXY),      -
CN    IF ANY, CORRESPOND TO INCOMING PARTIAL CURRENTS ON THE OUTER      -
CN    (POSSIBLY IRREGULAR) XY-PLANE BOUNDARY.                           -
CN                                                                      -
CN    THE FOLLOWING ORIENTATION IS USED TO DENOTE                       -
CN    SURFACES J=1,...,NSURF AND NEIGHBORING NODES J=1,...,NSURF:       -
CN                                                                      -
CN             *                                      Y                -
CN        J=3 *   * J=2                               ^                -
```

```
CN          *       *                     J=2         |                -
CN        *           *                 *******       |                -
CN        *           *                 *     *       |                -
CN    J=4 *           * J=1         J=3 *     * J=1   +----> X         -
CN        *           *                 *     *                        -
CN          *       *                   *******                        -
CN        J=5 *   * J=6                   J=4                          -
CN             *                                                       -
CN                                                                     -
CN     HEXAGONAL NODES                CARTESIAN NODES                  -
CN        NSURF = 6                      NSURF = 4                     -
C                                                                      -
C---------------------------------------------------------------------

C---------------------------------------------------------------------
CR          REGULAR  Z-DIRECTED PARTIAL CURRENTS   (5D RECORD)         -
C                                                                      -
CL    (((PCURRZ(M,I,J),M=1,NSCOEF),I=1,NINTXY),J=1,2)                  -
CL                                    ------SEE STRUCTURE BELOW---------
C                                                                      -
CW    NINTXY*NSCOEF*2*MULT = NUMBER OF WORDS                           -
C                                                                      -
C     DO 1 K=1,NINTK1                                                  -
C   1 READ(N)   *LIST AS ABOVE*                                        -
C                                                                      -
CC          WITH NINTK1 = NINTK + 1                                    -
C                                                                      -
CD    PCURRZ(M,I,J)     Z-DIRECTED PARTIAL CURRENTS IN                 -
CD                      PLUS- (J=1) AND MINUS- (J=2) Z DIRECTIONS      -
CD                      ACROSS ALL AXIAL BOUNDARIES FOR THE PRESENT    -
CD                      GROUP                                          -
C                                                                      -
CN                      E.G. INCOMING PARTIAL CURRENTS FOR NODE I ON   -
CN                      AXIAL MESH INTERVAL K ARE PCURRZ(1,I,1) ON THE -
CN                      LOWER BOUNDARY (RECORD K) AND PCURRZ(1,I,2) ON -
CN                      THE UPPER AXIAL BOUNDARY (RECORD K+1).         -
C---------------------------------------------------------------------
```

Appendix C. Format Descriptions of CURVE Interface File POWRFILE

```
!--------------------------------------------------------------------!
!               POWRFILE Description                                 !
!                                                                    !
!    File Structure:                                                 !
!                                                                    !
!    Record        Record Contents                                   !
!    ========      ===============                                   !
!      0D          Identification                                    !
!      1D          Dimension Specification                           !
!      2D          Mapping Information                               !
!      3D          Axial Interval Heights                            !
!      4D          Assembly Total Powers and Pin Power Skew          !
!      5D          Coefficients of Pin Power Profiles                !
!      6D          Power Profiles for Control Rods                   !
!      7D          Node Total Powers                                 !
!--------------------------------------------------------------------!
!                                                                    !
! 0D IDENTIFICATION                                                  !
!                                                                    !
!    'POWRFILE', TITLE (A8, A100)                                    !
!    TITLE     Description of problem case                           !
!--------------------------------------------------------------------!
! 1D SPECIFICATION                                                   !
!                                                                    !
!    NINTXY, NINTK, NTYPE, NSYPE, ZODER, MNPNT, NCTRL, MNROD         !
!                                                                    !
!    All integers(kind=4)                                            !
!                                                                    !
!    NINTXY    Number of hexagonal nodes on XY-plane                 !
!    NINTK     Number of third dimension fine mesh intervals         !
!    NTYPE     Number of assembly types                              !
!    NSYPE     Single-duct assembly types                            !
!    ZODER     (>=2) Order of axial polynomial                       !
!    MNPNT     Maximum number of intra-nodal evaluation positions on !
!              each axial plane of single node among all assembly    !
!              types. MNPNT = max{NPNT(I),I=1,NTYPE}                 !
!    *** the following two parameters are not used in SE2-UM currently!
!    NCTRL     Number of control assemblies                          !
!    MNROD     Maximum number of control rods in control assemblies  !
!--------------------------------------------------------------------!
! 2D MAPS                                                            !
!                                                                    !
!    (NPNT(I),I=1,NTYPE),(NNPIN(I),I=1,NTYPE), (TYPES(I),I=1,NINTXY),!
!    (ITRMAP(I),I=1,NINTXY), (ICTRL(I),I=1,NINTXY)                   !
!                                                                    !
!    All integers (kind=4)                                           !
!                                                                    !
!    NPNT(I)    Total evaluation points on each axial plane of       !
!                  single node of type I assemblies                  !
!                  NPNT(I) = NNPIN(I) + NINTERF(I)                   !
!                  NINTERF(I) is the number of evaluations points    !
!                  on the duct of type I.                            !
!    NNPIN(I)      Number of pins within a type I assembly           !
!    TYPES(I)      Type flag of hexagon I                            !
```

```
!    ITRMAP(I)     Transformation map of Nodal to GEODST ordering of  !
!                  hexagon I (VARIANT ordering)                       !
!    ICTRL(I)      Mapping hexagon index to control assembly index    !
!                  ICTRL(I)=0 means hexagon I is not control assembly !
!---------------------------------------------------------------------!
! 3D AXIAL INTERVAL HEIGHTS                                          !
!                                                                    !
!    (DLTAZ(I),I=1,NINTK)                                            !
!                                                                    !
!    Real numbers (kind=8)                                           !
!                                                                    !
!    DLTAZ(I)      Node height (cm) of the I_th axial interval        !
!                                                                    !
!         Note:    The coefficients given in 5D records are for      !
!                  dimensionless coordinates (-1/2 <= z <= 1/2).     !
!---------------------------------------------------------------------!
! 4D ASSEMBLY TOTAL POWERS AND FACIAL SKEW OF PIN POWER DISTRIBUTION  !
!                                                                    !
!    (ASSPWR(I),I=1,NINTXY), (SKEW(I),I=1,NINTXY)                    !
!                                                                    !
!    All real numbers (kind=8)                                       !
!                                                                    !
!    ASSPWR(I)     Total power (W) of the I_th assembly               !
!    SKEW(I)       The radial skew of pin powers in the I_th assembly.!
!                  It is calculated as:                              !
!                  Peak_Pin_Power / Lowest_Pin_Power,                !
!                  for every assembly.                               !
!---------------------------------------------------------------------!
! 5D COEFFICIENTS FOR POLYNOMIAL POWER PROFILES                      !
!                                                                    !
!    ((((COEF(I,J,K,N), I=0,ZODER),J=1,MNPNT),K=1,NINTK),N=1,NINTXY)  !
!                                                                    !
!    All real numbers (kind=8)                                       !
!                                                                    !
!    Usefuel data for a specific node N at axial plane K:            !
!    (COEF(I,J,K,N), I=0,ZODER),J=1,NM)                              !
!      NM = NNPIN + 2 * NONPIN    for single-duct assembly           !
!      NM = NNPIN + 4 * NONPIN    for double-duct assembly           !
!      NNPIN  = number of pins in this assembly                      !
!      NONPIN = number of evaluation points on the assembly duct walls!
!                                                                    !
!    Power shape for the K-th segment of J-th pin in N-th assembly:  !
!    p(z) = SUM{COEF(i,J,K,N)*z**i, i=0,ZODER}                       !
!                                                                    !
!    The coefficients for duct walls and coolant gaps follows the    !
!    coefficients for pin segments.                                  !
!                                                                    !
!    The ordering of pins is displayed below:                        !
!    Central pin is indexed as pin 1, the pins on the second ring    !
!    are indexed from 2 to 7, so on and so forth.                    !
!    S1 ~ S6 are ordering for hex surfaces                           !
!    C1 ~ C6 are ordering for hex vertices                           !
!    Following pins' profiles, power profiles on the duct are ordered !
!    the similar way, but starting from the first points on surface 1.!
!    Following the profiles for duct walls, the coefficients of the  !
!    power profiles for the inter-assembly gaps are recorded. The    !
!    ordering of the coefficients for gaps are the same as for duct  !
!    walls. Further, for a double-duct assembly, the coefficients are !
```

```
!    recorded in sequence: first the coefficients for pins, then the  !
!    outer duct walls, then the inter-assembly gap, then the inner    !
!    duct walls, at last the bypass gap between inner and outer ducts.!
!                                                                     !
!                                                  Y                  !
!                                                  |                  !
!                                C2                |                  !
!                              ======              |                  !
!                      S3      = 12 =      S2      -|-------> X       !
!                       ======  ======  ======                        !
!           C3           = 13 =          = 11 =          C1           !
!               ======  ======  ======  ======  ======                !
!               = 14 =          =  4 =          = 10 =                !
!               ======  ======  ======  ======  ======                !
!                       = 5  =          = 3  =                        !
!               ======  ======  ======  ======  ======                !
!           S4  = 15 =          =  1 =          = 9  =  S1           !
!               ======  ======  ======  ======  ======                !
!                       = 6  =          = 2  =                        !
!               ======  ======  ======  ======  ======                !
!               = 16 =          = 7  =          = 8  =                !
!               ======  ======  ======  ======  ======                !
!           C4           = 17 =          = 19 =          C6           !
!                        ======  ======  ======                       !
!                      S5      = 18 =      S6                         !
!                              ======                                 !
!                                C5                                   !
!                                                                     !
!---------------------------------------------------------------------!
! 6D COEFFICIENTS FOR CONTROL ROD POWER PROFILES                      !
!                                                                     !
!    ((((COEF(I,J,K,N), I=0,ZODER),J=1,MNROD),K=1,NINTK),N=1,NCTRL)   !
!                                                                     !
!    All real numbers (kind=8)                                        !
!                                                                     !
!    Similar ordering of control rods as 5D record. These power       !
!    profiles are especially for control rod segments, in which case, !
!    the gamma heating in sodium coolant is not redistributed among   !
!    control absorber rods like for fuel assemblies.                  !
!    This block of data is not really used in SE2-UM currently.       !
!---------------------------------------------------------------------!
! 7D TOTAL POWERS OF HEXAGONAL NODES OF VARIANT                       !
!                                                                     !
!    ((NODE(K,N), K=1,NINTK), N=1,NINTXY)                             !
!    All real numbers (kind=8)                                        !
!---------------------------------------------------------------------!
```

Appendix D. Verification Tests of CURVE Code

D.1 Verification of Flux Reconstruction Scheme

A complete set of polynomial functions are used as the trial functions for the intra-nodal flux shape in CURVE as in VARIANT. Therefore, as the first verification test of the flux reconstruction scheme, it was tested whether the CURVE code could reproduce any arbitrary polynomial shape. For a given flux shape of arbitrary 6th order polynomial, the intra-nodal flux distribution was reconstructed using a set of complete trial polynomials of 6th order, and the reconstructed fluxes were compared to the given flux shape at multiple random points.

As an analytical benchmark, the following polynomial shape of the flux distribution within a node was assumed:

$$\phi(x,y,z) = x^6 + y^5 + xy^4 + z^3 \tag{D.1}$$

The corresponding flux moments were calculated up to 6th order with a symbolic mathematical computational software, Wolfram Mathematica 10.2, using a weighted integration defined as:

$$\zeta_i = \frac{1}{V}\iiint_V \phi(x,y,z) f_i(x,y,z) dydxdz \tag{D.2}$$

The orthonormal trial functions f_i in Eq. (D.2) were obtained through the Gram-Schmidt orthogonalization procedure implemented in the CURVE code. Using these flux moments, the intra-nodal fluxes at 10 randomly selected points were evaluated separately with Mathematica and CURVE. Table D.1 compares the reconstructed flux values using CURVE and Mathematics with the values obtained from the analytical evaluation of the given flux shape.

Table D.1. Reconstructed Intra-nodal Fluxes for Given Polynomial Flux Shape

Evaluation Position			Flux Results			CURVE – Mathematica	CURVE – Analytical Evaluation
x/p	y/p	$z/\Delta z$	CURVE	Mathematica	Analytical Evaluation		
0.00	0.00	0.50	1.25000E-01	1.25000E-01	1.25000E-01	0.00000E+00	-5.29550E-11
0.10	0.10	0.30	2.70302E-02	2.70302E-02	2.70302E-02	0.00000E+00	-1.49360E-11
-0.20	0.10	0.10	1.08421E-03	1.08421E-03	1.08421E-03	0.00000E+00	1.91765E-11
0.25	0.25	0.40	6.71742E-02	6.71742E-02	6.71742E-02	0.00000E+00	1.56597E-11
0.00	0.58	0.50	2.16633E-01	2.16633E-01	2.16633E-01	0.00000E+00	6.28500E-12
0.00	-0.58	-0.10	-9.26331E-02	-9.26331E-02	-9.26331E-02	0.00000E+00	1.25474E-11
-0.40	0.30	-0.50	-1.19854E-01	-1.19854E-01	-1.19854E-01	0.00000E+00	-2.75230E-11
-0.30	0.10	-0.50	-1.23906E-01	-1.23906E-01	-1.23906E-01	0.00000E+00	1.72130E-11
-0.20	0.30	-0.50	-1.23741E-01	-1.23741E-01	-1.23741E-01	0.00000E+00	7.31801E-12
-0.10	0.20	-0.50	-1.24769E-01	-1.24769E-01	-1.24769E-01	0.00000E+00	7.15300E-12

As can be seen in Table D.1, there is no noticeable difference in double precision limit between the Mathematica and CURVE results. Since they used the same set of polynomials, the errors due to function evaluation were proved negligibly small. The errors compared to analytical results mainly come from the polynomial basis functions, which are not perfectly orthogonal to each other owing to the truncation errors of the Gram-Schmidt procedure implemented in the CURVE code. Checking the orthogonality of polynomials showed a non-orthogonality up to the order of magnitude of 10^{-11}.

D.2 Examination of Quadratic Approximation for Axial Power Profile

To test the adequacy of the piecewise quadratic polynomial representation for axial pin power distributions, the axial pin power distribution in a fuel assembly of the reference ABTR metal core [27] was investigated. VARIANT transport calculations were performed with a spatial expansion of sixth order polynomials for intra-nodal fluxes. A piecewise quadratic shape of pin power distribution was derived from the VARIANT transport solution and was compared to the sixth order VARIANT solution. The linear power distribution of the central pin of a fuel assembly is compared in the left-hand-side plot of Fig. D.1 over the active core region. The axial configuration of the selected assembly is shown in the right-hand-side plot of Fig. D.1. It is seen that the piecewise quadratic form representation of the axial pin power profiles agrees well with the original VARIANT solution, with a root mean square (RMS) error of 0.46% and a maximum error of 1.86%. The maximum error occurs at the core bottom next to the lower reflector. Nevertheless, the user can specify the axial pin power profile to be evaluated using the original high-order polynomial shape in VARIANT solution for the best achievable accuracy.

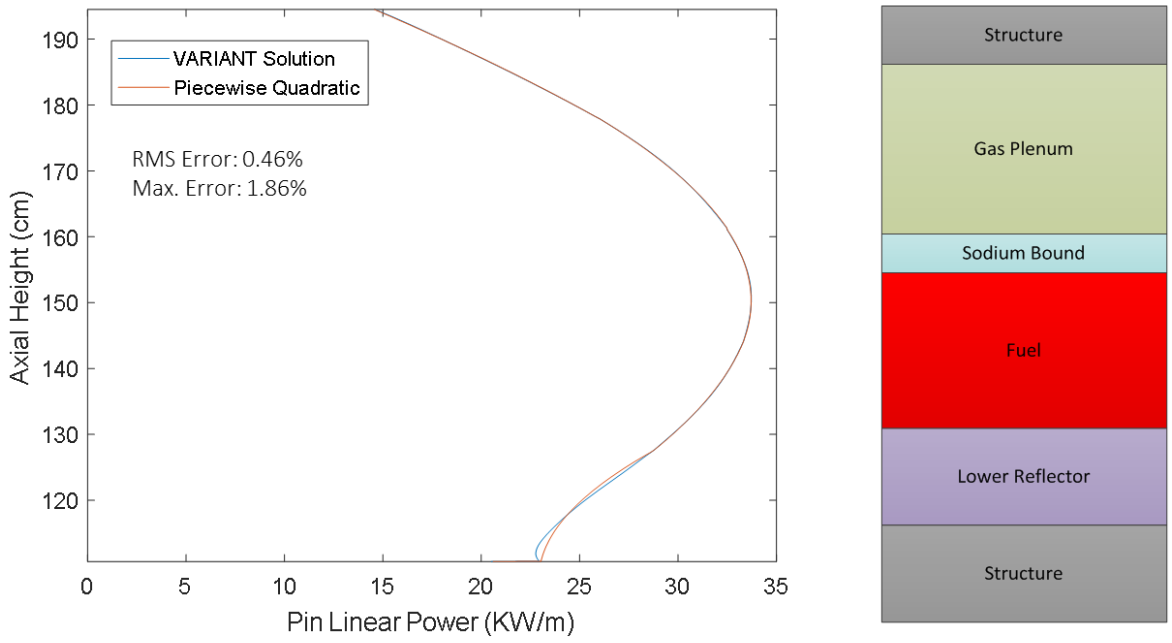

Fig. D.1 Axial Pin Power Profiles at Fuel Region of One Fuel Assembly in ABTR Core (Left) and Axial Configuration of Fuel Assembly (Right)

D.3 Pin Power Comparison with RCT for ABR-1000 Metal Core

Pin power reconstruction calculations were performed for the ABR-1000 metal core [25], and the calculated results were compared with those obtained with the RCT code. The ABR-1000 core configurations are shown in Fig. D.2 and Fig. D.3. Material compositions were obtained from the REBUS-3 model of the ABR-1000 metal core design with startup fuel. Nuclide densities in each region were retrieved at the beginning of a one-year equilibrium cycle. The fuel pin power densities were reconstructed without considering gamma heating explicitly for three assemblies: IC21, IC53 and OC61 marked as (2,1), (5,3) and (6,1) respectively in Fig. D.2. The fuel part of each assembly was equally divided into five axial regions (nodes) as marked as D, E, F, G and H in the left figure of Fig. D.3. Each fuel assembly has 271 fuel pins arranged in a triangular lattice as schematically shown in the right figure of Fig. D.3. The pin power densities at the top and bottom of pin segments were reconstructed as well as the segment-averaged values.

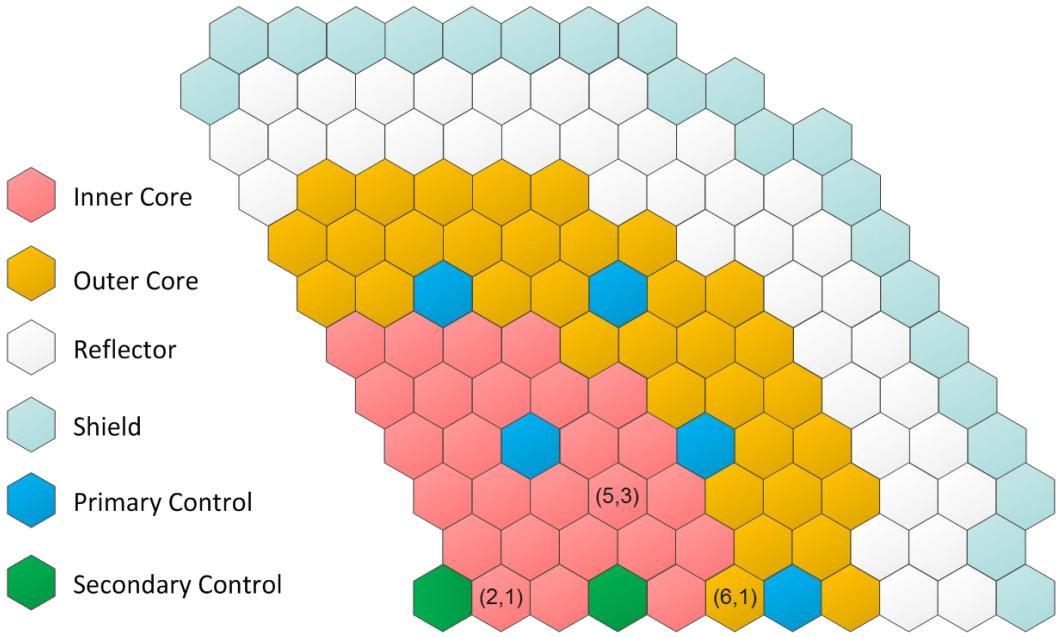

Fig. D.2 Planar Layout of Metal Core Configuration of ABR-1000 (1/3 core)

The RCT code reconstructs the pin power densities using the hexagonal nodal flux solution obtained from a DIF3D-Nodal diffusion calculation. To eliminate the transport effects in the comparisons, the preceding VARIANT calculation for the CURVE run was performed using P_1 approximation for angular expansion of the intra-nodal flux distribution and the scattering source was assumed isotropic. The DIF3D-Nodal and VARIANT calculations resulted in around 200-pcm difference in k-effective. Comparison of the segment-averaged and end-point power values of the fuel pin segments of interest showed that the segment-averaged power densities obtained with CURVE agreed well with the RCT results with less than 2% differences. Bigger differences were observed for the power densities at the segment top and bottom points. It is around 4% for the assemblies IC21 and IC53, and around 6% for the assembly OC61. Bigger differences usually occur in D or H segment of the periphery pins

where the flux variation becomes steeper and the power density is small. Detailed comparisons over all the pin segments gave the maximum difference in power densities as summarized in Table D.2.

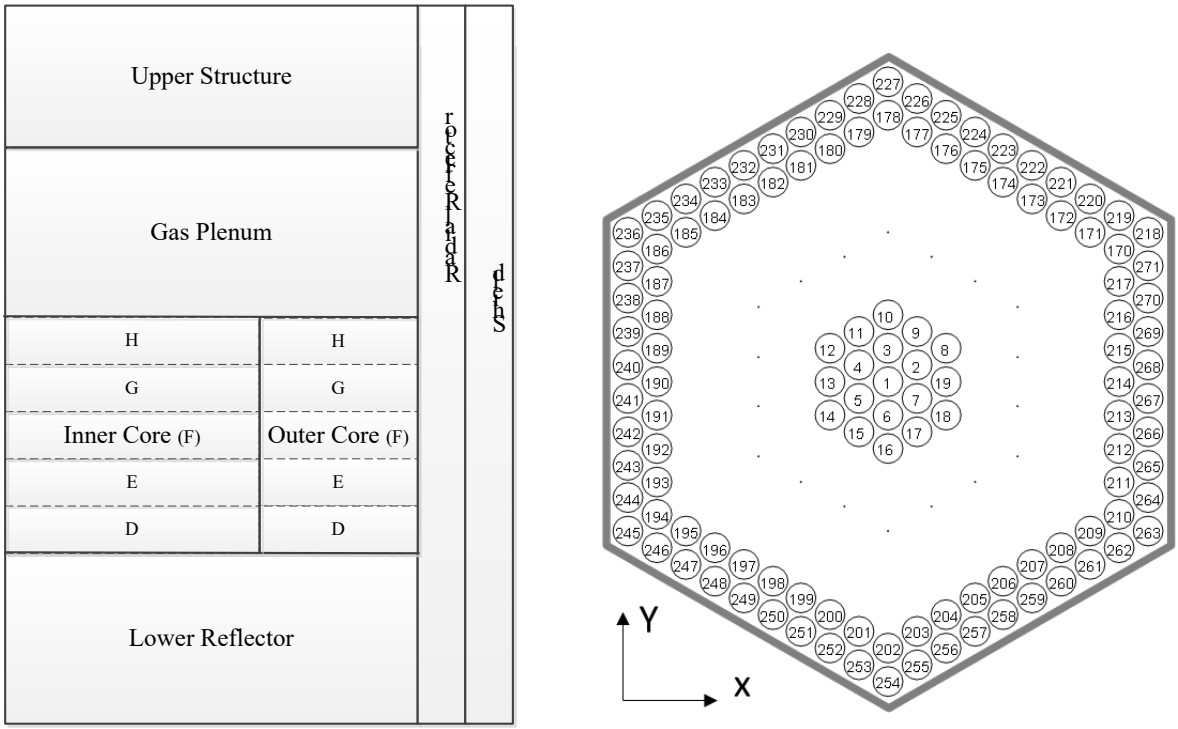

Fig. D.3 Vertical Layout of ABR-1000 Metal Core (Left) and Pin Numbering Scheme within Fuel Assembly (Right)

Table D.2 Maximum Difference in Pin Power Densities between CURVE and RCT Results

Segment Values	Maximum Difference* (%)	Assembly	Pin Number	Pin Location (Ring #, Position #)	Pin Segment
Average	-2.23	OC61	218	(10, 1)	H
Bottom	-11.94	OC61	267	(10, 50)	D
Top	-12.20	OC61	267	(10, 50)	H

* % difference of CURVE results relative to RCT results.

The main reason for the observed discrepancies between the RCT and CURVE power densities appears to be the approximation used in RCT. In RCT, it is assumed that the flux within a node is separable in the hexagonal plane and axial directions. With this separability assumption, the axial flux distribution of a node is interpolated by a cubic polynomial, and the hexagonal plane flux distribution is interpolated as a non-separable polynomial of x and y. The separability assumption may not be valid in a fuel assembly next to a control assembly, especially when the control assembly is out of the core, and result in significant differences in axial profiles. For example, Fig. D.4 shows the axial distributions of the node-average and

surface power densities in a node in the U-TRU-10Zr and U-10Zr fuel cores of the Small Modular Fast Reactor (SMFR). The surface 4 of this assembly is adjacent to a control assembly, which is out of the core. It can be seen clearly that the surface 4 distributions are very different from the node-average and other surface distributions. These results indicate that the flux separability assumption is not valid for this node.

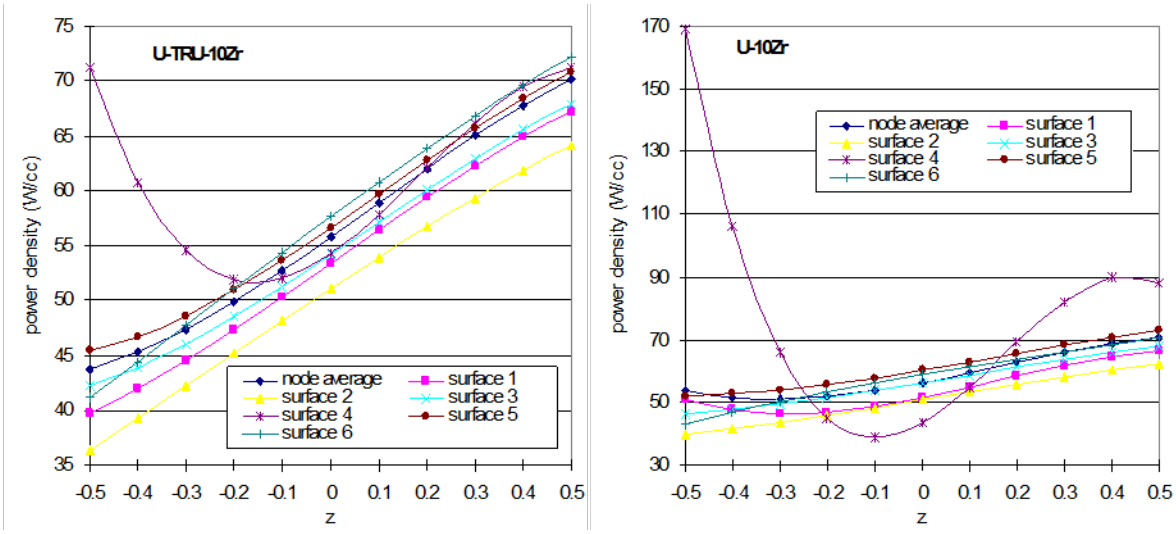

Fig. D.4 Axial Power Density Distributions of a Node Next to Control Assembly (SMFR)

In the OC61 assembly that is next to a control assembly, the relative difference in nodal power between CURVE and RCT is -1.13% for segment H and 0.68% for segment D. The pin power distribution for segments H and D of assembly OC61 is plotted in Fig. D.5. Due to the neighboring control assembly, large flux gradients are expected in assembly OC61, which lead to the tilted pin power distribution along the x direction.

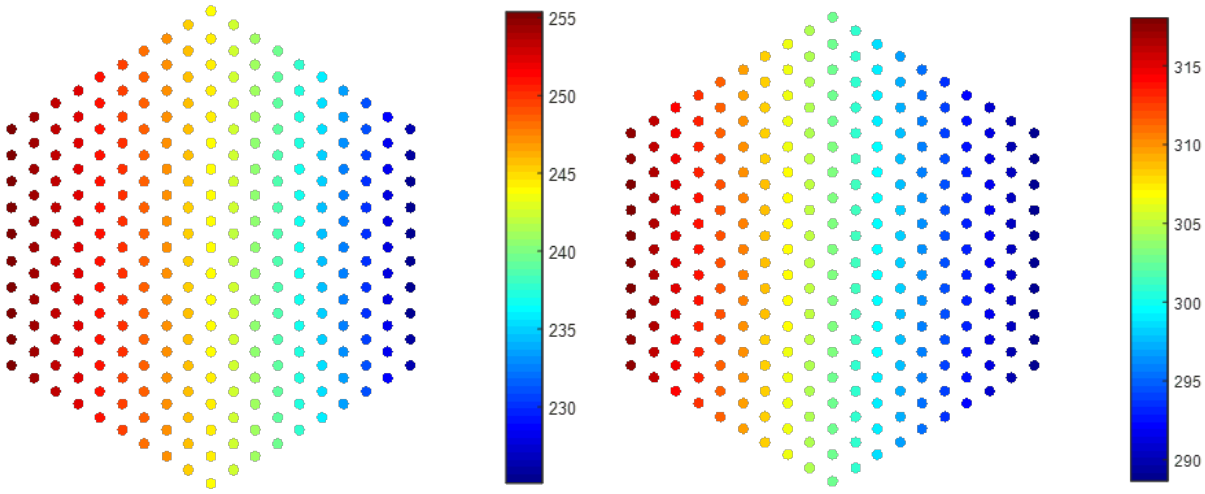

Fig. D.5 Pin Average Power Density (W/cc) given by RCT for Segments H (left) and D (Right) of Assembly OC61

For a consistent comparison of pin power distribution within assembly, the pin power distributions obtained with CURVE and RCT were renormalized by making the node total power of each segment equal. Fig. D.6 shows the relative difference of segment-averaged pin power densities in the segment H of the assembly OC61. One can still see 1% difference occurred at periphery pins near the left and right boundaries of assembly. CURVE yields a steeper pin power distribution along the x direction since RCT adopted the same axial flux profile for each node using the same surface-averaged fluxes and partial currents on the top and bottom interfaces. This influence can be more pronounced when we compare the power densities near the segment ends as displayed in Fig. D.7 and Fig. D.8. The difference in the total nodal power contributes only less than 1% of deviation, which means large radial variations occur on the interfaces.

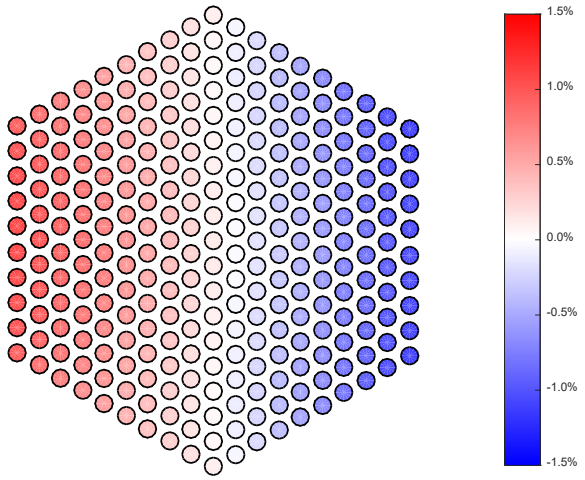

Fig. D.6 Relative Difference of Segment-Averaged Power Density between CURVE and RCT for Segment H of Assembly OC61

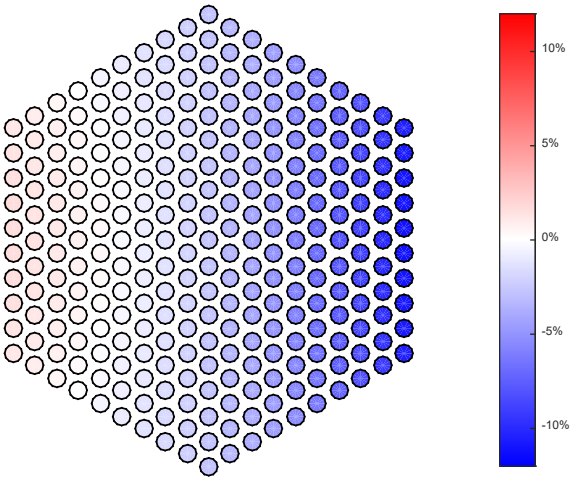

Fig. D.7 Relative Difference of Power Density between CURVE and RCT near Top Interface of Segment H of Assembly OC61

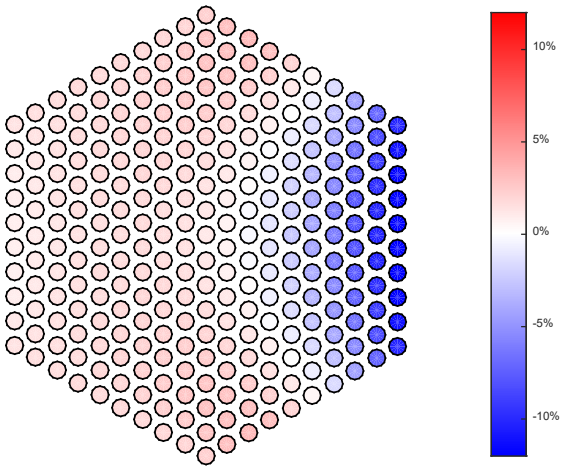

Fig. D.8 Relative Difference of Power Density between CURVE and RCT near Bottom Interface of Segment D of Assembly OC61

Appendix E. Description of CURVE Internal Data Structures

Table E.1. Contents of Data Structure ECF

Element	Data Type	Dimension	Content
DEFINED	Logical	—	Label to tell whether the structure is defined.
NCMP	Integer	—	Number of compositions.
NGROUP	Integer	—	Number of neutron energy groups.
GGROUP	Integer	—	Number of gamma energy groups.
NKERMA	Real, Pointer	(NGROUP, NCMP)	Macroscopic neutron heating cross sections.
GKERMA	Real, Pointer	(GGROUP, NCMP)	Macroscopic gamma heating cross sections.

Table E.2. Contents of Data Structure ZBASIS

Element	Data Type	Dimension	Content
DEFINED	Logical	—	Label to tell whether the structure is defined.
OneSet	Logical	—	Label to tell whether only one set of basis functions are constructed.
NTERM	Integer	—	Total number of polynomial basis functions for neutron flux expansion.
GTERM	Integer	—	Total number of polynomial basis functions for gamma flux expansion.
MTERM	Integer	—	The bigger one of NTERM and GTERM
NZMAX	Integer	—	Maximum flux expansion order in the axial dimension (z-direction)
GZMAX	Integer	—	Gamma flux expansion order in the axial dimension (z-direction)
NTYPE	Integer	—	Number of assembly types.
MNPNT	Integer	—	Maximum number of planar positions of power evaluation in a node among all types of nodes.
NPNT	Integer, Pointer	(NTYPE)	NPNT(I) is the number of planar positions of power evaluation in a node of type I assembly
NPIN	Integer, Pointer	(NTYPE)	NPIN(I) is the number of pins in a type I assembly

Table E.2. Contents of Data Structure ZBASIS (Continued)

Element	Data Type	Dimension	Content
BASE	Real, Pointer	(0:NZMAX, MTERM, MNPNT, NTYPE)	Coefficients for axial distribution along each pin or duct face in a representative node of each assembly type.
GBASE	Real, Pointer	(0:GZMAX, MTERM, MNPNT, NTYPE)	Similar as BASE, defined when OneSet is false, for the separate set of basis functions for gamma flux expansion. In this case, the dimension of BASE becomes (0:NZMAX, NTERM, MNPNT, NTYPE) and stores the basis functions for neutron flux expansion only.

Table E.3. Contents of Data Structure PINFILE

Element	Data Type	Dimension	Content
DEFINED	Logical	—	Label to tell whether the structure is defined.
OneSet	Logical	—	Label to tell whether only one set of basis functions are constructed.
NTERM	Integer	—	Total number of polynomial basis functions for neutron flux expansion.
GTERM	Integer	—	Total number of polynomial basis functions for gamma flux expansion.
MTERM	Integer	—	The bigger one of NTERM and GTERM
NTYPE	Integer	—	Number of assembly types.
MNPNT	Integer	—	Maximum number of planar positions of power evaluation in a node among all types of nodes.
NPNT	Integer, Pointer	(NTYPE)	NPNT(I) is the number of planar positions of power evaluation in a node of type I assembly
NPIN	Integer, Pointer	(NTYPE)	NPIN(I) is the number of pins in a type I assembly
EVALUE	Real, Pointer	(3, MTERM, MNPNT, NTYPE)	Evaluated values of basis functions at the top and bottom points of each segment and averaged values over each segment in a node of each type.
GVALUE	Real, Pointer	(3, GTERM, MNPNT, NTYPE)	Similar as EVALUE, defined when OneSet is false, for the separate set of basis functions for gamma flux expansion.

Appendix F. Broad Energy Group Structures Used in Heating Calculations

Neutron Group		Gamma Group	
Group Index	Upper Energy Boundary (eV)	Group Index	Upper Energy Boundary (eV)
1	1.42E+07	1	2.00E+07
2	1.00E+07	2	1.00E+07
3	6.07E+06	3	8.00E+06
4	3.68E+06	4	7.00E+06
5	2.23E+06	5	6.00E+06
6	1.35E+06	6	5.00E+06
7	8.21E+05	7	4.00E+06
8	4.98E+05	8	3.00E+06
9	3.02E+05	9	2.50E+06
10	1.83E+05	10	2.00E+06
11	1.11E+05	11	1.50E+06
12	6.74E+04	12	1.00E+06
13	4.09E+04	13	7.00E+05
14	2.48E+04	14	4.50E+05
15	1.50E+04	15	3.00E+05
16	9.12E+03	16	1.50E+05
17	5.53E+03	17	1.00E+05
18	3.35E+03	18	7.50E+04
19	2.03E+03	19	4.50E+04
20	1.23E+03	20	3.00E+04
21	7.49E+02	21	2.00E+04
22	4.54E+02		
23	2.75E+02		
24	1.67E+02		
25	1.01E+02		
26	6.14E+01		
27	3.73E+01		
28	2.26E+01		
29	1.37E+01		
30	8.32E+00		
31	3.93E+00		
32	5.32E-01		
33	4.17E-01		

Appendix G. Description of the Input File of SE2-UM

BLOCK 1 : GENERAL INPUT DATA

```
INPUT 1.1
/TITLES/ TEXT
TEXT      Text identifier (11 CHARACTER*6 constants)

INPUT 1.2
/UNITS/ IFORM, JFORM
IFROM     Input parameter unit
              = 0    International engineering (SI) units
              = 1    British engineering units
JFROM     Output parameter unit
              = 0    International engineering (SI) units
              = 1    British engineering units

INPUT 1.3
/CONTROL/ CALTYPE, BOC, EOC, MXITRF, MXOITE, IPAXTM
CALTYPE   Calculation type of the flow allocation
              = 1    Calculate temperature for given flow rates
              = 2    Perfect orifice calculation
              = 3    Flow iteration with given orifice zones and initial flow rates
              = 4    Automatic Flow iteration
              = 5    Flow iteration with user input of orifice zones
BOC       Control parameter for calculation in begin of cycle
              = 1    Temperature calculation for begin of cycle
              = 0    No calculation for begin of cycle
EOC       Control parameter for calculation in end of cycle
              = 1    Temperature calculation for end of cycle
              = 0    No calculation for end of cycle
MXITRF    Maximum number of iterations to be performed in equating the peak 2-sigma
              cladding mid-wall temperature in each fueled orifice zone at certain time
MXOITE    Maximum number of iterations to be performed in equating the peak 2-sigma
              cladding mid-wall temperature in each fueled orifice zone over the entire cycle
IPAXTM    Control parameter for detailed axial temperature output
              = 1    Detailed axial temperature output
              = 0    No output for detailed axial temperature

INPUT 1.4
/COREINFO/ NONASSM, NOASSM, NTYPE, NSTYPE, HEIGHT, NHEIGHT, NORFZN,
           NFRFZN, ICORE, GAPFLO, GAPTH, IHCFCL, IHCFFL
NONASSM   Total number of assemblies in neutronics model
NOASSM    Total number of assemblies in thermal-hydraulic model
NTYPE     Total number of assembly types
NSTYPE    Total number of single-duct assembly types
HEIGHT    Axial height of the thermal-hydraulic model
NHEIGHT   Axial height of the neutronics model
NORFZN    Number of orifice zone
NFRFZN    Number of fueled orifice zone
ICORE     Core geometry type
              = 1    Full core
              = 2    1/3 core
              = 3    1/6 core
GAPFLO    Inter-assembly gap mass flux
GAPTH     Inter-assembly gap thickness
IHCFCL    Input flag for the hot channel sub-factors used in calculating 2σ cladding
          mid-wall temperatures with the semi-statistical horizontal method
              = 0    No hot channel sub-factor is input
```

```
              = 1    Hot channel sub-factors are input
IHCFFL    Input flag for the hot channel sub-factors used in calculating 2σ fuel centerline
          temperatures with the semi-statistical horizontal method
              = 0    No hot channel sub-factor is input
              = 1    Hot channel sub-factors are input

INPUT 1.5
/AXINFO/ NAXMSH, NPMSH, NTCMAP, NTDMAP, NHSTGM, THETA, MAXIT, EPSI, ISCHK
NAXMSH    Number of axial meshes in thermal-hydraulic model
NPMSH     Number of axial meshes in neutronics model
NTCMAP    Number of axial locations for coolant temperature map printout
NTDMAP    Number of axial locations for duct wall temperature map printout
NHSTGM    Number of axial locations for cladding temperature histogram printout
THETA     θ value of the θ-method used in the axial differencing
              = 0.0  Fully explicit scheme
              = 1.0  Fully implicit scheme
MAXIT     Maximum number of iterations for iterative coolant temperature calculation
EPSI      Convergence criteria for iterative coolant temperature calculation (Default 1.0E-04)
ISCHK     Axial stability check indicator when the fully explicit scheme is used for
          coolant temperature calculation
              = 0    Check axial stability and stop if NAXMSH is too small for stability
              = 1    Check axial stability and set NAXMSH to a minimum for stability
              = 2    Check axial stability and change NAXMSH only if stability is violated
              = 3    Do not check stability

INPUT 1.6
/TEMPERATURE/ TIN, TOUT
TIN       Assembly coolant inlet temperature (C or F)
TOUT      Average assembly coolant outlet temperature (C or F)

INPUT 1.7
/MATERIAL/ NCLCOR, NDTCOR
NCLCOR    Coolant property
              = -1   Use the code correlations for NaK
              =  0   Use the code correlations for Sodium
              =  N   A table of N values is input in INPUT 1.10
NDTCOR    Clad and duct property
              = -2   Use the code correlations for HT-9
              = -1   Use the code correlations for D9
              =  0   Use the code correlations for SS316
              =  N   A table of N values is input in INPUT 1.11

INPUT 1.8
/ZTCMAP/ APRNT(1: NTCMAP)
          Axial positions of the coolant temperature map printouts in increasing order
          (cm or in.)

INPUT 1.9
/ZTDMAP/ DPRNT(1: NDTMAP)
          Axial positions for average duct temperature map printouts in increasing order
          (cm or in.)

INPUT 1.10
/ZTDMAP/ HPRNT(1: NHSTGM)
          Axial positions for average duct temperature map printouts in increasing order
          (cm or in.)

INPUT 1.11  (Optional input for NCLCOR >0)
/COOLTPROP/ TEMPC(1: NCLCOR), RHOC(1: NCLCOR), CPC(1: NCLCOR), CONDC(1: NCLCOR),
            VISC(1: NCLCOR)
TEMPC     Coolant property temperatures (C or F)
RHOC      Coolant densities corresponding to the temperatures in TEMPC (kg/m^3 or lbm/ft^3)
```

```
CPC       Coolant specific heats corresponding to the temperatures in TEMPC (J/kg-K or lbm-F)
CONDC     Coolant thermal conductivities corresponding to the temperatures in
          TEMPC (W/m-K or Btu/hr-ft-F)
VISC      Coolant dynamic viscosities corresponding to the temperatures in
          TEMPC (pa-s or lbm/ft-hr)

INPUT 1.12  (Optional input for NDTCOR >0)
/DUCTPROP/ TEMPD(1: NDTCOR), RHOD(1: NDTCOR), CPD(1: NDTCOR), CONDD(1: NDTCOR)
TEMPD     Duct property temperatures (C or F)
RHOD      Duct densities corresponding to the temperatures in TEMPD(kg/m3 or lbm/ft3)
CPD       Duct specific heats corresponding to the temperatures in TEMPD(J/kgK or lbm-F)
CONDD     Duct thermal conductivities corresponding to the temperatures in
          TEMPD (W/m-K or Btu/hr-ft-F)

INPUT 1.13
/CURVE_MISCEL/ IRAD, IAXL, IBOT, ITOP, IPRINT, IPBOT, IPTOP
IRAD      Pin flux evaluation option
              =  0   Use flux evaluated at pin centerline
              =  1   Use averaged flux over pin cross-sectional area
IAXL      Axial pin power profile polynomial order
              =  0   Approximate axial power profile with quadratic polynomial
              =  1   Use the original high-order polynomial in VARIANT solution
IBOT      The lowest axial node plane in the active core
ITOP      The highest axial node plane in the active core
IPRINT    Pin power edit flag
              =  0   Print pin segment power for all assemblies
              =  N   Print pin segment power for the assembly indexed N (N > 0)
              = -N   Print pin segment power for all assemblies of type N (N <= NTYPE)
              = -N   No pin segment power will be printed out (N > NTYPE)
IPBOT     Lowest axial node plane for pin segment power edit, when not given or given as 0,
          set to IBOT
IPTOP     Highest axial node plane for pin segment power edit, when not given or given as 0,
          set to ITOP

INPUT 1.14
/NUMISO/ NDISO, NABISO, NDRENM
NDISO     Number of duct and cladding material isotopes will be input in INPUT 1.15
          (Used only when NDTCOR >0)
NABISO    Number of absorber isotopes
              =  0   Use the default Isotopes. The default isotope names are:
                         'C12', 'B10', 'B11'
              =  N   The name of N isotopes will be input in INPUT 1.19
NDRENM    Number of isotopes in duct and cladding material should be renamed in INPUT 1.16

INPUT 1.15(Optional input for NDISO >0)
/DUCTISO/ DUCISO(1: NDISO), DUCDEN(1: NDISO)
DUCISO    Names for isotopes in the duct and cladding material
DUCDEN    Corresponding atomic fraction of each isotopes in the duct material

INPUT 1.16(Optional input for NDRENM>0)
/DUCTRENM/ DNAME1(1: NDRENM), DNAME2(1: NDRENM)
DNAME1    Nuclide names embedded in the code for duct materials, the embedded nuclides
          include:
              'FE54', 'FE56', 'FE57', 'FE58', 'NI58', 'NI60', 'NI61',
              'NI62', 'NI64', 'CR50', 'CR52', 'CR53', 'CR54', 'MO92',
              'MO94', 'MO95', 'MO96', 'MO97', 'MO98', 'MO00', 'MN55'
DNAME2    Corresponding name in the DIF3D input that is different from the default name DNAME1

INPUT 1.17(Optional input for NABISO >0)
/ABSISO/ ABISO(1: NABISO)
ABISO     Absorber isotope names
```

```
INPUT 1.18
/HTCOEFS/ HT1, HT2, HT3, HT4
          Nu Coefficients for the duct wall-to-coolant heat transfer correlation of the form:
              Nu = HT1 {(RE**HT2)*(Pr**HT3)} + HT4
          When HT1 and HT2 are zero, default is the Lyon-Martinelli correlation:
              HT1 = 0.025, HT2 = HT3 = 0.8 and HT4 = 7.0

INPUT 1.19 (Optional input for IHCFCL = 1)
/NHSETCL/ NHSETC
          Number of hot channel sub-factor sets for 2σ cladding mid-wall temperature
          calculation (NHSETC ≤ 5)

/HCFSETC/ DIRFCL((I,J),I=1,3),J=1,10), STATCL((I,J),I=1,3),J=1,13)

DIRFCL    Direct sub-factors
          I   =  1:  Coolant axial delta T
                 2:  Film delta T
                 3:  Cladding delta T
          J   =  1:  Inlet flow maldistribution
                 2:  Flow distribution calculational uncertainty
                 3:  Cladding circumferential temperature variation
                 4:  Fuel to cladding eccentricity
                 5:  Physics modeling
                 6:  Control rod banking
                 7:  Experimental (nuclear)
                 8:  Criticality
                 9:  Heavy metal
                10:  U-235
STATCL    3σ statistical sub-factors
          I   =  1:  Coolant axial delta T
                 2:  Film delta T
                 3:  Cladding delta T
          J   =  1:  Reactor delta T and inlet temperature variation
                 2:  Inlet flow maldistribution
                 3:  Loop temperature imbalance
                 4:  Subchannel flow area
                 5:  Film heat transfer coefficient
                 6:  Coolant properties
                 7:  Flow distribution calculation uncertainties
                 8:  Experimental
                 9:  Criticality
                10:  Pellet diameter
                11:  Unirradiated fuel conductivity
                12:  Porosity of swollen fuel (conductivity)
                13:  Plutonium weight percent (conductivity)

INPUT 1.20 (Optional input for IHCFFL = 1)
/NHSETFL/ NHSETF
          Number of hot channel sub-factor sets for fuel centerline temperature calculation
          (NHSETF ≤ 5)
/HCFSETF/ DIRFFL((I,J),I=1,3),J=1,10), STATFL((I,J),I=1,3),J=1,15)

DIRFFL    Direct sub-factors
          I   =  1:  Coolant axial delta T
                 2:  Film delta T
                 3:  Cladding delta T
          J   =  1:  Inlet flow maldistribution
                 2:  Flow distribution calculational uncertainty
                 3:  Cladding circumferential temperature variation
                 4:  Fuel to cladding eccentricity
                 5:  Physics modeling
                 6:  Control rod banking
```

```
                 7:  Experimental (nuclear)
                 8:  Criticality
                 9:  Heavy metal
                10:  U-235
STATFL    3σ statistical sub-factors
          I   =  1:  Coolant axial delta T
                 2:  Film delta T
                 3:  Cladding delta T
          J   =  1:  Reactor delta T and inlet temperature variation
                 2:  Inlet flow maldistribution
                 3:  Loop temperature imbalance
                 4:  Subchannel flow area
                 5:  Film heat transfer coefficient
                 6:  Coolant properties
                 7:  Flow distribution calculation uncertainties
                 8:  Experimental
                 9:  Criticality
                10:  Pellet diameter
                11:  Unirradiated fuel conductivity
                12:  Porosity of swollen fuel (conductivity)
                13:  Plutonium weight percent (conductivity)
                14:  Zirconium (conductivity)
                15:  Fissile fuel distribution (conductivity)
```

BLOCK 2: ASSEMBLY TYPE DATA

```
INPUT 2.1
/ASSEMTYPE/ NROD(1:NTYPE), FP(1:NTYPE), LEAD(1:NTYPE), FLAT(1:NTYPE), DUCTTH(1:NTYPE),
          CLADOD(1:NTYPE), WIREOD(1:NTYPE), SHWIRE(1:NTYPE), SF(1:NTYPE), CLADTH(1:NTYPE),
          GAK(1:NTYPE), TYLAB(1:NTYPE), TYDSCPT(1:NTYPE), IFUEL(1:NTYPE), TYPELIST(1:NONASSM)
NROD      Number of fuel pins in each assembly type
FP        Fuel pin pitch (cm or in.)
LEAD      Wire wrap lead length (cm or in.)
FLAT      Duct inside flat-to-flat distance. For a bypass assembly, this is the innermost
          duct (cm or in.)
DUCTTH    Duct wall thickness. For a bypass assembly, this is the outer duct thickness
          (cm or in.)
CLADOD    Fuel pin diameter (cm or in.)
WIREOD    Wire wrap diameter (cm or in.)
SHWIRE    Wire wrap diameter in the side and corner subchannels. Default to WIREOD (cm or in.)
SF        Conductivity shape factor.
          Multiplier on the conduction term for the pin assembly.
          This factor is not applied in bypass or inter-assembly
          gap flow subchannels. A value of 1.0 - 1.3 is recommended,
          although 0.0 may be used if the user wished to eliminate
          the conduction contribution to the radial energy mixing.
CLADTH    Cladding thickness (cm or in.)
GAPK      Fuel pin gap conductivity (W/m-K or Btu/hr-ft-F)
TYLAB     Label for identification of assembly type (CHARACTER*6)
TYDSCPT   Description of assembly type (CHARACTER*24)
IFUEL     Indicator for fuel assembly type or non-fuel type
              =  1   Fuel assembly type
              =  0   Non-fuel assembly type
TYPELIST  Assembly type number
              >  0   Fuel assembly type
              =  0   No real assembly in this position
              = -1   Assembly is ignored in the thermal-hydraulic model
INPUT 2.2
/HTCOR/ JHCF(1:NTYPE), IHCF(1:NTYPE), VHCFC((I,J),I=1,NTYPE),J=1,4)
JHCF      Set number of the hot channel sub-factors for fuel temperature calculation
IHCF      Set number of the hot channel sub-factors for cladding temperature calculation
```

```
VHCFC     Hot channel factors for vertical method
              VHCFC(I,1) - HCF for coolant delta T of assembly type I
              VHCFC(I,2) - HCF for film delta T of assembly type I
              VHCFC(I,3) - HCF for clad delta T of assembly type I
              VHCFC(I,4) - Direct factor for heat flux variation of assembly type I

INPUT 2.3 (Parameters for the three-zone fuel model for furl temperature calculation)
/FUELMODEL/ RF((I,J),I=1,3),J=1,NTYPE), WZ((I,J),I=1,3),J=1,NTYPE),
            WP((I,J),I=1,3),J=1,NTYPE), PO((I,J),I=1,3),J=1,NTYPE)
RF(I,J)   Outer radius of zone I of assembly type J
WZ(I,J)   Zr weight fraction in zone I of assembly type J
WP(I,J)   Pu weight fraction in zone I of assembly type J
PO(I,J)   Porosity in zone I of assembly type J

INPUT 2.4 (Optional input for NTYPE>NSTYPE)
/BYPSINF/ CWALLT(1:NTYPE-NSTYPE), CGAPTH(1:NTYPE-NSTYPE)
CWALLT    Thickness of the interior duct (cm or in.)
CGAPTH    Thickness of the bypass gap (cm or in.)

INPUT 2.5
/MIXPARM/ NPARAM, NFSPLT
NPARAM    Mixing parameters ε*1L and C1L index
              = -1   Use Cheng-Todreas correlation in the code
              =  0   Use the Chiu-Rohsenow-Todreas correlation in the code
              >  1   Use profile number MIXPRM to be read in INPUT 3.3
NFSPLT    Flow split index
              = -2   Use Cheng-Todreas correlation in the code
              = -1   Use the Novendstern correlation in the code
              =  0   Use the Chiu-Rohsenow-Todreas correlation in the code
              >  1   Use profile number NFSPLT to be read in INPUT 3.2
```

BLOCK 3: MIXING PARAMETER PROFILES

```
INPUT 3.1
/NUMPROF/ NFSPRF, NMIXPF
NFSPRF    Number of flow split versus Reynolds number profiles to be read in INPUT 3.2
NMIXPF    Number of ε*1L and C1L vs Reynolds number profiles to be read in INPUT 3.3

INPUT 3.2 (Repeat INPUT 3.2 NFSPRF times)
/FSPROF/ NSFPEN, REYNOLF(1:NFSPEN), VELINTR(1:NFSPEN), VELSIDE(1:NFSPEN), VELCONR(1:NFSPEN)
NSFPEN    Number of tabular entries in the current flow split versus Reynolds number profile
REYNOLF   Reynolds number based on the interior subchannel equivalent diameter
VELINTR   Interior subchannel bulk assembly velocity multiplier (V1/V) at the Reynolds number
          in the ARRAY of group REYNOLF
VELSIDE   Side subchannel bulk assembly velocity multiplier (V2/V) at the Reynolds number in
          the ARRAY of group REYNOLF
VELCONR   Corner subchannel bulk assembly velocity multiplier (V3/V) at the Reynolds number
          in the ARRAY of group REYNOLF

INPUT 3.3 (Repeat INPUT 3.2 NMIXPF times)
/MIXPROF/ NMXENT, REYNOLX(1:NMXENT), EDDYDIF(1:NMXENT), SWIRLVE(1:NMXENT)
NMXENT    Number of tabular entries in the current ε*1L and C1L versus Reynolds number profile
REYNOLX   Reynolds number based on the interior Subchannel equivalent diameter at which ε*1L and
          C1L are applied
EDDYDIF   Dimensionless enhanced eddy diffusivity ε*1L applied at the Reynolds number in the
          ARRAY of REYNOLX
SWIRLVE   Ratio of the circumferential swirl velocity to the side subchannel axial velocity,
          C1L, applied at the Reynolds number in the ARRAY of REYNOLX
```

BLOCK 4: BUNDLE SPECIFIC DATA

```
INPUT 4.1 (Optional input for CALTYPE = 1, 3, 5)
/ORIFLO/ FLOW(1:NOASSM), NOZ(1:NOASSM)
FLOW      Assembly nominal flow rate in thermal-hydraulic model (kg/s or lbm/hr)
NOZ       Orifice zone number for assembly in thermal-hydraulic model

INPUT 4.2
/NSTAGF/ NSTGB, NSTGE
NSTGB     Number of input stage factor for BOC
NSTGE     Number of input stage factor for EOC

INPUT 4.3 (Optional input for NSTGB > 0 or NSTGE > 0)
/STAGEFACTOR/ REGB(1:NSTGB), STGFB(1:NSTGB), REGE(1:NSTGE), STGFE(1:NSTGE)
REGB      Region name of stage factor for BOC
STGFB     Corresponding Stage factor for BOC
REGE      Region name of stage factor for EOC
STGFE     Corresponding Stage factor for EOC
```

Appendix H. Post-processing of the PROTEUS-SN Solution

A computational module for post-processing of PROTEUS-SN solutions has been developed to generate element-averaged fluxes that will be used for calculating form functions in the RAINBOW code.

H.1. Method for Calculation of Element-averaged Flux

In the preliminary RAINBOW code, we only deal with 3-node triangular element and 4-node quadrilateral element that appears in the heterogeneous assembly model as shown in Fig. H.1. Additional types of element including higher order elements need to be added to the RAINBOW code in the future development.

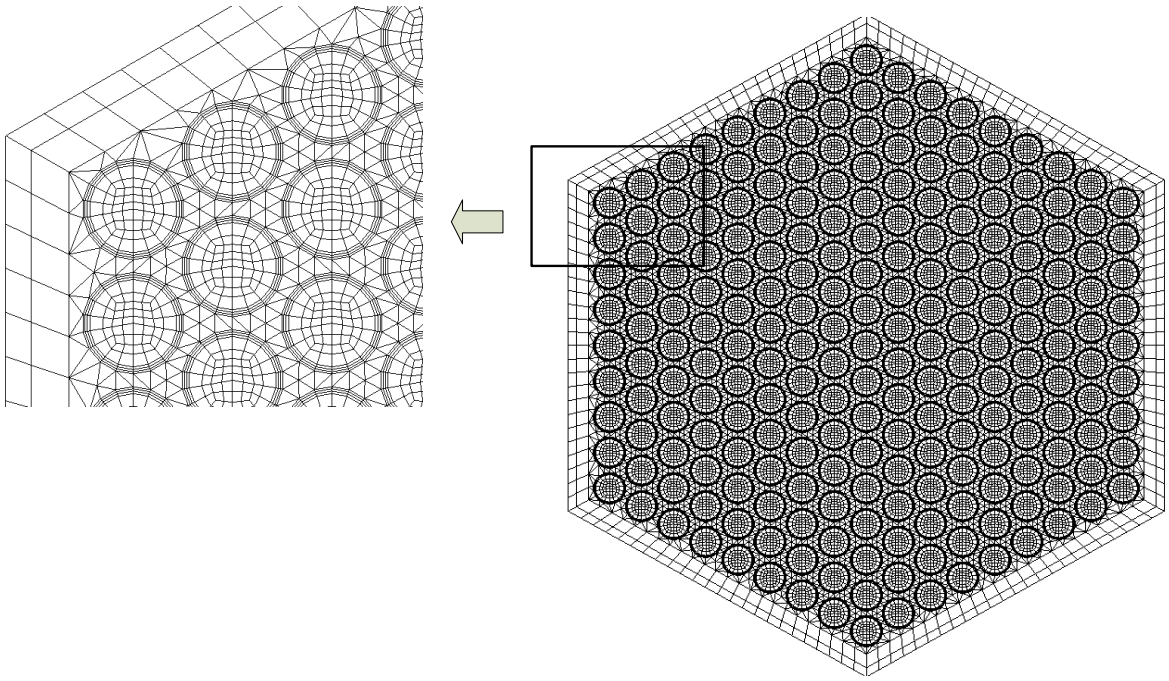

Fig. H.1 Finite Element Mesh for Heterogeneous Assembly Model with 3-Node Triangular Element and 4-Node Quadrilateral Element

The 3-node triangular element and 4-node quadrilateral element in Cartesian coordinates are pictured in Fig. H.2. The 3-node triangular element is linear, that is, a within-element distribution of quantity z (such as flux) can be written as

$$z = ax + by + c\,. \tag{H.1}$$

For linear triangular element, the element-averaged value is equivalent to the volume underneath the triangle divided by the element area. After some algebra, we have

$$V = \frac{\left|(z1+z2+z3)*\left[(x1y2-x2y1)+(x2y3-x3y2)+(x3y1-x1y3)\right]\right|}{6}, \tag{H.2}$$

$$A = \frac{\left|(x1y2 - x2y1) + (x2y3 - x3y2) + (x3y1 - x1y3)\right|}{2}, \tag{H.3}$$

$$\overline{z} = \frac{V}{A} = \frac{(z1 + z2 + z3)}{3}. \tag{H.4}$$

Eq. (H.4) can also be obtained directly from the linearity of the element.

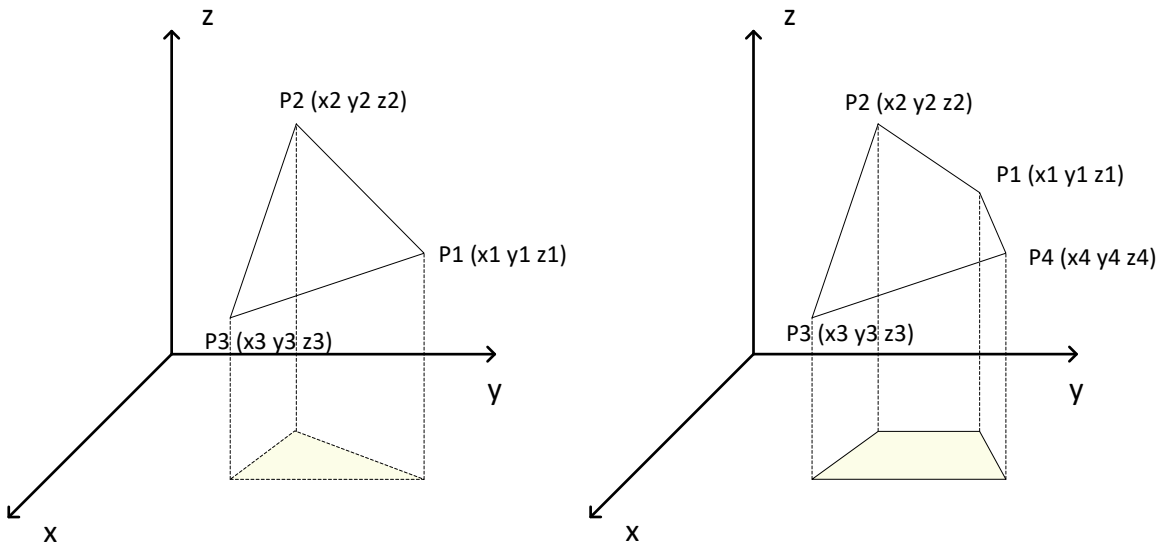

Fig. H.2 Illustrations of 3-Node Triangular Element (Left) and 4-Node Quadrilateral Element (Right)

The 4-node quadrilateral element is bilinear element, that is, it is linear at the edges and the within element flux is given by

$$z(x, y) = a1 + a2 \cdot x + a3 \cdot y + a4 \cdot xy = u(x, y). \tag{H.5}$$

To calculate the element averaged flux, we can use an iso-parametric mapping to translate the element to a square as shown in Fig. H.3. The shape functions are given by

$$\begin{aligned} N1(s,t) &= \frac{1}{4}(1+s)(1+t) \\ N2(s,t) &= \frac{1}{4}(1-s)(1+t) \\ N3(s,t) &= \frac{1}{4}(1-s)(1-t) \\ N4(s,t) &= \frac{1}{4}(1+s)(1-t) \end{aligned} \tag{H.6}$$

Then we have

$$
\begin{aligned}
x(s,t) &= N1(s,t)x1 + N2(s,t)x2 + N3(s,t)x3 + N4(s,t)x4 \\
y(s,t) &= N1(s,t)y1 + N2(s,t)y2 + N3(s,t)y3 + N4(s,t)y4 \\
v(s,t) &= N1(s,t)u1 + N2(s,t)u2 + N3(s,t)u3 + N4(s,t)u4
\end{aligned}
\tag{H.7}
$$

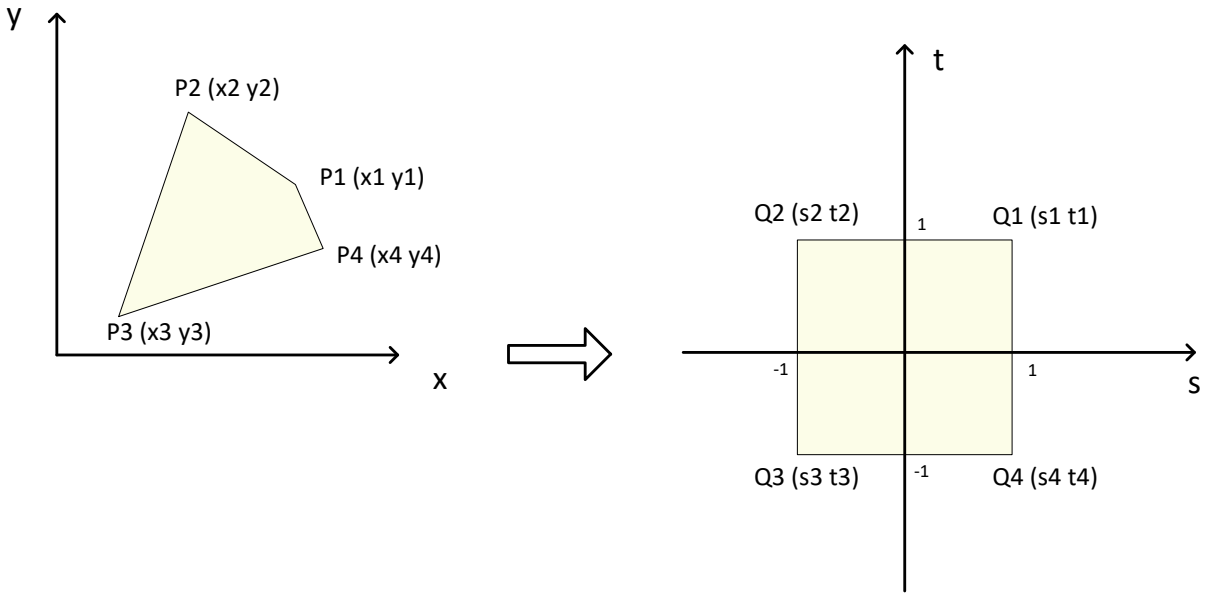

Fig. H.3 Isoparametric Mapping

Representing the shape function in a matrix form, we have

$$
\vec{N}(s,t) = \frac{1}{4} \cdot \begin{bmatrix} 1 & 1 & 1 & 1 \\ 1 & -1 & 1 & -1 \\ 1 & -1 & -1 & 1 \\ 1 & 1 & -1 & -1 \end{bmatrix} \begin{bmatrix} 1 \\ s \\ t \\ st \end{bmatrix} = N \cdot \vec{p}\,, \tag{H.8}
$$

with

$$
\vec{p} = \begin{bmatrix} 1 \\ s \\ t \\ st \end{bmatrix}. \tag{H.9}
$$

Then, we can write Eq. (H.7) in a matrix form as

$$
\begin{aligned}
x(s,t) &= \vec{x}^{\mathrm{T}} \cdot \vec{N}(s,t) = \vec{x}^{\mathrm{T}} \cdot N \cdot \vec{p} = \overrightarrow{xst}^{\mathrm{T}} \cdot \vec{p} \\
y(s,t) &= \vec{y}^{\mathrm{T}} \cdot \vec{N}(s,t) = \vec{y}^{\mathrm{T}} \cdot N \cdot \vec{p} = \overrightarrow{yst}^{\mathrm{T}} \cdot \vec{p}\,, \\
v(s,t) &= \vec{u}^{\mathrm{T}} \cdot \vec{N}(s,t) = \vec{u}^{\mathrm{T}} \cdot N \cdot \vec{p}
\end{aligned}
\tag{H.10}
$$

where we have

$$\overrightarrow{xst} = N^T \vec{x}\,, \tag{H.11}$$

and

$$\overrightarrow{yst} = N^T \vec{y}\,. \tag{H.12}$$

The integration of flux over the element is

$$I_e = \iint u(x,y)dxdy = \iint v(s,t)\left|J\right|dsdt\,, \tag{H.13}$$

where

$$\left|J\right| = \mathrm{Det}\begin{bmatrix} \dfrac{\partial x}{\partial s} & \dfrac{\partial y}{\partial s} \\ \dfrac{\partial x}{\partial t} & \dfrac{\partial y}{\partial t} \end{bmatrix}. \tag{H.14}$$

We need to find the expressions for $v(s,t)$ and $\left|J\right|(s,t)$. Let

$$v(s,t) = a1 + a2\cdot s + a3\cdot t + a4\cdot st = a^{\mathrm{T}}\cdot \vec{p}\,. \tag{H.15}$$

Comparing Eq. (H.15) to Eq. (H.10), we have

$$a = N^{\mathrm{T}}\cdot \vec{u}\,. \tag{H.16}$$

Let

$$\left|J\right|(s,t) = b1 + b2\cdot s + b3\cdot t + b4\cdot st = b^{\mathrm{T}}\cdot \vec{p}\,. \tag{H.17}$$

By using Eq. (H.14), we can obtain

$$\vec{b} = \begin{bmatrix} xst(2)yst(3) - yst(2)xst(3) \\ xst(2)yst(4) - yst(2)xst(3) \\ xst(4)yst(3) - yst(4)xst(3) \\ 0 \end{bmatrix}. \tag{H.18}$$

Expanding the integration in Eq. (H.13), the element total flux can be written as

$$I_e = \iint v(s,t)\left|J\right|dsdt = \int_{-1}^{1}\int_{-1}^{1} (a1 + a2\cdot s + a3\cdot t + a4\cdot st)\cdot(b1 + b2\cdot s + b3\cdot t + b4\cdot st)dsdt\,. \tag{H.19}$$

By performing the integration in Eq. (H.19), we have the algebraic expression of the total flux as

$$I_e = 4a1b1 + \frac{4}{3}(a2b2 + a3b3) + \frac{4}{9}a4b4\,. \tag{H.20}$$

H.2. Programming Information

The full solution of PROTEUS-SN code is stored in an HDF5 data format. As an example, the data structure of the HDF5 output file for a single pin cell problem is shown in Fig. H.4. The pin cell model has three blocks representing three regions with different material

assignments. The output flux is on the finite element vertices and stored in the dataset VERTEXDATA. The dataset XYZ stores the coordinates of each vertex. The dataset GLOBALID provides the information on to which element each vertex belongs. With these datasets, we can calculate the element-averaged flux used to generate the assembly form functions.

```
HDF5 "example.hdf5" {
FILE_CONTENTS {
 group     /
 group     /BLOCK000000000001
 dataset   /BLOCK000000000001/ELEMENTDATA
 dataset   /BLOCK000000000001/GLOBALID
 dataset   /BLOCK000000000001/INFO
 dataset   /BLOCK000000000001/VERTEXDATA
 dataset   /BLOCK000000000001/XYZ
 group     /BLOCK000000000002
 dataset   /BLOCK000000000002/ELEMENTDATA
 dataset   /BLOCK000000000002/GLOBALID
 dataset   /BLOCK000000000002/INFO
 dataset   /BLOCK000000000002/VERTEXDATA
 dataset   /BLOCK000000000002/XYZ
 group     /BLOCK000000000003C
 dataset   /BLOCK000000000003/ELEMENTDATA
 dataset   /BLOCK000000000003/GLOBALID
 dataset   /BLOCK000000000003/INFO
 dataset   /BLOCK000000000003/VERTEXDATA
 dataset   /BLOCK000000000003/XYZ
 dataset   /CONTROL
 dataset   /ELEMENT_VECTOR_NAMES
 dataset   /VERTEX_VECTOR_NAMES
 }
}
```

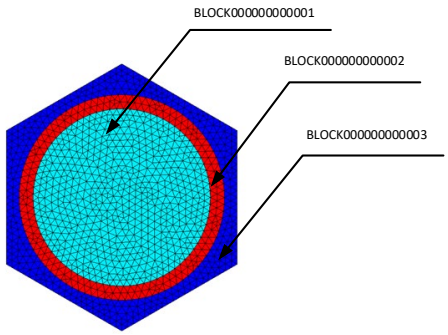

Fig. H.4 Output Structure of PROTEUS-SN in HDF5 Format

Table H.1 presents a sample input for the utility program for postprocessing the PROTEUS-SN HDF5 output file. The input file contains three data blocks. The PROGLEM_CONTROL block specifies the HDF5 file name, model dimension, number of groups, number of blocks being processed and number of vertices within each assembly. It also specifies the number of elements in each block and the element types. The type 11 indicates 3-node linear element and type 21 indicates 4-node bilinear element. These are the only two types of element that are supported by the current RAINBOW code. The DATASETS data block gives the raw data sets that are to be extracted from the hdf5 file. The OUTPUTFILE data block specifies the output file names.

H.3. A Test Problem

The numerical test of the PROTEUS-SN post-processing utility program has been performed based on a simple two-dimensional model shown in Fig. H.5. The core has two rings of fuel assembly with fully heterogeneous assembly model. We extracted the power data of fuel assembly 5 from the HDF5 output and calculated the element averaged flux using the method presented in this appendix. The element-averaged data is visualized using MATLAB and compared with the results obtained using data processing software VisIt as shown in Fig. H.6. The element-averaged power for assembly 5 calculated using the post-processing module is identical to that obtained from VisIt.

Table H.1 Sample Input for Utility Program for Postprocessing HDF5 File

```
&PROBLEM_CONTROL
  FileName='FUEL_ASSEMBLY_REFLECTIVE.hdf5'
  Dims                        = 2
  NumGroup                    = 33
  NumVertex                   = 1445
  NumBlockOut                 = 3
  NumElement(1:5)             = 1592, 288, 288
  NodePerElement(1:5)         = 3,4,4
  ElementType(1:5)            = 11,21,21
/
&DATASETS
  DataSetFlux(1:5) = '/BLOCK000000000001/VERTEXDATA'
                     '/BLOCK000000000002/VERTEXDATA'
                     '/BLOCK000000000003/VERTEXDATA'

  DataSetGlobalID(1:5) = '/BLOCK000000000001/GLOBALID'
                         '/BLOCK000000000002/GLOBALID'
                         '/BLOCK000000000003/GLOBALID'

  Dataset(1:5) = '/BLOCK000000000001/XYZ'
                 '/BLOCK000000000002/XYZ'
                 '/BLOCK000000000003/XYZ'
/
&OUTPUTFILE
  output(1:5) = 'BLOCK000000000001.out'
                'BLOCK000000000002.out'
                'BLOCK000000000003.out'
/
```

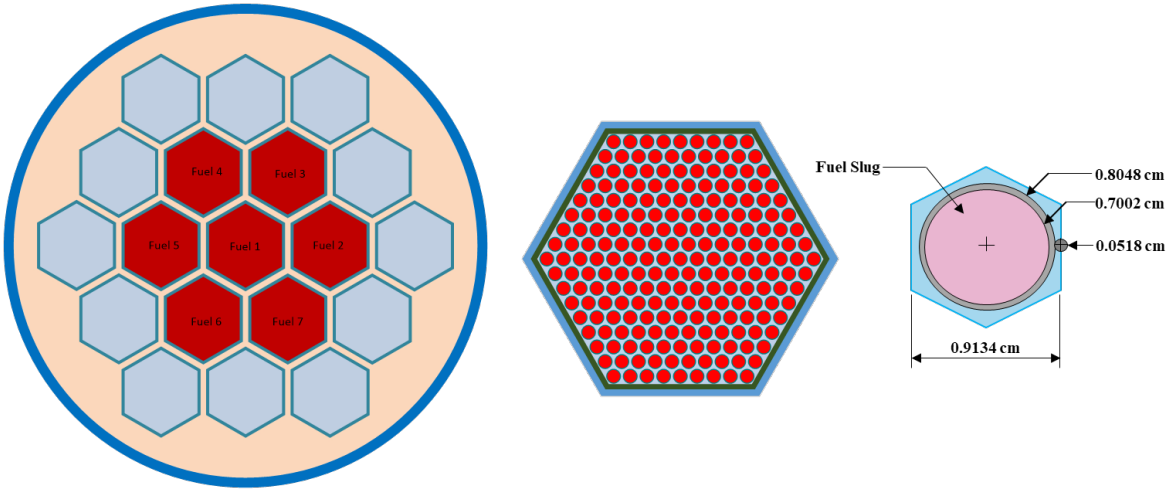

Fig. H.5 A 2D Toy Model for Testing PROTESU-SN Post-Processing Module

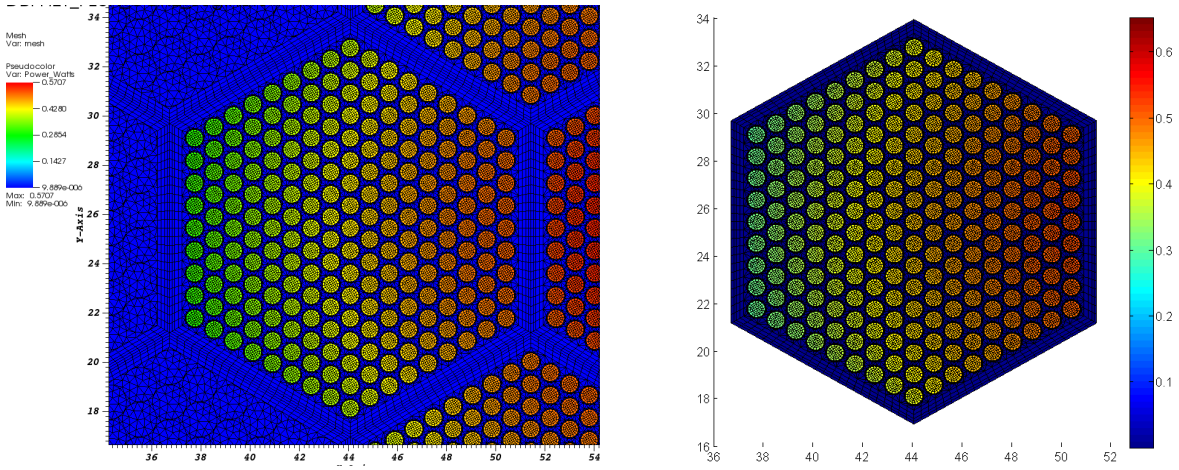

Fig. H.6 Element Averaged Power In Assembly 5 obtained using the Post-Processing Module (Right) and VisIt (Left)

Appendix I. Material Temperatures in AFR-100 Bowing Reactivity Analysis

I	Fuel Inner Core	Material Temperature
IA	Lower Structure	668
IB	Lower Shield	668
IC	Lower Reflector	668
ID	Inner Bottom Fuel	Coolant 733 / Structure 743 / Fuel 883
IE	Inner Middle Fuel	Coolant 733 / Structure 743 / Fuel 883
IF	Inner Top Fuel	Coolant 733 / Structure 743 / Fuel 883
IG	Gas Plenum Bond	798
IH	Gas Plenum Gas	798
II	Upper Structure	798

M	Fuel Middle Core	Material Temperature
MA	Lower Structure	668
MB	Lower Shield	668
MC	Lower Reflector	668
MD	Middle Bottom Fuel	Coolant 747 / Structure 757 / Fuel 897
ME	Middle Middle Fuel	Coolant 747 / Structure 757 / Fuel 897
MF	Middle Top Fuel	Coolant 747 / Structure 757 / Fuel 897
MG	Gas Plenum Bond	826
MH	Gas Plenum Gas	826
MI	Upper Structure	826

O	Fuel Outer Core	Material Temperature
OA	Lower Structure	668
OB	Lower Shield	668
OC	Lower Reflector	668
OD	Outer Bottom Fuel	Coolant 755 / Structure 765 / Fuel 905
OE	Outer Middle Fuel	Coolant 755 / Structure 765 / Fuel 905
OF	Outer Top Fuel	Coolant 755 / Structure 765 / Fuel 905
OG	Gas Plenum Bond	842
OH	Gas Plenum Gas	842
OI	Upper Structure	842

C	Primary Control (Center) – Natural B4C	Material Temperature
CA	Lower Structure	668
CB	Lower Shield	668
CC	Empty	Coolant 668 / Structure 729
CG	Control Absorber (Primary Natural)	789

E	Primary Control (Non-Center) – Enriched B4C	Material Temperature
EA	Lower Structure	668
EB	Lower Shield	668
EC	Empty	Coolant 668 / Structure 729
EG	Control Absorber (Primary Enriched)	789

N	Secondary Control– Natural B4C	Material Temperature
NA	Lower Structure	668
NB	Lower Shield	668
NC	Empty	Coolant 668 / Structure 729
NG	Control Absorber (Secondary Natural)	789

R	Radial Reflector	Material Temperature
RA	Lower Structure	668
RB	Lower Shield	668
RC	Reflector Pins	734
RI	Upper Structure	799

S	Radial Shield	Material Temperature
SA	Lower Structure	668
SB	Lower Shield	668
SC	Shield Pins	725
SI	Upper Structure	782

Appendix J. Assembly Bowing Reactivity Coefficients for AFR-100

Unit: pcm/mm displacement

SEGMENT 1	Assembly No.	Direction 1	Direction 2	Direction 3	Direction 4	Direction 5	Direction 6
	1	-0.00010	-0.00011	-0.00011	-0.00011	-0.00011	-0.00011
	2	-0.00033	-0.00019	0.00007	0.00020	0.00007	-0.00019
	3	-0.00018	-0.00030	-0.00018	0.00006	0.00017	0.00006
	4	0.00015	0.00005	-0.00016	-0.00027	-0.00016	0.00005
	5	-0.00006	-0.00006	-0.00005	-0.00005	-0.00005	-0.00005
	6	0.00005	0.00013	0.00004	-0.00015	-0.00025	-0.00015
	7	-0.00005	-0.00006	-0.00006	-0.00005	-0.00005	-0.00005
	8	-0.00005	-0.00007	-0.00009	-0.00011	-0.00009	-0.00007
	9	0.00005	-0.00014	-0.00025	-0.00015	0.00004	0.00013
	10	-0.00014	0.00005	0.00014	0.00005	-0.00015	-0.00025
	11	-0.00007	-0.00006	-0.00008	-0.00010	-0.00011	-0.00009
	12	0.00017	0.00007	-0.00015	-0.00027	-0.00016	0.00005
	13	-0.00027	-0.00015	0.00006	0.00016	0.00005	-0.00016
	14	-0.00025	-0.00014	0.00007	0.00018	0.00007	-0.00014
	15	-0.00013	-0.00024	-0.00014	0.00005	0.00015	0.00007
	16	-0.00005	-0.00005	-0.00004	-0.00003	-0.00003	-0.00004
	17	-0.00026	-0.00014	0.00008	0.00018	0.00007	-0.00015
	18	-0.00013	-0.00023	-0.00013	0.00006	0.00015	0.00006
	19	0.00007	-0.00013	-0.00024	-0.00014	0.00005	0.00015
	20	-0.00004	-0.00005	-0.00005	-0.00004	-0.00003	-0.00003
	21	-0.00014	-0.00023	-0.00013	0.00007	0.00015	0.00005
	22	-0.00001	-0.00001	-0.00003	-0.00003	-0.00003	-0.00001
	23	-0.00003	-0.00004	-0.00003	-0.00001	-0.00001	-0.00002
	24	0.00001	0.00005	0.00001	-0.00007	-0.00011	-0.00007
	25	0.00005	0.00001	-0.00007	-0.00011	-0.00007	0.00001
	26	-0.00004	-0.00003	-0.00002	-0.00001	-0.00001	-0.00003
	27	-0.00001	-0.00001	-0.00001	-0.00003	-0.00004	-0.00003
	28	-0.00002	-0.00003	-0.00004	-0.00003	-0.00001	-0.00001
	29	-0.00007	0.00001	0.00005	0.00001	-0.00007	-0.00011
	30	0.00001	0.00005	0.00001	-0.00007	-0.00011	-0.00007
	31	-0.00003	-0.00004	-0.00003	-0.00002	-0.00001	-0.00001
	32	-0.00002	-0.00001	-0.00001	0.00000	-0.00001	-0.00001
	33	-0.00002	-0.00003	-0.00002	-0.00001	0.00000	-0.00001
	34	-0.00005	0.00002	0.00005	0.00001	-0.00005	-0.00009
	35	0.00001	0.00000	-0.00004	-0.00007	-0.00007	-0.00003
	36	0.00002	-0.00005	-0.00008	-0.00005	0.00001	0.00005
	37	-0.00003	-0.00002	-0.00001	0.00000	-0.00001	-0.00002
	38	-0.00001	-0.00001	-0.00001	-0.00001	0.00000	-0.00001
	39	-0.00001	-0.00002	-0.00003	-0.00002	-0.00001	0.00000

	40	-0.00009	-0.00005	0.00003	0.00006	0.00002	-0.00006
	41	-0.00003	-0.00001	-0.00001	-0.00003	-0.00006	-0.00006
	42	0.00006	0.00003	-0.00005	-0.00009	-0.00006	0.00002
	43	-0.00002	-0.00003	-0.00002	-0.00001	0.00000	-0.00001
	44	-0.00001	-0.00001	0.00000	0.00001	0.00000	-0.00001
	45	-0.00001	-0.00001	-0.00001	0.00000	0.00000	-0.00001
	46	-0.00001	0.00000	0.00001	0.00000	-0.00001	-0.00002
	47	-0.00010	-0.00005	0.00005	0.00009	0.00003	-0.00006
	48	-0.00004	-0.00009	-0.00005	0.00003	0.00007	0.00004
	49	0.00000	-0.00001	-0.00002	-0.00001	0.00000	0.00001
	50	-0.00001	-0.00001	-0.00001	0.00000	0.00000	-0.00001
	51	-0.00001	-0.00001	-0.00001	0.00000	0.00001	0.00000
	52	-0.00001	-0.00001	-0.00001	-0.00001	0.00000	0.00000
	53	-0.00002	-0.00001	0.00000	0.00001	0.00000	-0.00001
	54	-0.00005	-0.00008	-0.00004	0.00003	0.00007	0.00002
	55	0.00003	-0.00004	-0.00008	-0.00005	0.00002	0.00007
	56	0.00001	0.00000	-0.00001	-0.00002	-0.00001	0.00000
	57	-0.00001	-0.00001	-0.00001	-0.00001	0.00000	0.00000
	58	0.00000	0.00000	0.00000	0.00000	0.00000	0.00000
	59	-0.00001	-0.00001	0.00001	0.00001	0.00001	-0.00001
	60	-0.00001	-0.00001	0.00000	0.00001	0.00001	-0.00001
	61	-0.00001	-0.00001	0.00000	0.00001	0.00001	0.00000
	62	-0.00002	-0.00002	0.00000	0.00002	0.00002	0.00000
	63	-0.00001	-0.00001	0.00000	0.00001	0.00001	0.00000
	64	-0.00001	-0.00001	-0.00001	0.00001	0.00001	0.00000
	65	-0.00001	-0.00001	-0.00001	0.00001	0.00001	0.00001
	66	0.00000	0.00000	0.00000	0.00000	0.00000	0.00000
	67	-0.00001	-0.00001	-0.00001	0.00001	0.00001	0.00001
	68	-0.00001	-0.00001	-0.00001	0.00000	0.00001	0.00001
	69	0.00000	-0.00001	-0.00001	0.00000	0.00001	0.00001
	70	0.00000	-0.00002	-0.00002	0.00000	0.00002	0.00002
	71	0.00000	-0.00001	-0.00001	0.00000	0.00001	0.00001
	72	0.00000	-0.00001	-0.00001	-0.00001	0.00001	0.00001
	73	0.00001	-0.00001	-0.00001	-0.00001	0.00001	0.00001
SEGMENT 2	Assembly No.	Direction 1	Direction 2	Direction 3	Direction 4	Direction 5	Direction 6
	1	-0.00044	-0.00044	-0.00044	-0.00044	-0.00044	-0.00044
	2	-0.01446	-0.00720	0.00817	0.01627	0.00817	-0.00720
	3	-0.00724	-0.01451	-0.00721	0.00822	0.01634	0.00819
	4	0.00634	0.00321	-0.00227	-0.00461	-0.00227	0.00321
	5	-0.00391	-0.00399	0.00025	0.00456	0.00464	0.00041
	6	0.00360	0.00712	0.00359	-0.00265	-0.00534	-0.00263
	7	0.00024	-0.00399	-0.00391	0.00042	0.00465	0.00456

	8	-0.00173	-0.00105	0.00032	0.00100	0.00032	-0.00105
	9	-0.00034	-0.01060	-0.00941	0.00123	0.01149	0.01109
	10	-0.01093	-0.00001	0.01175	0.01181	0.00090	-0.01007
	11	-0.00105	-0.00175	-0.00109	0.00026	0.00096	0.00031
	12	0.01183	0.00005	-0.01095	-0.01015	0.00085	0.01184
	13	-0.00941	-0.01060	-0.00035	0.01107	0.01148	0.00123
	14	-0.02691	-0.01346	0.01415	0.02831	0.01415	-0.01346
	15	-0.01561	-0.02069	-0.00507	0.01635	0.02219	0.00587
	16	-0.00861	-0.00867	0.00021	0.00918	0.00923	0.00032
	17	-0.02150	-0.01595	0.00635	0.02303	0.01669	-0.00555
	18	-0.01384	-0.02763	-0.01381	0.01453	0.02907	0.01451
	19	0.00635	-0.01594	-0.02149	-0.00555	0.01669	0.02304
	20	0.00021	-0.00866	-0.00861	0.00032	0.00923	0.00917
	21	-0.00513	-0.02077	-0.01563	0.00593	0.02228	0.01637
	22	-0.01701	-0.00843	0.00883	0.01750	0.00883	-0.00843
	23	-0.01393	-0.01113	0.00307	0.01438	0.01151	-0.00260
	24	-0.01117	-0.00689	0.00437	0.01177	0.00797	-0.00371
	25	-0.00690	-0.01115	-0.00369	0.00797	0.01175	0.00435
	26	-0.01110	-0.01387	-0.00257	0.01149	0.01433	0.00304
	27	-0.00842	-0.01699	-0.00841	0.00883	0.01749	0.00881
	28	-0.00258	-0.01387	-0.01110	0.00305	0.01433	0.01149
	29	-0.00368	-0.01116	-0.00692	0.00435	0.01177	0.00799
	30	0.00435	-0.00693	-0.01117	-0.00369	0.00799	0.01178
	31	0.00306	-0.01113	-0.01392	-0.00260	0.01151	0.01438
	32	-0.01525	-0.00757	0.00781	0.01550	0.00781	-0.00757
	33	-0.01547	-0.01037	0.00527	0.01581	0.01069	-0.00495
	34	-0.01625	-0.00819	0.00840	0.01668	0.00868	-0.00765
	35	-0.00246	-0.00251	-0.00019	0.00219	0.00224	-0.00009
	36	-0.00816	-0.01628	-0.00771	0.00865	0.01672	0.00847
	37	-0.01038	-0.01547	-0.00495	0.01069	0.01580	0.00526
	38	-0.00759	-0.01527	-0.00757	0.00782	0.01552	0.00781
	39	-0.00495	-0.01547	-0.01037	0.00527	0.01580	0.01069
	40	-0.00774	-0.01629	-0.00814	0.00849	0.01672	0.00863
	41	-0.00014	-0.00257	-0.00257	-0.00014	0.00229	0.00229
	42	0.00851	-0.00813	-0.01629	-0.00775	0.00863	0.01673
	43	0.00527	-0.01037	-0.01547	-0.00495	0.01068	0.01580
	44	-0.01013	-0.00506	0.00517	0.01033	0.00517	-0.00506
	45	-0.01276	-0.00802	0.00482	0.01293	0.00817	-0.00469
	46	-0.01282	-0.01025	0.00264	0.01300	0.01045	-0.00247
	47	-0.02364	-0.01512	0.00890	0.02431	0.01531	-0.00862
	48	-0.01506	-0.02352	-0.00855	0.01525	0.02417	0.00883
	49	-0.01026	-0.01282	-0.00247	0.01046	0.01300	0.00263
	50	-0.00801	-0.01277	-0.00471	0.00816	0.01295	0.00484

	51	-0.00507	-0.01012	-0.00505	0.00517	0.01032	0.00515
	52	-0.00468	-0.01277	-0.00803	0.00481	0.01294	0.00818
	53	-0.00247	-0.01284	-0.01028	0.00263	0.01301	0.01048
	54	-0.00858	-0.02359	-0.01510	0.00886	0.02425	0.01529
	55	0.00887	-0.01509	-0.02359	-0.00859	0.01528	0.02425
	56	0.00264	-0.01027	-0.01284	-0.00247	0.01047	0.01301
	57	0.00481	-0.00803	-0.01276	-0.00468	0.00817	0.01293
	58	0.00000	0.00000	0.00000	0.00000	0.00000	0.00000
	59	-0.00854	-0.00537	0.00319	0.00862	0.00546	-0.00313
	60	-0.00933	-0.00638	0.00299	0.00945	0.00649	-0.00291
	61	-0.01000	-0.00801	0.00206	0.01015	0.00813	-0.00196
	62	-0.00997	-0.00997	0.00005	0.01011	0.01010	0.00003
	63	-0.00802	-0.01000	-0.00195	0.00813	0.01015	0.00205
	64	-0.00638	-0.00933	-0.00291	0.00649	0.00945	0.00299
	65	-0.00536	-0.00855	-0.00315	0.00545	0.00863	0.00321
	66	0.00000	0.00000	0.00000	0.00000	0.00000	0.00000
	67	-0.00312	-0.00853	-0.00538	0.00318	0.00861	0.00547
	68	-0.00291	-0.00933	-0.00639	0.00298	0.00945	0.00649
	69	-0.00195	-0.01001	-0.00803	0.00205	0.01015	0.00813
	70	0.00005	-0.00999	-0.00999	0.00004	0.01012	0.01012
	71	0.00205	-0.00802	-0.01001	-0.00195	0.00813	0.01015
	72	0.00298	-0.00639	-0.00932	-0.00291	0.00649	0.00944
	73	0.00318	-0.00538	-0.00853	-0.00311	0.00546	0.00861
SEGMENT 3	Assembly No.	Direction 1	Direction 2	Direction 3	Direction 4	Direction 5	Direction 6
	1	-0.00008	-0.00009	-0.00009	-0.00008	-0.00009	-0.00009
	2	0.00746	0.00396	-0.00374	-0.00797	-0.00375	0.00396
	3	0.00441	0.00821	0.00430	-0.00421	-0.00883	-0.00407
	4	-0.05430	-0.02703	0.02725	0.05429	0.02725	-0.02703
	5	-0.02961	-0.02973	-0.00024	0.02936	0.02947	-0.00001
	6	-0.02721	-0.05449	-0.02703	0.02742	0.05444	0.02725
	7	-0.00021	-0.02969	-0.02959	-0.00003	0.02943	0.02934
	8	-0.00006	-0.00009	-0.00014	-0.00016	-0.00014	-0.00009
	9	-0.06123	-0.03329	0.02775	0.06132	0.03355	-0.02799
	10	-0.03346	-0.06070	-0.02727	0.03371	0.06082	0.02710
	11	0.00000	0.00001	-0.00011	-0.00025	-0.00029	-0.00015
	12	-0.02690	-0.06070	-0.03381	0.02676	0.06081	0.03406
	13	0.02699	-0.03373	-0.06085	-0.02713	0.03398	0.06095
	14	-0.06243	-0.03115	0.03111	0.06207	0.03111	-0.03115
	15	-0.06673	-0.03747	0.02960	0.06683	0.03700	-0.02947
	16	-0.06888	-0.06889	-0.00015	0.06847	0.06849	-0.00011
	17	-0.03835	-0.06716	-0.02901	0.03795	0.06729	0.02913
	18	-0.03081	-0.06181	-0.03081	0.03077	0.06135	0.03079

	19	-0.02951	-0.06655	-0.03730	0.02961	0.06667	0.03678
	20	-0.00015	-0.06890	-0.06887	-0.00011	0.06849	0.06847
	21	0.02989	-0.03701	-0.06653	-0.02979	0.03647	0.06665
	22	-0.08473	-0.04238	0.04237	0.08477	0.04237	-0.04238
	23	-0.09651	-0.07568	0.02077	0.09629	0.07530	-0.02105
	24	-0.09537	-0.08243	0.01287	0.09547	0.08301	-0.01254
	25	-0.08225	-0.09519	-0.01253	0.08285	0.09529	0.01285
	26	-0.07565	-0.09641	-0.02097	0.07527	0.09619	0.02069
	27	-0.04235	-0.08465	-0.04232	0.04235	0.08469	0.04231
	28	-0.02098	-0.09643	-0.07567	0.02070	0.09621	0.07529
	29	-0.01239	-0.09501	-0.08222	0.01271	0.09512	0.08283
	30	0.01281	-0.08221	-0.09511	-0.01249	0.08282	0.09522
	31	0.02081	-0.07567	-0.09654	-0.02109	0.07529	0.09632
	32	-0.08188	-0.04109	0.04104	0.08239	0.04105	-0.04109
	33	-0.09133	-0.06441	0.02696	0.09152	0.06444	-0.02705
	34	-0.08301	-0.07966	0.00362	0.08359	0.08002	-0.00329
	35	-0.00175	-0.00175	-0.00010	0.00157	0.00157	-0.00009
	36	-0.08005	-0.08267	-0.00259	0.08039	0.08323	0.00285
	37	-0.06444	-0.09133	-0.02702	0.06447	0.09151	0.02693
	38	-0.04113	-0.08194	-0.04110	0.04109	0.08244	0.04105
	39	-0.02699	-0.09132	-0.06446	0.02689	0.09150	0.06449
	40	-0.00329	-0.08308	-0.07971	0.00363	0.08365	0.08007
	41	-0.00009	-0.00178	-0.00178	-0.00009	0.00159	0.00160
	42	0.00371	-0.07965	-0.08309	-0.00338	0.08001	0.08367
	43	0.02693	-0.06440	-0.09130	-0.02702	0.06443	0.09149
	44	-0.02391	-0.01199	0.01209	0.02425	0.01209	-0.01199
	45	-0.07393	-0.04805	0.02598	0.07430	0.04844	-0.02576
	46	-0.06781	-0.05540	0.01241	0.06807	0.05571	-0.01237
	47	-0.06683	-0.05664	0.01046	0.06734	0.05693	-0.01015
	48	-0.05655	-0.06659	-0.00999	0.05683	0.06707	0.01029
	49	-0.05547	-0.06783	-0.01231	0.05578	0.06809	0.01235
	50	-0.04809	-0.07400	-0.02580	0.04847	0.07437	0.02601
	51	-0.01203	-0.02397	-0.01200	0.01213	0.02429	0.01209
	52	-0.02575	-0.07399	-0.04813	0.02596	0.07437	0.04852
	53	-0.01231	-0.06785	-0.05549	0.01235	0.06810	0.05581
	54	-0.00980	-0.06631	-0.05646	0.01009	0.06675	0.05673
	55	0.01015	-0.05642	-0.06634	-0.00987	0.05669	0.06678
	56	0.01239	-0.05543	-0.06783	-0.01235	0.05574	0.06808
	57	0.02595	-0.04807	-0.07393	-0.02574	0.04846	0.07430
	58	0.00000	0.00000	0.00000	0.00000	0.00000	0.00000
	59	-0.02299	-0.01473	0.00837	0.02326	0.01492	-0.00823
	60	-0.02463	-0.01738	0.00735	0.02495	0.01761	-0.00725
	61	-0.02312	-0.01967	0.00354	0.02344	0.01995	-0.00340

	62	-0.02147	-0.02146	0.00009	0.02176	0.02175	0.00006
	63	-0.01970	-0.02313	-0.00337	0.01998	0.02344	0.00351
	64	-0.01742	-0.02466	-0.00723	0.01766	0.02498	0.00733
	65	-0.01471	-0.02301	-0.00827	0.01489	0.02328	0.00841
	66	0.00000	0.00000	0.00000	0.00000	0.00000	0.00000
	67	-0.00821	-0.02301	-0.01477	0.00835	0.02328	0.01495
	68	-0.00721	-0.02467	-0.01745	0.00731	0.02499	0.01768
	69	-0.00336	-0.02315	-0.01973	0.00351	0.02345	0.02000
	70	0.00009	-0.02149	-0.02150	0.00007	0.02177	0.02177
	71	0.00352	-0.01971	-0.02314	-0.00338	0.01998	0.02345
	72	0.00731	-0.01742	-0.02465	-0.00721	0.01765	0.02496
	73	0.00835	-0.01475	-0.02298	-0.00820	0.01493	0.02325
SEGMENT 4	Assembly No.	Direction 1	Direction 2	Direction 3	Direction 4	Direction 5	Direction 6
	1	-0.00001	-0.00003	-0.00003	-0.00001	-0.00003	-0.00003
	2	0.00798	0.00405	-0.00407	-0.00825	-0.00407	0.00405
	3	0.00495	0.00959	0.00482	-0.00501	-0.01007	-0.00486
	4	-0.01333	-0.00664	0.00663	0.01321	0.00663	-0.00664
	5	-0.00474	-0.00475	-0.00007	0.00459	0.00461	-0.00004
	6	-0.00752	-0.01501	-0.00739	0.00746	0.01471	0.00735
	7	-0.00007	-0.00475	-0.00473	-0.00004	0.00461	0.00459
	8	0.00003	-0.00001	-0.00005	-0.00005	-0.00005	-0.00001
	9	-0.01561	-0.00455	0.01085	0.01551	0.00452	-0.01121
	10	-0.00449	-0.01541	-0.01107	0.00445	0.01533	0.01073
	11	0.00005	0.00005	-0.00001	-0.00006	-0.00009	-0.00003
	12	-0.00949	-0.01477	-0.00532	0.00933	0.01470	0.00533
	13	0.00932	-0.00533	-0.01476	-0.00949	0.00533	0.01470
	14	-0.01346	-0.00665	0.00658	0.01301	0.00658	-0.00665
	15	-0.01511	-0.00281	0.01246	0.01502	0.00231	-0.01254
	16	-0.01702	-0.01700	-0.00008	0.01686	0.01684	-0.00013
	17	-0.00427	-0.01583	-0.01173	0.00396	0.01579	0.01167
	18	-0.00573	-0.01180	-0.00587	0.00561	0.01115	0.00577
	19	-0.01269	-0.01498	-0.00256	0.01259	0.01491	0.00203
	20	-0.00009	-0.01697	-0.01699	-0.00012	0.01682	0.01684
	21	0.01266	-0.00259	-0.01508	-0.01276	0.00206	0.01500
	22	-0.07378	-0.03709	0.03649	0.07339	0.03650	-0.03709
	23	-0.02744	-0.02384	0.00369	0.02737	0.02351	-0.00377
	24	-0.03003	-0.01465	0.01515	0.02977	0.01507	-0.01493
	25	-0.01335	-0.02925	-0.01539	0.01392	0.02903	0.01562
	26	-0.02385	-0.02735	-0.00368	0.02352	0.02729	0.00359
	27	-0.03707	-0.07373	-0.03705	0.03648	0.07333	0.03646
	28	-0.00367	-0.02735	-0.02385	0.00359	0.02728	0.02351
	29	-0.01503	-0.02953	-0.01403	0.01525	0.02930	0.01452

	30	0.01536	-0.01404	-0.02965	-0.01514	0.01453	0.02942
	31	0.00368	-0.02385	-0.02744	-0.00377	0.02351	0.02737
	32	-0.08541	-0.04294	0.04269	0.08583	0.04269	-0.04293
	33	-0.08209	-0.06483	0.01694	0.08159	0.06471	-0.01723
	34	-0.06854	-0.07669	-0.00817	0.06855	0.07641	0.00785
	35	0.00253	0.00259	0.00003	-0.00257	-0.00268	-0.00014
	36	-0.07732	-0.06821	0.00875	0.07703	0.06822	-0.00918
	37	-0.06494	-0.08211	-0.01713	0.06481	0.08161	0.01685
	38	-0.04303	-0.08557	-0.04300	0.04277	0.08598	0.04275
	39	-0.01714	-0.08212	-0.06494	0.01685	0.08162	0.06481
	40	0.00739	-0.06893	-0.07658	-0.00763	0.06897	0.07631
	41	-0.00003	0.00269	0.00268	-0.00004	-0.00275	-0.00274
	42	-0.00745	-0.07643	-0.06896	0.00721	0.07617	0.06899
	43	0.01695	-0.06482	-0.08210	-0.01723	0.06470	0.08160
	44	-0.03055	-0.01528	0.01541	0.03083	0.01541	-0.01528
	45	-0.09822	-0.06517	0.03300	0.09829	0.06571	-0.03265
	46	-0.07615	-0.06316	0.01287	0.07614	0.06343	-0.01283
	47	-0.05647	-0.05281	0.00379	0.05645	0.05295	-0.00337
	48	-0.05246	-0.05565	-0.00286	0.05259	0.05552	0.00327
	49	-0.06329	-0.07617	-0.01273	0.06356	0.07617	0.01277
	50	-0.06523	-0.09838	-0.03275	0.06577	0.09845	0.03309
	51	-0.01535	-0.03057	-0.01520	0.01551	0.03082	0.01534
	52	-0.03257	-0.09835	-0.06537	0.03293	0.09843	0.06591
	53	-0.01271	-0.07631	-0.06345	0.01275	0.07629	0.06371
	54	-0.00268	-0.05563	-0.05261	0.00307	0.05545	0.05273
	55	0.00323	-0.05252	-0.05570	-0.00284	0.05263	0.05551
	56	0.01286	-0.06331	-0.07628	-0.01282	0.06357	0.07627
	57	0.03292	-0.06524	-0.09822	-0.03257	0.06578	0.09829
	58	0.00000	0.00000	0.00000	0.00000	0.00000	0.00000
	59	-0.03812	-0.02463	0.01369	0.03859	0.02495	-0.01344
	60	-0.03773	-0.02662	0.01124	0.03818	0.02698	-0.01106
	61	-0.03198	-0.02755	0.00456	0.03237	0.02793	-0.00430
	62	-0.02804	-0.02799	0.00021	0.02840	0.02834	0.00010
	63	-0.02761	-0.03194	-0.00419	0.02800	0.03231	0.00445
	64	-0.02671	-0.03776	-0.01099	0.02709	0.03820	0.01117
	65	-0.02461	-0.03816	-0.01350	0.02492	0.03861	0.01374
	66	0.00000	0.00000	0.00000	0.00000	0.00000	0.00000
	67	-0.01341	-0.03817	-0.02470	0.01366	0.03863	0.02502
	68	-0.01098	-0.03772	-0.02668	0.01116	0.03814	0.02703
	69	-0.00419	-0.03186	-0.02753	0.00445	0.03220	0.02789
	70	0.00017	-0.02793	-0.02796	0.00013	0.02825	0.02828
	71	0.00449	-0.02749	-0.03186	-0.00423	0.02784	0.03219
	72	0.01117	-0.02662	-0.03767	-0.01099	0.02697	0.03809

	73	0.01364	-0.02465	-0.03809	-0.01339	0.02496	0.03855
SEGMENT 5	Assembly No.	Direction 1	Direction 2	Direction 3	Direction 4	Direction 5	Direction 6
	1	-0.00007	-0.00007	-0.00007	-0.00007	-0.00007	-0.00007
	2	0.00481	0.00245	-0.00243	-0.00497	-0.00243	0.00245
	3	0.00275	0.00535	0.00271	-0.00275	-0.00558	-0.00271
	4	-0.01273	-0.00631	0.00633	0.01256	0.00633	-0.00631
	5	-0.00374	-0.00374	-0.00003	0.00366	0.00365	-0.00004
	6	-0.00671	-0.01351	-0.00667	0.00671	0.01325	0.00667
	7	-0.00003	-0.00375	-0.00375	-0.00004	0.00367	0.00367
	8	-0.00039	-0.00023	0.00009	0.00025	0.00009	-0.00023
	9	-0.01382	-0.00387	0.00980	0.01375	0.00382	-0.01009
	10	-0.00379	-0.01374	-0.01009	0.00374	0.01367	0.00980
	11	-0.00023	-0.00047	-0.00030	0.00011	0.00033	0.00017
	12	-0.00941	-0.01349	-0.00416	0.00921	0.01343	0.00413
	13	0.00919	-0.00420	-0.01350	-0.00939	0.00417	0.01345
	14	-0.01615	-0.00799	0.00792	0.01567	0.00792	-0.00799
	15	-0.01511	-0.00615	0.00911	0.01506	0.00575	-0.00916
	16	-0.01808	-0.01795	0.00007	0.01795	0.01783	-0.00018
	17	-0.00680	-0.01528	-0.00863	0.00649	0.01525	0.00859
	18	-0.00756	-0.01537	-0.00761	0.00746	0.01479	0.00753
	19	-0.00904	-0.01489	-0.00605	0.00898	0.01484	0.00564
	20	0.00007	-0.01792	-0.01805	-0.00018	0.01779	0.01791
	21	0.00917	-0.00607	-0.01509	-0.00923	0.00566	0.01504
	22	-0.07308	-0.03676	0.03613	0.07270	0.03613	-0.03676
	23	-0.03107	-0.02767	0.00347	0.03100	0.02734	-0.00359
	24	-0.03309	-0.02406	0.00891	0.03289	0.02429	-0.00871
	25	-0.02317	-0.03240	-0.00886	0.02353	0.03221	0.00906
	26	-0.02775	-0.03102	-0.00346	0.02742	0.03095	0.00333
	27	-0.03681	-0.07313	-0.03676	0.03618	0.07275	0.03613
	28	-0.00342	-0.03099	-0.02777	0.00329	0.03093	0.02743
	29	-0.00860	-0.03253	-0.02361	0.00879	0.03235	0.02389
	30	0.00907	-0.02355	-0.03277	-0.00889	0.02383	0.03258
	31	0.00345	-0.02769	-0.03107	-0.00357	0.02735	0.03100
	32	-0.08379	-0.04215	0.04187	0.08423	0.04187	-0.04215
	33	-0.08000	-0.06560	0.01405	0.07947	0.06545	-0.01437
	34	-0.06495	-0.07839	-0.01356	0.06489	0.07805	0.01306
	35	0.00282	0.00288	0.00001	-0.00287	-0.00297	-0.00015
	36	-0.07916	-0.06465	0.01408	0.07880	0.06458	-0.01467
	37	-0.06587	-0.08009	-0.01419	0.06572	0.07956	0.01388
	38	-0.04231	-0.08411	-0.04229	0.04203	0.08453	0.04201
	39	-0.01419	-0.08011	-0.06588	0.01388	0.07957	0.06573
	40	0.01281	-0.06535	-0.07851	-0.01323	0.06531	0.07818

	41	-0.00003	0.00294	0.00293	-0.00006	-0.00300	-0.00299
	42	-0.01287	-0.07813	-0.06535	0.01244	0.07781	0.06531
	43	0.01405	-0.06559	-0.07999	-0.01437	0.06544	0.07946
	44	-0.03028	-0.01513	0.01528	0.03052	0.01528	-0.01513
	45	-0.10555	-0.07062	0.03481	0.10551	0.07123	-0.03440
	46	-0.07654	-0.06411	0.01231	0.07647	0.06437	-0.01221
	47	-0.05034	-0.05004	0.00035	0.05011	0.05019	0.00012
	48	-0.04988	-0.04959	0.00075	0.05001	0.04925	-0.00029
	49	-0.06439	-0.07661	-0.01200	0.06466	0.07653	0.01209
	50	-0.07081	-0.10588	-0.03455	0.07142	0.10584	0.03495
	51	-0.01522	-0.03029	-0.01501	0.01540	0.03049	0.01515
	52	-0.03429	-0.10584	-0.07101	0.03472	0.10580	0.07161
	53	-0.01197	-0.07681	-0.06463	0.01206	0.07673	0.06488
	54	0.00088	-0.04974	-0.05017	-0.00044	0.04937	0.05029
	55	-0.00010	-0.04997	-0.04989	0.00053	0.05009	0.04952
	56	0.01230	-0.06434	-0.07675	-0.01221	0.06459	0.07667
	57	0.03471	-0.07073	-0.10555	-0.03429	0.07133	0.10551
	58	0.00000	0.00000	0.00000	0.00000	0.00000	0.00000
	59	-0.04384	-0.02852	0.01554	0.04437	0.02891	-0.01523
	60	-0.04133	-0.02897	0.01250	0.04180	0.02938	-0.01228
	61	-0.03310	-0.02861	0.00465	0.03349	0.02901	-0.00433
	62	-0.02831	-0.02823	0.00027	0.02867	0.02858	0.00010
	63	-0.02873	-0.03306	-0.00414	0.02915	0.03342	0.00446
	64	-0.02912	-0.04139	-0.01217	0.02955	0.04185	0.01240
	65	-0.02853	-0.04393	-0.01531	0.02891	0.04444	0.01561
	66	0.00000	0.00000	0.00000	0.00000	0.00000	0.00000
	67	-0.01520	-0.04394	-0.02865	0.01550	0.04445	0.02903
	68	-0.01217	-0.04131	-0.02905	0.01239	0.04175	0.02945
	69	-0.00415	-0.03293	-0.02859	0.00447	0.03325	0.02897
	70	0.00023	-0.02810	-0.02815	0.00013	0.02841	0.02847
	71	0.00455	-0.02849	-0.03292	-0.00424	0.02887	0.03324
	72	0.01241	-0.02894	-0.04123	-0.01219	0.02934	0.04165
	73	0.01547	-0.02853	-0.04379	-0.01517	0.02891	0.04430
SEGMENT 6	Assembly No.	Direction 1	Direction 2	Direction 3	Direction 4	Direction 5	Direction 6
	1	-0.00007	-0.00007	-0.00007	-0.00007	-0.00007	-0.00007
	2	0.00346	0.00175	-0.00173	-0.00352	-0.00173	0.00175
	3	0.00201	0.00393	0.00199	-0.00201	-0.00406	-0.00197
	4	-0.00825	-0.00410	0.00412	0.00819	0.00412	-0.00410
	5	-0.00241	-0.00237	0.00001	0.00234	0.00230	-0.00007
	6	-0.00449	-0.00902	-0.00445	0.00449	0.00887	0.00447
	7	0.00000	-0.00238	-0.00241	-0.00007	0.00231	0.00234
	8	-0.00023	-0.00016	0.00000	0.00009	0.00000	-0.00016

	9	-0.00979	-0.00316	0.00655	0.00974	0.00313	-0.00671
	10	-0.00306	-0.00975	-0.00676	0.00302	0.00970	0.00661
	11	-0.00017	-0.00034	-0.00024	0.00003	0.00019	0.00009
	12	-0.00620	-0.00954	-0.00337	0.00611	0.00950	0.00335
	13	0.00603	-0.00345	-0.00953	-0.00611	0.00343	0.00949
	14	-0.01454	-0.00723	0.00716	0.01423	0.00716	-0.00723
	15	-0.01279	-0.00658	0.00630	0.01275	0.00633	-0.00633
	16	-0.01499	-0.01469	0.00026	0.01486	0.01455	-0.00035
	17	-0.00714	-0.01275	-0.00570	0.00697	0.01273	0.00567
	18	-0.00682	-0.01379	-0.00687	0.00673	0.01340	0.00679
	19	-0.00604	-0.01242	-0.00651	0.00599	0.01237	0.00625
	20	0.00026	-0.01465	-0.01497	-0.00036	0.01453	0.01483
	21	0.00635	-0.00651	-0.01277	-0.00639	0.00625	0.01273
	22	-0.06437	-0.03238	0.03180	0.06400	0.03180	-0.03238
	23	-0.02667	-0.02443	0.00229	0.02659	0.02413	-0.00241
	24	-0.02767	-0.01983	0.00771	0.02751	0.02011	-0.00753
	25	-0.01917	-0.02686	-0.00734	0.01955	0.02671	0.00752
	26	-0.02463	-0.02667	-0.00221	0.02432	0.02658	0.00209
	27	-0.03255	-0.06465	-0.03251	0.03197	0.06429	0.03192
	28	-0.00217	-0.02664	-0.02465	0.00205	0.02656	0.02434
	29	-0.00711	-0.02696	-0.01953	0.00728	0.02681	0.01985
	30	0.00786	-0.01938	-0.02739	-0.00768	0.01970	0.02724
	31	0.00228	-0.02445	-0.02667	-0.00239	0.02414	0.02659
	32	-0.07598	-0.03822	0.03795	0.07637	0.03795	-0.03822
	33	-0.07201	-0.05929	0.01241	0.07151	0.05914	-0.01269
	34	-0.05856	-0.06969	-0.01121	0.05848	0.06938	0.01083
	35	0.00243	0.00250	0.00001	-0.00250	-0.00259	-0.00015
	36	-0.07081	-0.05838	0.01209	0.07048	0.05829	-0.01255
	37	-0.05986	-0.07230	-0.01241	0.05971	0.07180	0.01212
	38	-0.03850	-0.07653	-0.03848	0.03823	0.07690	0.03821
	39	-0.01241	-0.07231	-0.05987	0.01212	0.07181	0.05973
	40	0.01097	-0.05899	-0.07024	-0.01129	0.05894	0.06993
	41	-0.00003	0.00255	0.00253	-0.00007	-0.00262	-0.00260
	42	-0.01061	-0.06947	-0.05890	0.01029	0.06917	0.05885
	43	0.01241	-0.05928	-0.07200	-0.01269	0.05913	0.07151
	44	-0.02773	-0.01385	0.01399	0.02795	0.01399	-0.01385
	45	-0.09601	-0.06435	0.03156	0.09598	0.06490	-0.03118
	46	-0.06958	-0.05863	0.01084	0.06952	0.05887	-0.01076
	47	-0.04697	-0.04654	0.00051	0.04683	0.04669	-0.00007
	48	-0.04659	-0.04620	0.00079	0.04674	0.04597	-0.00036
	49	-0.05917	-0.06973	-0.01037	0.05941	0.06967	0.01045
	50	-0.06479	-0.09661	-0.03135	0.06534	0.09657	0.03171
	51	-0.01398	-0.02781	-0.01378	0.01414	0.02800	0.01391

	52	-0.03111	-0.09657	-0.06498	0.03149	0.09653	0.06553
	53	-0.01035	-0.06993	-0.05939	0.01043	0.06985	0.05962
	54	0.00091	-0.04635	-0.04687	-0.00050	0.04609	0.04699
	55	0.00012	-0.04650	-0.04660	0.00029	0.04662	0.04634
	56	0.01083	-0.05884	-0.06979	-0.01075	0.05907	0.06971
	57	0.03147	-0.06446	-0.09602	-0.03109	0.06500	0.09599
	58	0.00000	0.00000	0.00000	0.00000	0.00000	0.00000
	59	-0.04013	-0.02613	0.01421	0.04061	0.02648	-0.01393
	60	-0.03775	-0.02655	0.01134	0.03819	0.02692	-0.01113
	61	-0.03023	-0.02623	0.00413	0.03058	0.02660	-0.00384
	62	-0.02590	-0.02579	0.00029	0.02623	0.02611	0.00005
	63	-0.02642	-0.03020	-0.00360	0.02681	0.03053	0.00390
	64	-0.02678	-0.03790	-0.01103	0.02717	0.03831	0.01123
	65	-0.02623	-0.04034	-0.01403	0.02657	0.04080	0.01430
	66	0.00000	0.00000	0.00000	0.00000	0.00000	0.00000
	67	-0.01392	-0.04034	-0.02633	0.01420	0.04081	0.02668
	68	-0.01102	-0.03783	-0.02672	0.01122	0.03822	0.02708
	69	-0.00361	-0.03007	-0.02629	0.00391	0.03037	0.02663
	70	0.00025	-0.02567	-0.02575	0.00008	0.02595	0.02604
	71	0.00405	-0.02613	-0.03006	-0.00377	0.02647	0.03035
	72	0.01125	-0.02652	-0.03765	-0.01105	0.02688	0.03805
	73	0.01414	-0.02614	-0.04009	-0.01386	0.02649	0.04055
SEGMENT 7	Assembly No.	Direction 1	Direction 2	Direction 3	Direction 4	Direction 5	Direction 6
	1	-0.00002	-0.00003	-0.00003	-0.00002	-0.00003	-0.00003
	2	-0.00082	-0.00044	0.00042	0.00091	0.00042	-0.00044
	3	-0.00002	-0.00007	-0.00008	-0.00003	0.00005	0.00004
	4	0.00250	0.00118	-0.00119	-0.00224	-0.00119	0.00118
	5	-0.00121	-0.00132	-0.00016	0.00110	0.00121	0.00007
	6	-0.00003	0.00009	0.00003	-0.00001	-0.00001	-0.00007
	7	-0.00016	-0.00132	-0.00121	0.00007	0.00121	0.00110
	8	0.00063	0.00028	-0.00039	-0.00072	-0.00039	0.00028
	9	-0.00198	-0.00429	-0.00225	0.00193	0.00427	0.00238
	10	-0.00353	-0.00257	0.00101	0.00349	0.00253	-0.00093
	11	0.00028	0.00054	0.00023	-0.00035	-0.00064	-0.00032
	12	0.00182	-0.00225	-0.00396	-0.00164	0.00221	0.00395
	13	-0.00310	-0.00472	-0.00152	0.00334	0.00471	0.00149
	14	-0.01287	-0.00650	0.00643	0.01300	0.00643	-0.00650
	15	-0.01078	-0.00865	0.00205	0.01071	0.00871	-0.00208
	16	-0.00916	-0.00871	0.00037	0.00899	0.00854	-0.00051
	17	-0.00852	-0.01017	-0.00159	0.00863	0.01011	0.00156
	18	-0.00546	-0.01093	-0.00553	0.00537	0.01088	0.00545
	19	-0.00209	-0.00971	-0.00762	0.00203	0.00964	0.00762

	20	0.00037	-0.00869	-0.00914	-0.00051	0.00853	0.00897
	21	0.00216	-0.00853	-0.01076	-0.00220	0.00857	0.01069
	22	-0.04837	-0.02433	0.02385	0.04798	0.02385	-0.02433
	23	-0.01595	-0.01585	0.00012	0.01584	0.01560	-0.00021
	24	-0.01492	-0.00374	0.01095	0.01480	0.00424	-0.01079
	25	-0.00317	-0.01379	-0.01019	0.00377	0.01367	0.01033
	26	-0.01607	-0.01589	0.00004	0.01580	0.01579	-0.00014
	27	-0.02475	-0.04921	-0.02474	0.02427	0.04881	0.02425
	28	0.00005	-0.01589	-0.01607	-0.00015	0.01579	0.01580
	29	-0.00998	-0.01394	-0.00355	0.01011	0.01382	0.00411
	30	0.01108	-0.00334	-0.01467	-0.01093	0.00389	0.01457
	31	0.00011	-0.01586	-0.01595	-0.00021	0.01560	0.01584
	32	-0.06390	-0.03212	0.03193	0.06419	0.03193	-0.03212
	33	-0.05935	-0.04770	0.01137	0.05891	0.04758	-0.01161
	34	-0.04967	-0.05220	-0.00247	0.04959	0.05196	0.00245
	35	0.00191	0.00199	0.00002	-0.00201	-0.00211	-0.00016
	36	-0.05392	-0.04983	0.00395	0.05365	0.04976	-0.00404
	37	-0.04878	-0.06009	-0.01127	0.04866	0.05965	0.01103
	38	-0.03261	-0.06486	-0.03259	0.03241	0.06514	0.03239
	39	-0.01127	-0.06009	-0.04879	0.01103	0.05965	0.04866
	40	0.00307	-0.05029	-0.05344	-0.00304	0.05025	0.05321
	41	-0.00002	0.00205	0.00201	-0.00009	-0.00215	-0.00212
	42	-0.00203	-0.05205	-0.04992	0.00206	0.05181	0.04986
	43	0.01137	-0.04770	-0.05935	-0.01161	0.04757	0.05891
	44	-0.02323	-0.01161	0.01172	0.02344	0.01172	-0.01161
	45	-0.07377	-0.04927	0.02445	0.07383	0.04967	-0.02420
	46	-0.05734	-0.04838	0.00888	0.05734	0.04857	-0.00885
	47	-0.04680	-0.04329	0.00369	0.04700	0.04346	-0.00336
	48	-0.04359	-0.04602	-0.00225	0.04376	0.04616	0.00258
	49	-0.04926	-0.05769	-0.00832	0.04945	0.05769	0.00834
	50	-0.05001	-0.07468	-0.02437	0.05041	0.07474	0.02462
	51	-0.01179	-0.02347	-0.01167	0.01191	0.02367	0.01177
	52	-0.02422	-0.07465	-0.05013	0.02448	0.07471	0.05053
	53	-0.00830	-0.05780	-0.04939	0.00833	0.05779	0.04957
	54	-0.00213	-0.04603	-0.04372	0.00244	0.04613	0.04387
	55	0.00334	-0.04316	-0.04637	-0.00303	0.04331	0.04647
	56	0.00887	-0.04851	-0.05746	-0.00885	0.04869	0.05745
	57	0.02439	-0.04934	-0.07377	-0.02414	0.04973	0.07383
	58	0.00000	0.00000	0.00000	0.00000	0.00000	0.00000
	59	-0.02905	-0.01885	0.01035	0.02941	0.01909	-0.01016
	60	-0.02850	-0.02037	0.00823	0.02883	0.02064	-0.00809
	61	-0.02409	-0.02115	0.00304	0.02437	0.02143	-0.00284
	62	-0.02145	-0.02132	0.00025	0.02172	0.02157	-0.00002

	63	-0.02141	-0.02411	-0.00259	0.02170	0.02437	0.00279
	64	-0.02067	-0.02874	-0.00801	0.02096	0.02907	0.00815
	65	-0.01903	-0.02937	-0.01028	0.01929	0.02971	0.01047
	66	0.00000	0.00000	0.00000	0.00000	0.00000	0.00000
	67	-0.01020	-0.02937	-0.01911	0.01039	0.02971	0.01937
	68	-0.00801	-0.02871	-0.02065	0.00815	0.02902	0.02091
	69	-0.00260	-0.02405	-0.02134	0.00279	0.02429	0.02161
	70	0.00023	-0.02127	-0.02138	0.00000	0.02150	0.02162
	71	0.00299	-0.02110	-0.02400	-0.00279	0.02137	0.02425
	72	0.00817	-0.02037	-0.02845	-0.00803	0.02063	0.02876
	73	0.01031	-0.01886	-0.02903	-0.01011	0.01911	0.02937
SEGMENT 8	Assembly No.	Direction 1	Direction 2	Direction 3	Direction 4	Direction 5	Direction 6
	1	0.00001	0.00001	0.00001	0.00001	0.00001	0.00001
	2	-0.01207	-0.00609	0.00601	0.01211	0.00601	-0.00609
	3	-0.00512	-0.01011	-0.00515	0.00501	0.01021	0.00505
	4	0.00042	0.00001	-0.00009	0.00021	-0.00009	0.00001
	5	-0.01276	-0.01095	0.00159	0.01229	0.01047	-0.00205
	6	-0.00381	-0.00735	-0.00376	0.00372	0.00762	0.00367
	7	0.00160	-0.01093	-0.01275	-0.00206	0.01045	0.01229
	8	0.00015	0.00007	-0.00011	-0.00018	-0.00011	0.00007
	9	-0.01422	-0.02368	-0.00922	0.01407	0.02361	0.00977
	10	-0.02059	-0.01545	0.00523	0.02052	0.01535	-0.00505
	11	0.00021	0.00040	0.00017	-0.00026	-0.00045	-0.00022
	12	0.00502	-0.01561	-0.02055	-0.00487	0.01550	0.02047
	13	-0.00937	-0.02379	-0.01416	0.00995	0.02371	0.01401
	14	-0.05167	-0.02604	0.02586	0.05214	0.02586	-0.02604
	15	-0.04264	-0.04039	0.00194	0.04252	0.04080	-0.00203
	16	-0.03394	-0.03080	0.00292	0.03339	0.03027	-0.00334
	17	-0.03389	-0.03622	-0.00227	0.03395	0.03607	0.00217
	18	-0.02229	-0.04430	-0.02227	0.02209	0.04443	0.02209
	19	-0.00219	-0.03624	-0.03397	0.00211	0.03610	0.03405
	20	0.00293	-0.03081	-0.03395	-0.00334	0.03027	0.03339
	21	0.00203	-0.04023	-0.04257	-0.00213	0.04062	0.04245
	22	-0.04755	-0.02381	0.02366	0.04738	0.02366	-0.02381
	23	-0.04927	-0.03931	0.00980	0.04887	0.03886	-0.01017
	24	-0.04222	-0.02960	0.01235	0.04215	0.03011	-0.01230
	25	-0.03291	-0.04099	-0.00773	0.03349	0.04089	0.00775
	26	-0.04223	-0.05096	-0.00894	0.04178	0.05056	0.00857
	27	-0.02487	-0.04965	-0.02486	0.02473	0.04953	0.02472
	28	-0.00893	-0.05096	-0.04224	0.00855	0.05057	0.04179
	29	-0.00770	-0.04091	-0.03286	0.00771	0.04081	0.03345
	30	0.01235	-0.02951	-0.04213	-0.01229	0.03005	0.04206

	31	0.00982	-0.03931	-0.04929	-0.01019	0.03886	0.04889
	32	-0.05305	-0.02660	0.02656	0.05329	0.02656	-0.02660
	33	-0.05572	-0.03962	0.01604	0.05569	0.03956	-0.01619
	34	-0.05628	-0.04214	0.01445	0.05647	0.04219	-0.01397
	35	-0.00236	-0.00231	0.00003	0.00231	0.00224	-0.00009
	36	-0.04445	-0.05704	-0.01243	0.04451	0.05723	0.01288
	37	-0.04119	-0.05725	-0.01615	0.04114	0.05724	0.01601
	38	-0.02731	-0.05443	-0.02729	0.02726	0.05469	0.02725
	39	-0.01614	-0.05725	-0.04121	0.01599	0.05724	0.04115
	40	-0.01264	-0.05717	-0.04435	0.01312	0.05736	0.04441
	41	0.00001	-0.00229	-0.00233	-0.00007	0.00223	0.00227
	42	0.01441	-0.04216	-0.05627	-0.01393	0.04221	0.05645
	43	0.01603	-0.03962	-0.05571	-0.01617	0.03956	0.05569
	44	-0.01387	-0.00695	0.00704	0.01413	0.00704	-0.00695
	45	-0.04570	-0.03013	0.01565	0.04597	0.03035	-0.01555
	46	-0.04436	-0.03797	0.00640	0.04456	0.03814	-0.00641
	47	-0.05507	-0.04613	0.00924	0.05577	0.04638	-0.00909
	48	-0.04673	-0.05480	-0.00821	0.04699	0.05550	0.00837
	49	-0.03895	-0.04488	-0.00595	0.03913	0.04508	0.00594
	50	-0.03091	-0.04665	-0.01571	0.03114	0.04693	0.01581
	51	-0.00709	-0.01411	-0.00706	0.00718	0.01436	0.00715
	52	-0.01567	-0.04664	-0.03095	0.01577	0.04693	0.03117
	53	-0.00594	-0.04490	-0.03898	0.00593	0.04511	0.03915
	54	-0.00813	-0.05472	-0.04672	0.00829	0.05539	0.04697
	55	0.00917	-0.04612	-0.05499	-0.00902	0.04636	0.05567
	56	0.00639	-0.03801	-0.04438	-0.00640	0.03817	0.04458
	57	0.01563	-0.03015	-0.04570	-0.01554	0.03036	0.04597
	58	0.00000	0.00000	0.00000	0.00000	0.00000	0.00000
	59	-0.01367	-0.00891	0.00483	0.01383	0.00903	-0.00473
	60	-0.01397	-0.01017	0.00386	0.01417	0.01033	-0.00379
	61	-0.01297	-0.01167	0.00135	0.01317	0.01185	-0.00126
	62	-0.01229	-0.01219	0.00017	0.01249	0.01237	-0.00005
	63	-0.01187	-0.01300	-0.00109	0.01207	0.01320	0.00118
	64	-0.01039	-0.01416	-0.00375	0.01055	0.01436	0.00383
	65	-0.00908	-0.01395	-0.00483	0.00921	0.01410	0.00493
	66	0.00000	0.00000	0.00000	0.00000	0.00000	0.00000
	67	-0.00477	-0.01395	-0.00913	0.00488	0.01410	0.00926
	68	-0.00375	-0.01418	-0.01041	0.00382	0.01438	0.01057
	69	-0.00109	-0.01303	-0.01191	0.00118	0.01322	0.01209
	70	0.00016	-0.01223	-0.01234	-0.00005	0.01242	0.01253
	71	0.00135	-0.01171	-0.01299	-0.00125	0.01188	0.01319
	72	0.00384	-0.01020	-0.01399	-0.00377	0.01035	0.01418
	73	0.00481	-0.00891	-0.01366	-0.00471	0.00904	0.01381

SEGMENT 9	Assembly No.	Direction 1	Direction 2	Direction 3	Direction 4	Direction 5	Direction 6
	1	-0.00388	-0.00395	-0.00396	-0.00389	-0.00395	-0.00393
	2	-0.00471	-0.00232	0.00253	0.00500	0.00253	-0.00232
	3	-0.00213	-0.00439	-0.00221	0.00229	0.00463	0.00238
	4	0.02029	0.01011	-0.00975	-0.01942	-0.00975	0.01011
	5	-0.00015	-0.00039	-0.00021	0.00023	0.00047	0.00027
	6	0.00179	0.00363	0.00187	-0.00168	-0.00347	-0.00176
	7	-0.00021	-0.00039	-0.00015	0.00028	0.00047	0.00023
	8	-0.02148	-0.00881	0.01708	0.03030	0.01707	-0.00882
	9	0.00580	-0.01171	-0.01719	-0.00552	0.01213	0.01798
	10	-0.00378	-0.00027	0.00362	0.00395	0.00041	-0.00343
	11	0.00549	0.01389	0.00531	-0.01164	-0.02011	-0.01157
	12	0.00381	-0.00022	-0.00391	-0.00361	0.00036	0.00409
	13	-0.01770	-0.01190	0.00616	0.01854	0.01231	-0.00586
	14	-0.01523	-0.00761	0.00800	0.01601	0.00800	-0.00761
	15	-0.01082	-0.01545	-0.00459	0.01128	0.01624	0.00499
	16	-0.00191	-0.00175	0.00021	0.00197	0.00181	-0.00012
	17	-0.00425	-0.00401	0.00035	0.00449	0.00421	-0.00017
	18	-0.00245	-0.00503	-0.00253	0.00259	0.00523	0.00268
	19	0.00023	-0.00396	-0.00409	-0.00007	0.00415	0.00433
	20	0.00020	-0.00174	-0.00189	-0.00011	0.00181	0.00196
	21	-0.00443	-0.01551	-0.01103	0.00481	0.01630	0.01152
	22	-0.00330	-0.00163	0.00167	0.00331	0.00167	-0.00163
	23	-0.00355	-0.00175	0.00180	0.00361	0.00186	-0.00176
	24	0.00214	0.01019	0.00803	-0.00195	-0.00970	-0.00777
	25	0.01030	0.00301	-0.00702	-0.00981	-0.00284	0.00723
	26	-0.00185	-0.00388	-0.00199	0.00197	0.00395	0.00203
	27	-0.00182	-0.00369	-0.00183	0.00187	0.00370	0.00187
	28	-0.00199	-0.00389	-0.00186	0.00203	0.00396	0.00197
	29	-0.00679	0.00284	0.00988	0.00699	-0.00267	-0.00941
	30	0.00789	0.01009	0.00218	-0.00764	-0.00961	-0.00197
	31	0.00179	-0.00175	-0.00355	-0.00175	0.00186	0.00361
	32	-0.00421	-0.00209	0.00213	0.00423	0.00213	-0.00209
	33	-0.00370	-0.00244	0.00128	0.00375	0.00247	-0.00126
	34	-0.00951	-0.00115	0.00861	0.00975	0.00125	-0.00825
	35	-0.02907	-0.02709	0.00427	0.03350	0.03115	-0.00005
	36	-0.00141	-0.01047	-0.00896	0.00149	0.01073	0.00935
	37	-0.00264	-0.00401	-0.00137	0.00267	0.00406	0.00139
	38	-0.00223	-0.00447	-0.00222	0.00227	0.00450	0.00226
	39	-0.00137	-0.00401	-0.00264	0.00139	0.00405	0.00267
	40	-0.00918	-0.01052	-0.00122	0.00959	0.01077	0.00131
	41	0.00428	-0.02699	-0.02898	0.00013	0.03107	0.03323

	42	0.00899	-0.00100	-0.00972	-0.00860	0.00110	0.00997
	43	0.00128	-0.00244	-0.00371	-0.00126	0.00247	0.00375
	44	-0.00327	-0.00163	0.00175	0.00349	0.00175	-0.00163
	45	-0.00303	-0.00194	0.00110	0.00306	0.00195	-0.00109
	46	-0.00385	-0.00319	0.00069	0.00389	0.00322	-0.00063
	47	-0.00747	-0.00666	0.00095	0.00783	0.00693	-0.00076
	48	-0.00683	-0.00746	-0.00057	0.00711	0.00781	0.00075
	49	-0.00333	-0.00399	-0.00064	0.00335	0.00403	0.00069
	50	-0.00201	-0.00313	-0.00113	0.00201	0.00317	0.00113
	51	-0.00167	-0.00334	-0.00165	0.00179	0.00355	0.00177
	52	-0.00109	-0.00312	-0.00203	0.00110	0.00316	0.00205
	53	-0.00065	-0.00401	-0.00334	0.00071	0.00405	0.00337
	54	-0.00044	-0.00753	-0.00704	0.00061	0.00789	0.00732
	55	0.00074	-0.00669	-0.00731	-0.00057	0.00695	0.00765
	56	0.00069	-0.00321	-0.00386	-0.00064	0.00323	0.00391
	57	0.00108	-0.00195	-0.00301	-0.00107	0.00196	0.00305
	58	0.00000	0.00000	0.00000	0.00000	0.00000	0.00000
	59	-0.00582	-0.00353	0.00233	0.00590	0.00358	-0.00228
	60	-0.00403	-0.00330	0.00077	0.00411	0.00339	-0.00068
	61	-0.00226	-0.00331	-0.00106	0.00231	0.00344	0.00113
	62	-0.00219	-0.00208	0.00015	0.00229	0.00218	-0.00007
	63	-0.00351	-0.00229	0.00131	0.00365	0.00233	-0.00123
	64	-0.00345	-0.00413	-0.00063	0.00355	0.00421	0.00071
	65	-0.00368	-0.00609	-0.00239	0.00373	0.00617	0.00245
	66	0.00000	0.00000	0.00000	0.00000	0.00000	0.00000
	67	-0.00237	-0.00609	-0.00370	0.00243	0.00617	0.00375
	68	-0.00063	-0.00415	-0.00347	0.00072	0.00423	0.00356
	69	0.00131	-0.00229	-0.00352	-0.00123	0.00233	0.00365
	70	0.00013	-0.00197	-0.00207	-0.00006	0.00206	0.00216
	71	-0.00109	-0.00333	-0.00225	0.00116	0.00345	0.00229
	72	0.00074	-0.00331	-0.00401	-0.00066	0.00339	0.00409
	73	0.00232	-0.00353	-0.00581	-0.00227	0.00357	0.00588
SEGMENT10	Assembly No.	Direction 1	Direction 2	Direction 3	Direction 4	Direction 5	Direction 6
	1	-0.00087	-0.00097	-0.00098	-0.00089	-0.00098	-0.00097
	2	-0.00044	-0.00022	0.00025	0.00051	0.00025	-0.00022
	3	-0.00026	-0.00052	-0.00026	0.00029	0.00059	0.00030
	4	0.00031	0.00016	-0.00011	-0.00023	-0.00011	0.00016
	5	-0.00006	-0.00006	0.00000	0.00007	0.00008	0.00001
	6	0.00017	0.00034	0.00017	-0.00014	-0.00029	-0.00015
	7	0.00001	-0.00003	-0.00005	-0.00001	0.00005	0.00006
	8	-0.00481	-0.00214	0.00351	0.00648	0.00351	-0.00214
	9	0.00036	0.00001	-0.00031	-0.00030	0.00004	0.00039

	10	0.00001	0.00031	0.00032	0.00001	-0.00028	-0.00027
	11	0.00049	0.00161	0.00041	-0.00187	-0.00312	-0.00195
	12	0.00034	0.00031	0.00000	-0.00028	-0.00028	0.00003
	13	-0.00033	0.00000	0.00038	0.00041	0.00005	-0.00032
	14	-0.00070	-0.00034	0.00039	0.00076	0.00039	-0.00034
	15	-0.00001	-0.00047	-0.00045	0.00005	0.00053	0.00049
	16	-0.00003	-0.00008	-0.00003	0.00005	0.00009	0.00005
	17	-0.00047	-0.00013	0.00037	0.00053	0.00016	-0.00033
	18	-0.00030	-0.00059	-0.00029	0.00033	0.00064	0.00032
	19	0.00038	-0.00012	-0.00047	-0.00035	0.00014	0.00052
	20	-0.00005	-0.00011	-0.00005	0.00006	0.00012	0.00007
	21	-0.00044	-0.00048	-0.00003	0.00049	0.00054	0.00007
	22	-0.00016	-0.00008	0.00009	0.00017	0.00009	-0.00008
	23	-0.00031	-0.00017	0.00014	0.00031	0.00017	-0.00013
	24	0.00015	0.00007	-0.00008	-0.00012	-0.00002	0.00010
	25	0.00023	0.00015	-0.00005	-0.00018	-0.00013	0.00008
	26	-0.00017	-0.00024	-0.00007	0.00017	0.00025	0.00008
	27	-0.00005	-0.00011	-0.00005	0.00006	0.00011	0.00005
	28	-0.00007	-0.00023	-0.00016	0.00007	0.00024	0.00017
	29	-0.00001	0.00017	0.00021	0.00004	-0.00014	-0.00015
	30	-0.00010	0.00007	0.00017	0.00012	-0.00002	-0.00014
	31	0.00014	-0.00017	-0.00030	-0.00013	0.00017	0.00031
	32	0.00017	0.00009	-0.00008	-0.00017	-0.00008	0.00009
	33	-0.00004	0.00004	0.00008	0.00005	-0.00003	-0.00007
	34	-0.00003	0.00034	0.00038	0.00005	-0.00031	-0.00034
	35	-0.00554	-0.00493	0.00108	0.00638	0.00562	-0.00029
	36	0.00043	0.00003	-0.00038	-0.00039	0.00000	0.00041
	37	0.00009	-0.00001	-0.00009	-0.00008	0.00001	0.00010
	38	0.00011	0.00021	0.00011	-0.00011	-0.00021	-0.00010
	39	-0.00009	-0.00001	0.00008	0.00009	0.00001	-0.00007
	40	-0.00039	-0.00001	0.00041	0.00043	0.00003	-0.00037
	41	0.00103	-0.00485	-0.00542	-0.00015	0.00554	0.00616
	42	0.00038	0.00031	-0.00005	-0.00035	-0.00027	0.00008
	43	0.00009	0.00004	-0.00004	-0.00008	-0.00003	0.00005
	44	-0.00049	-0.00025	0.00026	0.00053	0.00026	-0.00025
	45	0.00029	0.00022	-0.00006	-0.00028	-0.00022	0.00007
	46	0.00010	0.00030	0.00019	-0.00010	-0.00029	-0.00019
	47	-0.00042	0.00003	0.00047	0.00045	0.00000	-0.00043
	48	0.00005	-0.00042	-0.00046	-0.00003	0.00045	0.00049
	49	0.00033	0.00013	-0.00020	-0.00033	-0.00013	0.00021
	50	0.00025	0.00032	0.00007	-0.00025	-0.00031	-0.00006
	51	-0.00025	-0.00050	-0.00024	0.00027	0.00053	0.00026
	52	0.00007	0.00032	0.00025	-0.00006	-0.00031	-0.00025

	53	-0.00020	0.00013	0.00033	0.00021	-0.00013	-0.00033
	54	-0.00044	-0.00041	0.00004	0.00047	0.00044	-0.00001
	55	0.00045	0.00004	-0.00039	-0.00043	-0.00001	0.00043
	56	0.00019	0.00030	0.00011	-0.00019	-0.00029	-0.00011
	57	-0.00006	0.00022	0.00028	0.00007	-0.00021	-0.00027
	58	0.00000	0.00000	0.00000	0.00000	0.00000	0.00000
	59	-0.00140	-0.00077	0.00065	0.00143	0.00077	-0.00064
	60	-0.00083	-0.00087	-0.00003	0.00085	0.00089	0.00005
	61	-0.00055	-0.00086	-0.00030	0.00057	0.00088	0.00031
	62	-0.00021	-0.00017	0.00005	0.00023	0.00018	-0.00003
	63	-0.00094	-0.00056	0.00039	0.00097	0.00057	-0.00038
	64	-0.00095	-0.00087	0.00009	0.00096	0.00088	-0.00007
	65	-0.00081	-0.00149	-0.00068	0.00082	0.00151	0.00069
	66	0.00000	0.00000	0.00000	0.00000	0.00000	0.00000
	67	-0.00069	-0.00150	-0.00082	0.00069	0.00153	0.00083
	68	0.00008	-0.00089	-0.00095	-0.00005	0.00090	0.00097
	69	0.00039	-0.00055	-0.00092	-0.00037	0.00056	0.00095
	70	0.00005	-0.00013	-0.00017	-0.00003	0.00013	0.00017
	71	-0.00033	-0.00083	-0.00050	0.00034	0.00085	0.00051
	72	-0.00004	-0.00087	-0.00081	0.00007	0.00088	0.00083
	73	0.00064	-0.00075	-0.00139	-0.00063	0.00077	0.00141

Department of Nuclear Engineering and Radiological Sciences

University of Michigan

2355 Bonisteel Blvd.

Ann Arbor, MI 48109-2104

https://ners.engin.umich.edu/